EFFECTS OF PLANAR ANISOTROPY ON ELIASHBERG SUPERCONDUCTORS

By

Chao Jiang, B.Sc., M.Sc.

A Thesis

Submitted to the Faculty of Graduate Studies

in Partial Fulfilment of the Requirements

for the Degree

Doctor of Philosophy

McMaster University

December 1992

EFFECTS OF PLANAR ANISOTROPY ON ELIASHBERG SUPERCONDUCTORS

DOCTOR OF PHILOSOPHY(1992) McMASTER UNIVERSITY

(Physics) Hamilton, Ontario

TITLE: Effects of Planar Anisotropy on Eliashberg Superconductors

AUTHOR: Chao Jiang, B.Sc. (Fudan University)

M.Sc. (Shanghai Institute of Metallurgy)

SUPERVISOR: Dr. Jules P. Carbotte

NUMBER OF PAGES: ix, 202

ABSTRACT

Within the context of Eliashberg theory, we have studied the effects of planar anisotropy on many superconducting properties. Planar anisotropy is of interest for superconductors with layered crystal structure, such as the metallic transition metal dichalcogenide and high-T_c oxide superconductors.

To describe planar anisotropy we use a model dispersion relation which gives free-particle-like electronic states in the direction parallel to the layers and the tight-binding form in the direction perpendicular to the layers. Using this dispersion relation and the Fermi-Surface-Harmonic (FSH) expansion technique, we specify the general anisotropic Eliashberg equations for the problem of planar anisotropy.

We begin with the study of the effects of planar anisotropy on the superconducting transition temperature, the thermodynamic critical magnetic field, and the quasiparticle density of states in the superconducting state. For all these properties, especially the quasiparticle density of states, the effects of planar anisotropy are usually quite significant.

Next, we study some thermodynamic and transport properties, namely, the specific heat, the thermal conductivity, and the ultrasound attenuation. The effects of planar anisotropy on these properties are closely related to the changes in the quasiparticle density of states due to anisotropy. The changes in the quasiparticle lifetime due to the superconducting phase transition and anisotropy are also important for the unusual behaviors of thermal conductivity at low temperature.

Several electromagnetic properties are also studied. The introduction of anisotropy usually reduces the value of the London penetration depth

below its isotropic value, and strongly depresses the Hebel-Slichter peak in the nuclear spin relaxation rate. The theoretical results for the nuclear spin relaxation rate with strong coupling, anisotropy and Fermi liquid corrections have been compared with the experimental data for the high-T_c oxides. The major effect of planar anisotropy on the infrared conductivity is to reduce the frequency at which the absorption starts.

Finally, we have examined the changes of the phonon self-energy when the superconducting phase transition occurs. It is found that there is a qualitative difference between the results for isotropic superconductors and for anisotropic ones. This may be displayed in experiment under certain conditions. Anisotropy also complicates the analysis of the structures in the phonon self-energy.

It is generally true, for all the properties which we have studied, that the effects of anisotropy will be diminished if we increase the coupling strengths, and/or introduce impurity scatterings.

Besides the problem of planar anisotropy, we briefly discuss the problem of an energy dependent electronic density of states (EDOS) for Eliashberg superconductors. This is of interest for a model of two-dimensional tight-binding dispersion relation. For a Lorentzian form for EDOS around the Fermi level, we have discussed the modifications of the Eliashberg equations and, then, calculated the quasiparticle density of states in the superconducting state. The effects of an energy dependent electronic density of states on the temperature evolution of the quasiparticle density of states below T_c is particularly interesting.

To my father,
Fu Ji Jiang

ACKNOWLEDGEMENTS

I would like to thank my supervisor, Dr. Jules P. Carbotte, for his guidance and encouragement during the course of my Ph.D work. He is the most wonderful supervisor in many respects that I could ever have had.

I am greatly indebted to the faculty of the physics and astronomy department for their help and encouragement; in particular, Drs. Goodings, Kallin, Pudritz, and Timusk.

My supervisory committee members, Dr. Bruce. D. Gaulin and Dr. Randall S. Dumont, are acknowledged for their interest in my work and encouragement.

I have benefited greatly from discussions with several present and former post doctoral fellows and students in our group, namely, Dr. Richard Akis, Matt Greeson, Dr. Steven Lenck, Dr. Frank Marsiglio, Dr. Elisabeth Nicol, Dr. Michael Prohammer, and Dr. Peter Williams. Dr. Michael Prohammer, in particular, was very helpful with regards to the programs used in this work. Dr. Elisabeth Nicol also deserved special thanks for her help and friendship over these years.

The programs used in this work were based on programs written by former students; in particular, Dr. Frank Marsiglio.

The help and friendship of my officemates, Shuxi Li and Tom Szeredi, were very much appreciated.

Finally, I wish to thank my wife, Weiping Xiao, for her support and understanding through these years, and especially in the past several months as she took all the responsibilities for caring for our new born child, Jeremy Jiang.

Acknowledgements

As to financial support, I have benefited from Centennial Scholarships, Desmond G. Burns Graduate Scholarship, Ontario Graduate Scholarships (OGS), and The Yates Scholarship Fund.

Table of Contents

Chapter 1

Introduction

Superconductivity was first discovered by Kamerlingh Onnes in mercury (Hg) with a superconducting transition temperature of $4K$ in 1911. Since then superconductivity has been found in many other materials and the transition temperature or T_c for short, has been steadily increased [Hulm and Matthias (1981)]. However, until 1986 all superconductors discovered had T_c values well below liquid nitrogen temperature ($\sim 77K$). The low transition temperature makes the application of superconductivity very costly since liquid helium has to be used as the cooling media. Begining with the discovery by J.G. Bednorz and K.A. Müller in early 1986 that $Ba_xLa_{5-x}Cu_5O_{5(3-y)}$ became superconducting at $T \sim 30$ K, a large class of Cu-based oxide superconductors with T_c well above the liquid nitrogen temperature ($\sim 77K$) has soon been discovered [Wu *et al.* (1987); Maeda *et al.* (1988); Chu *et al.* (1988); Sheng and Hermann (1988a,b)]. With this remarkable discovery, the application of superconductivity on a large scale becomes possible and the existence

of superconductivity at room temperature is closer to reality. These surprising discoveries and the new challenges they present have kept superconductivity one of the most fascinating fields for physicists both theoretically and experimentally. Here, we will give a brief introduction to the theory of superconductivity and to the problems which we are interested in this thesis.

1.1 THEORY OF SUPERCONDUCTIVITY

The first successful microscopic theory of superconductivity was proposed by Bardeen, Cooper and Schrieffer in 1957, which is referred to as BCS theory. In the framework of BCS theory, electrons attract with one another through the exchange of virtual phonons. With this attractive interaction, which overcomes the repulsive interaction between electrons from the Coulomb pseudopotential, the electrons in the system form so-called Cooper pairs and condense into a new ground state, the superconducting state. A single Cooper pair, as first discussed by Cooper in 1956, is referred to a bound state in momentum space of two electrons of opposite momentum and opposite spin under an arbitrary weak attractive interaction in the presence of a filled Fermi sea. In the superconducting state, however, Cooper pairs are overlapping highly in the real space. The size of a Cooper pair can be as large as the order of 10^4 Angstroms, for example in Al, compared with the typical distance between electrons in a metal which is only a few Angstroms. In fact, all electrons in the system are condensed, although only the electrons within a rim of thickness $\sim 2\hbar\omega_D$ centered at Fermi level are important, where ω_D is a characteristic phonon frequency. It is this highly correlated ground state that is responsible for superconductivity.

Neglecting the effects due to the retarded nature of a phonon mediated interaction and to the finite lifetimes of quasiparticles, BCS theory gives many universal relationships among various superconducting properties, for example

$$\frac{2\Delta_o}{k_B T_c} = 3.53 \quad \text{and} \quad \frac{\Delta C(T_c)}{\gamma T_c} = 1.43, \tag{1.1.1}$$

where Δ_o is the minimum energy which is needed to break a Cooper pair from the superconducting condensate at zero temperature and is often called the energy gap, k_B is the Boltzmann's constant, $\Delta C(T_c)$ is the jump of the electronic specific heat (C_{es}) at T_c, and γ is the Sommerfeld constant. All these relationships have proved to be qualitatively correct, although not quantitatively, for many conventional superconductors by which we mean most of the superconductors discovered prior to 1986 [Parks (1969); Carbotte (1987)].

To achieve a quantitative agreement with experiment, it is necessary to extend the simple BCS theory to fully include the effects of a retarded interaction and of the finite lifetime of quasiparticles. Such an extension was formulated by Migdal (1958) for the normal state and by Eliashberg (1960) for the superconducting state. It is conventional to call the extended BCS theory, the strong coupling and/or Eliashberg theory of superconductivity. Eliashberg theory is a very accurate and sophisticated theory for phonon mediated superconductors [Carbotte (1990)]. The agreement between the theory and experiment is remarkable. For many superconducting properties it is within a few percent. With these extraordinary successes, the correctness of BCS theory and Eliashberg theory has been firmly established .

There are exceptions, however. For superconductivity in some heavy-Fermion systems and organic materials, Eliashberg theory may not be applicable [Stewart (1984); Ishiguro and Yamaji (1990)]. For the high-T_c oxide superconductors, it is now generally believed that Eliashberg theory can not be applied, at least directly, due to many novel normal and superconducting state properties. The mechanism for the high-T_c oxides has remained to be a mystery. Many exotic theories have been proposed for the high-T_c oxides, for which we refer to the books edited by Halley (1988) and by Bedell *et al.* (1990). These new theories are not our prime interests here, however. Instead we would like to develop a better understanding of Eliashberg theory under various extended conditions. The conditions which we are interested are planar anisotropy in the electron-phonon coupling and energy dependence in the electronic density of states around Fermi level. These two extensions can be applied to some conventional superconductors as well as the high-T_c oxide superconductors. In the next two sections we will have a little more discussion on these two aspects. It is worth noticing that, although Eliashberg theory has been established for a phonon mediated interaction only, it may be extended to any interaction that involves the exchange of virtual bosons, at least to a first order approximation.

1.2 PLANAR ANISOTROPY

Planar anisotropy is of interest for superconductors with layered structure. The high-T_c oxide superconductors are well known to have a layered structure [Yvon and Francois (1989)]. The common building block, a CuO_2 plane, is believed to be essential for superconductivity in all these materials. Despite the fact that we do not know the mechanism for the high-T_c

oxides yet, it is certainly true that any successful theory will need to incorporate the layered structure.

There is also a large class of conventional superconductors with layered structure. They are the metallic transition metal dichalcogenides, *e.g.*, TaS_2 and $NbSe_2$, and the transition metal dichalcogenides intercalated with organic molecules. Extensive studies were carried out in 60s and 70s on these systems [Wilson and Yoffe (1969); Mattheiss (1973a)]. Band structure calculations gave good agreement with experiment [Mattheiss (1973a,b); Kasowski (1973)]. The study of superconducting properties was mostly concentrated on the fluctuation behavior near critical points (T_c, H_c, *etc.*) which is only manifest in low-dimensional systems [Thompson (1973); Craven, Thomas, and Parks (1973); Monceau and Waysand (1974); Klemm (1974)]. Near critical points, the Ginzburg-Landau (GL) theory [Ginzburg and Landau (1950)] with anisotropic mass and the Lawrence and Doniach (LD) theory [Lawrence and Doniach (1972)] can be used. The LD equations are of the form of the GL equations for a system of two-dimensional superconductors, coupled by Josephson tunneling of electron pairs. Although both theories are phenomenological, they are easy to work with and usually describe most superconducting behaviors near the critical points very well.

Transition metal dichalcogenide superconductors are well within the category of phonon-mediated superconductors. The study of planar symmetric anisotropy, based on Eliashberg theory, is more appropriate to this system. However, such a study should also cast some light on the problems of high-T_c oxides because of the similar quasi-two-dimensional structure. In our approach we will not take fluctuations into account since most of our

studies are in the temperature range well below T_c where fluctuation effects are not important.

To describe planar anisotropy of a layered structure, we will use a model dispersion relation. This dispersion relation gives a constant electronic density of states around Fermi level provided that Fermi energy is high enough. Other dispersion relations could also be chosen and may result in a situation where as a function of energy, the density of states around the Fermi level is not constant. To study the problems of anisotropy, we use the Fermi-Surface-Harmonic (FSH) expansion technique [Allen and Mitrović (1982)] as a general approach. Detailed discussion of the model dispersion relation and of the FSH expansion will be given in the next chapter.

1.3 NON-CONSTANT ELECTRONIC DENSITY OF STATES

For most conventional superconductors, a constant electronic density of states (EDOS) around Fermi level ($\sim \hbar\omega_D$) has been assumed in simple BCS and its extension, Eliashberg theory. This assumption can be well justified for a free fermion gas model and the model which we are going to use for a layered structure. However, for some conventional $A15$ superconductors and the high-T_c oxide superconductors, this assumption, a constant EDOS, has been questioned.

Electronic band structure calculations for some A15 superconductors, *e.g.*, V_3Si, V_3Ga, Nb_3Sn and Nb_3Ge, have shown some sharp structures in the EDOS, on the scale of the Debye energy (a few tens of meV), near Fermi level [Klein, Papaconstantopoulos, and Boyer (1980); Pickett (1980)]. These sharp structures have been used to explain some unusual behaviors of the normal and superconducting state properties in these materials, *e.g.*, the temperature

dependence of electronic specific heat coefficient γ in the normal state and the effects of irradiation damage on T_c [Ghosh and Strongin (1980); Lie and Carbotte (1980)].

For the high-T_c oxide superconductors, a quasi-two-dimensional tight-binding model has been used by many people [Emery and Reiter (1988); Schneider, Raedt and Frick (1989); Zhou and Shulz (1992)]. For this model a van Hove singularity will be present in the electronic density of states. The position of this van Hove singularity is related to the Fermi level and depends on the chemical potential or the doping level. There are arguments that for a stoichiometric high-T_c oxide compound, the van Hove singularity should be very close to the Fermi level, based on the isotope effect, the T_c value and the temperature dependence of the normal state resistivity, *etc.* [Tsuei *et al.* (1990); Newns, Pattnaik, and Tsuei (1991)]. If this is the case, many physical properties will be significantly different from the predictions of a constant EDOS. One, then, should take the effects of an energy dependent electronic density of state into consideration.

To study the effects of a non-constant electronic density of states on various superconducting properties, we will use a Lorentzian distribution centered at the Fermi level as a model for the EDOS. The height and width of Lorentzian distribution are adjusted to give different strengths of the Lorentzian peak, from very flat to a δ-function like. Both the imaginary and real axis Eliashberg equations will be modified according to this model. The Eliashberg equations on the imaginary axis has been used by Lie and Carbotte (1980) and by Mitrović and Carbotte (1983a,b,c) in the study of many thermodynamic properties. What we will study here are some transport and electromagnetic properties. Using the Eliashberg equations on the

real frequency axis, we study the effects of a non-constant EDOS on the nuclear spin relaxation rate, the thermal conductivity, the infrared conductivity, the phonon self-energy, *etc.*, in the superconducting state. Due to the length of this thesis we will not report all the work here. We will show the Eliashberg equations with a Lorentzian distribution for the electronic density of states on both the imaginary and real axis in Appendix B. We will also discuss briefly the effects of a non-constant EDOS on the quasiparticle density of states in the superconducting state. This is one of the most fundamental properties of superconductors. Many other properties are directly related to the quasiparticle density of states as we will see through out the discussions in this thesis.

1.4 SCOPE AND OUTLINE OF THESIS

Planar anisotropy and a non-constant EDOS are closely related in some instances and, in principle, they can be treated together in the context of Eliashberg theory. However, the combination of these two problems is, in practice, too complicated to work with at present, by this we mean that an unreasonable amount of computing time is required. In this thesis, we will therefore treat them separately. Due to the length of this thesis we will mainly concentrate on the problem of planar anisotropy. A few of our results for the effects of a non-constant EDOS are included in an Appendix. The outline of this thesis is the following.

In the next chapter, we will introduce a model dispersion relation to describe the motion of electrons in a layered system. With this dispersion relation we show that an approach involving a constant electronic density of

states around Fermi level can still be used. The general anisotropic Eliashberg equations will then be specified.

In chapter 3, we study the effects of planar anisotropy on the critical temperature T_c, the change of the free energy upon entering the superconducting state, the quasiparticle density of states in the superconducting state and the phonon structure in the quasiparticle density of states. Using various electron-phonon coupling strengths we show how the effects of anisotropy are affected by strong coupling. The changes in the quasiparticle density of states in the superconducting state due to anisotropy are particularly interesting since this has a large impact on many of the other superconducting properties which we will discuss in the following chapters.

In chapter 4, the effects of anisotropy on the electronic specific heat, the ultrasound attenuation, and the thermal conductivity are discussed. There are several quantities associated with the electronic specific heat that are of interest. The ultrasound attenuation is studied for the directions of the ultrasonic wave both parallel and perpendicular to the layers. As a result of a selection rule [Clem (1966)] only a small portion of quasiparticles on the Fermi surface are involved for a particular direction. In principle, we can map out the quasiparticle excitation spectrum on the whole Fermi surface from ultrasound attenuation measurements. From the thermal conductivity results, the changes in the quasiparticle excitation spectrum due to anisotropy and the effects of quasiparticle lifetime are discussed.

Chapter 5 is devoted to the study of the London penetration depth, the nuclear spin relaxation, and the infrared conductivity. The London penetration depth has been measured in the high-T_c oxide superconductors by many groups [Harshman *et al.* (1987,1989); Fiory *et al.* (1988); Mitra *et al.*

(1989)]. Most experimental results favored the prediction of the two fluid model [Gorter and Casimir (1934a,b); Ginsburg and Landau (1950)]. With this in mind, we study the effects of anisotropy for various coupling strengths and for different directions (parallel or perpendicular to the planes). For the nuclear spin relaxation, the effects of anisotropy on the coherence peak just below the superconducting transition temperature T_c (the Hebel-Slitcher peak) are discussed with special emphasis since no such peak has been observed in the high-T_c oxides. To compare with the experimental data, we also study the Fermi liquid corrections of Monien and Pines (1990). The absorption edge in the infrared conductivity is studied for various anisotropic parameters, coupling strengths, and non-magnetic impurity concentrations. Adding impurities affects the effects of anisotropy strongly.

In chapter 6, the changes of the phonon self-energy due to the superconducting phase transition have been investigated for various anisotropic parameters, coupling strengths, and temperatures. Due to the interaction between electrons and phonons, we can get the information on the energy gap and on the electron-phonon coupling strength from measuring the phonon shifts and lifetimes. For an anisotropic superconductor complications will arise in the analysis of the phonon self-energy.

A summary of the work on planar anisotropy is included in Chapter 7.

In Appendix A we show how the effect of anisotropy on T_c is diminished under the limit of a very large electron-phonon coupling, the asymptotic limit. The problem of a non-constant electronic density of states near the Fermi level will be addressed in Appendix B. Where, we will show the modified Eliashberg equations for a Lorentzian distribution EDOS near Fermi

level on both the imaginary and real axis, together with the results on the quasiparticle density of states in the superconducting state which is one of the most interesting properties for us.

Chapter 2

Formal Theory

All the work in this thesis has been done within the framework of Eliashberg theory [Eliashberg (1960); Schrieffer (1964); Scalapino (1969); Allen and Mitrović (1982)]. As we discussed briefly in the opening chapter, Eliashberg theory is an extension of BCS theory to fully include the effects of a retarded interaction between quasiparticles (phonon mediated) giving them a finite lifetime. For most conventional superconductors, Eliashberg theory has been well established as a powerful and accurate theory for describing the superconducting state. Quantitative agreement with experiment for many physical properties has be obtained using the Eliashberg equations. Many excellent books and reviews exist on the theory and its application [Schrieffer (1964); Parks (1969); Tinkham (1975); Allen and Mitrović (1982); Carbotte (1990)]. For the purpose of this thesis, here we will only show the anisotropic Eliashberg equations which we are going to use frequently in the

next several chapters. References should be consulted for a detailed discussion of Eliashberg theory and the derivation of Eliashberg equations.

In the first section, we will introduce a model dispersion relation for quasiparticles in a system with a layered crystal structure. All our studies are based on this model. The general form of the anisotropic Eliashberg equations will be shown in section II. In section III, we will write down explicitly the particular form of the equations, specific to the model in section I, which we are going to use. Some notation and characteristic parameters used in our study will also be discussed.

2.1 THE MODEL

For a layered structure, it is natural to use the following dispersion relation for the quasiparticles of momentum $\vec{k}$ in the system ($\hbar = 1$),

$$\epsilon(\vec{k}) = \frac{1}{2m^*}(k_x^2 + k_y^2) + \mu\cdot(1 + cos(k_z c)), \tag{2.1.1}$$

where m^* is the effective mass, $\mu = t/m^*$ with t the transfer matrix from one layer to another layer and c is the lattice constant in the z-direction. This dispersion relation describes the single particle electronic states to be free-particle-like for motion parallel to the layers, and to be of the tight-binding form for motion perpendicular to the layers. A similar dispersion relation was used by Kats (1969, 1970) in the first attempt to describe layered superconductors and by some others [Pint, Langmann, and Schachinger (1989)].

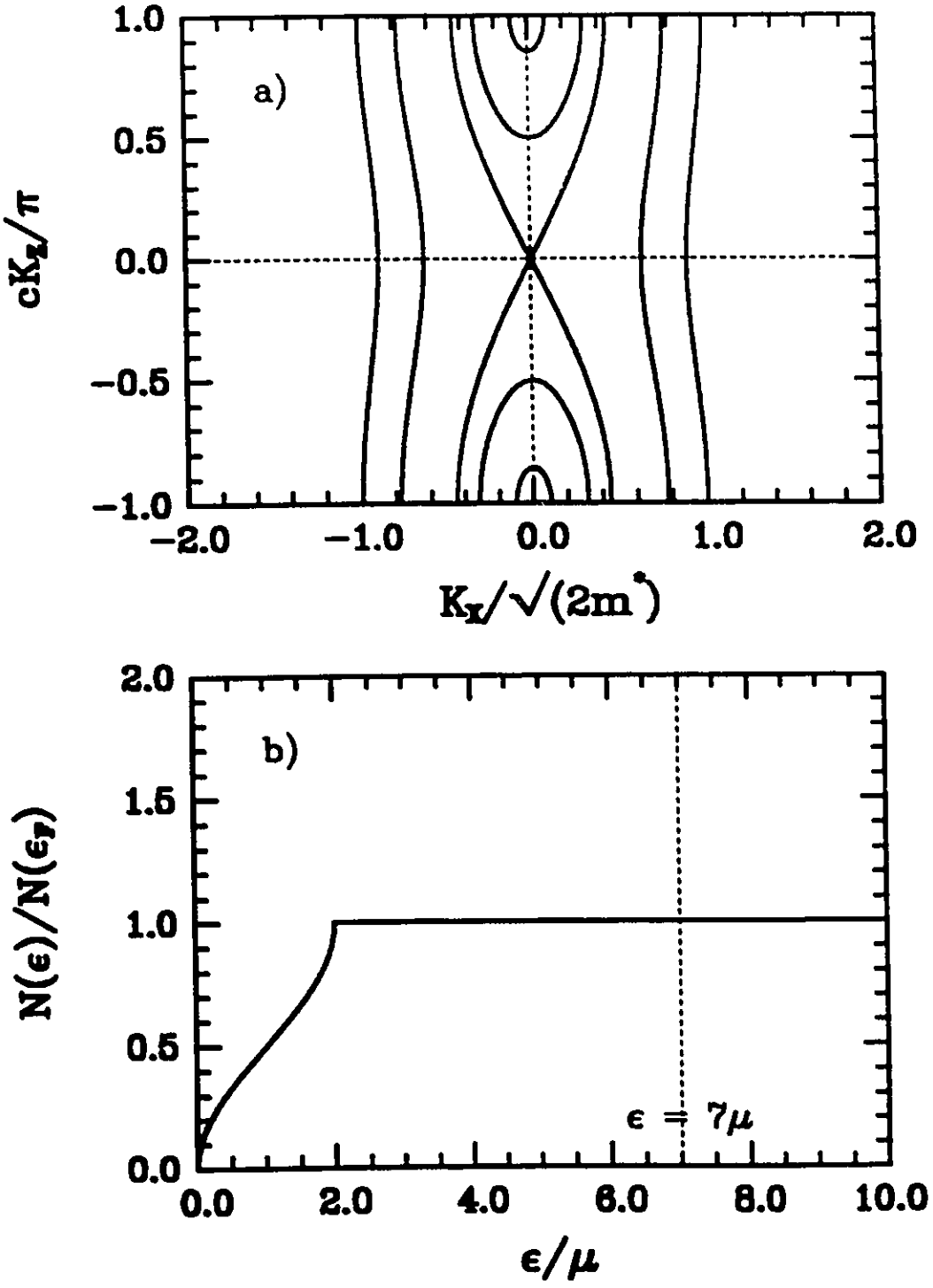

Fig. 2.1.1) From the dispersion relation (2.1.1), a) the constant energy surfaces and b) the electronic density of states.

Having the dispersion relation, we can work out the constant energy surface in the momentum space and the electronic density of states, which we show in Fig. 2.1.1 a) and b) respectively. In Fig. 2.1.1 a), we only showed the projections of the constant energy surfaces on $k_x k_z$ plane. All the surfaces have a rotation symmetry about the k_z axis. It is worthwhile to note that the constant energy surface will remain "open", by which we mean that $\sqrt{(k_x)^2 + (k_y)^2} > 0$ for any allowed value of k_z, until $\epsilon \leq 2\mu$. In evaluating the energy density of states, we used the formula:

$$N(\epsilon) = \int_{S(\epsilon)} \frac{dS}{(2\pi)^3} \frac{1}{\mid \nabla\epsilon(\vec{p}) \mid}, \tag{2.1.2}$$

where the integration is over a constant energy surface. There are many other methods to do it. The most important feature in Fig 2.1.1 b), for us, is perhaps that $N(\epsilon) = \frac{1}{2\pi}\frac{m^*}{c}$, a constant, for $\epsilon \geq 2\mu$. This corresponds to an "open" constant energy surface shown in Fig. 2.1.1 a).

In all our studies, we assume that the Fermi energy of the system $\epsilon_F \gg \mu$, *i.e.*, ϵ_F is of the order of 10μ. Therefore, from the above discussion, we will have $N(\epsilon)$ to be a constant rigorously around the Fermi level within a distance of $\hbar\omega_D$, where ω_D is a characteristic frequency of the bosonic excitation responsible for the superconductivity. For most cases which are known, $\hbar\omega_D$ is less than one tenth of ϵ_F. We will use this fact, that $N(\epsilon)$ is a constant, to determine the Fermi Surface Harmonic (FSH) expansions, which is a general way to solve the problem of an anisotropic superconductor in the framework of Eliashberg theory [Allen and Mitrović (1982)].

2.2 THE GENERAL ANISOTROPIC ELIASHBERG EQUATIONS

The final form of Eliashberg theory is a set of coupled non-linear integral equations, the Eliashberg equations. The solution of Eliashberg equations yields two important quantities for a superconductor, the pairing potential $\tilde{\Delta}_{\vec{p}}(\omega,T)$, which is non-zero only in the superconducting state, and the renormalized frequency $\tilde{\omega}_{\vec{p}}(\omega,T) = \omega Z_{\vec{p}}(\omega,T)$, with $Z_{\vec{p}}(\omega,T)$ a dimensionless mass enhancement factor resulting from electron-boson interaction. Both of them are in general complex functions of momentum $\vec{p}$, frequency ω and temperature T. It is interesting to notice that the corresponding quantities in simple BCS theory are real and not frequency dependent, as there the interaction is instantaneous and the lifetime of quasiparticles is infinite. Thus, things are much simpler in BCS formalism than in Eliashberg formalism, although Eliashberg theory is more realistic. Knowing these quantities, $\tilde{\Delta}_{\vec{p}}(\omega,T)$ and $\tilde{\omega}_{\vec{p}}(\omega,T)$, we can calculate all other physical properties, both in the normal and superconducting states, as they are functions of $\tilde{\Delta}_{\vec{p}}(\omega,T)$ and $\tilde{\omega}_{\vec{p}}(\omega,T)$.

Two forms of the Eliashberg equations are most frequently used, one written on the imaginary axis and the other on the real axis. On the imaginary axis, the Eliashberg equations are written in terms of Matsubara frequencies $i\omega_n = i\pi T(2n-1)$ with $n = 0, \pm 1, \pm 2, \ldots$ and T the temperature. In this Matsubara representation, the full anisotropic Eliashberg equations are

$$\tilde{\Delta}_{\vec{p}}(i\omega_n) = \pi T \sum_{m=-\infty}^{\infty} \left([\lambda_{\vec{p}\vec{p}'}(i\omega_n - i\omega_m) - \mu^* \theta(\omega_c - |\omega_m|)] \frac{\tilde{\Delta}_{\vec{p}'}(i\omega_m)}{\sqrt{\tilde{\omega}^2_{\vec{p}'}(i\omega_m) + \tilde{\Delta}^2_{\vec{p}'}(i\omega_m)}} \right)' + \pi(t^+ - t^-) \left(\frac{\tilde{\Delta}_{\vec{p}'}(i\omega_n)}{\sqrt{\tilde{\omega}^2_{\vec{p}'}(i\omega_n) + \tilde{\Delta}^2_{\vec{p}'}(i\omega_n)}} \right)'$$

(2.2.1)

and

$$\tilde{\omega}_{\vec{p}}(i\omega_n) = \omega_n + \pi T \sum_{m=-\infty}^{\infty} \langle \lambda_{\vec{p}\vec{p}'}(i\omega_n - i\omega_m) \frac{\tilde{\omega}_{\vec{p}'}(i\omega_m)}{\sqrt{\tilde{\omega}^2_{\vec{p}'}(i\omega_m) + \tilde{\Delta}^2_{\vec{p}'}(i\omega_m)}} \rangle' + \pi(t^+ + t^-) \langle \frac{\tilde{\omega}_{\vec{p}'}(i\omega_n)}{\sqrt{\tilde{\omega}^2_{\vec{p}'}(i\omega_n) + \tilde{\Delta}^2_{\vec{p}'}(i\omega_n)}} \rangle', \tag{2.2.2}$$

with

$$\lambda_{\vec{p}\vec{p}'}(i\omega_n - i\omega_m) = \int_0^\infty \frac{2\omega(\alpha^2 F(\omega))_{\vec{p}\vec{p}'} d\omega}{\omega^2 + (\omega_n - \omega_m)^2}. \tag{2.2.3}$$

In these equations, T is the temperature and $\langle\rangle$ denotes a Fermi surface average, $\frac{1}{N(0)}\int_{S(\epsilon_F)} \frac{dS}{(2\pi)^3} \frac{1}{|\nabla\epsilon(\vec{p})|}$, with $N(0)$ the electronic density of states at the Fermi level. For an isotropic case, where all quantities are $\vec{p}$ independent, Eqs. (2.2.1)-(2.2.3) will be reduced to the usual isotropic Eliashberg equations since the Fermi surface average by itself is equal to 1.

The kernel $(\alpha^2 F(\omega))_{\vec{p}\vec{p}'}$ is a directional electron-phonon spectral density, which contains information about the electron-phonon interactions for superconductivity in the system and describes the scattering of an electron from momentum state $\vec{p}$ to $\vec{p}'$ through exchange of a phonon of energy ω. Typically, this spectrum is obtained from electron tunneling experiments where current (I) and voltage (V) characteristics are measured through a superconductor-insulator-normal metal (S-I-N) junction with the insulator providing a potential barrier for the free electrons on either side [McMillan

and Rowell (1969)]. A standard procedure, through 'inversion' of the Eliashberg equations, is used for which $(\alpha^2F(\omega))_{\vec{p}\vec{p}'}$ is varied to match the structures in the $I-V$ characteristics (in the phonon energy range). Such inversions have been done for many materials assuming isotropy [Carbotte (1990)]. A first principle calculation of $(\alpha^2F(\omega))_{\vec{p}\vec{p}'}$ is possible but very difficult, as we need to know not only the wave functions and energies of the conduction electrons in the normal state but also the coupling between these electrons and phonons [Carbotte (1990)].

The parameter μ^*, which comes with a cutoff at frequency ω_c and is assumed to be isotropic, is a measure of the effective Coulomb repulsive interaction reduced from the screened instantaneous repulsive interaction μ by the fact that Coulomb interaction is propagated much more rapidly than electron-phonon interaction,

$$\frac{1}{\mu^*(\omega_c)} = \frac{1}{\mu(\epsilon_F)} + ln(\frac{\epsilon_F}{\omega_c}). \tag{2.2.4}$$

The cutoff frequency ω_c is taken to be in the order of 10 of the characteristic phonon frequency ω_D of the system, since the electron-phonon interaction will be ineffective for $\omega \gg \omega_D$. The μ^* is also called the Coulomb pseudopotential, which, together with $\alpha^2F_{\vec{p}\vec{p}'}(\omega)$, serve as two input parameters to give the experimentally observed T_c.

The t^+ and t^- in the Eqs. (2.2.1)-(2.2.3) are the normal impurity scattering rate and the paramagnetic impurity scattering rate respectively. They are defined as $t^+ = 1/(2\pi\tau_N)$ for τ_N the normal impurity scattering time and $t^- = 1/(2\pi\tau_P)$ for τ_P the spin-flip lifetime, and are assumed to be $\vec{p}$

independent as well. The minus sign in front of the t^- in Eq. (2.2.2) reflects the pair-breaking effect from the spin-flip interactions.

The solution of Eqs. (2.2.1)-(2.2.2) gives us the pairing potentials and the renormalized frequencies on the imaginary axis, $\tilde{\Delta}_{\vec{p}}(i\omega_n)$ and $\tilde{\omega}_{\vec{p}}(i\omega_n)$, with which we will be able to calculate the thermodynamic properties of the system. For some transport properties, however, we need the solution on the real frequency axis, $\tilde{\Delta}_{\vec{p}}(\omega)$ and $\tilde{\omega}_{\vec{p}}(\omega)$. This can be obtained by either using Padé approximates [Vidberg and Serene (1977); Mitrović, Zarate, and Carbotte (1981)] which is an approximation method of analytic continuation of $\tilde{\Delta}_{\vec{p}}(i\omega_n)$ and $\tilde{\omega}_{\vec{p}}(i\omega_n)$ to real frequencies or solving $\tilde{\Delta}_{\vec{p}}(\omega)$ and $\tilde{\omega}_{\vec{p}}(\omega)$ directly on the real axis. The Padé approximates method, however, usually works fine only at low temperature, $T \sim 0K$, and for smooth functions, although it is much easier to work with than the real axis formulation of the Eliashberg equations. Some work have been done on improving their effectiveness at higher temperature [Blaschke and Blocksdarf (1982); Leavens and Ritchie (1985)]. Nevertheless, the real axis formalism of the Eliashberg equations should be used for temperature near the critical temperature T_c and for functions having fine structures. On the real axis, the full anisotropic Eliashberg equations are

$$\begin{aligned}\tilde{\Delta}_{\vec{p}}(\omega+i\delta) = &-\langle \int_{-\infty}^{\infty} d\omega' \int_0^{\infty} d\Omega(\alpha^2F(\Omega))_{\vec{p}\vec{p}'} I(\omega+i\delta,\Omega,\omega') Re\left(\frac{\tilde{\Delta}_{\vec{p}'}(\omega')}{\sqrt{\tilde{\omega}^2_{\vec{p}'}(\omega')-\tilde{\Delta}^2_{\vec{p}'}(\omega')}}\right)\rangle' \\ &- \mu^*(\omega_c)\langle \int_0^{\omega_c} d\omega' tanh\left(\frac{\omega'}{2T}\right) Re\left(\frac{\tilde{\Delta}_{\vec{p}'}(\omega')}{\sqrt{\tilde{\omega}^2_{\vec{p}'}(\omega')-\tilde{\Delta}^2_{\vec{p}'}(\omega')}}\right)\rangle' \\ &+ i\pi(t^+-t^-)\langle \frac{\tilde{\Delta}_{\vec{p}'}(\omega)}{\sqrt{\tilde{\omega}^2_{\vec{p}'}(\omega)-\tilde{\Delta}^2_{\vec{p}'}(\omega)}}\rangle'\end{aligned} \tag{2.2.5}$$

and

$$\tilde{\omega}_{\vec{p}}(\omega+i\delta) = \omega - \Big\langle \int_{-\infty}^{\infty} d\omega' \int_{0}^{\infty} d\Omega(\alpha^2F(\Omega))_{\vec{p}\vec{p}'} I(\omega+i\delta,\Omega,\omega') Re\left(\frac{\tilde{\omega}_{\vec{p}'}(\omega')}{\sqrt{\tilde{\omega}^2_{\vec{p}'}(\omega')-\tilde{\Delta}^2_{\vec{p}'}(\omega')}}\right)\Big\rangle'$$
$$+ i\pi(t^+ + t^-)\Big\langle \frac{\tilde{\omega}_{\vec{p}'}(\omega)}{\sqrt{\tilde{\omega}^2_{\vec{p}'}(\omega)-\tilde{\Delta}^2_{\vec{p}'}(\omega)}}\Big\rangle' \tag{2.2.6}$$

with

$$I(\omega+i\delta,\Omega,\omega') = \frac{N(\Omega)+1-f(\omega')}{\omega+i\delta-\Omega-\omega'} + \frac{N(\Omega)+f(\omega')}{\omega+i\delta+\Omega-\omega'}, \tag{2.2.7}$$

where $N(\omega)$ and $f(\omega)$ are the Boson and Fermi thermal factors, respectively. All other quantities are the real frequency counterparts of the corresponding ones in Eqs. (2.2.1)-(2.2.3).

The real axis formulation of the Eliashberg equations (2.2.5)-(2.2.6) involves two integrals, besides the Fermi surface average, and they involve complex quantities. It is much more complicated than the imaginary axis formulation as there we only have a sum over Matsubara frequencies, in addition to the Fermi surface average, and all quantities are real. Thus, it takes much longer to numerically solve the Eliashberg equations on the real axis than on the imaginary axis. In some instances, it takes too long to be practical. Fortunately, this problem is solved partially by Marsiglio, Schossmann and Carbotte (1988). They derived a new set of equations by doing one of the integrals in Eqs. (2.2.5)-(2.2.7) analytically using the residue theorem. The resulting equations are, with the symmetry $(\alpha^2F(\Omega))_{\vec{p}\vec{p}'} = -(\alpha^2F(-\Omega))_{\vec{p}\vec{p}'}$,

$$\tilde{\Delta}_{\vec{p}}(\omega) = i\pi T \sum_{m=-\infty}^{\infty} \langle \lambda_{\vec{p}\vec{p}'}(\omega - i\omega_m) \frac{\tilde{\Delta}_{\vec{p}'}(i\omega_m)}{\sqrt{\tilde{\omega}^2_{\vec{p}'}(i\omega_m) + \tilde{\Delta}^2_{\vec{p}'}(i\omega_m)}} \rangle'$$
$$+ i\pi \langle \int_{-\infty}^{\infty} d\Omega (\alpha^2 F(\Omega))_{\vec{p}\vec{p}'} (N(\Omega) + f(\Omega - \omega)) \frac{\tilde{\Delta}_{\vec{p}'}(\omega - \Omega)}{\sqrt{\tilde{\omega}^2_{\vec{p}'}(\omega - \Omega) - \tilde{\Delta}^2_{\vec{p}'}(\omega - \Omega)}} \rangle'$$
$$- \mu^*(\omega_c) \langle \int_0^{\omega_c} d\omega' tanh\left(\frac{\omega'}{2T}\right) Re\left(\frac{\tilde{\Delta}_{\vec{p}'}(\omega')}{\sqrt{\tilde{\omega}^2_{\vec{p}'}(\omega') - \tilde{\Delta}^2_{\vec{p}'}(\omega')}}\right) \rangle'$$
$$+ i\pi(t^+ - t^-) \langle \frac{\tilde{\Delta}_{\vec{p}'}(\omega)}{\sqrt{\tilde{\omega}^2_{\vec{p}'}(\omega) - \tilde{\Delta}^2_{\vec{p}'}(\omega)}} \rangle' \tag{2.2.8}$$

and

$$\tilde{\omega}_{\vec{p}}(\omega) = \omega + i\pi T \sum_{m=-\infty}^{\infty} \langle \lambda_{\vec{p}\vec{p}'}(\omega - i\omega_m) \frac{\tilde{\omega}_{\vec{p}'}(i\omega_m)}{\sqrt{\tilde{\omega}^2_{\vec{p}'}(i\omega_m) + \tilde{\Delta}^2_{\vec{p}'}(i\omega_m)}} \rangle'$$
$$+ i\pi \langle \int_{-\infty}^{\infty} d\Omega (\alpha^2 F(\Omega))_{\vec{p}\vec{p}'} (N(\Omega) + f(\Omega - \omega)) \frac{\tilde{\omega}_{\vec{p}'}(\omega - \Omega)}{\sqrt{\tilde{\omega}^2_{\vec{p}'}(\omega - \Omega) - \tilde{\Delta}^2_{\vec{p}'}(\omega - \Omega)}} \rangle'$$
$$+ i\pi(t^+ + t^-) \langle \frac{\tilde{\omega}_{\vec{p}'}(\omega)}{\sqrt{\tilde{\omega}^2_{\vec{p}'}(\omega) - \tilde{\Delta}^2_{\vec{p}'}(\omega)}} \rangle' \tag{2.2.9}$$

with

$$\lambda_{\vec{p}\vec{p}'}(\omega) = -\int_{-\infty}^{\infty} \frac{(\alpha^2 F(\Omega))_{\vec{p}\vec{p}'} d\Omega}{\omega - \Omega + i0^+}. \tag{2.2.10}$$

Comparing Eqs. (2.2.5)-(2.2.6) with Eqs. (2.2.8)-(2.2.9), we see that the essential difference between the two sets of equations is that the double integral in the former set is replaced by a single integral plus a sum over the

Matsubara frequencies, which are the poles of Fermi distribution function $f(\omega)$ in a complex plane. The new set of equations (2.2.5)-(2.2.6) contains pairing potentials and renormalized frequencies both on the real axis and the imaginary axis, and acts as an intermediate set between the imaginary axis Eliashberg equations and the real axis Eliashberg equations. It is much easier to work with and can be solved much faster on a computer (by a factor of 10) than the full real axis equations (2.2.5)-(2.2.6). It is also more reliable to work with at temperature near T_c than the analytic continuation of the imaginary axis quantities using Padé approximants. In practice, we first solve the Eliashberg equation in Matsubara representation, Eqs. (2.2.1)-(2.2.2), then the imaginary axis pairing potentials $\tilde{\Delta}_{\vec{p}}(i\omega_n)$ and renormalized frequencies $\tilde{\omega}_{\vec{p}}(i\omega_n)$ are used as input parameters for Eqs. (2.2.8)-(2.2.9). The solution of Eqs. (2.2.8)-(2.2.9) gives us the real axis pairing potentials $\tilde{\Delta}_{\vec{p}}(\omega)$ and renormalized frequencies $\tilde{\omega}_{\vec{p}}(\omega)$. These two sets, Eqs. (2.2.1)-(2.2.2) and Eqs. (2.2.8)-(2.2.9) are the fundamental equations for our studies here.

2.3 THE ANISOTROPIC ELIASHBERG EQUATIONS FOR THE MODEL

In this section, the general anisotropic Eliashberg equations in the last section will be specialized to the model dispersion relation (1.1.1). A proper way to deal with the anisotropic equations introduced in the last section is using a Fermi Surface Harmonics (FSH) expansion technique [Butler and Allen (1976); Daams (1979, 1981); Allen and Mitrović (1982)], in which all angular dependent quantities, $\tilde{\omega}_{\vec{p}}(i\omega_n)$, $\tilde{\omega}_{\vec{p}}(\omega)$, $\tilde{\Delta}_{\vec{p}}(i\omega_n)$, $\tilde{\Delta}_{\vec{p}}(\omega)$, and $(\alpha^2F(\omega))_{\vec{p}\vec{p}'}$, are expanded by means of FSH's $Q_j(\vec{p})$, which form a complete set of orthonormal functions at the Fermi surface. According to the dispersion

relation (1.1.1), we have a cylindrical symmetric Fermi surface. Therefore, the FSH set, $\mathcal{Q}_j(\vec{p})$, can be the trigonometric functions $sin(jp_zc)$ and $cos(jp_zc)$, where c is the lattice constant in the z-direction of a crystal. It is easy to show the completeness and the orthogonality since the Fermi surface average is

$$\begin{aligned}\langle \mathcal{Q}_j(\vec{p})\mathcal{Q}_k(\vec{p})\rangle &= \frac{1}{N(0)}\int_{S(\epsilon)}\frac{dS}{(2\pi)^3}\frac{1}{\mid \nabla\epsilon(\vec{p})\mid}\mathcal{Q}_j(\vec{p})\mathcal{Q}_k(\vec{p}) \\ &= \frac{1}{2\pi}\int_{-\pi}^{\pi} d\theta\, \mathcal{Q}_j(\vec{p})\mathcal{Q}_k(\vec{p})\end{aligned} \tag{2.3.1}$$

with $\theta = p_zc$. From the symmetry consideration, however, we will drop $sin(jp_zc)$ part from the whole series and keep only the $cos(jp_zc)$ part. By doing this, we will have even symmetry, with regard to $\vec{p}$, for the pairing potential ($\tilde{\Delta}_{\vec{p}} = \tilde{\Delta}_{-\vec{p}}$) and the renormalized frequency ($\tilde{\omega}_{\vec{p}} = \tilde{\omega}_{-\vec{p}}$). The problem of completeness is not essential as we will always truncate the expansion series in numerical calculations.

To write out FSH expansion of each quantity explicitly, we have

$$\tilde{\omega}_{\vec{p}}(i\omega_n) = \sum_{j=0}^{\infty}\tilde{\omega}_j(n)cos(jp_zc), \quad \tilde{\omega}_{\vec{p}}(\omega) = \sum_{j=0}^{\infty}\tilde{\omega}_j(\omega)cos(jp_zc) \tag{2.3.2}$$

$$\tilde{\Delta}_{\vec{p}}(i\omega_n) = \sum_{j=0}^{\infty}\tilde{\Delta}_j(n)cos(jp_zc), \quad \tilde{\Delta}_{\vec{p}}(\omega) = \sum_{j=0}^{\infty}\tilde{\Delta}_j(\omega)cos(jp_zc) \tag{2.3.3}$$

and

$$(\alpha^2F(\omega))_{\vec{p}\vec{p}'} = \sum_{j=0}^{\infty}\sum_{k=0}^{\infty}\alpha^2F(\omega)g_{jk}cos(jp_zc)cos(kp'_zc) \tag{2.3.4}$$

with $\alpha^2F(\omega) = \langle\langle(\alpha^2F(\omega))_{\vec{p}\vec{p}'}\rangle\rangle'$ and $\tilde{\omega}_j$, $\tilde{\Delta}_j$, and g_{jk} the expansion coefficients. FSH expansions for $\lambda_{\vec{p}\vec{p}'}(i\omega_n - i\omega_m)$ and $\lambda_{\vec{p}\vec{p}'}(\omega)$ are similar to (2.3.4), following the relations (2.2.3) and (2.2.10), they are

$$\lambda_{\vec{p}\vec{p}'}(i\omega_n - i\omega_m) = \sum_{j=0}^{\infty}\sum_{k=0}^{\infty}\lambda_{00}(n-m)g_{jk}cos(jp_zc)cos(kp'_zc) \tag{2.3.5}$$

and

$$\lambda_{\vec{p}\vec{p}'}(\omega) = \sum_{j=0}^{\infty}\sum_{k=0}^{\infty}\lambda_{00}(\omega)g_{jk}cos(jp_zc)cos(kp'_zc) \tag{2.3.6}$$

with

$$\lambda_{00}(i\omega_n - i\omega_m) = \int_0^{\infty}\frac{2\omega\alpha^2F(\omega)d\omega}{\omega^2 + (\omega_n - \omega_m)^2}, \quad \lambda_{00}(\omega) = -\int_{-\infty}^{\infty}\frac{\alpha^2F(\Omega)d\Omega}{\omega - \Omega + i0^+}. \tag{2.3.7}$$

Substitution of these expansions, (2.3.2)-(2.3.6), into the coupled non-linear Eliashberg equations, (2.2.1)-(2.2.2) and (2.2.8)-(2.2.9), leads to two infinite sets of equations which need to be solved self-consistently:

$$\tilde{\Delta}_j(i\omega_n) = \pi T \sum_{k=0}^{\infty} \sum_{m=-\infty}^{\infty} [\lambda_{00}(n-m) g_{jk} - \mu^* \theta(\omega_c - |\omega_m|) \delta_{0,j} \delta_{0,k}] \langle \frac{\tilde{\Delta}_{\vec{p}'}(i\omega_m) cos(k p_z' c)}{\sqrt{\tilde{\omega}^2_{\vec{p}'}(i\omega_m) + \tilde{\Delta}^2_{\vec{p}'}(i\omega_m)}} \rangle'$$
$$+ \pi (t^+ - t^-) \langle \frac{\tilde{\Delta}_{\vec{p}'}(i\omega_n)}{\sqrt{\tilde{\omega}^2_{\vec{p}'}(i\omega_n) + \tilde{\Delta}^2_{\vec{p}'}(i\omega_n)}} \rangle' \tag{2.3.8}$$

$$\tilde{\omega}_j(i\omega_n) = \omega_n \delta_{j,0} + \pi T \sum_{k=0}^{\infty} \sum_{m=-\infty}^{\infty} \lambda_{00}(n-m) g_{jk} \langle \frac{\tilde{\omega}_{\vec{p}'}(i\omega_m) cos(k p_z' c)}{\sqrt{\tilde{\omega}^2_{\vec{p}'}(i\omega_m) + \tilde{\Delta}^2_{\vec{p}'}(i\omega_m)}} \rangle'$$
$$+ \pi (t^+ + t^-) \langle \frac{\tilde{\omega}_{\vec{p}'}(i\omega_n)}{\sqrt{\tilde{\omega}^2_{\vec{p}'}(i\omega_n) + \tilde{\Delta}^2_{\vec{p}'}(i\omega_n)}} \rangle' \tag{2.3.9}$$

and

$$\tilde{\Delta}_j(\omega) = i\pi T \sum_{k=0}^{\infty} \sum_{m=-\infty}^{\infty} \lambda_{00}(\omega - i\omega_m) g_{jk} \langle \frac{\tilde{\Delta}_{\vec{p}'}(i\omega_m) cos(k p_z' c)}{\sqrt{\tilde{\omega}^2_{\vec{p}'}(i\omega_m) + \tilde{\Delta}^2_{\vec{p}'}(i\omega_m)}} \rangle'$$
$$+ i\pi \sum_{k=0}^{\infty} \int_{-\infty}^{\infty} d\Omega \, \alpha^2 F(\Omega) g_{jk} (N(\Omega) + f(\Omega - \omega)) \langle \frac{\tilde{\Delta}_{\vec{p}'}(\omega - \Omega) cos(k p_z' c)}{\sqrt{\tilde{\omega}^2_{\vec{p}'}(\omega - \Omega) - \tilde{\Delta}^2_{\vec{p}'}(\omega - \Omega)}} \rangle'$$
$$- \mu^*(\omega_c) \langle \int_0^{\omega_c} d\omega' tanh\left(\frac{\omega'}{2T}\right) Re\left(\frac{\tilde{\Delta}_{\vec{p}'}(\omega')}{\sqrt{\tilde{\omega}^2_{\vec{p}'}(\omega') - \tilde{\Delta}^2_{\vec{p}'}(\omega')}}\right) \rangle'$$
$$+ i\pi (t^+ - t^-) \langle \frac{\tilde{\Delta}_{\vec{p}'}(\omega)}{\sqrt{\tilde{\omega}^2_{\vec{p}'}(\omega) - \tilde{\Delta}^2_{\vec{p}'}(\omega)}} \rangle' \tag{2.3.10}$$

$$\tilde{\omega}_j(\omega) = \omega \delta_{j,0} + i\pi T \sum_{k=0}^{\infty} \sum_{m=-\infty}^{\infty} \lambda_{00}(\omega - i\omega_m) g_{jk} \langle \frac{\tilde{\omega}_{\vec{p}'}(i\omega_m) cos(k p_z' c)}{\sqrt{\tilde{\omega}^2_{\vec{p}'}(i\omega_m) + \tilde{\Delta}^2_{\vec{p}'}(i\omega_m)}} \rangle'$$

$$+ i\pi \sum_{k=0}^{\infty} \int_{-\infty}^{\infty} d\Omega \alpha^2 F(\Omega) g_{jk} (N(\Omega) + f(\Omega - \omega)) \left(\frac{\tilde{\omega}_{\vec{p}'}(\omega - \Omega) cos(k p_z' c)}{\sqrt{\tilde{\omega}^2_{\vec{p}'}(\omega - \Omega) - \tilde{\Delta}^2_{\vec{p}'}(\omega - \Omega)}} \right)'$$

$$+ i\pi (t^+ + t^-) \left(\frac{\tilde{\omega}_{\vec{p}'}(\omega)}{\sqrt{\tilde{\omega}^2_{\vec{p}'}(\omega) - \tilde{\Delta}^2_{\vec{p}'}(\omega)}} \right)'. \tag{2.3.11}$$

Now equations (2.3.8)-(2.3.11) are ready to be solved on a computer, provided that we know the electron-phonon spectral density $\alpha^2 F(\omega)$, the expansion coefficients g_{jk}, the Coulomb pseudopotential μ^* and the impurity scattering parameters, t^+ and t^-. Since our main interest here is the effect of layered anisotropy on a superconductor, we will neglect the Coulomb pseudopotential μ^* and impurity scatterings t^+ and t^- in our numerical work hereafter, unless specified. It is worthwhile to notice that high-T_c oxide superconductors are generally believed to be in the clean limit, where impurity scattering is not important for superconducting properties. This is deduced by considering the small superconducting coherent length in these materials. We should also point out that impurity scattering will wash out anisotropies. In the extreme dirty limit, corresponding to large impurity scattering, anisotropies will not be effective.

For the expansion coefficients g_{jk}, it is convenient to assume that $g_{00} = 1$ and $g_{jk} = g_{kj}$. The relation $g_{jk} = g_{kj}$ means that the process of an electron scattering from state $\vec{p}$ to state $\vec{p}'$ is equivalent to the process of it scattering from state $\vec{p}'$ to state $\vec{p}$. In our numerical calculations, the parameters g_{jk} will be varied through a certain range to study the effects of anisotropy with different strengths. Consistent with the assumption in Section 2.1 that $\mu \ll \epsilon_F$, however, we restrict the range to the region where $g_{jk} \leq g_{00} = 1$. We also truncate the expansion series in Eqs. (2.3.8)-(2.3.11)

after the $cos(p_z c)$ or $cos(2p_z c)$ terms. We believe that this will be sufficient for understanding qualitatively the underlying physics of the anisotropic model we have used.

For the electron-phonon spectral density $\alpha^2F(\omega)$, the kernel of the Eliashberg equations (2.3.8)-(2.3.11), we will use a modified Pb spectral density. We multiply the original Pb $\alpha^2F(\omega)$, derived from tunneling measurements, by a constant to get a desired T_c. By doing this, we change the electron-phonon coupling strength. The parameter which we use to measure the electron-phonon coupling strength is the dimensionless ratio T_c/ω_{log}, where ω_{log} is a characteristic phonon energy, first introduced by Allen and Dynes (1975), given by

$$\omega_{log} = exp\left(\frac{2}{\lambda}\int_0^\infty \frac{\alpha^2F(\omega)}{\omega} ln(\omega) d\omega\right) \tag{2.3.12}$$

with λ the electron-phonon mass renormalization parameter given by

$$\lambda = \int_0^\infty 2\frac{\alpha^2F(\omega)}{\omega} d\omega \tag{2.3.13}$$

It is easy to see, from the definition above, that multiplying $\alpha^2F(\omega)$ by a constant will not affect this characteristic phonon energy ω_{log}, although T_c will be changed. Therefore we can change the ratio, T_c/ω_{log}, by multiplying the $\alpha^2F(\omega)$ of Pb with a constant. Other materials' spectral density could also be used but the particular shape of an $\alpha^2F(\omega)$ is not of interest here. All we are interested in here is the effects of planar symmetry on a strong coupling

superconductor, by which we mean that Eliashberg theory should be used, in general. The exact shape of $\alpha^2F(\omega)$ only matters when some quantitative details for a particular material are needed. Besides, it has been shown that, to a first approximation, T_c/ω_{log} is a more important quantity than the exact shape of the spectral density in determining most superconducting properties [Mitrović, Zarate, and Carbotte (1984); Marsiglio and Carbotte (1986, 1990); Marsiglio, Carbotte and Blezius (1990)]. Thus, throughout this thesis, we will use this ratio T_c/ω_{log} as the only parameter to classify different strength of coupling. We would like to point out that, for most conventional superconductors, T_c/ω_{log} runs from almost zero (0.004 for Al) to around 0.3 (0.320 for $Pb_{0.5}Bi_{0.5}$) [Marsiglio (1988)]. $T_c/\omega_{log} \to 0$ represents the BCS limit, which is equivalent to having the characteristic phonon energy at a very high energy limit.

In the following chapters, we will study the effects of a layered structure on various superconducting properties with the model and the Eliashberg equations given here. Since all physical properties are functions of the pairing potential $\tilde{\Delta}_{\vec{p}}(\omega)$ and the renormalized frequency $\tilde{\omega}_{\vec{p}}(\omega)$, the solutions of the Eliashberg equations, (2.3.8)-(2.3.11), for $\tilde{\Delta}_{\vec{p}}(\omega)$ and $\tilde{\omega}_{\vec{p}}(\omega)$ are necessary for all that follows.

Chapter 3

Fundamental Properties

In this chapter, we will use the anisotropic model introduced in the last chapter to study the effect of a layered structure on some fundamental physical quantities of a superconductor, namely the superconducting critical temperature (T_c), the free energy difference between the normal and superconducting state ($\Delta F = F_n - F_s$), and the electronic density of states of charged quasiparticles ($N(\omega)$) in the superconducting state.

The superconducting state below a certain temperature, T_c, is a highly correlated electronic state with lower energy than that of the normal free Fermi sea. The change in the free energy between the normal and superconducting state (ΔF) results in changes of many thermodynamic properties. The electronic density of states in this highly correlated new ground state is also qualitatively different from that in the normal state. The most important new feature, perhaps, is the appearance of an energy "gap" in the

energy spectrum in the superconducting state. The consequence of this energy "gap" will be seen in detail in the following chapters, when we discuss various physical properties. For many conventional superconductors where a phonon mechanism is responsible for the superconductivity, the electronic density of states also carrys the information on the electron-phonon spectral density $\alpha^2F(\omega)$ through some fine structures, which we call the phonon structure [Carbotte (1990)]. In fact, the electron-phonon spectral density itself can be extracted by exploiting the structure in the electronic density of states as we discussed in the previous chapter. The energy "gap" and the phonon structure are very closely related, as usually the phonon structure occurs at energies equal to the sum of the gap value plus the phonon energy of interest, which could be known independently from neutron scattering, at zero temperature.

In the following section, we will show the effect of the anisotropy on the critical temperature T_c, followed by a discussion on the free energy difference between the normal and superconducting state ΔF in section 3.2. Section 3.3 is devoted to the electronic density of states and energy gap in the superconducting state. Phonon structure and its relation to the energy gap will be discussed in section 3.4. A short conclusion is included as section 3.5.

3.1 THE CRITICAL TEMPERATURE

The superconducting critical temperature T_c is the temperature at which the superconducting phase transition happens. Ever since the discovery of superconductivity, to increase this critical temperature has been the number one challenge for people working in this field. Prior to 1986, the

highest T_c was found in the A15 compound Nb_3Ge with $T_c = 23.0K$ [Gavaler (1973); Gavaler, Janocko, and Jones (1974)]. This record was broken in early 1986 by Bednorz and Müller after they discovered superconductivity in the La-Ba-Cu-O system, the first copper oxide superconductor with a T_c around 30K. This discovery was so important not only because it was the highest T_c known at that time but also because it represented the discovery of a new class of superconducting oxides. The study of other copper oxides, initiated by this discovery, turned out to be very fruitful and many new superconductors were discovered soon after. The highest T_c now is $125K$ in the $Tl - Ba - Ca - Cu - O$ compounds [Sheng and Hermann (1988a,b)], well above the liquid nitrogen temperature ($77K$). The significance of Bednorz and Müller's discovery in 1986 was recognized by a Nobel Prize in physics in 1987.

Interestingly, the study of the dependence of critical temperature T_c on isotope mass (the isotope effect) also made, probably, the decisive contribution to the discovery of the first correct microscopic theory of superconductivity, BCS theory. It was discovered in 1950 [Fröhlich (1950); Maxwell (1950); Reynolds *et al.* (1950)] that, with sufficient precision, the following relationship holds for mercury (Hg)

$$T_c M^{1/2} = const., \tag{3.1.1}$$

where M is the isotope mass number. Since the isotope mass is a characteristic of the crystal lattice and the frequency of lattice vibrations (Ω) is related to the ion mass with $\Omega \sim M^{-1/2}$, superconductivity is, thus, related

to the state of the crystal lattice. It follows that superconductivity is due to the interaction between the charge carriers and the vibrations of the lattice (phonons). Based on this picture, Bardeen, Cooper and Schrieffer (1957) invented a microscopic theory of superconductivity which has proved to be remarkably correct for most conventional superconductors.

The problem of anisotropy was addressed right after BCS theory. In the 1950's, experiments on adding normal impurities into several superconductors showed that initially T_c would decrease with increasing normal impurity concentration and then saturate quickly. To explain this, Anderson [Anderson (1959)] argued that normal impurities would not affect the superconducting properties of an isotropic superconductor, including T_c. For a real material in the clean limit, however, there are always some anisotropies in the conduction bands due to the crystal structure, and usually the anisotropy will favor a higher critical temperature T_c. By adding normal impurities, we wash out the anisotropy and reduce T_c to its isotropic value.

A quantitative expression for the effect of anisotropy on T_c was first given by Markowitz and Kadanoff within BCS theory [Markowitz and Kadanoff (1963)]. They used a separable model where the effective phonon-induced matrix element in BCS theory had the form:

$$V_{\vec{p}\vec{p}'} = (1+\alpha_{\vec{p}})V(1+\alpha_{\vec{p}'}) \tag{3.1.2}$$

with the conditions $\langle \alpha_{\vec{p}} \rangle = 0$ and $\langle \alpha_{\vec{p}}{}^2 \rangle \simeq 0.02$, where $\langle\rangle$ is denotes a Fermi surface average. The T_c formula for a pure superconductor with anisotropy, then, is

$$k_B T_c = 1.14\omega_D \exp\left(-\frac{1}{(1+<\alpha^2>)N(0)V}\right) \tag{3.1.3}$$

compared with the T_c formula for an isotropic superconductor in BCS theory:

$$k_B T_c = 1.14\omega_D \exp\left(-\frac{1}{N(0)V}\right). \tag{3.1.4}$$

It is easy to see that T_c increases as $<\alpha^2>$ increases, although $<\alpha^2>$ is small in this model. The study of the separable model was extended to Eliashberg theory by Leavens and Carbotte [Leavens and Carbotte (1972)]. With some simplifications, they derived the formula for T_c from the Eliashberg equations for a weak coupling limit. The strong coupling case was studied by Daams and Carbotte [Daams and Carbotte (1981)].

Now we extend the study to the anisotropic model we have introduced in the last chapter. As we are dealing with arbitrary coupling and anisotropy strength, deriving analytic expression for T_c is not feasible. We have to do things numerically. The Eliashberg equations which we solved for T_c are the linearized equations of (2.3.8) and (2.3.9) with pairing potential $\tilde{\Delta}_{\vec{p}}(i\omega_n)$ set equal 0 in the denominators

$$\tilde{\Delta}_j(i\omega_n) = \pi T \sum_{k=0}^{\infty} \sum_{m=-\infty}^{\infty} \lambda_{00}(n-m) g_{jk} \left(\frac{\tilde{\Delta}_{\vec{p}'}(i\omega_m)\cos(kp_z'c)}{\tilde{\omega}_{\vec{p}'}(i\omega_m)}\right)' \tag{3.1.5}$$

$$\tilde{\omega}_j(i\omega_n) = \omega_n\delta_{j,0} + \pi T\sum_{k=0}^{\infty}\sum_{m=-\infty}^{\infty}\lambda_{00}(n-m)g_{jk}\langle\tilde{\omega}_{\vec{p}'}(i\omega_m)cos(kp_z{}'c)\,sgn(\omega_m)\rangle' \tag{3.1.6}$$

where we also set μ^*, t^+ and t^- equal to 0 as we discussed in the last chapter. We used a modified Pb electron-phonon spectral density with T_c/ω_{log} being adjusted to be 0.1 for an intermediate coupling and 0.25 for strong coupling. The anisotropic parameter g_{jk} is non-zero only for $g_{00} \equiv 1$, $g_{10} = g_{01}$ and $g_{20} = g_{02}$. By changing g_{10} and g_{20}, we show the effect of the anisotropy on T_c over a wide range. The results are plotted in Fig. 3.1.1.

In Fig. 3.1.1, T_{c0} is the value of T_c for the isotropic system, i.e. the value obtained when $g_{10} = g_{20} = 0.0$. What we have plotted is the ratio T_c/T_{c0} as a function of g_{10} for several values of g_{20} namely 0.0 (solid curve), 0.2 (dotted curve), 0.4 (short dashed curve), 0.6 (long dashed curve), 0.8 (short dashed-dotted curve), and 1.0 (long dashed-dotted curve). In the top frame, where $T_c/\omega_{log} = 0.1$, we see that the value of T_c rises monotonically with increasing g_{10} for any given value of g_{20}. Over 20% enhancement of T_c has been achieved over the isotropic value for $g_{10} = 1.0$ and $g_{20} = 0.0$, and it is over 40% for $g_{10} = 1.0$ and $g_{20} = 1.0$. However, for a given value of g_{10}, adding g_{20} anisotropy will not always help increasing T_c. When g_{10} is large, small additional anisotropy from g_{20} leads to a decrease in T_c, although T_c does increase monotonically when adding g_{20} anisotropy for small value of g_{10} anisotropy. It is clear that rather large values are needed in order to get a enhancement of T_c over 20% of its isotropic value for the cases we have studied here. As we increase the coupling strength to $T_c/\omega_{log} = 0.25$, the strong coupling case in the bottom frame, the pattern of behavior obtained

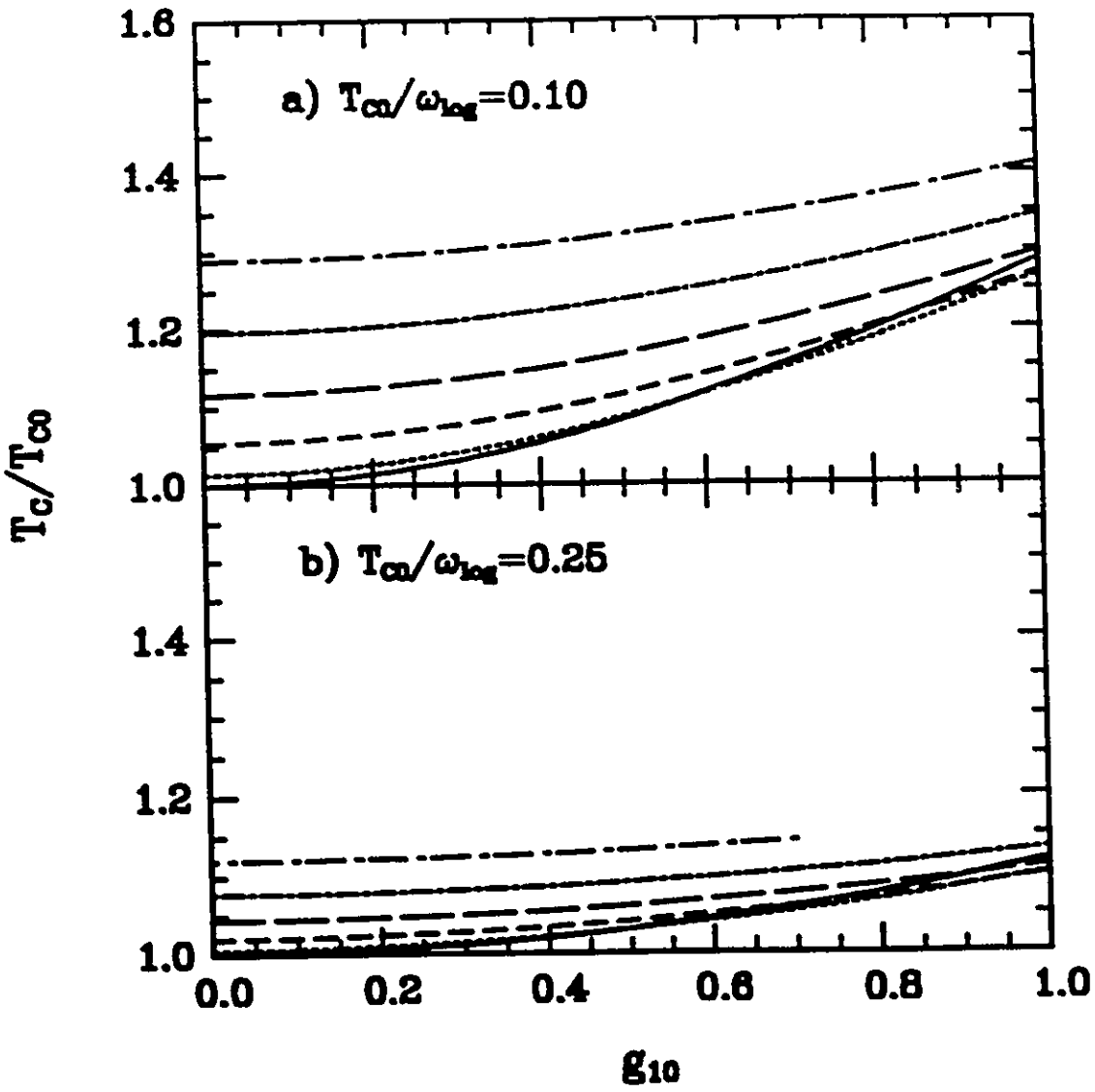

Fig. 3.1.1) The ratio of critical temperature (T_c) with anisotropy to its value without (T_{c0}) as a function of anisotropy parameter g_{10} for various values of g_{20}, namely 0.0 (solid curve), 0.2 (dotted curve), 0.4 (short dashed curve), 0.6 (long dashed curve), 0.8 (short dashed-dotted curve), and 1.0 (long dashed-dotted curve). The top frame is for an intermediate coupling case with strong coupling index $T_c/\omega_{log} = 0.1$ while the bottom frame is for strong coupling with $T_c/\omega_{log} = 0.25$.

remains the same as in the top frame. The resulting enhancements of the T_c value, however, are much smaller than those in the top frame for the same anisotropy parameters. Now the largest enhancement obtained is below 15%. This is not very significant. We can expect that further increase in coupling strength will make the enhancement effect from anisotropy even smaller. Indeed, in the asymptotic limit where coupling strength goes infinity, the effect of anisotropy will be totally washed out (see Appendix A).

Before leaving this section, we would like to point out that, within our model, the anisotropy due to layered structures will not affect the behavior of isotope effect directly since we have separated out the frequency dependent part and angular dependent part. The angular dependent part in our model does not change with frequency. There is a indirect effect on the isotope effect from the anisotropy, however [Jiang and Carbotte (1992a)]. Nevertheless the effect is very small and cannot account for the peculiar isotope effect found in high-T_c oxides [Crawford *et al.* (1990); Franck *et al.* (1990a,b)].

3.2 THE THERMODYNAMIC CRITICAL FIELD

Instead of looking at the free energy difference between the normal and superconducting state $\Delta F(T)$ directly, we study a closely related quantity, the thermodynamic critical field $H_c(T)$, which is defined as

$$H_c(T) = (8\pi \mid \Delta F(T) \mid)^{1/2}. \tag{3.2.1}$$

The formula for ΔF, generalized to include the anisotropy, is [Bardeen and Stephen (1958)]:

$$\frac{\Delta F(T)}{N(0)} = \pi T \sum_{n>0} \left\langle (\sqrt{\tilde{\omega}_{\vec{p}}^2(i\omega_n) + \tilde{\Delta}_{\vec{p}}^2(i\omega_n)} - |\,\tilde{\omega}_{\vec{p}}(i\omega_n)\,|) \cdot \left(1 - \frac{|\,\tilde{\omega}_{\vec{p}}^{o}(i\omega_n)\,|}{\sqrt{\tilde{\omega}_{\vec{p}}^2(i\omega_n) + \tilde{\Delta}_{\vec{p}}^2(i\omega_n)}}\right)\right\rangle \tag{3.2.2}$$

where the superscript zero on $\tilde{\omega_{\vec{p}}}^{o}(i\omega_n)$ indicates that this renormalized frequency is to be taken in the normal state, which follows from equation (2.3.9) with the $\tilde{\Delta}_{\vec{p}'}(i\omega_m)$'s set equal to zero on the right hand side of the equation.

The thermodynamic critical field measures the minimum value of the applied magnetic field which destroys superconductivity. This comes from the fact that if the applied magnetic field is sufficiently strong the energy cost associated with the Meissner effect (perfect diamagnetism) will be more than the effective energy savings due to the material being in the superconducting state, thus it is energetically favorable for the material to be in the normal state with the magnetic field freely permeating the sample rather than to be in the superconducting state.

For a type I superconductor, it is indeed a fact that the Meissner effect and superconductivity are totally destroyed at this point ($H_c(T)$) and the applied magnetic flux will fully penetrate into the material. There is another type of superconductor, type II, however, where a perfect diamagnetism remains until the applied field reaches the lower critical field $H_{c1}(T)$. Beyond this field $H_{c1}(T)$, a mixed state occurs where the applied magnetic field penetrates the superconductor partially in the form of vortex lines. For each vortex, the flux is a quantum number ($\Phi = \hbar c/2e$). Thus the material is in a state where superconducting regions and normal regions coexist. As the field increases ($H > H_{c1}$), the volume taken up by the normal regions increases, the vortex lines get closer together. The superconductivity will be

completely destroyed and there is full flux penetration when another critical field (the upper critical field) $H_{c2}(T)$ is reached. The thermodynamic critical field $H_c(T)$ is not directly related to $H_{c1}(T)$ and $H_{c2}(T)$ in type II superconductors, although the concept of it is still helpful. Type II superconductors are special in many ways. It is beyond the scope of this thesis to study any special properties of a type II superconductor, *e.g.*, upper critical field $H_{c2}(T)$. Interested readers might refer to the literature [Abrikosov (1957); Goodman (1966); Werthamer and McMillan (1967); Saint-James, Sarma, and Thomas (1968); Fetter and Hohenberg (1969); Serin (1969); Carbotte (1990)].

In BCS theory, there is a universal relationship between H_c and T_c,

$$\gamma_0 T^2{}_c / H^2{}_c(0) = 0.168 \tag{3.2.3}$$

where $H_c(0)$ is the zero temperature value of the thermodynamic critical field and γ_0 is the normal state Sommerfeld constant defined by

$$\gamma_0 = \frac{2}{3}\pi^2 N(0)(1+\lambda) \tag{3.2.4}$$

with $N(0)$ the electronic density of states at the Fermi level and λ the mass enhancement factor (see chapter 2). Like other universal relationships in BCS theory, this one only holds for superconductors in the weak coupling limit (*e.g.*, Al and In). For strong coupling superconductors, *e.g.*, Pb and Hg, deviations occur due to strong coupling theory (Eliashberg theory).

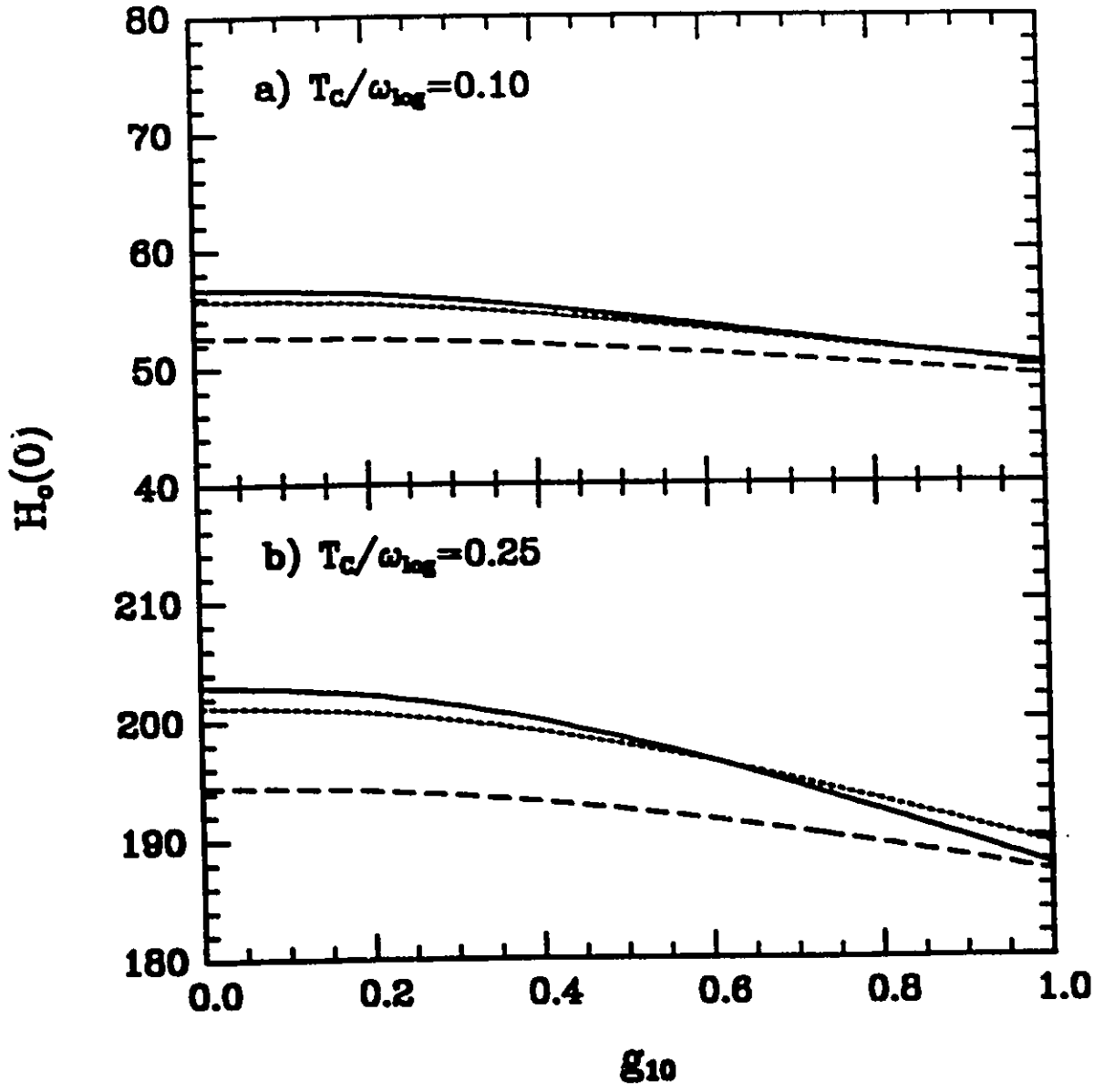

Fig. 3.2.1) The thermodynamic critical magnetic field at zero temperature $H_c(0)$ as a function of anisotropy parameter g_{10} for various values of g_{20}, namely 0.0 (solid curve), 0.3 (dotted curve), 0.7 (short dashed curve). The top frame applies to the intermediate coupling case ($T_c/\omega_{log} = 0.1$) while the bottom frame is for the strong coupling case ($T_c/\omega_{log} = 0.25$).

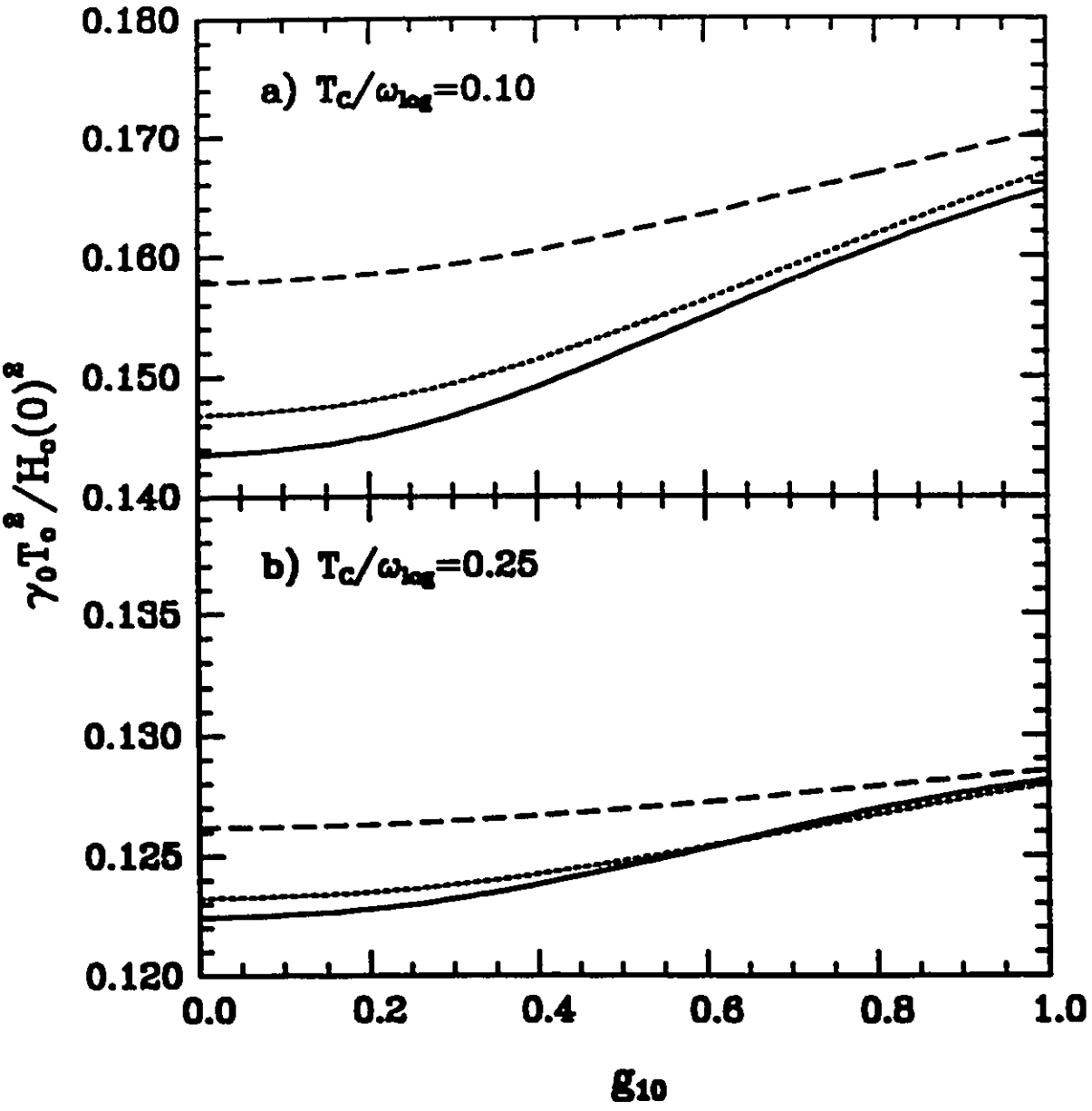

Fig. 3.2.2) The dimensionless ratio $\gamma_0 T^2{}_c/H^2{}_c(0)$ as a function of anisotropy parameter g_{10} for various values of g_{20}: 0.0 (solid curve), 0.3 (dotted curve), 0.7 (short dashed curve). The top frame applies to intermediate coupling with $T_c/\omega_{log} = 0.1$ while the bottom frame is for strong coupling with $T_c/\omega_{log} = 0.25$.

Since all the quantities in the formula for ΔF, Eq. (3.2.2), depend on the Matsubara frequencies only, we solve the anisotropic Eliashberg equations, (2.3.8) and (2.3.9), for different situations. The effect of the anisotropy on the thermodynamic critical field are then studied through the formulas (3.2.1) and (3.2.2). In Fig. 3.2.1, we plot the zero temperature value of $H_c(T)$ as a function of g_{10} for three values of g_{20}, namely, 0.0 (solid curve), 0.3 (dotted curve), and 0.7 (short dashed curve). The top frame applies to $T_c/\omega_{log} = 0.1$ intermediate coupling while the bottom frame is for $T_c/\omega_{log} = 0.25$ strong coupling. What we see here is that the anisotropy always reduces the value of $H_c(0)$ below its value in the isotropic case. We should note that $H_c(T)$ is proportional to the square root of the electronic density of states at the Fermi energy $N(0)$, so that the units for $H_c(0)$ are, in that sense, arbitrary. We have used $N(0) = 1.0 \times 10^{19}(cm^3 \cdot meV \cdot spin)^{-1}$ to be specific. A dimensionless way of plotting the same information is to plot the ratio $\gamma_0 T^2{}_c/H^2{}_c(0)$, as shown in Fig. 3.2.2. In this case anisotropy increases the ratio which is depressed from its BCS value by strong coupling effects. Note, the differences between the curves are smaller in the bottom frame where $T_c/\omega_{log} = 0.25$ (strong coupling) than they are in the top frame where $T_c/\omega_{log} = 0.1$ (intermediate coupling), also the solid and dotted curves now cross each other in the region of parameter space considered.

In Fig. 3.2.3, we show the effects of coupling strength and of the anisotropy on the temperature variation of the critical field. What is plotted is the deviation function denoted by $D(t)$ and defined by

$$D(t) = \frac{H_c(T)}{H_c(0)} - (1 - t^2)$$

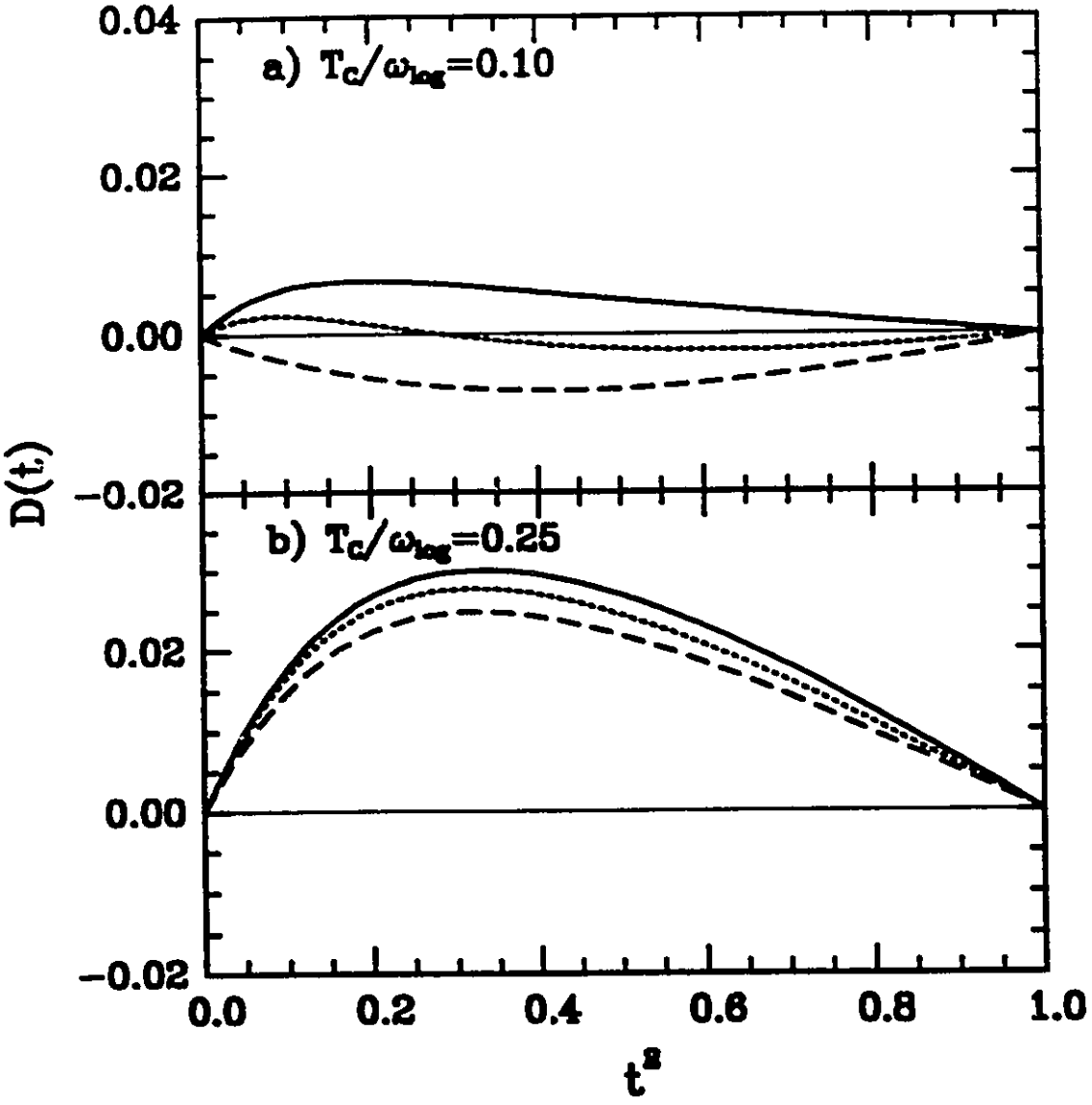

Fig. 3.2.3) The deviation function $D(t)$ as a function of reduced temperature T/T_c for the various anisotropy parameters, namely $g_{10} = 0.0$ (solid curve) isotropic case for comparison, $g_{10} = 0.4$ (dotted curve), and $g_{10} = 1.0$ (short dashed curve). $g_{20} = 0.0$ for all three cases. The top frame applies to intermediate coupling with $T_c/\omega_{log} = 0.1$ and the bottom frame to strong coupling with $T_c/\omega_{log} = 0.25$.

(3.2.5)

where the $1 - t^2$ law has been subtracted out so as to place emphasis on the differences in temperature variation from the two fluid model [Gorter and Casimir (1934a,b); Ginsburg and Landau (1950)]. The quantity $t = T/T_c$ is the reduced temperature. In the top frame, $T_c/\omega_{log} = 0.1$ (intermediate coupling), while $T_c/\omega_{log} = 0.25$ (strong coupling) in the bottom frame. In both cases the isotropic curve is everywhere positive (solid curves), and the anisotropy reduces $D(t)$. The dotted curve is for $g_{10} = 0.4$ and the short dashed curve is for $g_{10} = 1.0$. In both cases $g_{20} = 0.0$ which is sufficient for illustrative purposes. We see that anisotropy can make $D(t)$ negative definite in the intermediate coupling case in contrast to strong coupling where the curves remain positive definite for all reduced temperature values. In fact in this case the $g_{10} = 1.0$ curve is not very different from the isotropic case.

3.3 ELECTRONIC DENSITY OF STATES AND ENERGY GAP

As important as the electronic band structure is to normal metals, the distribution of electronic density of state in the superconducting states is the key for us to understand many superconducting properties in the thermal equilibrium state. Experimentally, the electronic density of states can be measured through superconducting tunneling experiments, where the characteristic current-voltage ($I - V$) curve is measured through a good tunnel junction with superconducting-insulator-metal configuration. For most conventional isotropic superconductors, except for a supercurrent at zero-voltage, there is no current (I) flow before the voltage (V) is equal to the energy gap (Δ_0) and then a sharp onset is observed [McMillan and Rowell

(1965, 1969)]. Phonon structure is also clearly shown and can be well matched with the gap value in most cases. In the high T_c oxides this is no longer the case. Usually there is always a zero bias and the value of the energy gap remains ambiguous and controversial [Lee, Kapitulnik, and Beasley (1989); Kirtley (1990); Valles *et al.* (1991)]. Further, these systems are by their very nature highly anisotropic because of their layered crystal structure. Here we wish to examine the electronic density of states with strong anisotropy for different coupling cases. We would like to understand better what information about the gap value (if there is one) and its temperature dependence can be obtained in principle from an examination of the electronic density of states and of phonon structure. The very strong coupling case is particularly interesting since, in that case, it is not at all clear that an energy gap will exist at non zero temperature, particularly in an anisotropic superconductor [Jiang and Carbotte (1992b)].

Using Green's function technique, the quasiparticle density of states is defined as [Schrieffer (1964)]

$$N(\omega) = -\frac{1}{\pi}\langle \int_{-\infty}^{\infty} d\epsilon N(\epsilon) Im\Big(G(\mathbf{k},\epsilon)\Big)\rangle \tag{3.3.1}$$

where $\langle\rangle$ denotes to a Fermi surface average as before, $\mathbf{k} = (\omega, \vec{k})$, $N(\epsilon)$ is the electronic density of states in the normal state, $G = \mathbf{G_{11}}$ is the electron Green's function with $\mathbf{G}$ the electron Green's function in Nambu notation, and Im denotes the imaginary part. Also the Fermi level is set at $\epsilon = 0$. Thus, $N(0)$ is the electronic density of states at the Fermi level. In Nambu notation, the normal state electron Green's function is

$$\mathbf{G}_n(\mathbf{k},\epsilon) = \frac{\tilde{\omega}_{\vec{k}}(\omega+i\delta)\tau_0 + \epsilon_{\vec{k}}\tau_3}{\tilde{\omega}^2_{\vec{k}}(\omega+i\delta) - \epsilon^2_{\vec{k}}} \tag{3.3.2}$$

while in the superconducting state, it is

$$\mathbf{G}_s(\mathbf{k},\epsilon) = \frac{\tilde{\omega}_{\vec{k}}(\omega+i\delta)\tau_0 + \epsilon_{\vec{k}}\tau_3 + \tilde{\Delta}_{\vec{k}}(\omega+i\delta)\tau_1}{\tilde{\omega}^2_{\vec{k}}(\omega+i\delta) - \epsilon^2_{\vec{k}} - \tilde{\Delta}^2_{\vec{k}}(\omega+i\delta)} \tag{3.3.3}$$

with $\tilde{\omega}$ the renormalized quasiparticle energy and $\tilde{\Delta}$ the pairing potential function in the superconducting state. The energy $\epsilon_{\vec{k}}$ is measured relative to the chemical potential μ, and τ_i is a Pauli matrix with

$$\tau_0 = \begin{pmatrix} 1 & 0 \\ 0 & 1 \end{pmatrix} \quad \tau_1 = \begin{pmatrix} 0 & 1 \\ 1 & 0 \end{pmatrix} \quad \tau_2 = \begin{pmatrix} 0 & -i \\ i & 0 \end{pmatrix} \quad \tau_3 = \begin{pmatrix} 1 & 0 \\ 0 & -1 \end{pmatrix}. \tag{3.3.4}$$

Both of the functions, $\mathbf{G}_n$ and $\mathbf{G}_s$, decrease rather quickly as ϵ increases. We also assume that $N(\epsilon)$ is constant around Fermi level over a large range, an assumption consistent with the discussion in section 1.1. Therefore, we can take $N(\epsilon)$ out off the integral and use its value at the Fermi level, $N(0)$, instead. All the results in the following will be presented in as normalized ratio $N(\omega)/N(0)$. This makes the formula much simpler. With the formulas (3.3.1) and (3.3.2), it is easy to work out, by contour integral, that in the normal state the ratio $N(\omega)/N(0) \equiv 1$ as expected. In the superconducting state, the ratio is

$$\frac{N(\omega)}{N(0)} = \langle Re(\frac{\tilde{\omega}_{\vec{k}}(\omega)}{\sqrt{\tilde{\omega}^2_{\vec{k}}(\omega) - \tilde{\Delta}^2_{\vec{k}}(\omega)}}) \rangle \tag{3.3.5}$$

To use the above formula for the ratio $N(\omega)/N(0)$, it is necessary to have solutions of the Eliashberg equations for the pairing potential $\tilde{\Delta}_{\vec{k}}(\omega)$ and renormalized energy $\tilde{\omega}_{\vec{k}}(\omega)$ on the real frequency axis. The Eliashberg equations which we used, therefore, are the equations (2.3.10) and (2.3.11). Also, we use the Pb spectrum ($\alpha^2F(\omega)$), as determined through tunneling spectroscopy, for numerical calculations. The height of it is adjusted to give the desired coupling strength measured by the parameter T_c/ω_{log}. Our purpose here is to look at the effects of the anisotropy and strong coupling, the exact form of the spectrum is not important.

In Fig. 3.3.1, we show, without emphasis of the phonon structure region, the changes in the quasiparticle density of states at low temperature ($T/T_c = 0.1$) when anisotropy is introduced using the simplest possible model, *i.e.*, it is assumed that only g_{10} is non-zero in the expansions (see the last chapter). All curves are for intermediate coupling with the monitoring parameter $T_c/\omega_{log} = 0.1$. The solid curve applies to the isotropic case and displays a sharp onset at the value $\omega/T_c \cong 2.05$ with a BCS type inverse square root singularity clearly evident at the onset. This value $\omega \cong 2.05T_c$ is often called the energy gap edge and written as Δ_0. It is close to the prediction from BCS theory that the energy gap Δ at zero temperature equals $1.76T_c$. The difference is the result of the stronger coupling here than in BCS theory. It is clear from the figure that when anisotropy is introduced the peak in $N(\omega)/N(0)$ becomes considerably attenuated and shifts to higher energies.

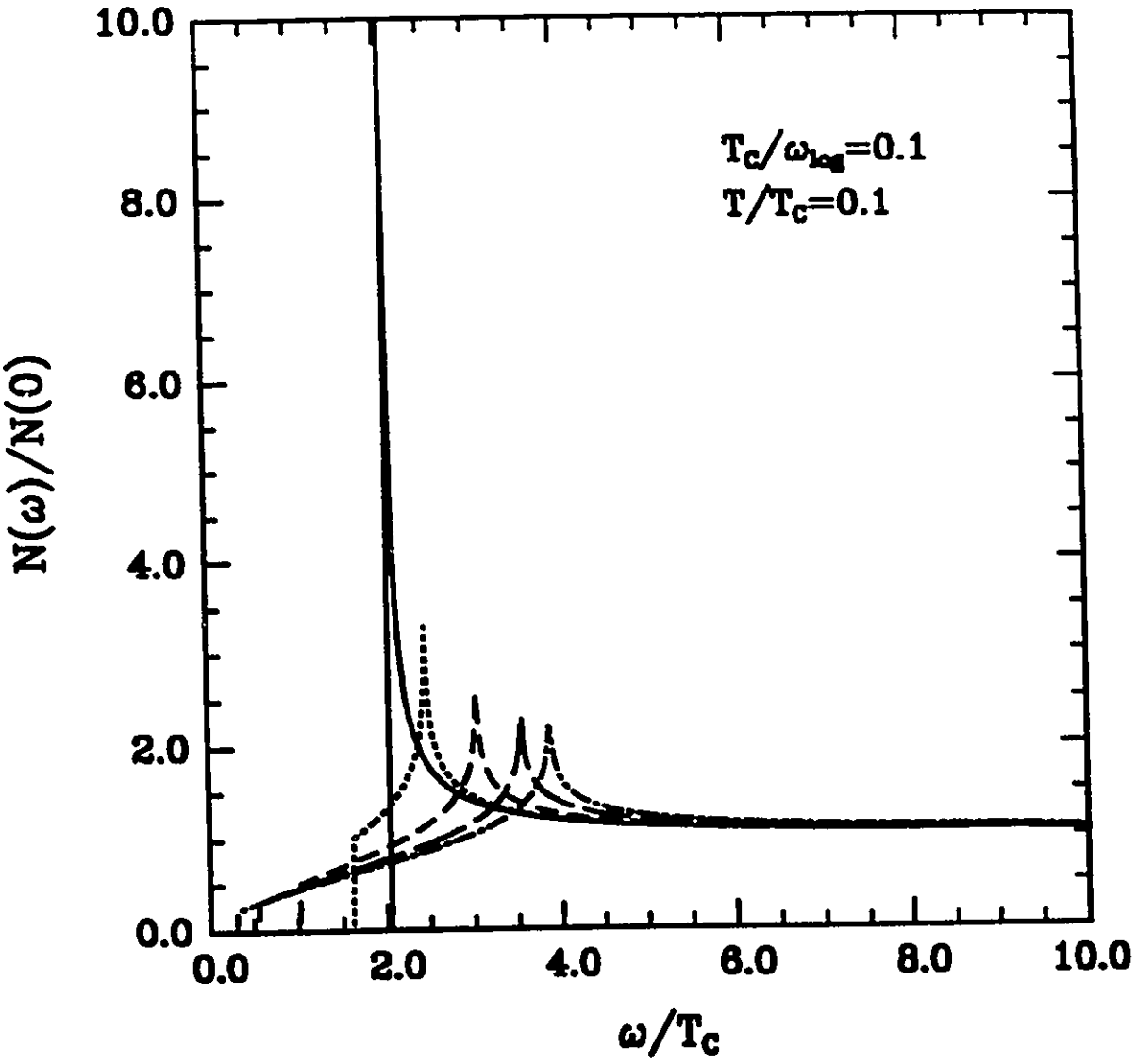

Fig. 3.3.1) The average quasiparticle density of states $N(\omega)/N(0)$ as a function of normalized frequency ω/T_c for low temperature $T/T_c = 0.1$ and an intermediate coupling parameter $T_c/\omega_{log} = 0.1$. The solid curve is for $g_{10} = 0.0$ the isotropic case while other curves have the anisotropy with $g_{10} = 0.2$ (dotted curve), 0.5 (short dashed curve), 0.8 (long dashed curve), and 1.0 (short dashed-dotted curve).

While a sharp onset at a minimum gap value is still clearly visible in this instance, it is now only a finite step and is therefore less pronounced. Note that, the peaks in each of these curves order monotonically in energy position on the horizontal axis according to the value of the anisotropy index g_{10} which ranges over values 0.0 (solid curve), 0.2 (dotted curve), 0.5 (short dashed curve), 0.8 (long dashed curve), and 1.0 (short dashed-dotted curve), so does the height of the peaks.

Our main interest here is in the temperature evolution of the curves for $N(\omega)/N(0)$ including shifts in position and shape of the peaks, and edges. In Fig. 3.3.2, we consider the isotropic case for two different coupling strengths. The top frame is for an intermediate coupling with $T_c/\omega_{log} = 0.1$, and the bottom frame is for a very strong coupling with $T_c/\omega_{log} = 0.3$. At near zero temperature ($T/T_c = 0.1$) (solid curve) the gap is easily identified as the position of the sharp onset and peak position for both cases. When the temperature T is increased towards T_c, however, things become quite different.

We first look at the intermediate coupling case, the top frame. It is evident that, a small tail in $N(\omega)/N(0)$ exists down to zero frequency in the region below the main rise even for a reduced temperature of 0.7 (the dotted curve). So, strictly speaking there is no gap in $N(\omega)/N(0)$ although, in practice, one could ignore the small leakage into the gap region and still define a value for the rapid onset defining the main peak in $N(\omega)/N(0)$. Note however that, the onset of this peak is not itself completely sharp and so some small ambiguity would arise in its identification. This ambiguity is not there at zero temperature. Also the height of the peak is attenuated relative to zero T and so everything is less well defined. As the temperature is further raised the trend continues towards more attenuation of the peak and more

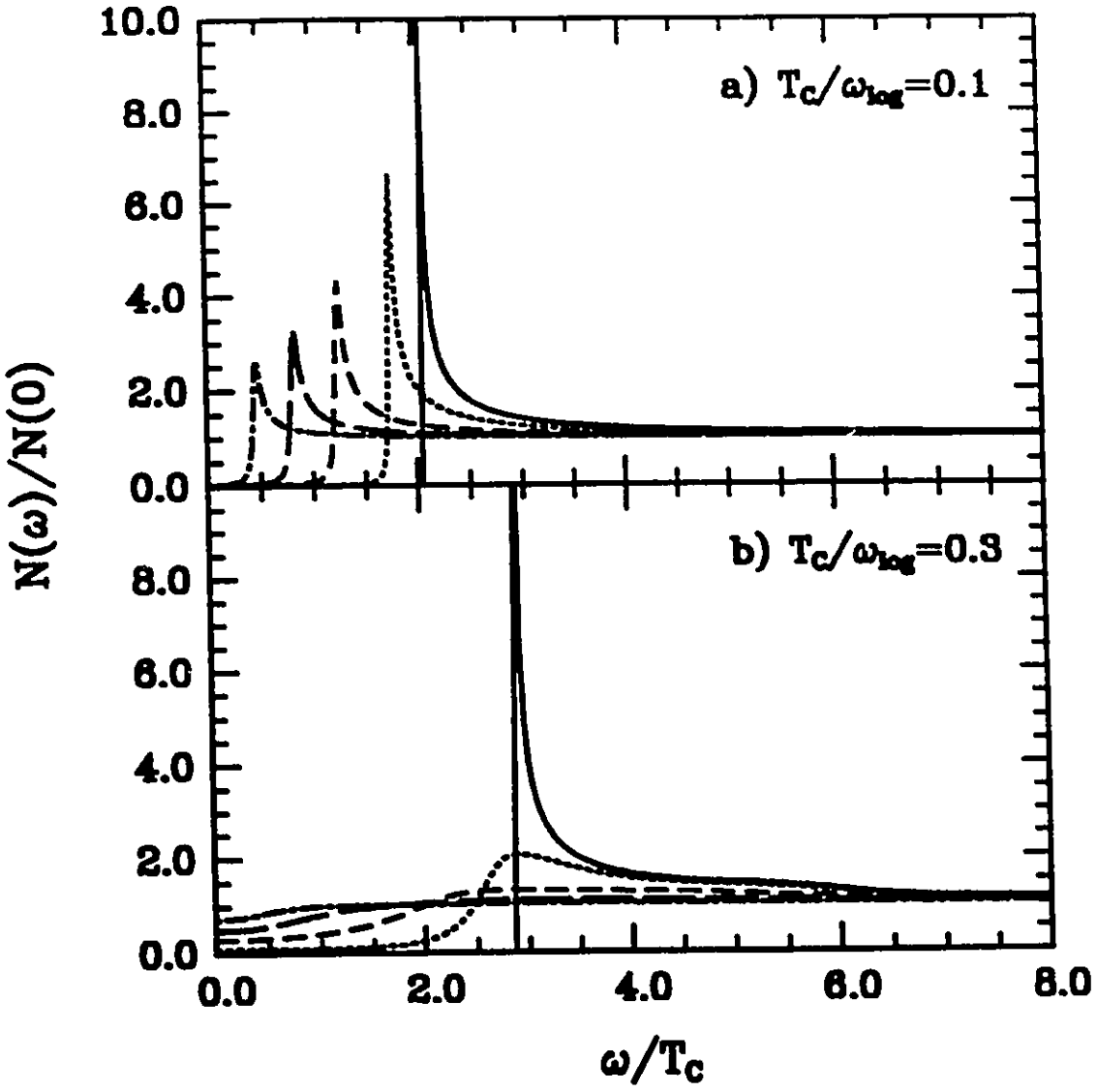

Fig. 3.3.2) The quasiparticle density of states $N(\omega)/N(0)$ as a function of normalized frequency ω/T_c for an isotropic case at different temperatures. The top frame is for intermediate coupling $T_c/\omega_{log} = 0.1$, while the bottom frame is for very strong coupling $T_c/\omega_{log} = 0.3$. For both cases, the solid curve is for $T/T_c = 0.1$, the dotted curve for 0.7, the short dashed curve for 0.875, the long dashed curve for 0.95, and the short dashed-dotted curve for 0.985.

smearing of the gap region making the concept of a gap somewhat less valid. The clearest unambiguous identification that can be made of an onset value for $N(\omega)/N(0)$ is the frequency defining the peak value. We will call this frequency the gap or the peak position and use the symbol $\Delta_p(T)$, with the subscript p denoting peak value.

When the coupling is increased, it becomes more and more difficult to define a gap value at finite temperature. This is illustrated in the bottom frame, a very strong coupling case with $T_c/\omega_{log} = 0.3$. Now even at $T/T_c = 0.7$ (dotted curve), the peak is much less well defined and the smearing into the low ω region is very significant. Certainly for $T/T_c = 0.875$ (short dashed curve), 0.950 (long dashed curve), and 0.985 (short dashed-dotted curve) no identifiable peak remains and no remanent of a gap concept is evident. Therefore, we can not even define a peak value $\Delta_p(T)$ here, as we could for the intermediate coupling case. We would like to mention that the similar curves as those here were also shown in the work by Allen and Rainer (1991) and by Karakozov *et al.* (1991).

In Fig. 3.3.3, we give details of the trend in the quasiparticle density of states as temperature is increased in one anisotropic case namely $g_{10} = 0.5$ for the same two couplings using in the last figure, *i.e.*, $T_c/\omega_{log} = 0.1$ in the top frame and $T_c/\omega_{log} = 0.3$ in the bottom frame. We see now that, in the top frame, the smearing below the lowest gap is more pronounced than in the corresponding isotropic case (the top frame in Fig. 3.3.2) and that the first rapid rise in $N(\omega)/N(0)$ is even less well defined particularly at the higher temperatures. No gap value can be unambiguously defined from this feature. However, the peak position remains a well defined quantity in all these curves: $T/T_c = 0.1$ (solid curve), 0.7 (dotted), 0.875 (short dashed), 0.95(long

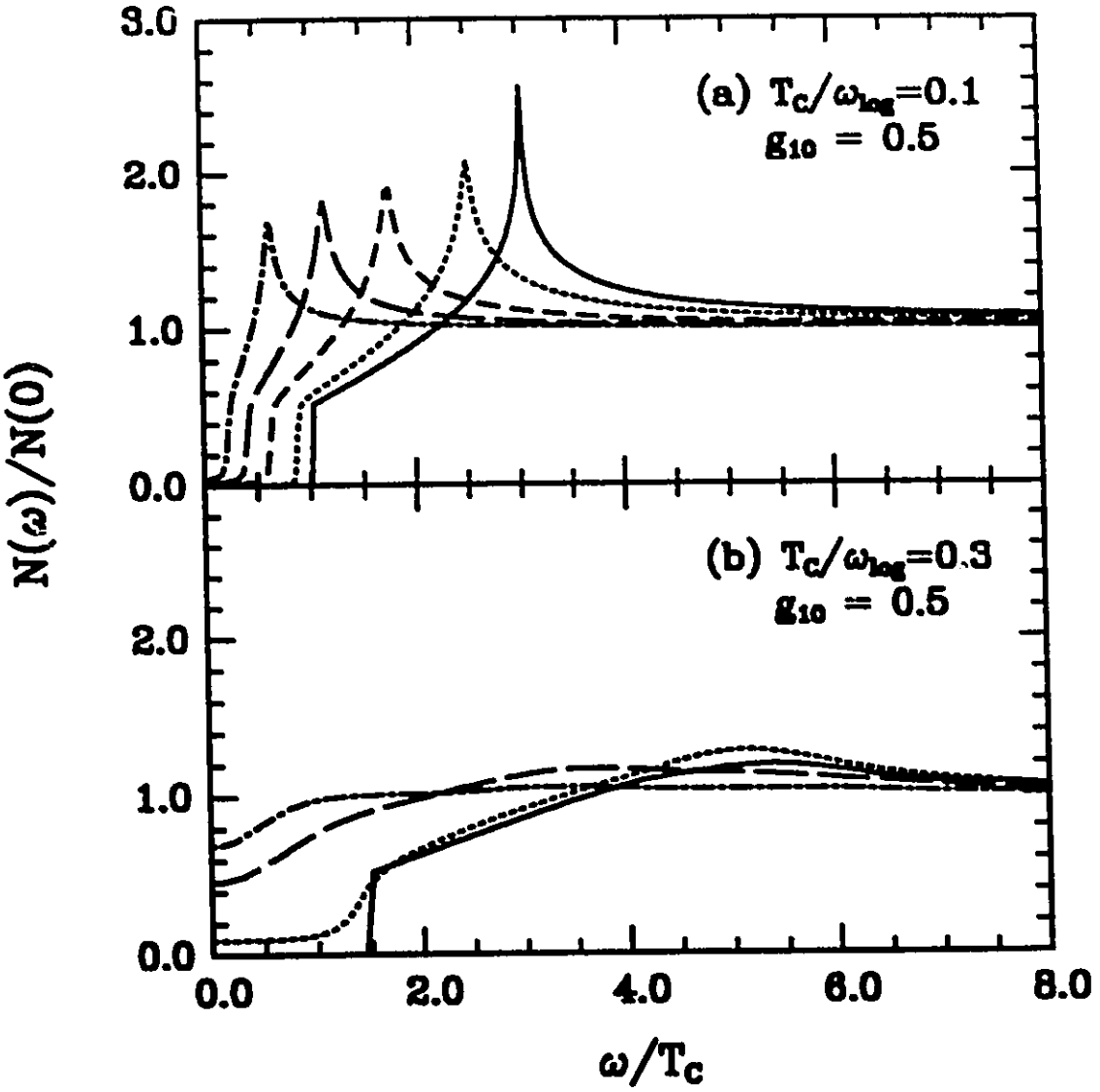

Fig. 3.3.3) The average quasiparticle density of states $N(\omega)/N(0)$ as a function of normalized frequency ω/T_c for the anisotropy model with $g_{10} = 0.5$ at various temperatures. The top frame is for intermediate coupling $T_c/\omega_{log} = 0.1$ and the bottom frame is for very strong coupling $T_c/\omega_{log} = 0.3$. For both cases, the solid curve is for $T/T_c = 0.1$, the dotted curve for 0.7, the short dashed curve for 0.875, the long dashed curve for 0.95, and the short dashed-dotted curve for 0.985.

dashed), and 0.985 (short dashed-dotted). But, in the bottom frame, where the coupling is strong, there is no well defined peak remaining, same as that in the corresponding isotropic case (the bottom frame in Fig. 3.3.2), and the smearing into the low frequency region is even more significant than that in the bottom frame in Fig. 3.3.2. Thus, we conclude that, as T_c/ω_{log} is increased the concept of a gap existing in the quasiparticle density of states rapidly loses its meaning with increasing temperature towards T_c, and adding anisotropy makes it even more so.

As we pointed out above for an intermediate coupling strength $T_c/\omega_{log} = 0.1$, there is an identifiable peak in the quasiparticle density of states at all the reduced temperatures we considered for either isotropic or anisotropic case. If we plot the value of this peak position, which we defined as $\Delta_p(t)$, as a function of temperature, we obtain for its variation with reduced temperature $t = T/T_c$ a very nearly BCS dependence as is shown in Fig. 3.3.4. The upper open circles, which corresponds to the isotropic case, are seen to fall slightly above the solid curve which is the BCS gap variation reproduced here for comparison. Thus, the peak value can certainly be used in this case, to trace out a temperature dependence of the gap which is only slightly different from BCS. The other data apply to the anisotropic cases with $g_{10} = 0.2$ (*), 0.5 (Δ), 0.8 ($\bullet$), and 1.0 ($\square$). They also fall closely to the BCS curve but a clear trend, towards a slightly more rapid drop to zero of $\Delta_p(T)/\Delta_p(0)$ as T_c is approached, is clearly indicated when g_{10} is increased. While the peak position in $N(\omega)/N(0)$ tracks closely the BCS temperature dependence of the gap it needs to be emphasized that the position of that peak, in an anisotropic superconductor, is neither at the minimum gap nor at its average value as seen previously in Fig. 3.3.1. Again, as the smearing

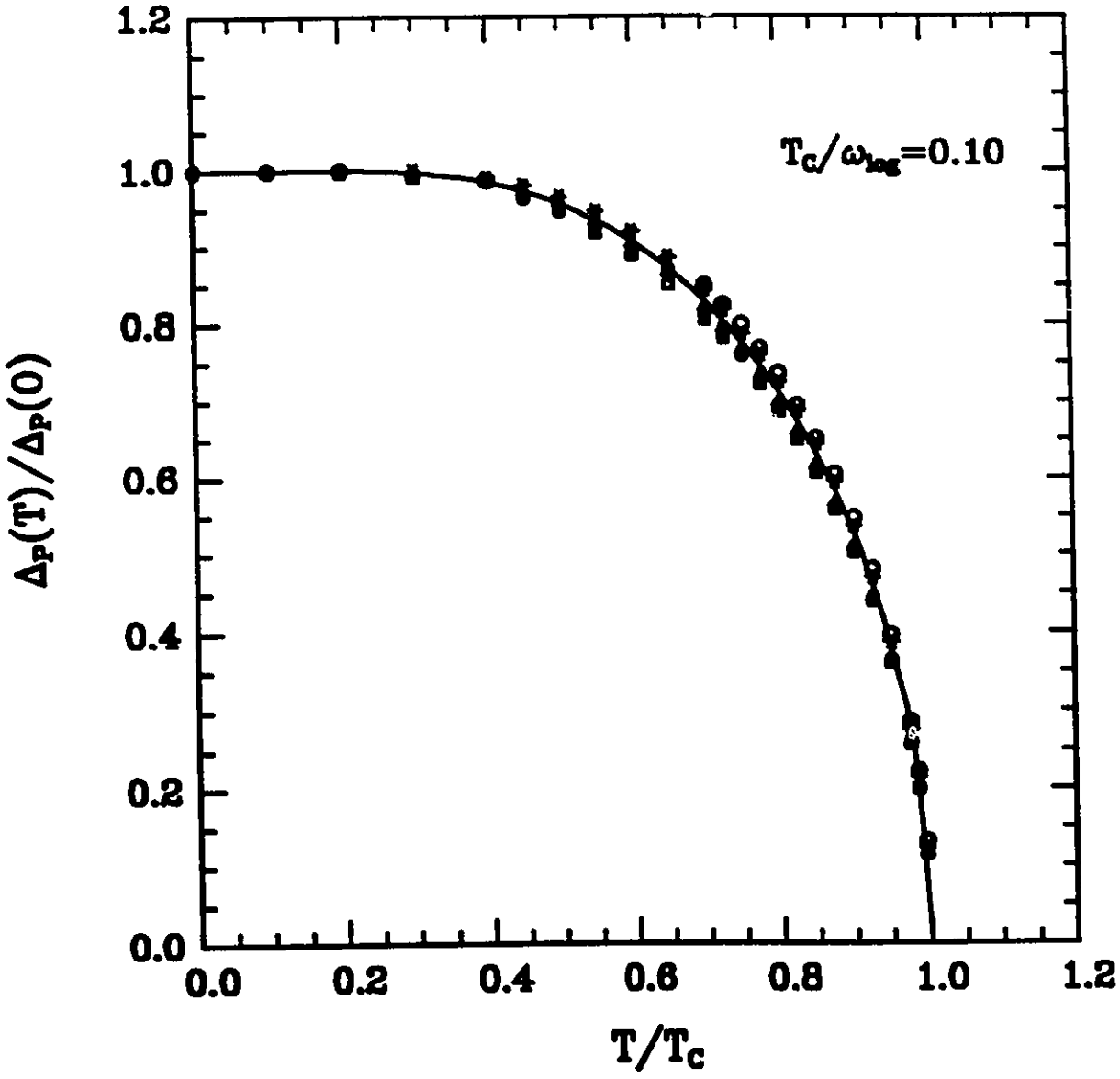

Fig. 3.3.4) The position of the peak in the quasiparticle density of states at temperature T normalized to its zero temperature value as a function of reduced temperature T/T_c. The BCS variation for the gap is also shown for comparison (solid curve). The open circles (o) are for $g_{10} = 0.0$, $*$ for 0.2, Δ for 0.5, $\bullet$ for 0.8, and $\square$ for 1.0.

in the low frequency region increases when temperature approaches T_c, there is no well defined gap edge, especially for an anisotropic superconductor, in the quasiparticle density of states.

3.4 THE PHONON STRUCTURE

In the last section our discussion about the quasiparticle density of states emphasized the frequency region where a gap edge exists for an isotropic superconductor at low temperature. Here we would like to examine another structure in the quasiparticle density of states, which is at a higher frequency, the phonon structure [Carbotte (1990); Jiang and Carbotte (1992b)]. It is so named since, for most conventional superconductors where a phonon mechanism has been well established, this structure carries the information on the electron-phonon spectral density from which the superconductivity arises. The electron-phonon spectral density can actually be obtained from this structure by inverting through the Eliashberg equations, as we discussed before [McMillan and Rowell (1964, 1969)]. Experimentally, the phonon structure can be measured from tunneling spectroscopy, where the derivative of the characteristic I(current)V(voltage) curve of the system, dI/dV, which is proportional to the $N(\omega)/N(0)$ at $T \to 0$, is measured through a tunneling junction. Because of this tunneling spectroscopy has an important role in the study of superconductivity, although technically it is difficult to make a good tunneling junctions, especially for high-T_c oxide superconductors.

What we would like to discuss here is the temperature dependence of the phonon structure and its relationship to the temperature dependent peak value $\Delta_p(T)$, which is shown in Fig 3.3.4, under the influences of anisotropy

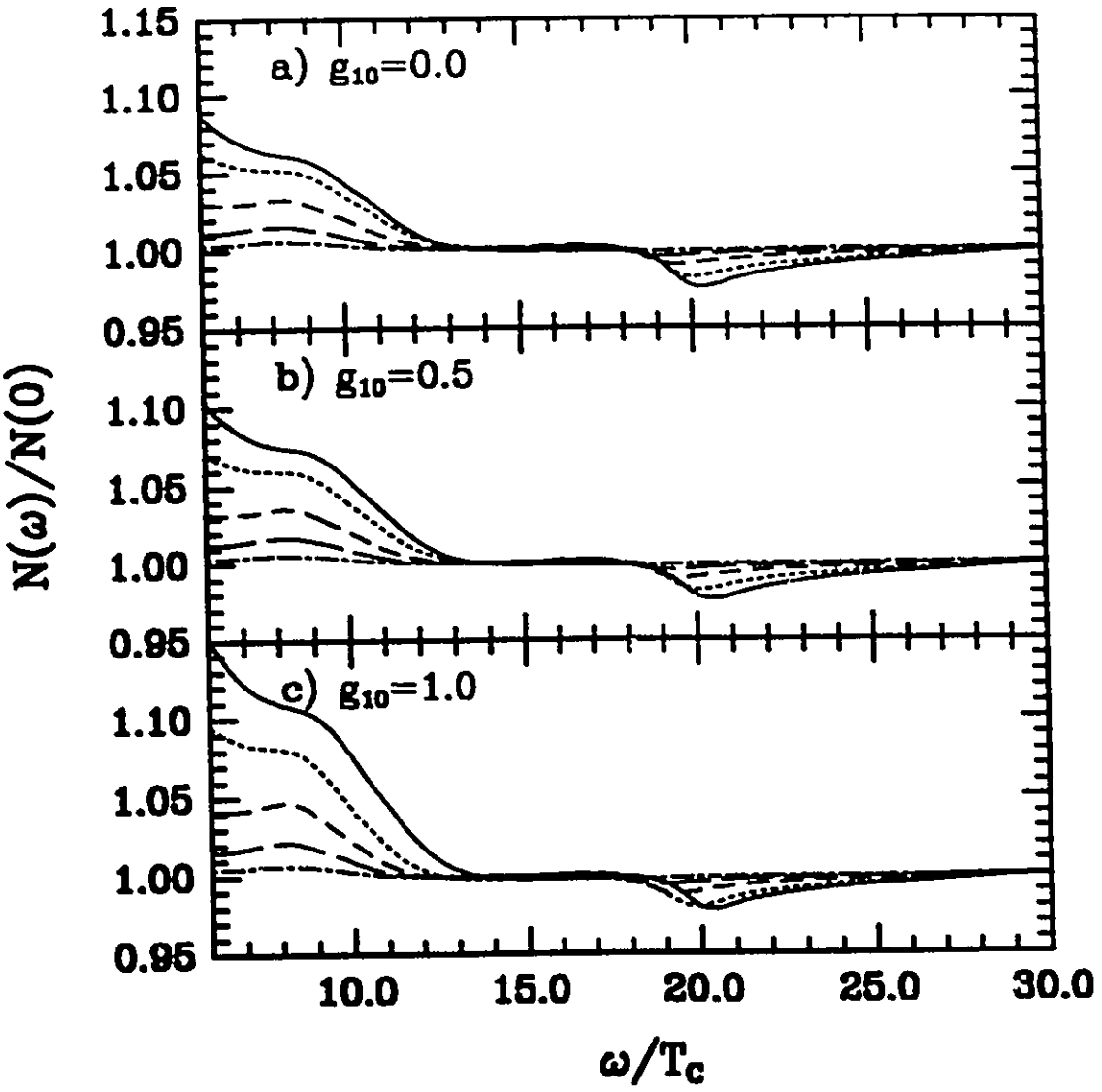

Fig. 3.4.1) The average quasiparticle density of states $N(\omega)/N(0)$ as a function of normalized frequency ω/T_c in the phonon region. All three frames are for temperatures $T/T_c = 0.1$ (solid curve), 0.7 (dotted curve), 0.875 (short dashed curve), 0.95 (long dashed curve), and 0.985 (short dashed-dotted curve). The top frame is for $g_{10} = 0.0$, the middle frame for $g_{10} = 0.5$, and the bottom frame for $g_{10} = 1.0$. All curves are for intermediate coupling $T_c/\omega_{log} = 0.1$.

and strong coupling. The question we want to address is: can we use the shift in phonon structure (or the peak structure) with increasing temperature to determine a temperature dependent "gap"? If so, what does this mean when there is large anisotropy? Do the structures fall at the lowest gap plus the phonon energy or at some other value? To answer these questions, we begin with the examination of an intermediate coupling case $T_c/\omega_{log} = 0.1$. In Fig. 3.4.1 we show $N(\omega)/N(0)$ vs ω in the phonon region for various temperature values: $T/T_c = 0.1$ (solid curve), 0.7 (dotted curve), 0.875 (short dashed curve), 0.95 (long dashed curve), and 0.985 (short dashed-dotted curve). The top frame applies to the isotropic case with $g_{10} = 0.0$. The middle frame is for $g_{10} = 0.5$ while the bottom frame has $g_{10} = 1.0$ which is a very anisotropic case with g_{10} now as large as g_{00}. On careful comparison of the top and middle frame we note that, in the region near $\omega/T_c = 6.0$ where our curves start, there is some change of the phonon structure introduced by increasing anisotropy. This change continues in the bottom frame. In this frequency region, however, there is no sufficiently well defined structure to focus on and to study its evolution with temperature. At higher frequencies near $\omega/T_c \cong 20$ a much more favorable opportunity is offered. We note first that, in this region, anisotropy changes the shape and the amplitude of the structure only a little between top and central frame. There is some measurable difference between top and lower frame however. Still, a well defined minimum or dip remains in all cases. We have traced out the temperature dependence of the position of this phonon structure for all cases in our Fig. 3.4.1, *i.e.*, different values of anisotropy g_{10} and have found that in all cases this structure, denoted by $\Delta_m(t)$ where the subscript m now stands for minimum, is closely related to

the peak position $\Delta_p(t)$ discussed previously, which we will show in the next figure.

What we have plotted in Fig. 3.4.2 is the quantity $\Delta(t) - \Delta(0.5)$ for both peak structure (open circles) and phonon structure (stars). The top frame is for an isotropic case, while the bottom is for the anisotropic model $g_{10} = 0.5$. We see that, for both cases, the peak and phonon structure follow the same temperature dependence. Two points of explanation are necessary. First we subtracted off $\Delta(0.5)$ in our comparison, because it is difficult to differentiate in our numerical data between $\Delta(0.5)$ and $\Delta(0.0)$. Secondly for the position of the phonon structure we have found from an examination of the data that it is necessary to multiply $\Delta_m(t) - \Delta_m(0.5)$ by the factor $(1+g_{10})$ ($g_{10} = 0.0$ and 0.5 in the top and bottom frame respectively) in order to get it to fall on the curve for the peak position $\Delta_p(t) - \Delta_p(0.5)$.

It is clear from the above results that one can indeed use the shift in position of phonon structure with temperature to trace out the temperature dependence of the "gap" for an intermediate coupling superconductor. For an isotropic superconductor the relation between the shift of the phonon structure and the change of the "gap" value is one by one. For an anisotropic case, however, we must have a knowledge of the anisotropy parameter g_{10} before we can tell the value of the "gap" from the phonon structure. With an examination of the electron-phonon spectral density $\alpha^2F(\omega)$ which we used, we also found that the position of the phonon structure ($\sim 9.5meV$) is approximately equal to the peak value in the quasiparticle density of states ($\sim 1.0meV$ at zero temperature) plus the peak value in the $\alpha^2F(\omega)$ ($\sim 8.5meV$) for an isotropic superconductor. This is not true for an anisotropic superconductor

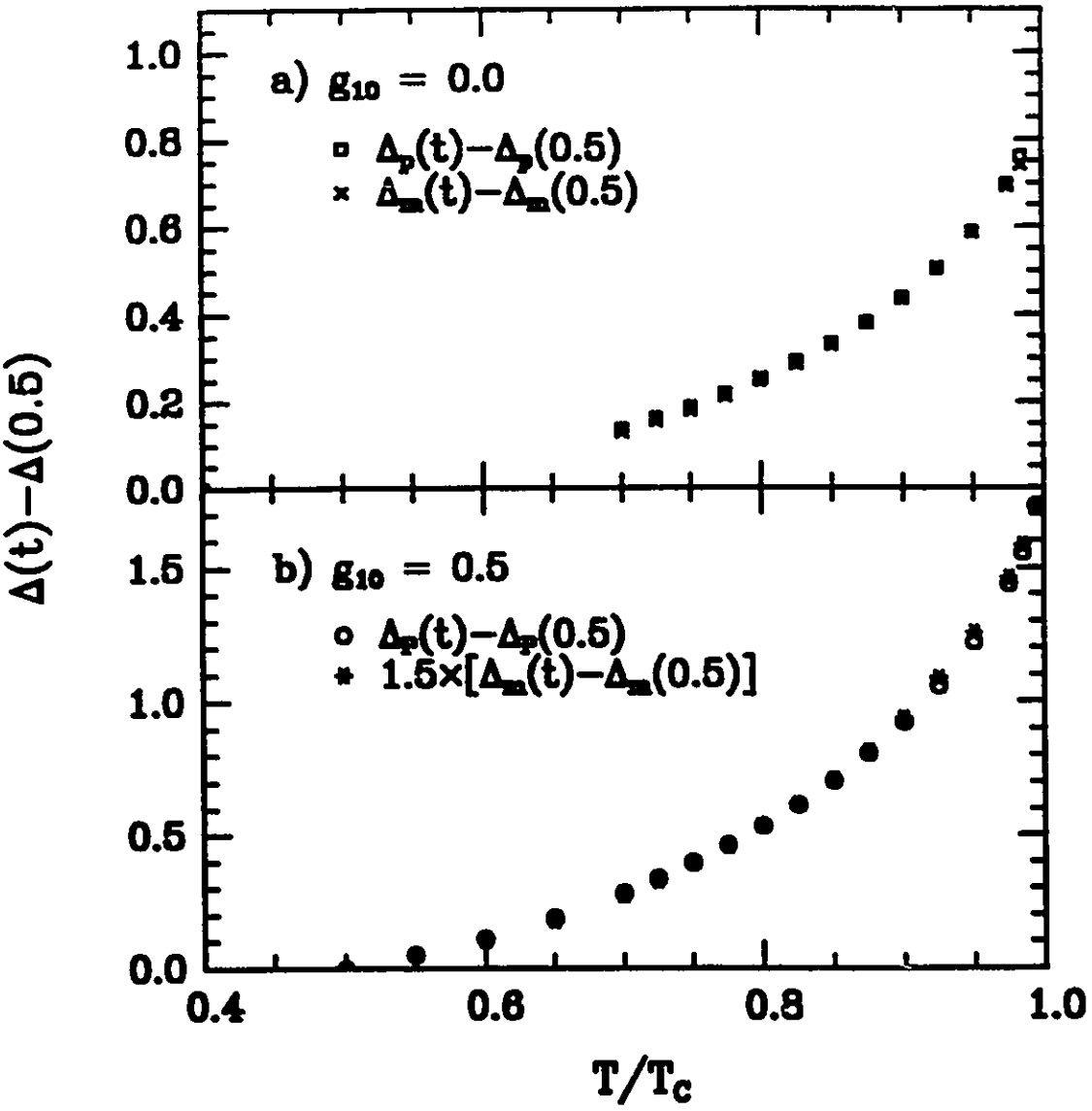

Fig. 3.4.2) The gap difference $\Delta(t) - \Delta(0.5)$ as a function of reduced temperature $t = T/T_c$ in the range $t \geq 0.4$. The top frame is for an isotropic case while the bottom frame is for the anisotropic model $g_{10} = 0.5$. In both frames the open circles are the peak positions in $N(\omega)/N(0)$ while the stars are the phonon positions multiplied by an empirical factor of $(1+g_{10})$, and the strong coupling parameter $T_c/\omega_{log} = 0.1$

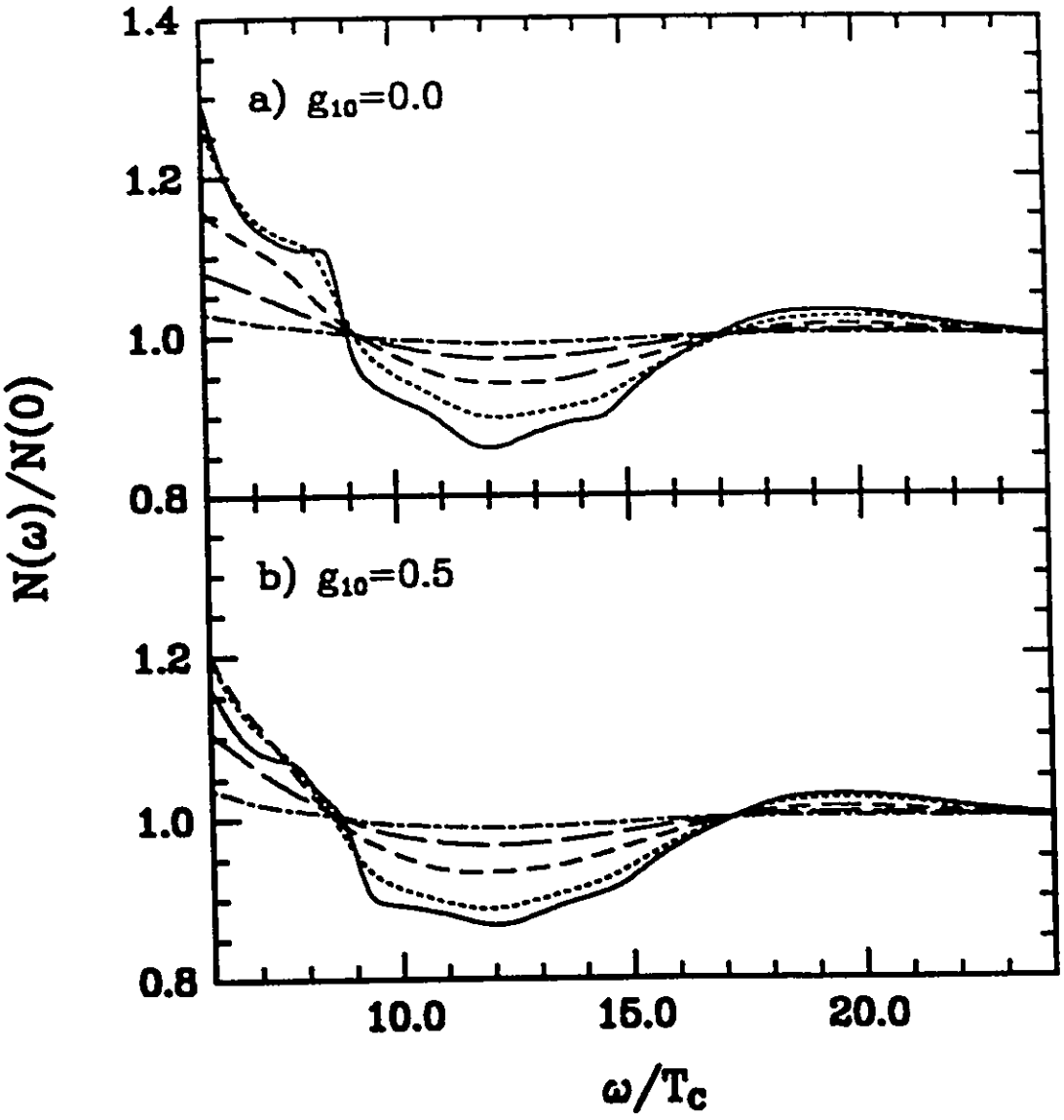

Fig. 3.4.3) The average quasiparticle density of states $N(\omega)/N(0)$ as a function of normalized frequency ω/T_c in the phonon region. Both frames are for temperatures $T/T_c = 0.1$ (solid curve), 0.7 (dotted curve), 0.875 (short dashed curve), 0.95 (long dashed curve), and 0.985 (short dashed-dotted curve). The top frame is for $g_{10} = 0.0$ while the bottom frame for $g_{10} = 0.5$. All curves are for a strong coupling parameter $T_c/\omega_{log} = 0.3$.

as we can see that the position of the phonon structure does not change much with the anisotropy but the peak value does.

All the above remarks apply only to the case $T_c/\omega_{log} = 0.1$. As the coupling is increased such analysis becomes less valid and has broken down completely for $T_c/\omega_{log} = 0.3$ as is shown in Fig. 3.4.3. In this case only two frames are shown and this is sufficient to make our main point. The top frame is for isotropic case while the bottom applies for $g_{10} = 0.5$. In each frame the temperatures considered are $T/T_c = 0.1$ (solid curve), 0.7 (dotted curve), 0.875 (short dashed curve), 0.95(long dashed curve), and 0.985 (short dashed-dotted curve). First we note that anisotropy does have some effect on phonon structure in the quasiparticle density of states but that the shift and changes in amplitude are never very large for the case considered. On examination of the curves in detail we note that there is now no well defined feature whose temperature dependence can be unambiguously traced. This is true even for the isotropic case. The prominent minimum in the solid curve for $T/T_c = 0.1$ for instance becomes completely blurred out as T is increased. This is all consistent with our previous analysis of peak structure in the low frequency region in Figs 3.3.2 and 3.3.3. In the very strong coupling region the gap ceases to have a precise meaning at finite temperature. The phonon structure seems to know this fact and so can not be used to trace out a temperature dependent "gap" value.

3.5 CONCLUSIONS

Using the anisotropic Eliashberg equations of the last chapter, we have investigated the effect of planar anisotropy on the critical temperature T_c, the thermodynamic critical field $H_c(T)$ which equals $\sqrt{8\pi \mid \Delta F(T) \mid}$ with

$\Delta F(T)$ the free energy difference between the normal and superconducting state, and the quasiparticle density of states. It is found that the effect is generally quite large, especially when the electron-phonon coupling is not very strong. The critical temperature can be enhanced by as much as 40% for large but reasonable value of the anisotropy when $T_c/\omega_{log} = 0.1$. At the same time, the thermodynamic critical field is always reduced as the anisotropy is increased.

In the quasiparticle density of states, a well defined gap structure of a modified BCS square root type singularity exists only at zero temperature for an isotropic Eliashberg superconductor. For an anisotropic Eliashberg superconductor, the Fermi surface average quasiparticle density of states is changed radically but there does remain a sharp edge corresponding to the value of the minimum gap with no attendant square root type singularity at zero temperature. When the temperature is increased towards T_c the singularity, in the isotropic case, and the step, in the anisotropic case, get smeared and, in principle, there can be a leakage of density of states into the low frequency region down to the zero. This makes it difficult to define an unambiguous finite temperature gap value. For intermediate coupling $T_c/\omega_{log} = 0.1$, where the smearing is small, there is a well defined peak structure in $N(\omega)/N(0)$ even with anisotropy. The position of the peak, which we called the gap, follows a temperature dependence that is only slightly modified from a BCS gap variation. As the coupling strength is increased to $T_c/\omega_{log} = 0.3$, the smearing becomes so severe that no well defined peak can be found even in the isotropic case.

The phonon structure in the quasiparticle density of states can be used to track the underlying temperature dependence of the gap or the

peak position even in the anisotropic case when the coupling is not strong ($T_c/\omega_{log} = 0.1$), provided that we have a precise knowledge of the underlying anisotropic model. For an isotropic superconductor, the attendant phonon structure also appears at energies equal to the sum of the gap plus the peak value in the $\alpha^2F(\omega)$ used.

Finally we should point out that, despite the fact that the energy gap in the quasiparticle density of states is not a well defined quantity in some cases discussed above, the concept is very useful in the discussion of many superconducting properties. In the following chapters we will use the concept of a energy gap frequently in our discussions, however, it should be understood as a finite pairing potential $\tilde{\Delta}$. For an Eliashberg superconductor, as long as $\tilde{\Delta}$ is not zero, we will have superconductivity and the quasiparticle density of states will be changed (see formula (3.3.5)). $\tilde{\Delta}$ is the most fundamental quantity for us.

Chapter 4

Thermodynamic and Transport Properties

In the last chapter, we showed the effects of anisotropy and strong coupling on the free energy difference between the normal and superconducting states and on the quasiparticle density of states in the superconducting state. As we know that many physical properties, especially thermodynamic and transport properties, are directly related to the free energy and/or the quasiparticle density of states, it is expected that anisotropy and strong coupling will have large effects on them as well. Several such properties are the electronic specific heat $\Delta C(T)$, the thermal conductivity $\mathcal{K}(T)$, and the ultrasound attenuation $\alpha(T)$. These are three of the most interesting properties both theoretically and experimentally for a superconductor and have been extensively studied .

What we are going to do in this chapter is examine in detail the effects of planar anisotropy and strong coupling on the three properties just mentioned, employing the formalism of chapter 2. We would like to show how the

anisotropy manifests itself in experiments which measure these properties. The major difference between the present study and previous studies [Schneider (1988, 1989, 1990a,b); Frick and Schneider (1990)] is that we incorporate the anisotropy of a layered structure in the strong coupling Eliashberg theory and in a consistent way. We will present first our results on $\Delta C(T)$—the specific heat difference. Then, in section 4.2, we will examine the thermal conductivity $\mathcal{K}(T)$, and then in section 4.3, discuss the ultrasound attenuation $\alpha(T)$. We will conclude this chapter with a short conclusion in section 4.4.

4.1 THE ELECTRONIC SPECIFIC HEAT

The specific heat of a metal has two components, the electronic part and the lattice part. It is well known from the theory of normal metals [Kittel (1986); Ashcroft and Mermin (1976)] that at low temperature the specific heat has the form

$$C(T) = \gamma_0 T + \beta T^3 \tag{4.1.1}$$

with the term linear in T an electronic contribution and the term cubic in T, the lattice contribution. The coefficient γ_0 is the Sommerfeld constant defined by formula (3.2.4) and β is a material dependent parameter.

For conventional superconductors (where T_c is small), the superconducting phase transition has practically no effect on the lattice part. The same temperature dependence remains, $C^s_{lat} \sim T^3$. In contrast, the electronic contribution changes drastically following the transition. There are

two things happening here. First, as a gap opens in the quasiparticle excitation spectrum, the electronic specific heat in the superconducting state C_{el}^{s} decays exponentially instead of linearly with temperature as long as the gap is non-zero everywhere on the Fermi surface. Second, as the normal-superconducting phase transition is a second-order phase transition, it is accompanied by a jump in the specific heat. Since the lattice specific heat does not change during the transition, the electronic specific heat must be responsible for this jump. In BCS theory, this jump is given by

$$\frac{C_{el}^{s}(T_c) - C_{el}^{n}(T_c)}{C_{el}^{n}(T_c)} = \frac{\Delta C(T_c)}{\gamma_0 T_c} = 1.43. \tag{4.1.2}$$

Here, γ_0 is again the Sommerfeld constant given by formula (3.2.4) with $\lambda = 0$ corresponding to BCS theory. This is an universal relation. Like many other universal relations in BCS theory, it is due to the weak electron-phonon coupling approximation. Whereas the specific heat jump is a universal property of all superconductors, its magnitude varies. For most conventional superconductors, the material dependence of the jump height can be well accounted for by Eliashberg theory, the strong coupling theory of superconductivity.

From standard thermodynamics, we know that the specific heat $\Delta C(T)$ is related to the free energy difference between normal state and superconducting state, $\Delta F = F_n - F_s$, by the formula:

$$\Delta C(T) = T\frac{d^2 \Delta F(T)}{dT^2}. \tag{4.1.3}$$

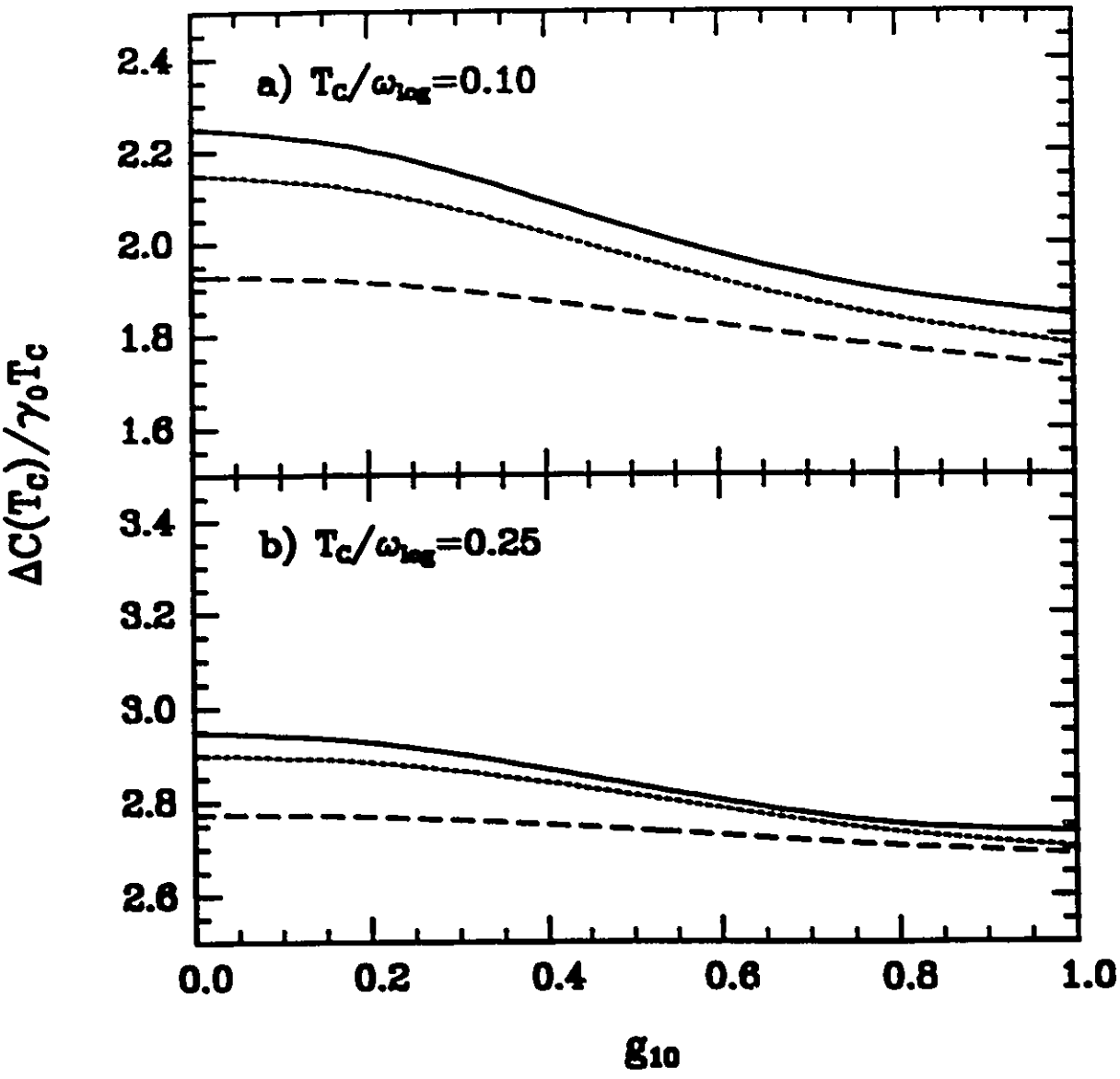

Fig. 4.1.1) The normalized specific heat jump at T_c, $\Delta C(T_c)/\gamma_0 T_c$, as a function of anisotropy parameter g_{10} for various values of g_{20}, namely 0.0 (solid curve), 0.3 (dotted curve), 0.7 (short-dashed curve). The top frame is for an intermediate coupling case with strong coupling index $T_c/\omega_{log} = 0.1$ while the bottom frame is for a strong coupling case ($T_c/\omega_{log} = 0.25$).

Here ΔF is the Fermi surface average of the free energy difference ΔF given by the formula (3.2.2) in the last chapter. Since the renormalized frequency $\tilde{\omega}$ and the pairing potential $\tilde{\Delta}$ in the formula (3.2.2) are functions of Matsubara frequency, we need to solve the imaginary axis Eliashberg equations only, Eqs. (2.3.8) and (2.3.9). The specific heat is then ready to be calculated through formula (4.1.3).

In Fig. 4.1.1, the specific heat jump at T_c, normalized by its normal state value $\gamma_0 T_c$ with γ_0 the normal state Sommerfeld constant, $\Delta C(T_c)/\gamma_0 T_c$, is plotted against the anisotropy parameter g_{10}. The solid curve corresponds to $g_{20} = 0.0$, the dotted curve to $g_{20} = 0.3$, and the short-dashed curve to $g_{20} = 0.7$. First for the solid curve in the top frame, we see that for no anisotropy $\Delta C(T_c)/\gamma_0 T_c \cong 2.25$ as compared with 1.43 in a BCS superconductor. This is expected since the strong coupling parameter T_c/ω_{log} is intermediate, equal to 0.1 in this instance. An even larger value of the normalized jump in the isotropic case, which equals approximate 2.95, applies when the strong coupling index T_c/ω_{log} is increased to 0.25 as in the bottom frame of Fig. 4.1.1. In real material, $Pb_{0.7}Bi_{0.3}$, this value is as big as 3.01 [Masiglio (1988)]. As the anisotropy is increased, the specific heat jump drops continuously in both intermediate ($T_c/\omega_{log} = 0.1$) and strong coupling ($T_c/\omega_{log} = 0.25$) cases. However the magnitude of the drop is much larger for the intermediate coupling than the strong coupling. For the most extreme values of anisotropy parameters considered here, the drop is about 23% in the top frame compared about 9% in the bottom frame. Also, adding g_{20} anisotropy has bigger effects on this drop for small value of g_{10} anisotropy than for larger values. In any cases, the value of $\Delta C(T_c)/\gamma_0 T_c$ is still well above the isotropic BCS value.

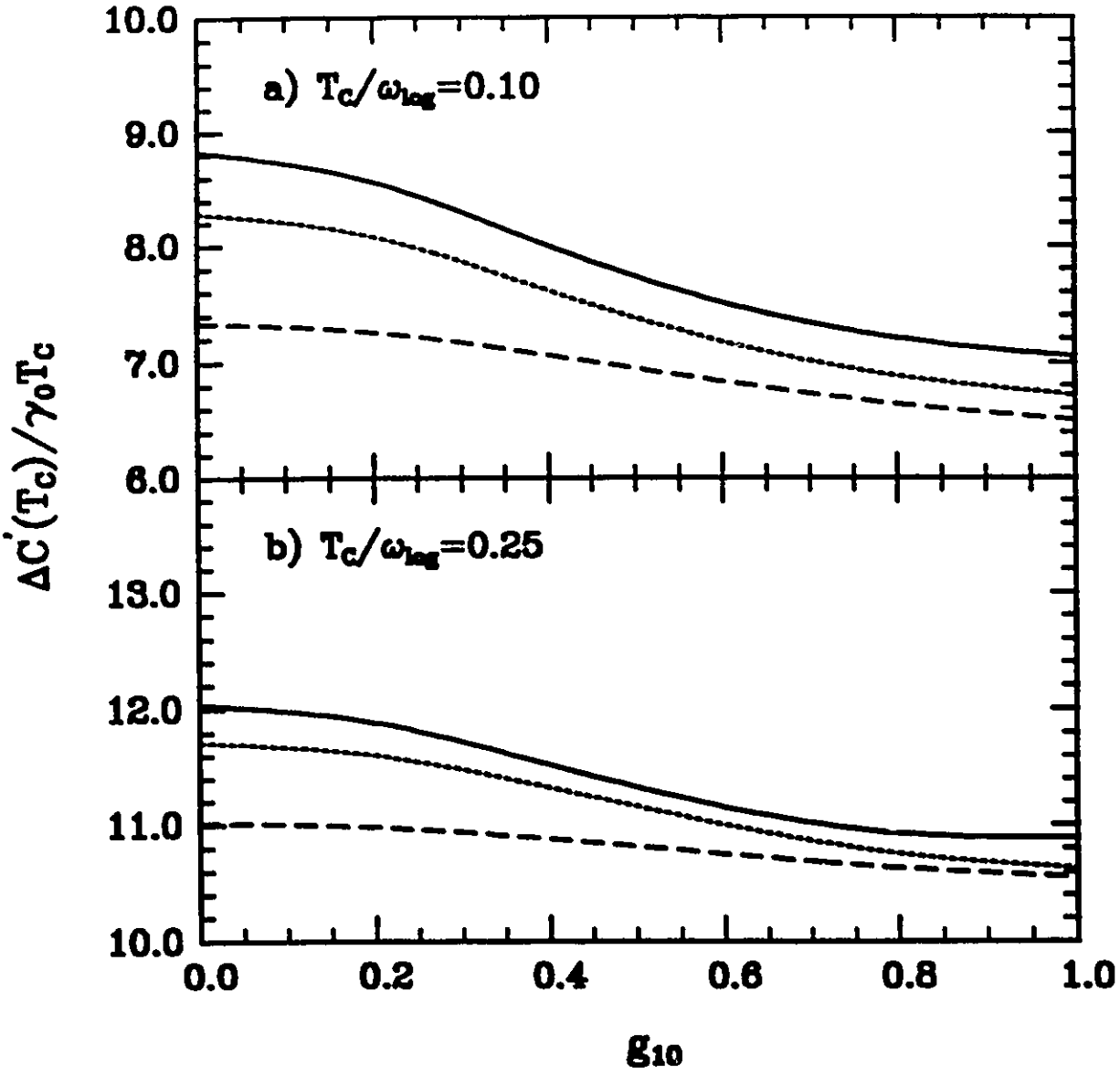

Fig. 4.1.2) The normalized specific heat slope at T_c, $\frac{1}{\gamma_0}\frac{d\Delta C(T)}{dT}|_{T_c}$, as a function of anisotropy parameter g_{10} for various values of g_{20}, namely 0.0 (solid curve), 0.3 (dotted curve), 0.7 (short-dashed curve). The top frame is for an intermediate coupling case with strong coupling index $T_c/\omega_{log} = 0.1$ while the bottom frame is for a strong coupling case ($T_c/\omega_{log} = 0.25$).

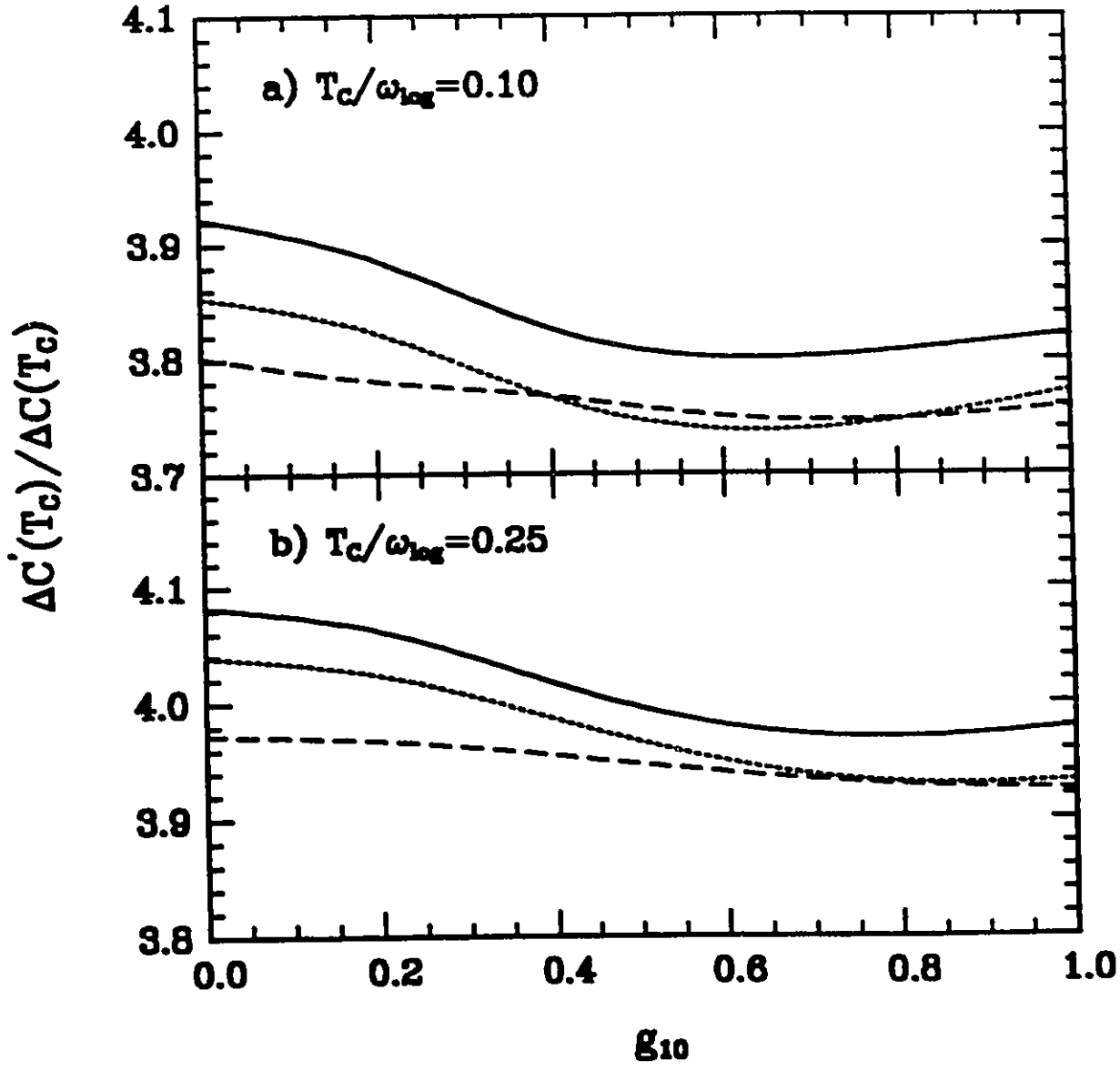

Fig. 4.1.3) The dimensionless ratio at T_c, $\Delta C'(T_c)/\Delta C(T_c)$, as a function of anisotropy parameter g_{10} for various values of g_{20}, namely 0.0 (solid curve), 0.3 (dotted curve), 0.7 (short-dashed curve). The top frame is for an intermediate coupling case with strong coupling index $T_c/\omega_{log} = 0.1$ while the bottom frame is for a strong coupling case ($T_c/\omega_{log} = 0.25$).

In fig. 4.1.2, we have plotted the normalized slope of the specific heat jump at T_c, $\Delta' C(T_c)/\gamma_0 T_c$, as a function of the anisotropy parameter g_{10} for three different g_{20} values. The solid curve is for $g_{20} = 0.0$, the dotted curve for $g_{20} = 0.3$, and short dashed curve for $g_{20} = 0.7$. It is seen that this normalized slope at T_c tracks closely the behavior of the normalized jump, shown in the last figure, as anisotropy is switched on. The same remarks can be applied. If we make the same plot except that the slope of the specific heat jump is now normalized by the jump at T_c, $\Delta' C(T_c)/\Delta C(T_c)$, instead of the normal state specific heat $\gamma_0 T_c$, a more complex behavior is observed as shown in Fig. 4.1.3. While in all cases considered the curves initially drop with increasing value of g_{10} they eventually show a minimum at some finite value of g_{10} and then an increase as g_{10} is increased further. The initial isotropic value is never reached again however in the phase space considered for the anisotropy parameters. Thus, anisotropy appears to always reduce this quantity below its isotropic value. It is not true, however, that in a given anisotropic situation, increasing the g_{ij}'s will necessarily lead to a further reduction in the ratio $\Delta C'(T_c)/\Delta C(T_c)$. This feature is clearly reflected in the crossing of dotted and short dashed curve seen in Fig. 4.1.3. We note once again, by comparing the top and bottom frame, that anisotropy effects become relatively less effective as the coupling strength T_c/ω_{log} is increased and we move away from the BCS limit ($T_c/\omega_{log} \to 0$). The ratio $\Delta C'(T_c)/\Delta C(T_c)$ is a more adequate quantity to study than the ratio $\Delta' C(T_c)/\gamma_0 T_c$ in some circumstances, for example, in high-T_c oxides where γ_0 is difficult to measure directly.

In Fig. 4.1.4 we show the temperature variation of $\Delta C(T)/\gamma_0 T_c$, the normalized specific heat difference between superconducting and normal state. The entire reduced temperature range is covered in the main frame

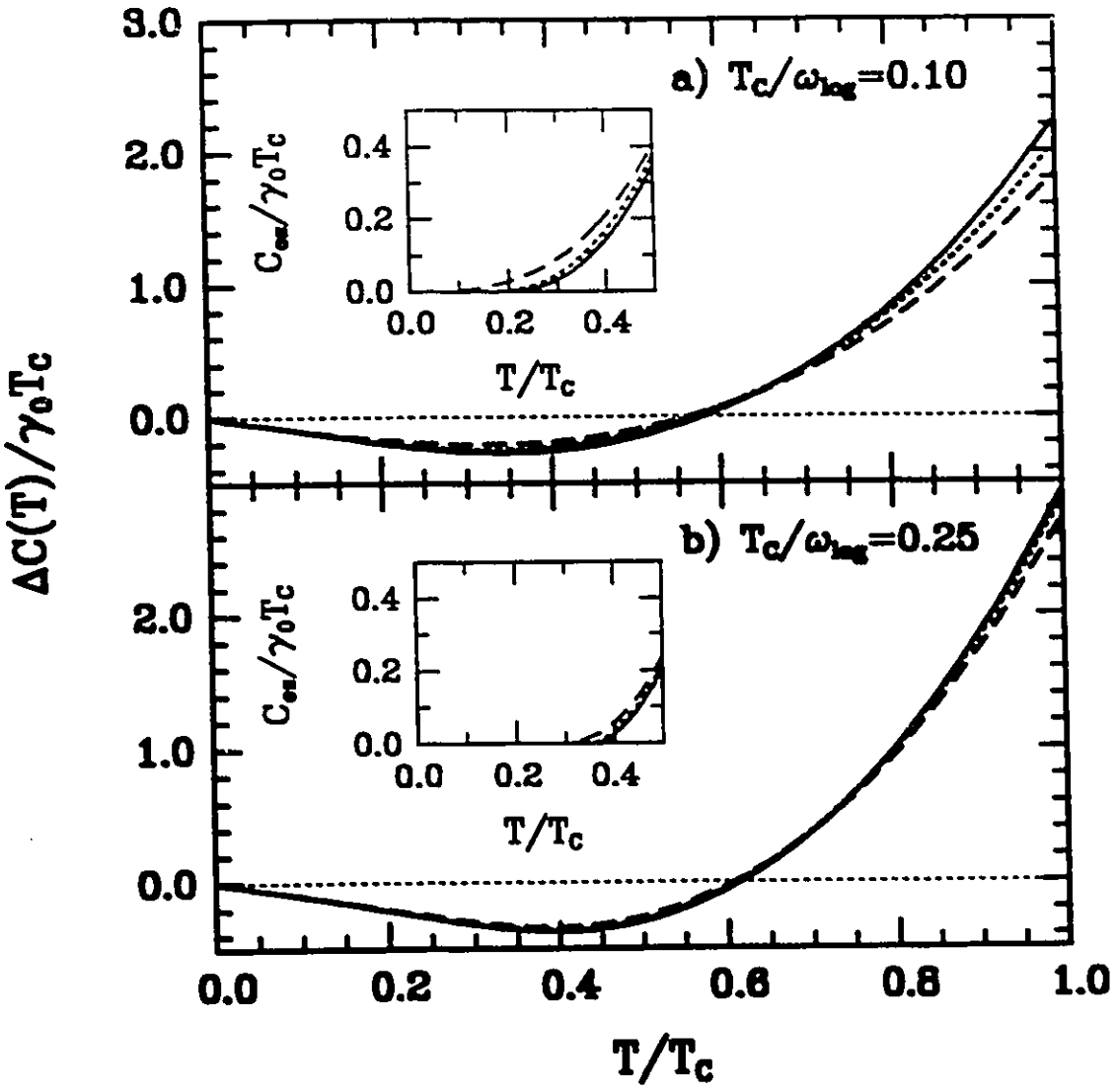

Fig. 4.1.4) The normalized specific heat difference between superconducting and normal state $\Delta C(T)/\gamma_0 T_c$ as a function of reduced temperature T/T_c for the various anisotropy parameters, namely $g_{10} = 0.0$ and $g_{20} = 0.0$ (solid curve, isotropic case for comparison), $g_{10} = 0.4$ and $g_{20} = 0.0$ (dotted curve), and $g_{10} = 1.0$ and $g_{20} = 0.0$ (short-dashed curve). In the insert we show the low temperature behavior of $C_{es}(T)/\gamma_0 T_c$. The top frame applies to an intermediate coupling case with $T_c/\omega_{log} = 0.1$ while the bottom frame is for strong coupling $T_c/\omega_{log} = 0.25$.

while the insert emphasizes the low temperature region. All curves are for $g_{20} = 0.0$ which should be sufficient to illustrate the kind of results one can obtain. Near T_c the anisotropy reduces the jump and initial slope compared with the isotropic case (solid curve) as discussed above. The dotted curve is for $g_{10} = 0.4$ and the short-dashed curve for $g_{10} = 1.0$. We note that as T/T_c is lowered the differences between all three curves shown are reduced and they all cross at points slight less than $T/T_c = 0.6$. At low temperature, as is seen more clearly in the insert where $C_{es}(T)/\gamma_0 T_c$ is plotted instead of the difference $\Delta C(T)/\gamma_0 T_c$, the electronic specific heat in the superconducting state $C_{es}(T)$ is larger for stronger anisotropy. This reflects the fact that a smaller minimum gap value for a larger anisotropy. A comparison of the bottom frame with $T_c/\omega_{log} = 0.25$ and the top frame with $T_c/\omega_{log} = 0.1$ clearly shows again that anisotropy affects the specific heat less significantly when the coupling is increased.

To conclude this section, we would like to point out that measurements on the specific heat of some high-T_c oxides, by many groups [Fisher, Gordon, and Phillips (1988); Junod (1988, 1990); Aleksashin *et al* (1988, 1989); Loram and Mizra (1988); Schill, Ott, and Hulliger (1989)], indicate a much larger slope of the jump at T_c than any conventional superconductors we know and even possibly exceed the theoretical maximum value which one can get from the isotropic Eliashberg equations [Akis and Carbotte (1989a,b,c)]. Unfortunately, our study here can not be of help in this matter as our anisotropic model always results in a reduction of this quantity. The reason for the "anomalously" large slope of the jump in the oxides is not yet clear, and its actual value is still controversial. Besides all possible exotic mechanisms for these materials, the effect from fluctuations is certainly

worth consideration in solving this problem [Salamon (1989)]. Fluctuation effects have been observed in superconducting dichalcogenides, which also have layered structures, for conductivity, diamagnetism, *etc.* Also from the Ginzberg criterion, which basically states that fluctuations are important only for temperatures above the reduced temperature $t_G \propto \xi^{-3}$ with ξ the superconducting cohere ıce length, we know that the effect of fluctuations will be more pronounced in the oxides than in conventional superconductors since ξ is more of the order of tens of angstroms in the former ones rather than thousands of angstroms in the latter ones. Some work has been done combining fluctuation effects with the Eliashberg theory [Bulaevskii and Dolgov (1988a,b)].

4.2 THERMAL CONDUCTIVITY

In the presence of a temperature gradient, dT/dx, a metal is not in a thermal equilibrium state and a heat flow will be present. The heat flux of the flow Q is proportional to the temperature gradient, $Q = -\kappa\, dT/dx$, where κ is the thermal conductivity. From kinetic theory, a familiar formula for κ is [Ashcroft and Mermin (1976)]

$$\kappa = \frac{1}{3} l v c \tag{4.2.1}$$

where v is the velocity of the quasiparticles carrying the heat, $l = v\tau$ is the mean free path (τ is the relaxation time), and c is the heat capacity. It is obvious that κ depends on the material and on temperature. The behaviors

of $\kappa(T)$ has been well studied experimentally in the normal state as well as in the superconducting state [Scalapino (1969)].

There are two contributions to the thermal conductivity of a metal, namely the motion of electrons and that of the crystal lattice, phonons. We can write it as a sum, $\kappa = \kappa_{el} + \kappa_{ph}$. From (4.2.1), we see that κ is restricted mainly by the relaxation time τ. The thermal conductivity would be infinity if τ were infinity. This is analogous to the fact that the electric conductivity would be infinite in the absence of any collisions. However, there is always some scattering. In general, the total electronic thermal conductivity can be calculated according to the rule

$$\frac{1}{\kappa_{el}} \simeq \frac{1}{\kappa_{el-ph}} + \frac{1}{\kappa_{el-imp}} + \frac{1}{\kappa_{el-el}} \tag{4.2.2}$$

where the subscripts $el-ph$, $el-imp$, and $el-el$ refer to electron-phonon, electron-impurity, and elcctron-electron scattering. A similar rule holds for the phonon thermal conductivity

$$\frac{1}{\kappa_{ph}} \simeq \frac{1}{\kappa_{ph-el}} + \frac{1}{\kappa_{ph-imp}} + \frac{1}{\kappa_{ph-ph}}. \tag{4.2.3}$$

Thus, there are six different relaxation mechanisms. Each one depends on the temperature, impurity concentration, *etc.*, in its own way. This makes the problem of the thermal conductivity complicated. For most conventional superconductors in the clean limit, however, the electrons are responsible for most of the heat transport in the normal state and near T_c.

Also, the electron-electron scattering is usually not important compared with electron-phonon scattering. Therefore, the problem can be reduced to calculate κ_{el-ph} only for the temperature range near and above T_c. We will study the effect of the anisotropy on the ratio $\kappa^s_{el-ph}/\kappa^n_{el-ph}$. The subscript $el-ph$ will be omitted then.

The thermal conductivity κ is, in general, a three by three tensor in general. For a isotropic superconductor, however, it is a scalar and has the form, in the superconducting state, [Ambegaokar and Tewordt (1964)]

$$\kappa^s = \frac{N(0)}{3T} {v_F}^2 \int_0^\infty d\omega \frac{\partial f}{\partial \omega} \frac{\omega^2 \left[1 + \frac{\tilde{\omega}^2(\omega) - |\tilde{\Delta}(\omega)|^2}{|\tilde{\omega}^2(\omega) - \tilde{\Delta}^2(\omega)|}\right]}{Im([\tilde{\omega}^2(\omega) - \tilde{\Delta}^2(\omega)]^{1/2})}. \tag{4.2.4}$$

For the anisotropic model we have, κ^s_{el-ph} is given by [Jiang and Carbotte (1992c)]:

$$\kappa^s_{jk} = \frac{N(0)}{3T} \left\langle (v_F)_j (v_F)_k \int_0^\infty d\omega \frac{\partial f}{\partial \omega} \frac{\omega^2 \left[1 + \frac{\tilde{\omega}^2_{\hat{p}}(\omega) - |\tilde{\Delta}(\omega)_{\hat{p}}|^2}{|\tilde{\omega}^2_{\hat{p}}(\omega) - \tilde{\Delta}^2_{\hat{p}}(\omega)|}\right]}{Im([\tilde{\omega}^2_{\hat{p}}(\omega) - \tilde{\Delta}^2_{\hat{p}}(\omega)]^{1/2})} \right\rangle \tag{4.2.5}$$

with T the temperature, $N(0)$ the electronic density of states at the Fermi level, $(v_F)_j$ the Fermi velocity in the j-direction, and $\langle\rangle$ the Fermi surface average. If $\tilde{\Delta}_{\hat{p}}(\omega)$ is set to zero in (4.2.5), we will get the normal state thermal conductivity κ^n_{jk}.

From the dispersion relation (2.2.1), it is easy to work out that

$$\vec{v}(\vec{p})\vec{v}(\vec{p}) = \begin{pmatrix} \frac{\rho^2}{m^{*2}}cos^2(\varphi) & \frac{\rho^2}{m^{*2}}cos(\varphi)sin(\varphi) & -\frac{\rho\mu c}{m^*}cos(\varphi)sin(p_z c) \\ \frac{\rho^2}{m^{*2}}cos(\varphi)sin(\varphi) & \frac{\rho^2}{m^{*2}}sin^2(\varphi) & -\frac{\rho\mu c}{m^*}sin(\varphi)sin(p_z c) \\ -\frac{\rho\mu c}{m^*}cos(\varphi)sin(p_z c) & -\frac{\rho\mu c}{m^*}sin(\varphi)sin(p_z c) & \mu^2 c^2 sin^2(p_z c) \end{pmatrix} \tag{4.2.6}$$

where we have set $\hbar = 1$, $p_x = \rho \cdot cos(\varphi)$, $p_y = \rho \cdot sin(\varphi)$ with φ the spherical coordinate angle in the xy plane. The Fermi surface average can also be worked out as in the last chapter

$$\langle\ \rangle = \frac{1}{N(0)}\int_{FS}\frac{dS}{|\vec{V}_F|} = \int_{-\frac{\pi}{c}}^{\frac{\pi}{c}}\frac{c\,dp_z}{2\pi}\int_0^{2\pi}\frac{d\varphi}{2\pi}. \tag{4.2.7}$$

Since $\tilde{\Delta}_{\vec{p}}(\omega)$ and $\tilde{\omega}_{\vec{p}}(\omega)$ depend on p_z only, (2.3.3), we can do the integral over φ and get finally

$$\kappa^s_{jj} = \frac{N(0)}{3T}\int_{-\frac{\pi}{c}}^{\frac{\pi}{c}}\frac{c\,dp_z}{2\pi}(v_j)^2\int_0^\infty d\omega\frac{\partial f}{\partial\omega}\frac{\omega^2\left[1+\frac{\tilde{\omega}^2_{\vec{p}}-|\tilde{\Delta}_{\vec{p}}(\omega)|^2}{|\tilde{\omega}^2_{\vec{p}}(\omega)-\tilde{\Delta}^2_{\vec{p}}(\omega)|}\right]}{Im([\tilde{\omega}^2_{\vec{p}}(\omega)-\tilde{\Delta}^2_{\vec{p}}(\omega)]^{1/2})}. \tag{4.2.8}$$

All other terms κ^s_{jk} with $j \neq k$ are zero. To be more specific, we have $\kappa_{xx} = \kappa_{yy}$ with

$$(v_x)^2 = (v_y)^2 = \frac{\rho^2}{2m^{*2}} = \frac{\epsilon_F}{m^*}[1 - \frac{\mu}{\epsilon_F}(1 + cos(p_z c))] \tag{4.2.9}$$

and κ_{zz} with

$$(v_z)^2 = \mu^2 c^2 sin^2(p_z).$$

(4.2.10)

The material dependent parameters $N(0)$, ϵ_F, m^*, μ, and c in the above equations are not important as we always normalize κ^s_{jj} by its normal state value κ^n_{jj}, thus, the proportional constant factors will be cancelled out. The only parameter which we need to specify is the ratio μ/ϵ_F. This ratio should be very small as we discussed in section 2.1 and we will take a value of 0.1. A different value for it would not make any qualitative change to our results.

We note that, in formula (4.2.5), $\tilde{\Delta}_{\vec{p}}(\omega)$ and $\tilde{\omega}_{\vec{p}}(\omega)$ are functions of real frequency ω. Therefore, we should solve for them using the real axis Eliashberg equations, (2.3.10) and (2.3.11), directly. To get them from the solutions of the Eliashberg equations on imaginary axis through Padé approximants is not reliable for temperature near T_c.

In Fig 4.2.1, we show results for the normalized ratio in the xy plane, $(\kappa^s(t))_{xx}/(\kappa^n(t))_{xx}$, as a function of reduced temperature $t = T/T_C$. The top frame is for intermediate coupling with $T_c/\omega_{log} = 0.1$. The bottom frame is for strong coupling with $T_c/\omega_{log} = 0.25$. For both cases, the solid line applies to the isotropic situation. The others correspond to various values of g_{10}, namely the dotted curve for $g_{10} = 0.2$, the short-dashed curve for $g_{10} = 0.5$, the long-dashed curve for $g_{10} = 0.55$, and the short-dashed-dotted curve for $g_{10} = 0.6$. We see that, for both cases, the thermal conductivity ratio is everywhere increased as the anisotropy (g_{10}) is increased. The difference is bigger as temperature is lowered, but the ratio finally goes to zero at $T = 0K$. For large anisotropy, the ratio does not decrease monotonically with decreasing

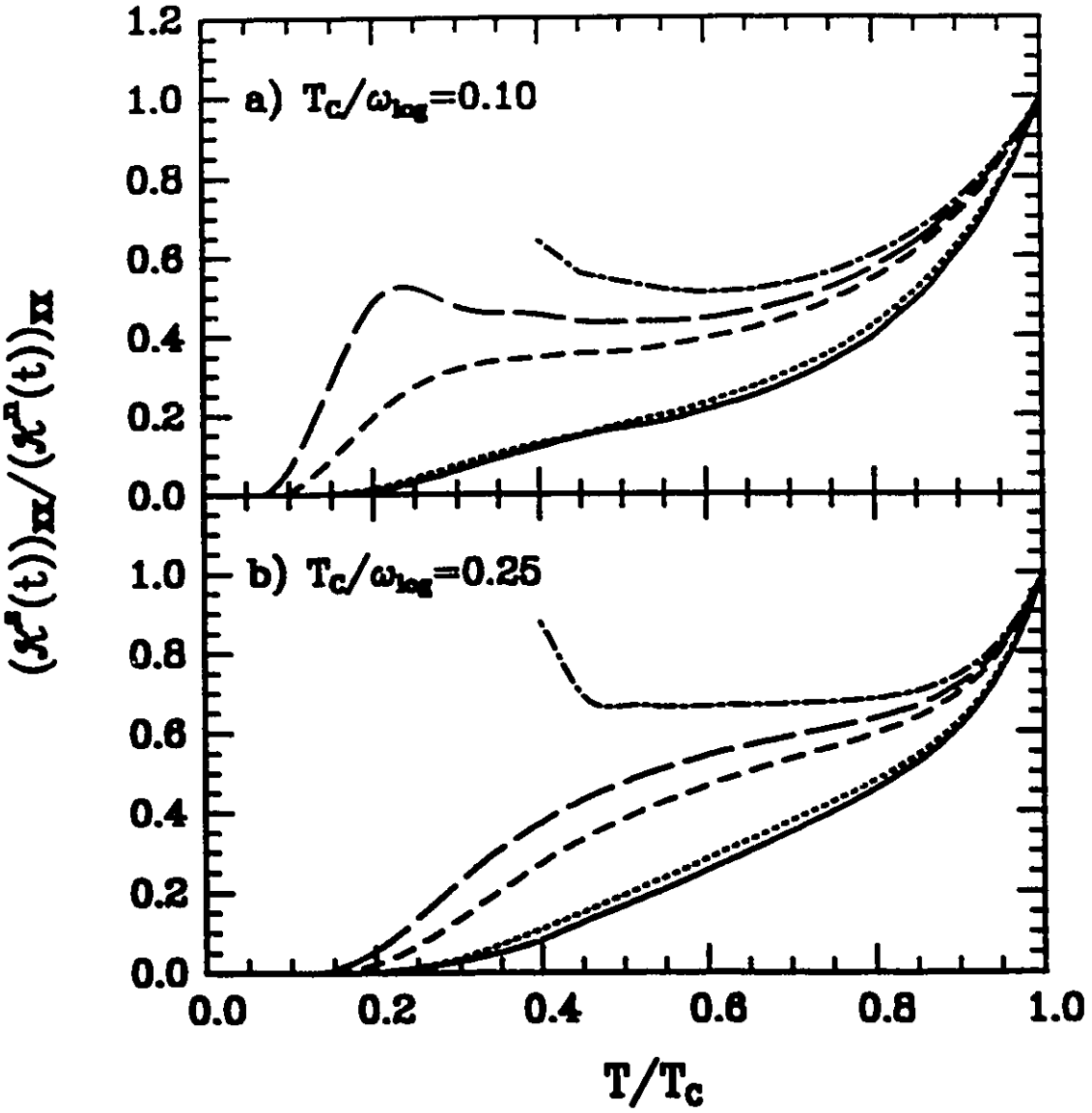

Fig. 4.2.1) The normalized ratio of thermal conductivity in the xy plane, $(\kappa^s(t))_{xx}/(\kappa^n(t))_{xx}$, as a function of the reduced temperature for various values of anisotropy parameter g_{10}, namely 0.0 (solid curve), 0.2 (dotted curve), 0.5 (short-dashed curve), 0.55 (long-dashed curve), and 0.6 (short-dashed-dotted curve). The top frame is for an intermediate coupling case with strong coupling index $T_c/\omega_{log} = 0.1$ while the bottom frame is for strong coupling with $T_c/\omega_{log} = 0.25$.

temperature, as in the isotropic case. Instead, we see an increasing after the initial decreasing for the largest anisotropy, $g_{10} = 0.6$, in the figure. In this case, the ratio actually goes beyond 1 at the temperature range around $t = 0.2$ to $t = 0.3$ for both coupling strengths, although we did not plot this region here.

The corresponding results for the normalized ratio in the z-direction, $(\kappa^s(t))_{zz}/(\kappa^n(t))_{zz}$, are shown in Fig. 4.2.2. We see qualitatively similar behaviors to those in the Fig. 4.2.1. The ratio is larger when anisotropy is larger. The magnitude of the difference, however, is smaller in the z-direction than that in the xy plane, which we believe is due to the different weighting factors from Fermi velocity as we average over the first Brillouin zone. The Fermi velocity has a different angular dependence for the two directions. Also, the Fermi velocity along the z-direction is proportional to μ, the hopping probability. Therefore the thermal conductivity along the z-direction will be much smaller than that in the xy plane and goes to zero as μ goes zero, although the normalized ratio would not show this.

The rather large increase of the normalized ratio for both directions with increase anisotropy is mainly due to the increasing number of quasiparticles from thermal excitations. As we know, the thermal conductivity is proportional to the number of quasiparticles. The number of quasiparticles will decrease exponentially with temperature if there is a gap in the energy excitation spectrum, as there is in the superconducting state. Therefore the thermal conductivity is smaller in the superconducting state than that in the normal state for most cases, as we have seen. Adding anisotropy will make the decrease in the quasiparticle number slower, compared with isotropic case, since the effective gap will be smaller. As temperature is lowered, the

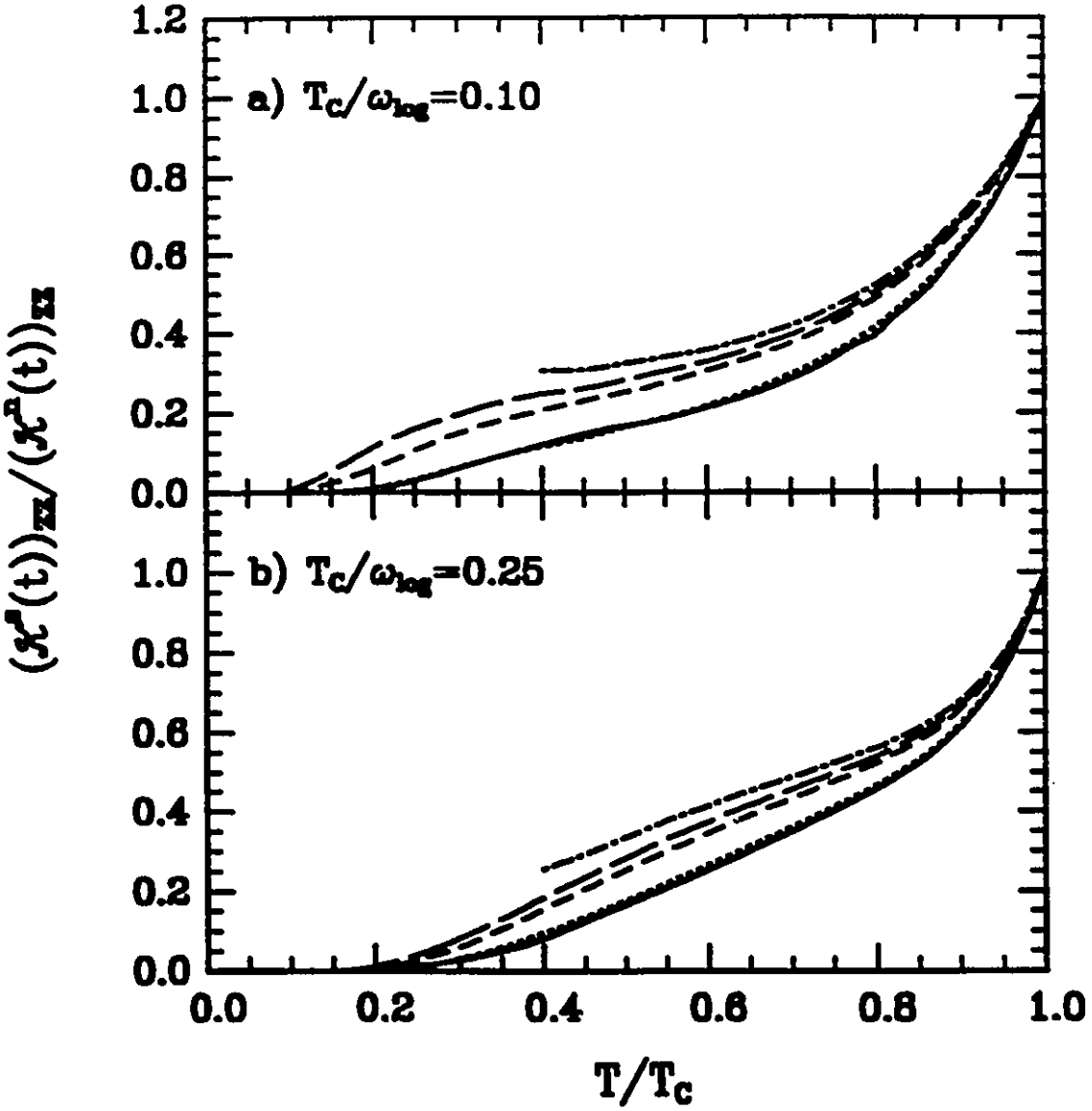

Fig. 4.2.2) The normalized ratio of thermal conductivity in the z direction, $(\kappa^s(t))_{zz}/(\kappa^n(t))_{zz}$, as a function of the reduced temperature for various values of anisotropy parameter g_{10}, namely 0.0 (solid curve), 0.2 (dotted curve), 0.5 (short-dashed curve), 0.55 (long-dashed curve), and 0.6 (short-dashed-dotted curve). The top frame is for an intermediate coupling case with strong coupling index $T_c/\omega_{log} = 0.1$ while the bottom frame is for strong coupling with $T_c/\omega_{log} = 0.25$.

minimum gap will be more dominant. Thus, an increase in the ratio results. To understand the larger magnitude thermal conductivity in the superconducting state compared with that in the normal state for large anisotropy, as we showed above where $(\kappa^s(t))_{xx}/(\kappa^n(t))_{xx}$ is bigger than 1 for $g_{10} = 0.6$ in a certain temperature range, we need to consider another factor, namely the quasiparticle lifetime, which is as important as the quasiparticle number in determining the thermal conductivity. Detailed study has shown that at small reduced temperature $t = T/T_c$ the lifetime of quasiparticles is much longer in the superconducting state than that in the normal state [Kaplan *et al.* (1976)]. This is due to the limitation of the number of final states into which quasiparticles can decay in the superconducting state. In the superconducting state, a quasiparticle with energy ω can not decay through the process of emitting a phonon with energy within the range ω to $\Delta(T) + \omega$, where $\Delta(T)$ is the energy gap. In the normal state, there is no such restriction. The combination of a much longer lifetime and an effectively much smaller energy gap due to the large anisotropy, at small reduced temperature, gives us a larger thermal conductivity in the superconducting state than in the normal state. However, as long as the effective energy gap is non-zero, the number of quasiparticles will be zero at zero temperature. Thus, the thermal conductivity will be strictly zero at $T = 0$ as we pointed out above.

Our results here are for the contribution from electrons scattered by phonons only. When compared with experiments, we may need to consider other contributions as well, as we discussed at the beginning of this section. In high-T_c oxides, for example, the lattice contribution should be considered since the transition temperature T_c is high, especially near T_c. [Cohn, Peacor, and Uher (1988); Tewordt and Wölkhausen (1989, 1990); Peacor *et al*

(1990)]. Even for the electronic part, other scattering mechanisms may be far more important than the phonon scattering process considering the strongly correlated nature of the system. We should always bear this in mind.

4.3 ULTRASOUND ATTENUATION

In metals, sound waves will decay primarily through their interaction with electronic excitations. Electrons will be excited to higher energy states by absorbing sound quanta. In the normal state, the electronic energy spectrum is continuous for most metals, where a free electron model is applicable. Thus, a sound quantum with an arbitrary small energy can be absorbed by the electronic system. The electronic energy spectrum becomes qualitatively different from that in the normal state when a superconducting transition happens. In the superconducting state, electrons are condensed to a new ground state accompanied by an energy gap in the energy spectrum. A sound quantum with energy smaller than the gap value cannot excite electrons from this condensate. The absorption of such sound quanta in the superconducting state is due primarily to the "normal" electrons coming from thermal excitations. At absolute zero temperature, since there are no "normal" electrons at all, the absorption is zero. As the temperature increases, the absorption increases, but it is always weaker than that in the normal state because of the presence of the energy gap, all the way up to the critical temperature T_c. In BCS theory, this phenomenon is described by a remarkably simple formula, which is valid for sound quanta with frequency $\hbar\omega < 2\Delta$ only,

$$\frac{\alpha_s}{\alpha_n} = \frac{2}{e^{\Delta(T)/k_B T} + 1}. \tag{4.3.1}$$

Here α_s and α_n are the absorption coefficients in the superconducting and normal states, respectively. Here, T is the temperature and $\Delta(T)$ is the BCS gap function.

The formula (4.3.1) mainly reflects the rapid decrease in the number of "normal" quasiparticles as the energy gap opens up below T_c. The interaction between electrons and acoustic phonons, induced by sound waves, is assumed to be the same in the normal and superconducting states. This assumption is proper only for purely longitudinal phonons, but not for transverse phonons. A transverse phonon will set up electromagnetic fields. This coupling will be greatly reduced in the superconducting state due to the Meissner effect. Thus, an essentially discontinuous drop of the transverse acoustic attenuation rate happens at T_c. This is observed experimentally in tin by Morse and Bohm (1957). To avoid the complications from the Meissner effect, however, we will focus on the problem of longitudinal phonons here.

The absorption of high-frequency longitudinal sound waves, the ultrasound attenuation, was among the first phenomena to be studied experimentally for superconductors. There are measurements performed on pure element superconductors, *e.g.*, on tin by Morse and Bohm (1957), on thallium by Saunders and Lawson (1964), on lead by Love and Shaw (1964), and on niobium by Dobbs and Perz (1964). All of these data show a sharp drop in the absorption as the temperature is lowered below T_c and an exponential

decay of it to zero as T approaches zero. More than that, the temperature dependence of the gap function calculated from the measured ratio α_s/α_n, using formula (4.3.1), is indistinguishable from the theoretical curve $\Delta(T)$ for some materials. The success of these confirms the validity of the principal ideas of BCS theory.

Besides the temperature dependence of the energy gap, the ultrasound attenuation method has also been used to study the gap anisotropy. From the consideration of energy conservation, it can be shown that the only electrons able to participate in the attenuation are those which have wavevectors $\vec{p}$ very nearly perpendicular to the incident sound wavevector $\vec{q}$. Thus, for a certain direction of $\vec{q}$, the ultrasound attenuation gives information on the gap only on a certain part of the Fermi surface. By changing the direction of $\vec{q}$, we are able to measure the gap as a function of direction on the Fermi surface. The work on a very pure tin single crystal by Morse, Olsen and Gavenda (1959) showed clearly that there were different gap values for different crystallographic orientations. A more detailed discussion can be found in the literature [Bardeen and Schrieffer (1961); Clem (1966); Hong and Carbotte (1978)].

For most conventional superconductors, anisotropy is quite small. A very pure sample is usually needed to show the effects of anisotropy, as we know that impurities will wash out anisotropies quickly. For the high T_c oxides, however, we know that they are very likely in the clean limit due to their small coherent length, also there is a large anisotropy in these compounds. Therefore, big difference for the ultrasound attenuation for different crystallographic orientations is expected. This is the main motivation for studying

the effects of anisotropy on the ultrasound attenuation based on our planar model.

We start with the general formula for the ratio α_s/α_n from Eliashberg theory [Hong and Carbotte (1978)]:

$$\frac{\alpha_s(\mu)}{\alpha_n(\mu)} = \frac{\lim_{\vec{q}\to 0}\int_{S(\epsilon_F)} \frac{dS}{|\nabla\epsilon(\vec{p})|} \mid g_{\vec{p},\vec{p}-\vec{q}} \mid^2 \delta(\vec{v}_{\vec{p}}\cdot\vec{q}) R_{\vec{p}}(\mu)}{\lim_{\vec{q}\to 0}\int_{S(\epsilon_F)} \frac{dS}{|\nabla\epsilon(\vec{p})|} \mid g_{\vec{p},\vec{p}-\vec{q}} \mid^2 \delta(\vec{v}_{\vec{p}}\cdot\vec{q})} \tag{4.3.2}$$

with

$$R_{\vec{p}}(\mu) = \int d\omega \left[\frac{f(\omega-\mu)-f(\omega)}{\mu}\right]\left[Re\left(\frac{\tilde{\omega}_{\vec{p}}(\omega)}{\sqrt{\tilde{\omega}^2_{\vec{p}}(\omega)-\tilde{\Delta}^2_{\vec{p}}(\omega)}}\right) Re\left(\frac{\tilde{\omega}_{\vec{p}}(\omega-\mu)}{\sqrt{\tilde{\omega}^2_{\vec{p}}(\omega-\mu)-\tilde{\Delta}^2_{\vec{p}}(\omega-\mu)}}\right)\right.$$
$$\left. - Re\left(\frac{\tilde{\Delta}_{\vec{p}}(\omega)}{\sqrt{\tilde{\omega}^2_{\vec{p}}(\omega)-\tilde{\Delta}^2_{\vec{p}}(\omega)}}\right) Re\left(\frac{\tilde{\Delta}_{\vec{p}}(\omega-\mu)}{\sqrt{\tilde{\omega}^2_{\vec{p}}(\omega-\mu)-\tilde{\Delta}^2_{\vec{p}}(\omega-\mu)}}\right)\right]. \tag{4.3.3}$$

Here $g_{\vec{p},\vec{p}-\vec{q}}$ is the electron-phonon matrix element, $\vec{v}_{\vec{p}} = \nabla\epsilon(\vec{p})$, $\vec{q}$ is the incident longitudinal sound wavevector, and $f(\omega)$ is the Fermi thermal factor. The renormalized frequency $\tilde{\omega}_{\vec{p}}(\omega)$ and the gap function $\tilde{\Delta}_{\vec{p}}(\omega)$ come from the solutions of the Eliashberg equations on the real axis.

The δ-function in the formula (4.3.2) reduces the Fermi surface integral to a line integral on the Fermi surface. The plane circled by the line should be perpendicular to $\vec{q}$. This is the selection rule we mentioned above. Here we will study the ultrasound attenuation numerically for two special cases only, $\vec{q} \parallel \hat{z}$ and $\vec{q} \perp \hat{z}$, which should be enough to illustrate the anisotropic effects of our model. The corresponding formula for the ratio α_s/α_n for these two cases are worked out in the following.

From the dispersion relation (2.1.1), we have

$$\vec{v}_{\vec{p}} = \frac{1}{m^*}\sqrt{2m^*\epsilon_{\vec{p}} - 2m^*\mu cos(p_z c)}(sin(\varphi)\vec{i} + cos(\varphi)\vec{j}) - \mu c sin(p_z c)\vec{k} \tag{4.3.4}$$

with φ the spherical coordinate angle in the xy plane. For $\vec{q} \parallel \hat{z}$, the condition $\vec{v}_{\vec{p}} \cdot \vec{q} = 0$ from the δ-function requires that p_z is either 0 or π/c. Therefore, formula (4.3.2) becomes

$$\frac{\alpha_s(\mu)}{\alpha_n(\mu)} = \frac{1}{2}[R_{p_z=0}(\mu) + R_{p_z=\pi/c}(\mu)]. \tag{4.3.5}$$

For $\vec{q} \perp \hat{z}$, it is also easy to see that formula (4.3.2) becomes

$$\frac{\alpha_s(\mu)}{\alpha_n(\mu)} = \frac{\int_0^{\pi/c} \frac{dp_z}{|\vec{v}_{\vec{p}}|} \mid g_{\vec{p}}(\hat{q}) \mid^2 R_{\vec{p}}(\mu)}{\int_0^{\pi/c} \frac{dp_z}{|\vec{v}_{\vec{p}}|} \mid g_{\vec{p}}(\hat{q}) \mid^2}. \tag{4.3.6}$$

In the limit $\vec{q}$ going to zero, we assume that

$$\mid g_{\vec{p}}(\hat{q}) \mid^2 = \mid g_0 \mid^2 (1 + \alpha cos(p_z c)), \tag{4.3.7}$$

where a is a measure of the anisotropy of the electron-phonon matrix element. It is reasonable for illustration, we believe, to set α equal g_{10} in the expansion of $(\alpha^2 F(\omega))_{\vec{p},\vec{p}'}$ as we defined in the last chapter. From (4.3.4), we get

$$| \vec{v}_{\vec{p}} | = (\frac{2\epsilon_F}{m^*})^{1/2}\Big[1 - \frac{\mu}{\epsilon_F}cos(p_z c) + \frac{\mu}{\epsilon_F}\frac{m^*\mu c^2}{2}sin^2(p_z c)\Big]. \tag{4.3.8}$$

Substituting (4.3.7) and (4.3.8) into (4.3.6), we finally get for $\vec{q} \perp \hat{z}$,

$$\frac{\alpha_s(\mu)}{\alpha_n(\mu)} = \frac{\int_0^{\pi/c} dp_z R_{\vec{p}}(\mu)(1+\alpha cos(p_z c))\Big/\Big[1 - \frac{\mu}{\epsilon_F}cos(p_z c) + \frac{\mu}{\epsilon_F}\frac{m^*\mu c^2}{2}sin^2(p_z c)\Big]}{\int_0^{\pi/c} dp_z (1+\alpha cos(p_z c))\Big/\Big[1 - \frac{\mu}{\epsilon_F}cos(p_z c) + \frac{\mu}{\epsilon_F}\frac{m^*\mu c^2}{2}sin^2(p_z c)\Big]}. \tag{4.3.9}$$

In our numerical calculation, we set $\mu/\epsilon_F = 0.1$, as we did in the last section, and $m^*\mu c^2/2 = 0.1$ by considering that $m^* \sim 5.0 \times 10^5 eV$, $\mu \sim 1.0eV$, and $c \sim 10A$. We also calculate the ratio α_s/α_n in the limit μ going to zero. Therefore, $R_{\vec{p}}(\mu)$ becomes,

$$R_{\vec{p}}(0) = \int d\omega \Big(\frac{-df(\omega)}{d\omega}\Big)\Big[Re\Big(\frac{\tilde{\omega}_{\vec{p}}(\omega)}{\sqrt{\tilde{\omega}^2_{\vec{p}}(\omega) - \tilde{\Delta}^2_{\vec{p}}(\omega)}}\Big)^2 - Re\Big(\frac{\tilde{\Delta}_{\vec{p}}(\omega)}{\sqrt{\tilde{\omega}^2_{\vec{p}}(\omega) - \tilde{\Delta}^2_{\vec{p}}(\omega)}}\Big)^2\Big]. \tag{4.3.10}$$

After solving the Eliashberg equations on the real axis (2.3.10)-(2.3.11), we calculate the temperature dependence of the ratio α_s/α_n with formulas (4.3.5), (4.3.9) and (4.3.10). In Fig. 4.3.1, the ratio $\alpha_s(t)/\alpha_n(t)$ is plotted for $\vec{q} \parallel \hat{z}$, with $t = T/T_c$ the reduced temperature. The top frame is for intermediate coupling with $T_c/\omega_{log} = 0.1$. The bottom frame is for strong coupling with $T_c/\omega_{log} = 0.25$. For both cases, the solid line is for the

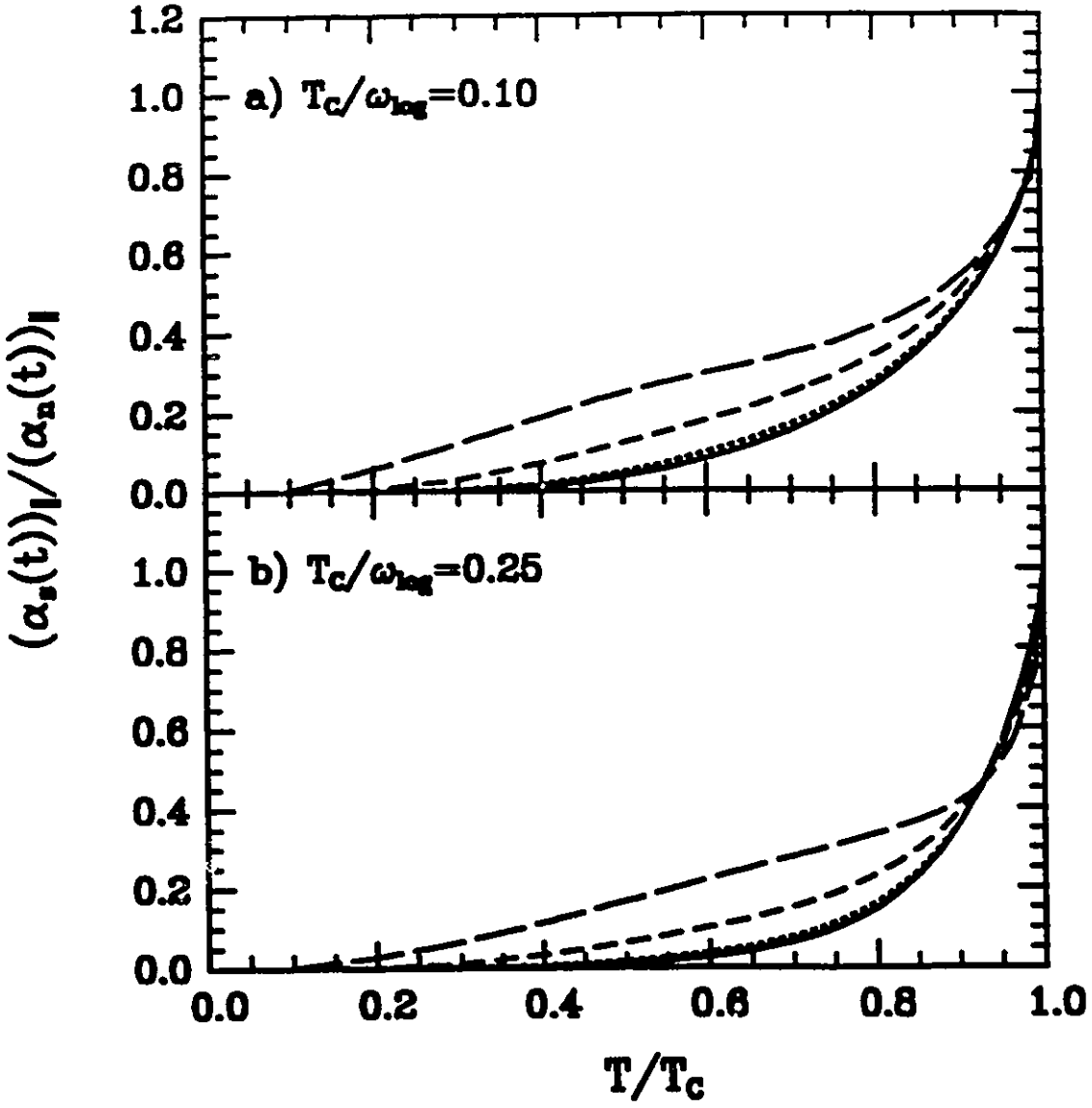

Fig. 4.3.1) The normalized ratio of ultrasound attenuation for $\vec{q} \parallel \hat{z}$, $(\alpha_s(t)/\alpha_n(t))_{\|}$, as a function of the reduced temperature for various values of anisotropic parameter g_{10}, namely namely 0.0 (solid curve), 0.2 (dotted curve), 0.5 (short dashed curve), and 0.8 (long dashed curve). The top frame is for an intermediate coupling case with strong coupling index $T_c/\omega_{log} = 0.1$ while the bottom frame is for strong coupling with $T_c/\omega_{log} = 0.25$.

isotropic situation, the dotted curve is for $g_{10} = 0.2$, the short-dashed curve is for $g_{10} = 0.5$, and the long-dashed curve is for $g_{10} = 0.8$. For both coupling strengths, the temperature dependence of the normalized ultrasound attenuation with g_{10} anisotropy is quite different from that of the isotropic situation. The difference is bigger for larger anisotropy, and increases as the temperature is lowered. At T near T_c, the ultrasound attenuation is weaker for the anisotropic case than the isotropic case. In contrast, it is much stronger in the low temperature region.

The results for the ratio α_s/α_n for $\vec{q} \perp \hat{z}$ are shown in Fig. 4.3.2. Again, the top frame is for intermediate coupling with $T_c/\omega_{log} = 0.1$ and the bottom frame is for strong coupling with $T_c/\omega_{log} = 0.25$. The solid line applies to the isotropic case, the dotted curve applies to $g_{10} = 0.2$, the short-dashed curve applies to $g_{10} = 0.5$, and the long-dashed curve applies to $g_{10} = 0.8$. Qualitatively, the changes in the attenuation resulted from the anisotropy is the same as for the $\vec{q} \parallel \hat{z}$ case. The attenuation decreases as anisotropy increases at T near T_c, but it increases with increasing anisotropy at T near zero. The difference is bigger near T_c than near zero, although it is relatively small compared with $\vec{q} \parallel \hat{z}$ case at low temperature region.

As we already know, the drop of ultrasound attenuation on entering the superconducting state is due to a gap opening in the energy spectrum and hence the "normal" quasiparticle number decreasing. The above results with anisotropy show that the effect of the anisotropy is a larger effective gap at T near T_c and a smaller effective gap at T near zero. In our anisotropic model, the gap depends on p_z only. For the $\vec{q} \parallel \hat{z}$ case, the attenuation is the average of an even weighting of that at the maximum gap and at the minimum gap. While for $\vec{q} \perp \hat{z}$, the attenuation is averaged over the whole first Brillouin

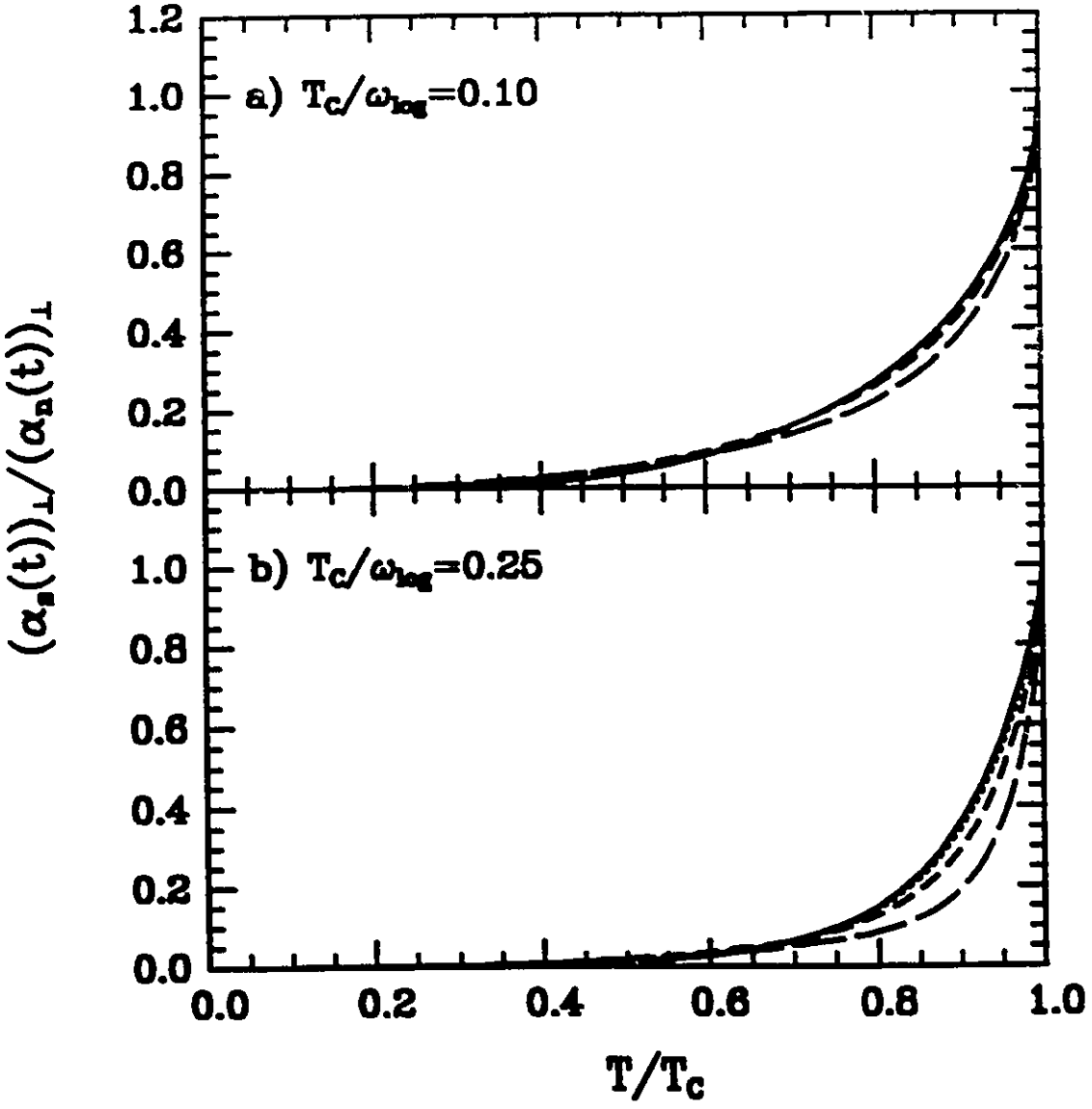

Fig. 4.3.2) The normalized ratio of ultrasound attenuation for $\vec{q} \perp \hat{z}$, $(\alpha_s(t)/\alpha_n(t))_\perp$, as a function of the reduced temperature for various values of anisotropic parameter g_{10}, namely namely 0.0 (solid curve), 0.2 (dotted curve), 0.5 (short dashed curve), and 0.8 (long dashed curve). The top frame is for an intermediate coupling case with strong coupling index $T_c/\omega_{log} = 0.1$ while the bottom frame is for strong coupling with $T_c/\omega_{log} = 0.25$.

zone with a weight factor which is the biggest for $p_z = 0$ (maximum gap) and smallest for $p_z = \pi/c$ (minimum gap). At T close to T_c, the effect from a bigger gap is important, while the effect from a smaller gap dominates at lower temperature. The weighting factor for the direction $\vec{q} \perp \hat{z}$ results in a bigger change of the attenuation near T_c and a smaller change near zero.

We see once again that the planar anisotropy has quite large effects on physically measurable quantities. It will be interesting to compare the results here with experimental data on both polycrystal and single crystal of high-T_c oxides. From such a comparison, we may be able to have an estimation about the electronic coupling between $Cu-O$ planes.

4.4 CONCLUSIONS

The effect of a planar anisotropy on the specific heat, the ultrasound attenuation and the thermal conductivity has been found to be large for an Eliashberg superconductor if the electron-phonon coupling is not too strong ($T_c/\omega_{log} \leq 0.25$). The effect is usually larger for weaker coupling superconductors. The specific heat jump and the slope of the specific heat jump at T_c are depressed below their isotropic value when anisotropy is introduced. The drop in the specific heat jump at T_c can be as big as 20% for an intermediate coupling superconductor ($T_c/\omega_{log} = 0.1$) in the anisotropic range we have investigated. This is not what has been seen in high-T_c oxide superconductors, although the situation is still controversial there. On the other hand, at low temperature, the electronic specific heat is larger as the anisotropy is increased. This reflects an effectively smaller gap for the larger anisotropy. This effectively smaller gap at low temperature due to the anisotropy appears also in the thermal conductivity and ultrasound attenuation.

For the thermal conductivity, adding anisotropy makes it increase. The difference between the anisotropic and isotropic cases is relatively bigger as temperature is lowered. A similar situation exists for the ultrasound attenuation in the low temperature region. At temperatures near T_c, however, the ultrasound attenuation is weaker for stronger anisotropy. This occurs mainly because of an effectively larger gap at T near T_c for stronger anisotropy. The difference between the temperature dependence of the thermal conductivity and ultrasound attenuation, we believe, comes from the fact that quasiparticle lifetime enters the formula of thermal conductivity but not the formula for ultrasound attenuation. Ultrasound attenuation is mainly proportional to the number of quasiparticles available while the thermal conductivity depends on both the number of quasiparticles and the lifetime of the quasiparticles. The phenomenon of thermal conductivity is more complicated since the quasiparticle lifetime will also be affected by the superconducting phase transition [Kaplan *et al.* (1976)].

For an anisotropic superconductor, a larger or smaller effective gap depends on temperature, the portion of the Fermi surface considered, and the properties under study, *etc.* The contribution from the minimum gap and the maximum gap will be different in general. We would like to emphasize again that although we used the concept of a energy gap opening in the superconducting state here to discuss the results, it does not necessary mean a sharp cut off in the energy spectrum. We have seen in the last chapter that a clear gap is hardly seen at finite temperature, especially for a strong coupling superconductor. The most essential quantity for us is the pairing potential $\tilde{\Delta}$. As long as $\tilde{\Delta}$ is finite, we will have a highly correlated new ground

state, the superconducting state. The quantity Δ measures the correlation of quasiparticles in the superconducting state.

Chapter 5

Electromagnetic Properties

A superconductor in the superconducting state will have a qualitatively different response to an external electromagnetic field as compared with the normal state. The different electromagnetic behavior between the superconducting and normal state of the system results not only from the qualitative changes in the electronic excitation spectrum but also from the highly correlated nature of the superconducting state. In this chapter we would like to discuss how planar anisotropy affects some electromagnetic properties in the superconducting state. In the next section we will show the results on the London penetration depth $\Lambda^L(T)$, followed by a discussion of the nuclear spin relaxation rate $R(T)$ in section 5.2. Section 5.3 is devoted to the infrared conductivity $\sigma(\omega)$ and a short conclusion is included in the last section (5.4).

5.1 THE LONDON PENETRATION DEPTH

A superconductor will expel magnetic field from its interior by building up shielding supercurrents in the surface layer whether the superconducting phase transition is taking place in the presence of the magnetic field or not. This phenomenon, discovered by Meissner and Ochsenfeld in 1933, is one of the most fundamental property of superconductivity and is named after its discoverers, the Meissner effect. It is the Meissner effect that distinguishes a superconductor from a perfect conductor. A perfect conductor with zero *dc* resistance will resist any change in internal magnetic flux, but does not demand the flux to be zero. The Meissner effect is intimately related to the phenomenon of zero resistance. They both have the same origin, as has been established by BCS theory [Schrieffer (1964)].

The Meissner effect is achieved through the fact that an external field will decay exponentially from the surface of a superconductor. The surface region where the magnetic field is not zero contains the persistent currents which screen out the external field. The distance from the surface that the external field decreases by a factor of e (nature logarithm) is called the penetration depth, Λ, which is one of the main characteristics of a superconductor and depends on temperature. For most conventional superconductors, the penetration depth is a few thousand angstroms. For high-T_c oxide superconductors, it is a few thousand angstroms ($\sim 2000A$) parallel to CuO_2 planes and several thousand angstroms ($\sim 7000A$) perpendicular to the planes, due to the highly anisotropic layered structure [Harshman *et al.* (1989)]. Here we would like to examine the penetration depth using the anisotropic model and the strong coupling formalism developed in chapter 2. It is our intent to

show the possible effects that can result from a layered structure with strong coupling. For weak coupling, a similar effect has been looked at by Schneider and coworkers (1989) using BCS theory.

From electrodynamics, the penetration depth is related to the surface impedance $\mathcal{Z}(\omega)$ by

$$\Lambda = \lim_{\omega \to 0} \frac{\mathcal{Z}(\omega)}{i\omega\mu_0}. \tag{5.1.1}$$

Here, μ_0 is the permeability [Rickayzen (1965)]. The surface impedance can be calculated from the electromagnetic response function $\mathcal{K}(\vec{q},\omega)$, which usually is a three by three tensor for three space coordinates and defined by [Nam (1967a,b)]

$$J_j(\vec{q},\omega) = -\mathcal{K}_{jk}(\vec{q},\omega)A^k(\vec{q},\omega) \tag{5.1.2}$$

where J is the current density and A is the electromagnetic vector potential. With the assumption that the reflection of electromagnetic waves at the superconductor surface is mirrorlike (specular reflection), the penetration depth is then given as:

$$\Lambda = \frac{2}{\pi}\int_0^\infty \frac{dq}{q^2 + \frac{\mu_0}{4\pi}\mathcal{K}(q,0)} \tag{5.1.3}$$

with

$$\mathcal{K}_{jk}(q,0) = \langle 8\pi^2 TN(0)e^2 V_j(\vec{p})V_k(\vec{p})Re\Big(\sum_{n>0}\frac{\tilde{\Delta}^2_{\vec{p}}(i\omega_n)}{\Big[\tilde{\omega}^2_{\vec{p}}(i\omega_n)+\tilde{\Delta}^2_{\vec{p}}(i\omega_n)\Big]^{3/2}}F_0(S_n(q,\vec{p}))\Big)\rangle \tag{5.1.4}$$

where $\langle\rangle$ again denotes a Fermi surface integral over $\vec{p}$, T is temperature, $N(0)$ is the quasiparticle density of states at the Fermi level, e is the electron charge and V_j is the Fermi velocity in the j direction. $\tilde{\Delta}_{\vec{p}}(i\omega_n)$ and $\tilde{\omega}_{\vec{p}}(i\omega_n)$ are angular dependent pairing potential and renormalized frequency written at the Matsubara frequencies respectively, and should be solved from Eqs. (2.3.8) and (2.3.9). The function F_0 in formula (5.1.4) is given by

$$F_0(S_n(q,\vec{p})) = \frac{(1+S_n^2(q,\vec{p}))tan^{-1}(S_n(q,\vec{p}))-S_n(q,\vec{p})}{S_n^3(q,\vec{p})} \tag{5.1.5}$$

with

$$S_n(q,\vec{p}) = \frac{qV_F(\vec{p})}{2\Big[\tilde{\omega}^2_{\vec{p}}(i\omega_n)+\tilde{\Delta}^2_{\vec{p}}(i\omega_n)\Big]^{1/2}}. \tag{5.1.6}$$

In the limit $q \to 0$, the London limit, $F_0(S_n(0,\vec{p})) = 2/3$. Therefore, from formulas (5.1.3) and (5.1.4),

$$\mathcal{K}_{jk}(q\to 0,0) = \langle\frac{16}{3}\pi^2 TN(0)e^2 V_j(\vec{p})V_k(\vec{p})Re\Big(\sum_{n>0}\frac{\tilde{\Delta}^2_{\vec{p}}(i\omega_n)}{\Big[\tilde{\omega}^2_{\vec{p}}(i\omega_n)+\tilde{\Delta}^2_{\vec{p}}(i\omega_n)\Big]^{3/2}}\Big)\rangle \tag{5.1.7}$$

and

$$\Lambda^L_{jk}(T) = \frac{2}{\pi}\int_0^\infty \frac{dq}{q^2 + \frac{\mu}{4\pi}\mathcal{K}_{jk}(0,0)} = \left[\frac{\mu_0}{4\pi}\mathcal{K}_{jk}(0,0)\right]^{-1/2}$$
$$= \left[\langle \frac{4}{3}\pi T N(0)\mu_0 e^2 V_j(\vec{p})V_k(\vec{p}) Re\left(\sum_{n>0}\frac{\tilde{\Delta}^2_{\vec{p}}(i\omega_n)}{\left[\tilde{\omega}^2_{\vec{p}}(i\omega_n) + \tilde{\Delta}^2_{\vec{p}}(i\omega_n)\right]^{3/2}}\right)\rangle\right]^{-1/2} \tag{5.1.8}$$

where the superscript L stands for the London limit [Nam (1967a,b); Blezius (1987)]. The London limit of penetration depth applies for a "strong" type II superconductor where $\Lambda >> \xi$ with ξ the coherence length. This is certainly the appropriate limit in the case of high-T_c copper oxide superconductors for which ξ is very small and probably as well, much smaller than the electron mean free path l (the clean limit).

Using the dispersion relation (2.1.1), we can have a more explicit form of Λ^L. Through the same procedures as that used for formula (4.2.6) to formula (4.2.10), the formula (5.1.8) can be reduced to

$$\Lambda^L_{xx}(T) = \Lambda^L_{yy}(T) = [\frac{4}{3}\pi T N(0)\mu_0 e^2 \frac{E_F}{m^*}]^{-\frac{1}{2}}$$
$$\times\left[\int_{-\frac{\pi}{c}}^{\frac{\pi}{c}}\frac{c\,dp_z}{2\pi}\sum_{n=1}^{\infty}\frac{\tilde{\Delta}^2_{\vec{p}}(i\omega_n)}{[\tilde{\omega}^2_{\vec{p}}(i\omega_n) + \tilde{\Delta}^2_{\vec{p}}(i\omega_n)]^{3/2}}\left(1 - \frac{\mu}{E_F}(1 + cos(p_z c))\right)\right]^{-\frac{1}{2}} \tag{5.1.9}$$

and

$$\Lambda^L_{zz}(T) = [\frac{4}{3}\pi T N(0)\mu_0 e^2 E_F^2 c^2]^{-\frac{1}{2}}$$

$$\times\left[\int_{-\frac{\pi}{c}}^{\frac{\pi}{c}}\frac{c\,dp_z}{2\pi}\sum_{n=1}^{\infty}\frac{\tilde{\Delta}_{\vec{p}}^2(i\omega_n)}{[\tilde{\omega}_{\vec{p}}^2(i\omega_n)+\tilde{\Delta}_{\vec{p}}^2(i\omega_n)]^{3/2}}\left(\frac{\mu}{E_F}sin(p_zc)\right)^2\right]^{-\frac{1}{2}}. \tag{5.1.10}$$

All other terms are zero [Jiang and Carbotte (1992d)]. Now we are ready to calculate the the penetration depth in the London limit for the geometry parallel and perpendicular to the layers. In solving the Eliashberg equations (2.3.8) and (2.3.9) for the pairing potential $\tilde{\Delta}_{\vec{p}}(i\omega_n)$ and renormalized frequency $\tilde{\omega}_{\vec{p}}(i\omega_n)$, we again used the Pb spectral density ($\alpha^2F(\omega)$) and scaled its height to get a desired coupling strength. All the constants in formulas (5.1.9)and (5.1.10) are unimportant as we always present the results in the ratio $\Lambda^L(0)/\Lambda^L(T)$, except for $\frac{\mu}{E_F}$ which we set to be 0.1 as before.

It is customary to plot $[\Lambda^L(0)/\Lambda^L(T)]^2$ as a function of reduced temperature $t = T/T_c$. This quantity is one by arrangement at $t = 0$ and goes to zero at $t = 1$ because in that limit the system is normal and the London penetration depth is infinite. In all the plots to be presented here we will include a solid curve which is the two fluid model [Gorter and Casimir (1934a,b); Ginsburg and Landau (1950)] temperature variation, $1 - t^4$, and is there for comparison. For high-T_c oxide superconductors several experiments favored this temperature variation over the BCS variation which falls considerably below the two fluid model temperature dependence [Fiory *et al.* (1988); Mitra *et al.* (1989); Cooke *et al.* (1988a,b); Harshman *et al.* (1989)].

In Fig. 5.1.1 we show the results for the London penetration depth in the xy plane which we denote by $[\Lambda_{xx}^L(0)/\Lambda_{xx}^L(T)]^2$. Only g_{10} anisotropy is included here so that the calculations involve the solution of four coupled Eliashberg equations for $\tilde{\Delta}_0(i\omega_n)$, $\tilde{\Delta}_1(i\omega_n)$, $\tilde{\omega}_0(i\omega_n)$ and $\tilde{\omega}_1(i\omega_n)$. The first two

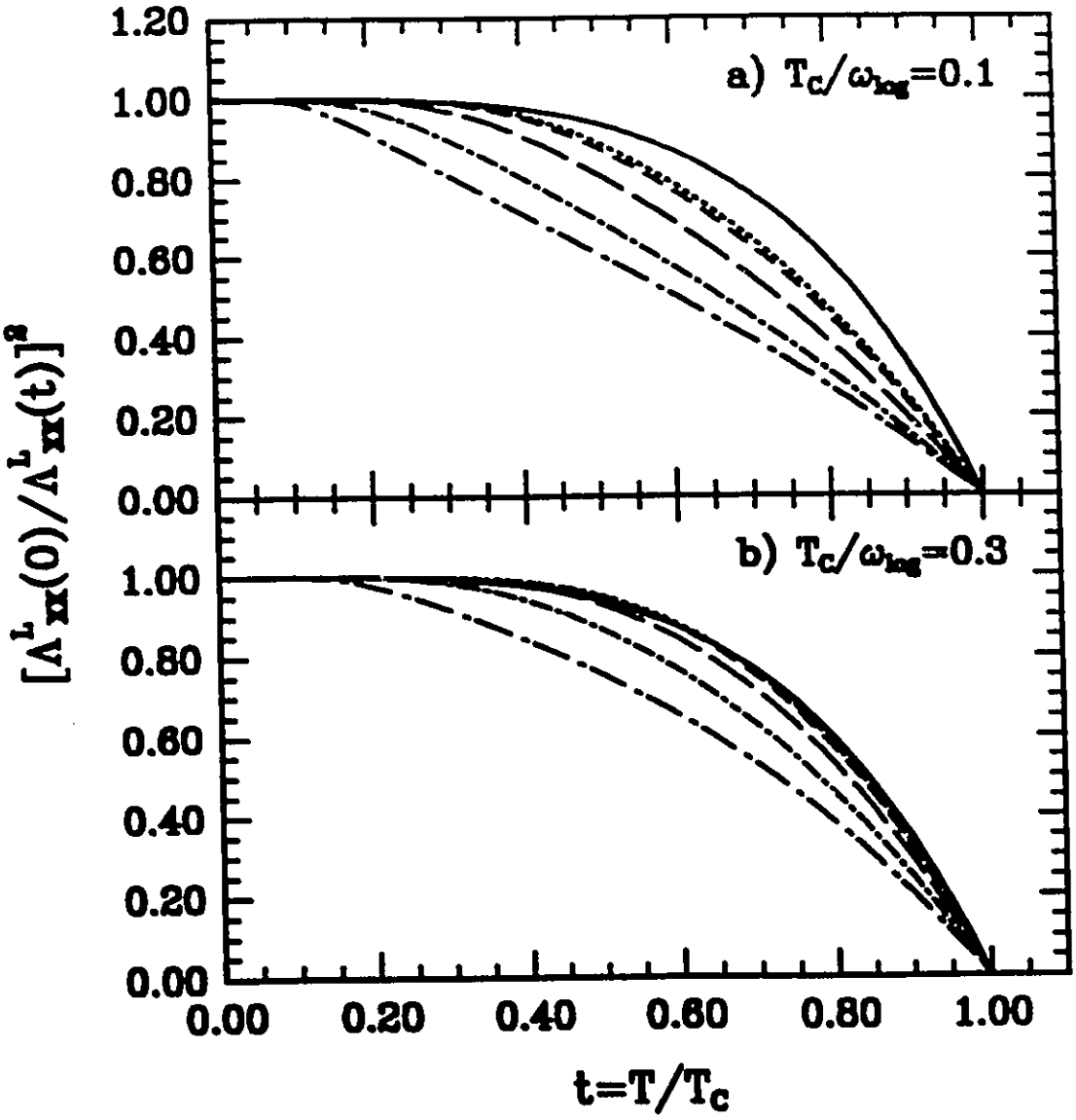

Fig. 5.1.1) The temperature dependence of the ratio $[\Lambda^L_{xx}(0)/\Lambda^L_{xx}(t)]^2$ of the London penetration depth in the xy plane with $t = T/T_c$ for intermediate coupling $T_c/\omega_{log} = 0.1$ (top frame) and strong coupling $T_c/\omega_{log} = 0.3$ (bottom frame). The two fluid model is shown for comparison (solid curve). The other curves are for various anisotropy models, namely $g_{10} = 0.0$ (dotted curve) isotropic case, 0.2 (short-dashed curve), 0.5 (long-dashed curve), 0.8 (short-dash-dotted curve), and finally 1.0 (long-dash-dotted curve).

equations are for the isotropic part of the paring energy ($\tilde{\Delta}_0(i\omega_n)$) at each Matsubara frequency $i\omega_n$ and the anisotropic part ($\tilde{\Delta}_1(i\omega_n)$) which, in momentum space, is multiplied by the modulating factor $cos(p_z c)$ with c the lattice parameter in the z-direction perpendicular to the layers. The second two equations are for the isotropic ($\tilde{\omega}_0(i\omega_n)$) and anisotropic part ($\tilde{\omega}_1(i\omega_n)$) which is also proportional to $cos(p_z c)$ of the renormalized Matsubara frequencies. This set of four equations are iterated self-consistently to convergence. The top frame applies to a superconductor of moderate coupling strength with $T_c/\omega_{log} = 0.1$ while the bottom frame is for a strong coupling case with $T_c/\omega_{log} = 0.3$. The curves are for $g_{10} = 0.0$ dotted curve, $g_{10} = 0.2$ short-dashed curve, $g_{10} = 0.5$ long-dashed curve, $g_{10} = 0.8$ short-dash-dotted curve, and for $g_{10} = 1.0$ long-dash-dotted curve. We see that in the top frame the isotropic curve (dotted) falls considerably below the solid curve from two fluid model although it is already substantially above the BCS results for the London penetration depth in the clean limit. In fact it falls roughly in between the two. As anisotropy is added the curves start falling even lower with respect to the two fluid results as seen in the BCS work of Schneider *et al.* (1989). The last two curves are below the isotropic BCS results. An important difference between our results for $T_c/\omega_{log} = 0.1$ and BCS results, which correspond to the limit $T_c/\omega_{log} \to 0$, is that the isotropic curve, which gives the starting curve for the anisotropic sequence, starts closer to the two fluid model than does the BCS curve. In the bottom frame where $T_c/\omega_{log} = 0.3$ for very strong coupling the isotropic curve (dotted) is pushed towards the two fluid model curve (solid). In fact, now the dotted curve is slightly above the solid curve at the lower temperature and slightly below it at T near T_c. The other striking feature, on comparing the two sets of curves in two frames, is that

the introduction of anisotropy is much less effective in pushing the curves down away from the two fluid model for $T_c/\omega_{log} = 0.3$ than for $T_c/\omega_{log} = 0.1$. Even for $g_{10} = 1.0$ (long-dash-dotted curve) the curve remains well above the curve for the BCS clean limit. In the strong coupling regime the introduction of anisotropy makes much less difference than it does in the weak coupling regime.

Similar results for the London penetration depth along the z-direction perpendicular to the xy plane are shown in Fig. 5.1.2. The effect of anisotropy on the temperature dependence of $[\Lambda^L_{zz}(0)/\Lambda^L_{zz}(t)]^2$ are more pronounced than for the xx direction just described as is seen on comparison of Fig. 5.1.2 with Fig. 5.1.1. Particularly note worthy is the results for $g_{10} = 1.0$, the long-dash-dotted curve, in which case the temperature dependence of $[\Lambda^L_{zz}(0)/\Lambda^L_{zz}(t)]^2$ does not in any way resemble the two fluid model prediction even for the very strong coupling $T_c/\omega_{log} = 0.3$. This is in striking disagreement with experiment on the high-T_c oxide superconductors which favors a variation near the solid curve. Comparing the top frame with the bottom frame, we see once again that anisotropy has relatively, a stronger effect for weak than for strong coupling.

It is interesting to wonder if other models for the anisotropy including higher Fermi surface harmonics in the expansions (2.3.2) to (2.3.7) for the renormalized Matsubara frequency, pairing potential and the electron-phonon kernel $\lambda_{\vec{p}\vec{p}'}(i\omega_n - i\omega_m)$, could lead to results substantially different from those of Fig. 5.1.1 to Fig. 5.1.2 and in particular give results near the two fluid model even for cases with substantial anisotropy. In Fig. 5.1.3 we show the results for the London penetration depth in the xy plane with both g_{10} and g_{20} anisotropies. Again, the top frame is for intermediate coupling

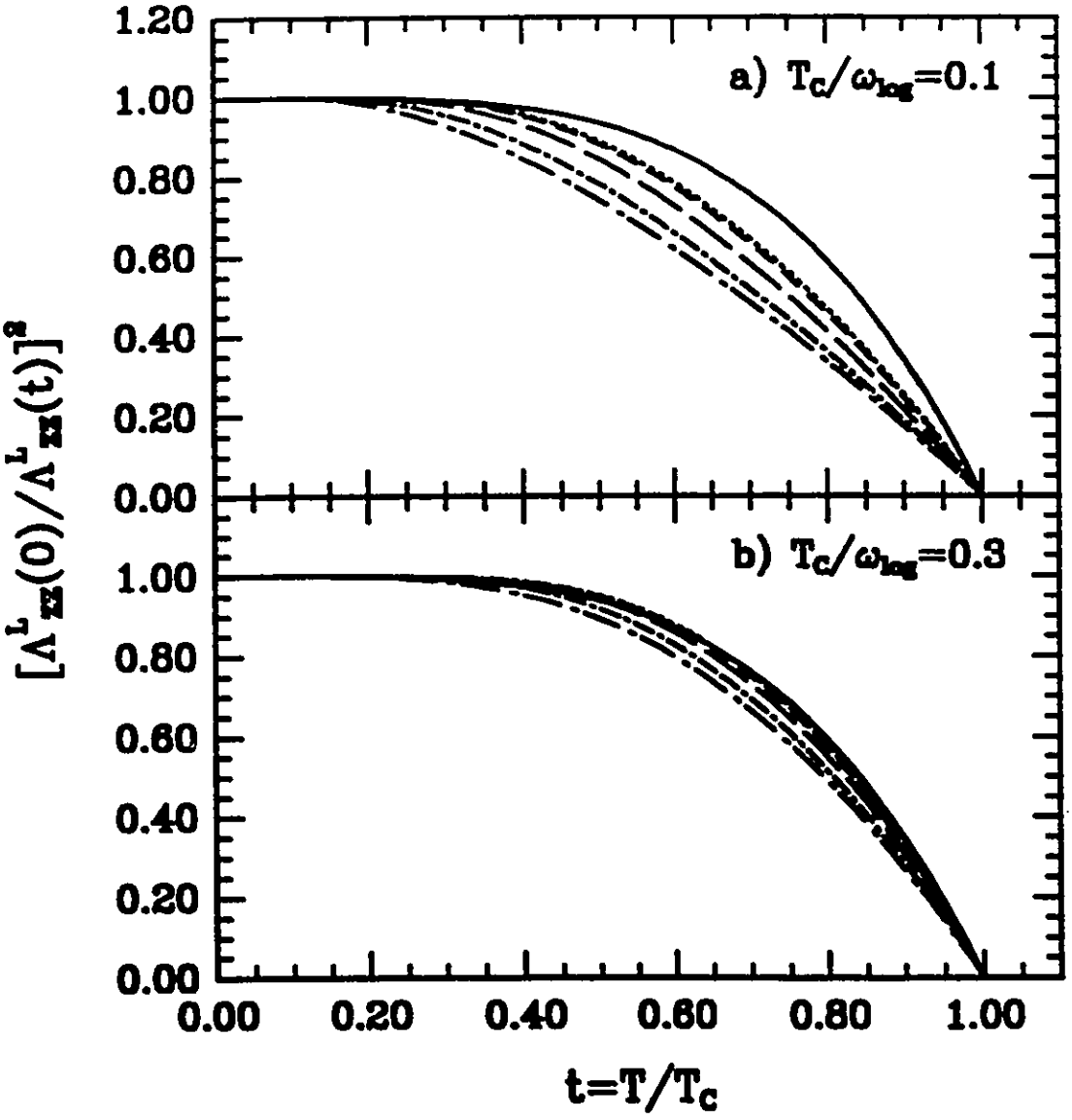

Fig. 5.1.2) The temperature dependence of the ratio $[\Lambda^L_{zz}(0)/\Lambda^L_{zz}(t)]^2$ of the London penetration depth in the z direction with $t = T/T_c$ for intermediate coupling $T_c/\omega_{log} = 0.1$ (top frame) and strong coupling $T_c/\omega_{log} = 0.3$ (bottom frame). The two fluid model is shown for comparison (solid curve). The other curves are for various anisotropy models, namely $g_{10} = 0.0$ (dotted curve) isotropic case, 0.2 (short-dashed curve), 0.5 (long-dashed curve), 0.8 (short-dash-dotted curve), and finally 1.0 (long-dash-dotted curve).

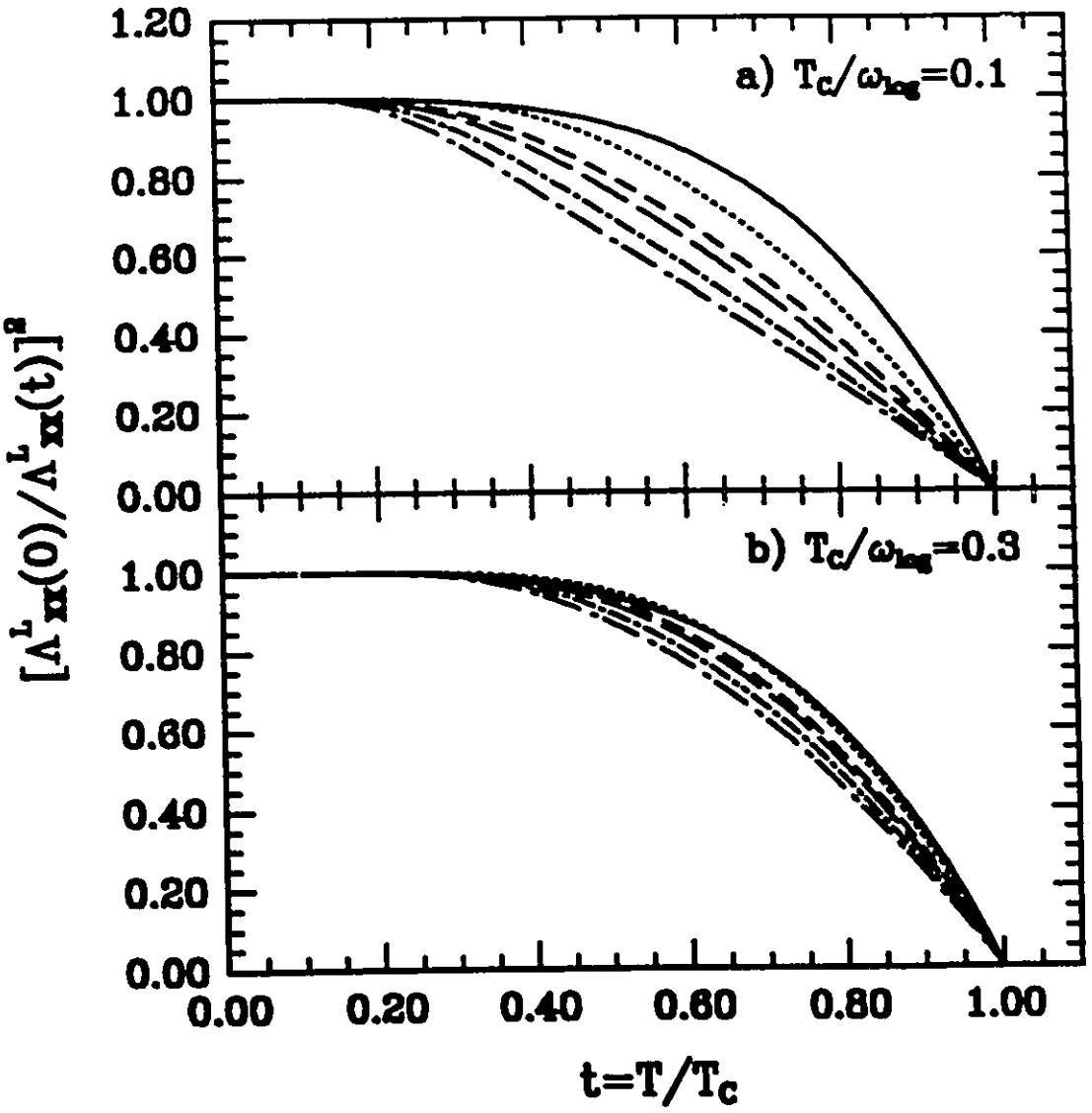

Fig. 5.1.3) The temperature dependence of the ratio $[\Lambda^L_{xx}(0)/\Lambda^L_{xx}(t)]^2$ of the London penetration depth in the xy plane with $t = T/T_c$ for intermediate coupling $T_c/\omega_{log} = 0.1$ (top frame) and strong coupling $T_c/\omega_{log} = 0.3$ (bottom frame). The two fluid model is shown for comparison (solid curve). The other curves are for various anisotropy models $g_{10} = 0.0$ and $g_{20} = 0.0$ (dotted curve) isotropic case, $g_{10} = 0.2$ and $g_{20} = 0.5$ (short-dashed curve), $g_{10} = 0.5$ and $g_{20} = 0.5$ (long-dashed curve), $g_{10} = 0.8$ and $g_{20} = 0.5$ (short-dash-dotted curve), and finally $g_{10} = 1.0$ and $g_{20} = 0.5$ (long-dash-dotted curve).

$T_c/\omega_{log} = 0.1$ and the bottom frame is for strong coupling $T_c/\omega_{log} = 0.3$. It is of some interest to compare in more detail Fig. 5.1.3 with Fig. 5.1.1, both are for the penetration in the xy plane. The solid (two fluid model) and dotted curves (isotropic case) are common to both plots. The short-dashed curve in both top and bottom frame of Fig. 5.1.1 is for $g_{10} = 0.2$ with no g_{20} anisotropy while in Fig. 5.1.3 it is for $g_{10} = 0.2$, again, and $g_{20} = 0.5$ so that additional $cos(2p_z c)$ anisotropy has been included. This has depressed the curve away further from the two fluid model. Adding extra anisotropy through a g_{20} term, for example, does not always act to reduce the curve for $[\Lambda^L(0)/\Lambda^L(t)]^2$, however, as can be seen by comparing the short-dash-dotted curves of Fig. 5.1.1 and Fig. 5.1.3 as well as the long-dash-dotted curves. In Fig. 5.1.1 only g_{10} anisotropy is included with $g_{10} = 0.8$ and 1.0 for short- and long-dash-dotted curves, respectively. In Fig. 5.1.3, g_{20} anisotropy is additionally included with $g_{20} = 0.5$. In both cases the addition of g_{20} anisotropy pushes the curves back up towards the two fluid model. Thus, the addition of anisotropy can either push the curves up or down although, here, all the curves with anisotropy are still below the isotropic curve for both intermediate and strong couplings.

Similar but more striking behavior is seen on comparison of Fig. 5.1.4 with Fig. 5.1.2 which give the results for magnetic field penetration along the z axis perpendicular to the xy plane. Adding g_{20} anisotropy has now pushed all curves back up no matter the strength of the coupling. The effect is particularly dramatic for the $g_{10} = 1.0$ (highly anisotropic) case. The very strong deviation from two fluid behavior seen in Fig. 5.1.2 (long-dash-dotted curve) when $g_{10} = 1.0$ with $g_{20} = 0.0$ is now largely eliminated for both coupling strengths by leaving $g_{10} = 1.0$ but taking a finite value for g_{20}, namely 0.5. Two other curves in the bottom frame of Fig. 5.1.4 where

$T_c/\omega_{log} = 0.3$, namely $g_{10} = 0.2$ and $g_{10} = 0.5$ with g_{20} fixed at 0.5, are pushed up even above the isotropic curve and the two fluid results (solid curve). This does not happen in the top frame of Fig. 5.1.4 where $T_c/\omega_{log} = 0.1$. For an anisotropic superconductor, the coupling strength also affects the behavior of the London penetration depth.

To conclude, we have used the anisotropic Eliashberg equations written on the imaginary (Matsubara) frequency axis, (2.3.8) and (2.3.9), to calculate the London penetration depth for various values of the strong coupling index T_c/ω_{log} and models for the anisotropy appropriate to layered structures. As is well known, in the clean limit, the temperature variation of the London penetration depth in weak coupling regime, near BCS limit, falls considerably below the two fluid model predictions for $[\Lambda^L(0)/\Lambda^L(t)]^2$ and so deviates from many experimental results which favor a two fluid behavior for high-T_c oxide superconductors [Fiory *et al.* (1988); Mitra *et al.* (1989); Cooke *et al.* (1988a,b); Harshman *et al.* (1989)]. Adding a simple anisotropy g_{10} to the theory to account for a layered crystal structure as did by Schneider *et al.* (1989) leads to even greater deviation from the two fluid model results, especially in the z direction. On the other hand it is known that increasing coupling strength pushes the curve up towards the two fluid model [Gorter and Casimir (1934a,b); Ginsburg and Landau (1950)]. Here we have found that adding anisotropy modifies the temperature variation of the London penetration depth both along and perpendicular to the c-axis much less when the coupling is strong than when it is weak. The results remain very close to a two fluid behavior for a strong coupling superconductor ($T_c/\omega_{log} = 0.3$) in both directions, parallel and perpendicular to the xy plane, even for what

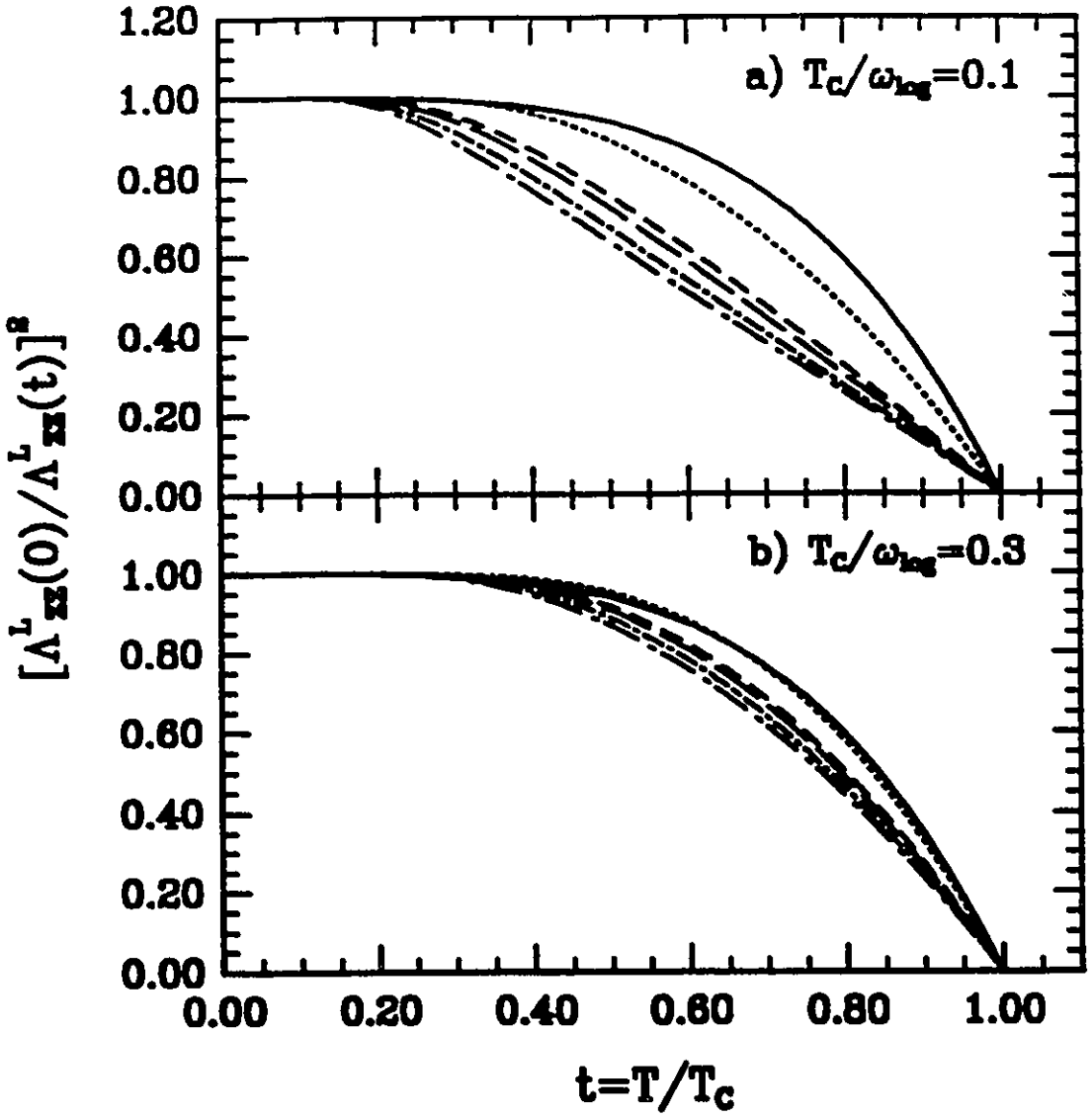

Fig. 5.1.4) The temperature dependence of the ratio $[\Lambda^L_{zz}(0)/\Lambda^L_{zz}(t)]^2$ of the London penetration depth in the z direction with $t = T/T_c$ for intermediate coupling $T_c/\omega_{log} = 0.1$ (top frame) and strong coupling $T_c/\omega_{log} = 0.3$ (bottom frame). The two fluid model is shown for comparison (solid curve). The other curves are for various anisotropy models $g_{10} = 0.0$ and $g_{20} = 0.0$ (dotted curve) isotropic case, $g_{10} = 0.2$ and $g_{20} = 0.5$ (short-dashed curve), $g_{10} = 0.5$ and $g_{20} = 0.5$ (long-dashed curve), $g_{10} = 0.8$ and $g_{20} = 0.5$ (short-dash-dotted curve), and finally $g_{10} = 1.0$ and $g_{20} = 0.5$ (long-dash-dotted curve).

appears to us to be fairly extreme values of the anisotropy. Also, by experimenting with more complex models for the anisotropy, *i.e.*, including higher order Fermi surface harmonics in our expansions, we have found that in some cases introducing more anisotropy can make the curve go up or down and even fall above the isotropic case (see the bottom frame in Fig. 5.1.4). We have not made an exhaustive study of the available parameter space for anisotropy, however, as this would have been too costly in computing time. For example, we have six coupled Eliashberg equations to solve for Figs. 5.1.3 and 5.1.4 compared with four for Figs. 5.1.1 and 5.1.2. From the results obtained it is clear that more complicated models for the anisotropy can indeed change the curves obtained quantitatively but not qualitatively. No simple conclusions can be made about the effect of layered anisotropy on the London penetration depth temperature dependence. It depends to some extent on details.

5.2 NUCLEAR MAGNETIC RESONANCE

Generally, a nucleus has a magnetic moment $\vec{\mu}$ and a angular momentum $\vec{J}$. The two are closely related with

$$\vec{\mu} = -\gamma \vec{J}. \tag{5.2.1}$$

Here, γ is the gyromagnetic ratio which depends on the state of the nucleus [Slichter (1978)]. The magnetic moment of the nucleus will interact with an applied magnetic field $\vec{H}$, taking it to be H_0 along the z-direction, with the interaction energy

$$E = -\vec{\mu} \cdot \vec{H} = -\gamma H_0 J_z. \tag{5.2.2}$$

The eigenvalues of J_z are $\hbar I, \hbar(I-1), \cdots, -\hbar I$ with I either integer or half-integer. The energy between the adjacent energy levels is

$$\Delta E = -\gamma \hbar H_0. \tag{5.2.3}$$

To detect this, we can apply another alternating magnetic field $\vec{\tilde{H}} = H_x cos(\omega t)\hat{x}$, perpendicular to the static field $\vec{H} = H_0\hat{z}$. An absorption peak will appear at

$$\hbar\omega = \Delta E = -\gamma \hbar H_0. \tag{5.2.4}$$

This is the so-called nuclear magnetic resonance (NMR).

In metals, the NMR will be strongly influenced by conduction electrons through the interaction of their magnetic moments with those of the nuclei [Abragam (1961); Slichter (1963); and Winter (1971)]. Two effects are most important here. One is the so-called Knight shift, K, the shift in the value of the applied field at which the NMR occurs in the metal, compared to a salt, as conduction electrons alter the static magnetic field seen by the nuclei from the value of the applied field. The Knight shift is proportional

to the Pauli spin susceptibility of the electrons and provides a static measurement. The other is the nuclear spin-lattice relaxation time, T_1, the characteristic time for the nuclear spins to come into thermal equilibrium with their surroundings through energy exchange with the conduction electrons at the top of the Fermi distribution, which is usually the quickest means in metals. The relaxation time depends not only on the states of electrons but also on the strength of electron-nucleus coupling and provides a dynamic measurement. Both the Knight shift K and the relaxation time T_1 will be strongly affected by the superconducting phase transition. Historically, the study of the NMR has played a big role in understanding superconductivity [MacLaughlin (1974)].

From BCS theory, one can derive that the ratio of the Knight shift in the superconducting state to that in the normal state K_s/K_n is proportional to $exp(-\Delta_0/k_BT)$ at low temperature, here, Δ_0 is the gap function at zero temperature and k_B is the Boltzman constant. The physics of this law can be viewed in the following way. Superconducting electrons are in the form of Cooper pair which have zero spin and hence make no contribution to the Knight shift while the number of normal electrons with net spin, which are thermally excited out of the superconducting condensate, is proportional to $exp(-\Delta_0/k_BT)$ at temperatures close to zero. Experiment on many conventional superconductors, *e.g.*, Al by Fine, Lipsieas and Strongin (1969), followed this relation convincingly. A full expression for the ratio K_s/K_n was first derived by Yosida (1958) within BCS theory and called the Yosida function $Y(T)$ thereafter. From Eliashberg theory, the Yosida function $Y(T)$ is given by

$$Y(T) = \frac{K_s}{K_n} = 2\int_0^\infty d\omega(-\frac{\partial f(\omega)}{\partial \omega})\langle Re\left(\frac{\tilde{\omega}_{\vec{p}}(\omega,T)}{\sqrt{\tilde{\omega}^2_{\vec{p}}(\omega,T) - \tilde{\Delta}^2_{\vec{p}}(\omega,T)}}\right)\rangle. \tag{5.2.5}$$

Here, T is temperature, f is the Fermi distribution function and $\langle\rangle$ again denotes a Fermi surface average. $\tilde{\omega}_{\vec{p}}(\omega,T)$ and $\tilde{\Delta}_{\vec{p}}(\omega,T)$ are the renormalized frequency and pairing potential, respectively, and are the solutions of Eqs. (2.3.10) and (2.3.11).

For the ratio of the spin-lattice relaxation rate R_s/R_n with the relaxation rate R the inverse of the relaxation time $R = 1/T_1$ and the subscripts s and n for the superconducting and normal states, respectively, the formula derived from Eliashberg theory is

$$\frac{R_s}{R_n} = 2\int_0^\infty dw\left(-\frac{\partial f(\omega)}{\partial \omega}\right)\left([\langle Re(\frac{\tilde{\omega}_{\vec{p}}(\omega,T)}{\sqrt{\tilde{\omega}_{\vec{p}}(\omega,T)^2 - \tilde{\Delta}^2_{\vec{p}}(\omega,T)}})\rangle]^2 + [\langle Re(\frac{\tilde{\Delta}_{\vec{p}}(\omega,T)}{\sqrt{\tilde{\omega}_{\vec{p}}(\omega,T)^2 - \tilde{\Delta}^2_{\vec{p}}(\omega,T)}})\rangle]^2\right). \tag{5.2.6}$$

Here, all the quantities in the integral are defined in the same way as in formula (5.2.5). The most interesting result from this ratio, perhaps, is a large enhancement of the relaxation rate just below T_c before the ratio falls off to zero at low temperature. This is the so called Hebel-Slichter peak [Hebel and Slichter (1957, 1959)] and comes from the coherent nature of the population of Cooper pair states in the formation of the condensed superconducting phase. A detailed discussion of the role of 'coherent factor' in scattering in superconductivity was given by Schrieffer (1964). The observation of this peak

in many conventional superconductors, *e.g.*, Al [Hebel and Slichter (1957, 1959); Masuda and Redfield (1962)], is a crucial aspect in the establishment of BCS theory.

The shape of Hebel-Slichter peak is material dependent. Unlike the prediction from simple BCS theory, a logarithm singularity at T_c, the peak in fact is much wider and smaller in magnitude in real materials. It has been shown that the Hebel-Slichter peak will be greatly depressed by increasing coupling strength and/or introducing anisotropy [Statt (1990a,b); Monien and Pines (1990); Akis, Jiang and Carbotte (1991); Jiang and Carbotte (1992e)]. Another effect, Fermi liquid corrections, will also diminish the peak. Fermi liquid corrections were introduced by Monien and Pines (1990) recently to account for a nearly antiferromagnetic liquid behavior in high T_c oxide superconductors where no Hebel-Slichter peak has been observed in NMR experiment. The formula for the ratio of the spin-lattice relaxation rate R_s/R_n including Fermi liquid corrections is given by [Monien and Pines (1990)]

$$\frac{R_s}{R_n} = (\frac{R_s}{R_n})^{sc} \frac{[1-\lambda(T_c)]^2}{[1-\lambda(T_c)Y(T)]^2} \tag{5.2.7}$$

where $\lambda(T_c)$ is a parameter that enters the enhanced spin susceptibility. It starts at zero when there is no enhancement and increases as the antiferromagnetic transition is approached. In (5.2.7) $Y(T)$ is the Yosida function given by (5.2.5) and $(R_s/R_n)^{sc}$ denotes strong coupling results without the inclusion of Fermi liquid corrections (formula (5.2.6)).

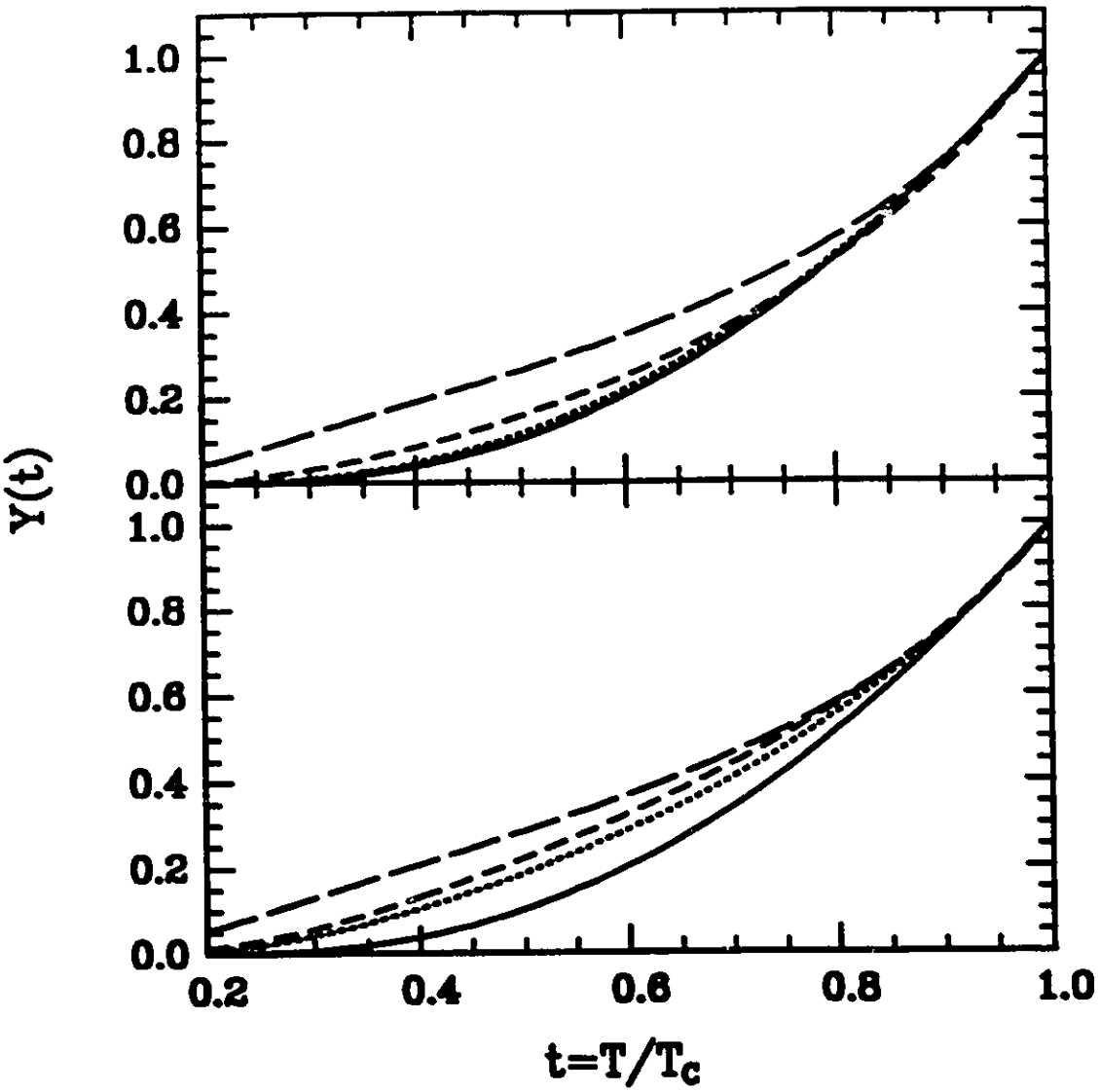

Fig. 5.2.1) The Yosida function $Y(T)$ as a function of reduced temperature $t = T/T_c$ for intermediate coupling $T_c/\omega_{log} = 0.1$ and various values of anisotropy. In the top frame, where $g_{20} = 0.0$, the solid curve is for isotropic case with $g_{10} = 0.0$, the dotted curve for $g_{10} = 0.2$, the short-dashed curve for $g_{10} = 0.5$, and the long-dashed curve for $g_{10} = 0.8$. In the bottom frame the solid curve is again for isotropic case with $g_{10} = g_{20} = 0.0$, the dotted curve for $g_{10} = 0.2$ and $g_{20} = 0.5$, the short-dashed curve for $g_{10} = 0.5$ and $g_{20} = 0.5$, and the long-dashed curve for $g_{10} = 0.8$ and $g_{20} = 0.5$.

Here, we would like to study the effect of planar anisotropy on both the Yosida function and the ratio of the relaxation rate R_s/R_n using the formalism of Eliashberg theory. The difference between the work here and previous ones [Statt (1990a,b); Monien and Pines (1990); Akis, Jiang and Carbotte (1991)] is that we include the effects of strong coupling and anisotropy in a consistent way. We will also study the effect of Fermi liquid corrections when we come to the experiment data of the NMR on high-T_c oxide superconductors.

We begin with the Yosida function $Y(T)$. After solving for $\tilde{\Delta}_{\hat{p}}(\omega, T)$ and $\tilde{\omega}_{\hat{p}}(\omega, T)$ from Eqs. (2.3.10) and (2.3.11), we calculate the Yosida function $Y(T)$ from (5.2.5). In Fig. 5.2.1 we show results for the Yosida function $Y(T)$ as a function of reduced temperature T/T_c for the case $T_c/\omega = 0.1$ (intermediate coupling strength) for various values of g_{10} namely 0.0 (solid curve) which corresponds to the isotropic case, 0.2 (dotted curve), 0.5 (short-dashed curve) and 0.8 (long-dashed curve). In the top frame we have the second anisotropic parameter $g_{20} = 0.0$ while in the bottom frame it equals 0.5 except for the solid curve which is the isotropic case for comparison. In both cases we see that near T_c anisotropy has very little effect on $Y(T)$ whereas at lower temperature adding anisotropy leads to much larger $Y(T)$. As we pointed out above the Yosida function is proportional to the Pauli spin susceptibility of quasiparticles, therefore, of the population of quasiparticles being thermal excited out of superconducting condensation at a given temperature. From the discussion of previous chapters we know that the superconducting gap minimum decreases with increasing anisotropy and the effect from the gap minimum will be more significant at lower temperature. Therefore at low

temperature more quasiparticles will be thermal excited out of the condensation, compared with an isotropic case, through the gap minimum and, hence, a larger $Y(T)$. A more complicated anisotropy, comparing the bottom with top frames in Fig. (5.2.1), only makes quantitatively change of $Y(T)$ but not qualitatively. We have generally found that such complication introduces no new physics.

We would like to point out that the results here are similar to those presented in Akis *et al.* (1991) for the same T_c/ω_{log} value but using an ansatz for the anisotropy which is

$$\tilde{\Delta}_{\vec{p}}(\omega) = \tilde{\Delta}^{i}(\omega)(1 + \alpha cos(p_z c)) \tag{5.2.8}$$

where α is an anisotropy parameter and $\tilde{\Delta}^{i}(\omega)$ is the solution of the isotropic Eliashberg equations. By comparing the top frame in Fig. 5.2.1 and Fig. 9 in Akis *et al.* (1991), we have found that the curves for $Y(T)$ are very nearly the same if we identify the value of g_{10} with the value of α for small values. For larger values of the anisotropic parameters g_{10} and α, however, the correspondence between the ansatz (5.2.8) and the full solutions of the anisotropic Eliashberg equations, Eqs. (2.3.10) and (2.3.11), starts to fail more importantly.

We turn now to our results for the nuclear spin-lattice relaxation rate R_s/R_n given by equation (5.2.6). In the top frame of Fig. 5.2.2 we show the temperature dependence of R_s/R_n for the case $T_c/\omega_{log} = 0.1$ (intermediate coupling) and various values of anisotropy $g_{10} = 0.0$ (solid curve) isotropic case, $g_{10} = 0.2$ (dotted curve), 0.5 (short-dashed curve) and 0.8 (long-dashed

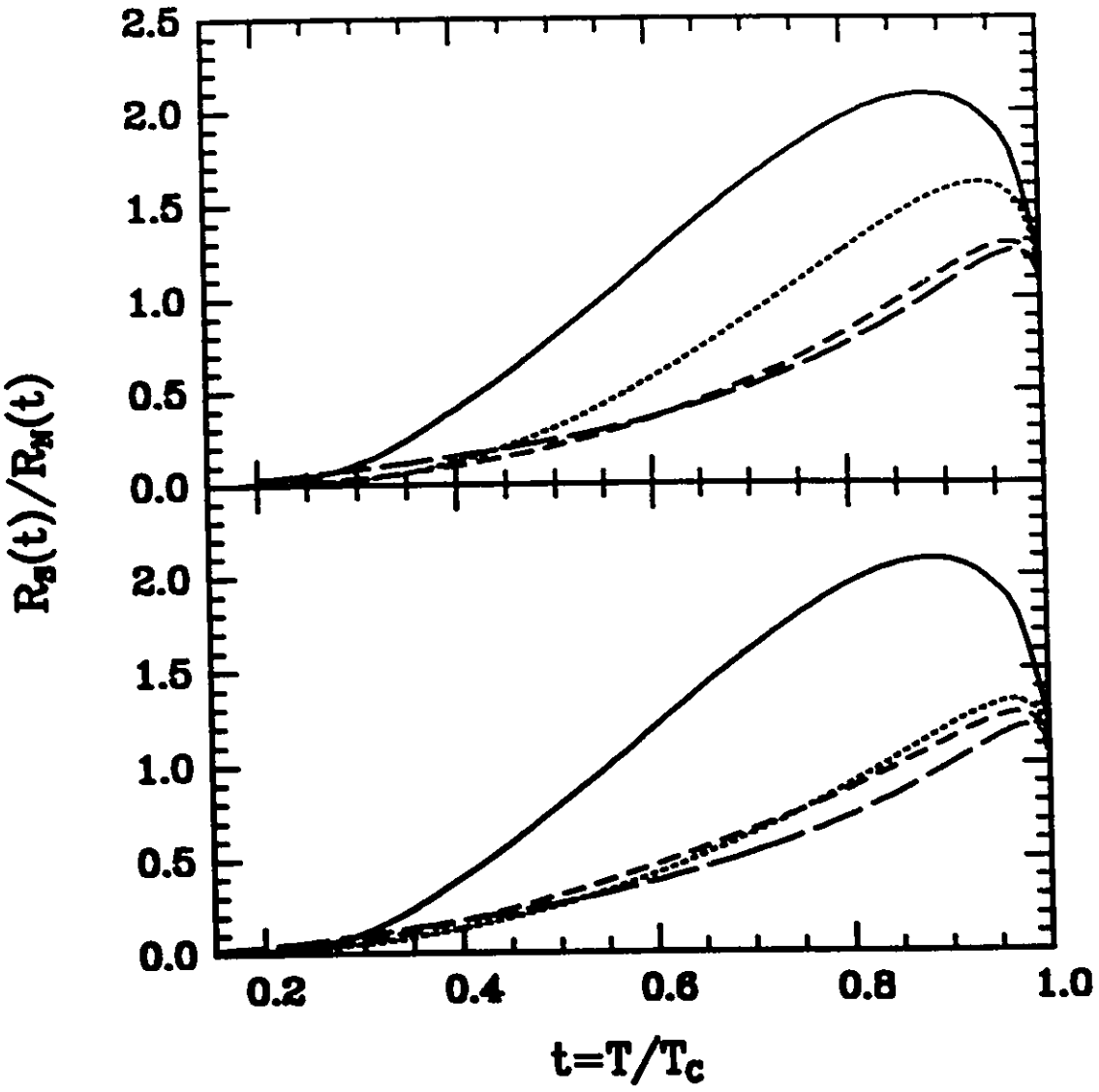

Fig. 5.2.2) The nuclear spin lattice relaxation rate ratio R_s/R_n as a function of temperature T/T_c for intermediate coupling $T_c/\omega_{log} = 0.1$ and various anisotropy parameters. In the top frame, where $g_{20} = 0.0$, the solid curve is for isotropic case with $g_{10} = 0.0$, the dotted curve for $g_{10} = 0.2$, the short-dashed curve for $g_{10} = 0.5$, and the long-dashed curve for $g_{10} = 0.8$. In the bottom frame the solid curve is again for isotropic case with $g_{10} = g_{20} = 0.0$, the dotted curve for $g_{10} = 0.2$ and $g_{20} = 0.5$, the short-dashed curve for $g_{10} = 0.5$ and $g_{20} = 0.5$, and the long-dashed curve for $g_{10} = 0.8$ and $g_{20} = 0.5$.

curve). We see that increasing anisotropy, *i.e.*, g_{10} value, can greatly suppress the Hebel-Slichter peak in R_s/R_n even where damping effects are not so significant (see the large peak in the solid curve for the isotropic case). As for the Yosida function $Y(T)$ the results obtained here compare well with those of Akis *et al.* (1991) based on the simple ansatz (5.2.8) provided the anisotropy is small. At larger anisotropy quantitative changes are observed to occur but no qualitative differences are found. Additional anisotropy can further reduce the peak height. This is illustrated in the bottom frame of Fig. 5.2.2 where we plot the temperature dependence of R_s/R_n for cases similar to those in the top frame except we now add some g_{20} anisotropy. The solid curve still represents the isotropic results $g_{10} = g_{20} = 0.0$ for comparison, while the dotted curve is for $g_{10} = 0.2$ and $g_{20} = 0.5$, the short-dashed curve is for $g_{10} = 0.5$ and $g_{20} = 0.5$, and the long-dashed curve is for $g_{10} = 0.8$ and $g_{20} = 0.5$. A more complicated anisotropy does not always mean a reduction in the Hebel-Slichter peak. In fact the peak is higher for $g_{10} = 0.2$ and $g_{20} = 0.5$ than for $g_{10} = 0.5$ along with $g_{20} = 0.0$, although it is lower than for $g_{10} = 0.2$ and $g_{20} = 0.0$. Complicated assumptions for the details of the anisotropy can lead to significant quantitative differences in R_s/R_n which can not be captured by any simple semi-phenomenological model such as (5.2.8) but no qualitative changes result.

Finally, we would like to show the kind of fit which can be obtained through formula (5.2.7) with experiment data on high-T_c oxides. In Fig. 5.2.3 the solid dots and the open circles are the data of Imai *et al.* (1988) for coppers in CuO chains Cu1 and in CuO_2 planes Cu2 of $YBa_2Cu_3O_{7-x}$ with $T_c = 92K$. All theoretical curves correspond to $T_c/\omega_{log} = 0.05$ and $g_{10} = 1.0$ with all other g_{jk} left out. The solid curve is for an antiferromagnetic spin susceptibility

enhancement factor $\lambda(T_c)$ of 0.2 and fits reasonably well the solid points. Better fits could be obtained by introducing different anisotropy parameters but this is not the point of our study here. The dotted curve is for $\lambda(T_c) = 0.7$, the short dashed curve for 0.8 and the long dashed curve for 0.85. None of these curves fit perfectly the Cu2 data (open circle) which however falls within the range delineated by this set of curves. The much larger value of $\lambda(T_c)$ needed to fit the Cu2 data than the Cu1 data is in agreement with the picture of strong antiferromagnetic correlations in the CuO_2 planes of these compounds which means that the Cu2 site is much more influenced than Cu1 site by these correlations.

In summary, we have studied the effect of planar anisotropy on the Yosida function $Y(T)$ which gives the magnetic susceptibility and on the nuclear spin-lattice relaxation rate R_s/R_n using the formalism of Eliashberg theory in a consistent way. We found a larger value of $Y(T)$ at low temperature and a strong depression of the Hebel-Slichter peak in the ratio R_s/R_n due to the introduction of anisotropy. These largely agree with previous results by Akis *et al.* (1991) (especially for small values of anisotropy) which were obtained using a semi-phenomenological ansatz for the anisotropy, formula (5.2.8), and strictly isotropic solutions for the Eliashberg equations. More complicated model anisotropy was also explored here but this resulted only in quantitative but not qualitative changes. Good agreement with experiment on high-T_c oxides has been found after taking account of the Fermi liquid corrections of Monien and Pines (1990), although we did not search for the set of parameters that would produced the best fit to data, as this was not the aim of our study here.

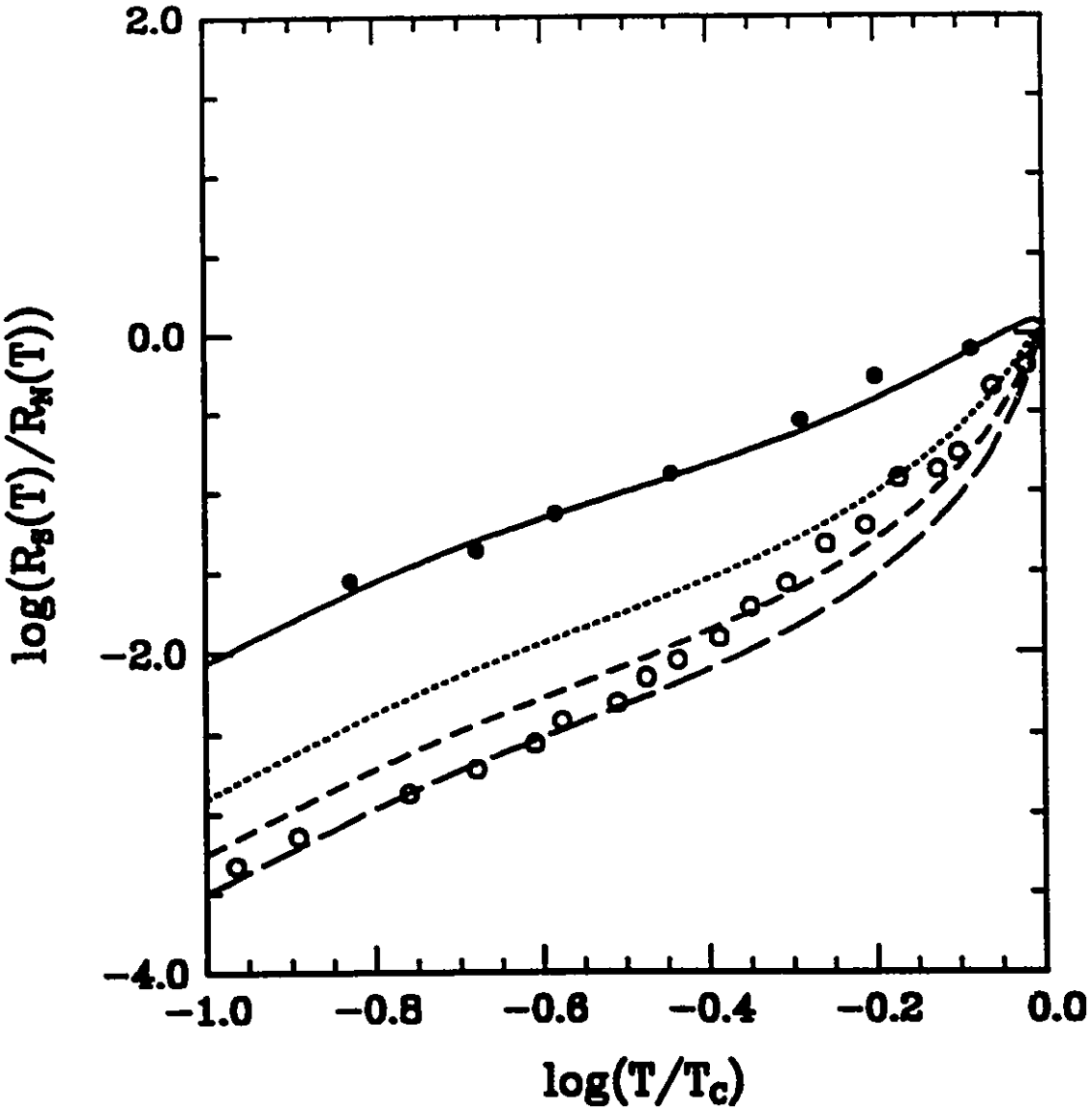

Fig. 5.2.3) The *log* of the spin lattice relaxation rate ratio R_s/R_n as a function of the *log* of the reduced temperature for a model with $T_c/\omega_{log} = 0.05$ and $g_{10} = 1.0$ for various values of the spin susceptibility enhancement parameter $\lambda(T_c)$ of Monien and Pines, namely 0.2 (solid curve), 0.7 (dotted curve), 0.8 (short-dashed curve) and 0.85 (long-dashed curve). Also shown for comparison are the experimental data of Imai *et al.* (1988) for the *Cu*1 site (solid dot) and the *Cu*2 site (open circle).

5.3 INFRARED CONDUCTIVITY

The infrared conductivity, measured by infrared spectroscopy, has been an important physical quantity in the study of superconductivity [Timusk and Tanner (1989)]. As a probe of the particle-hole excitation spectrum of superconductors, the infrared conductivity contains the information about the energy gap as well as the coupling of electrons to low lying excitations, such as phonons in conventional superconductors. Here we would like to discuss how the conductivity is affected by planar anisotropy with or without normal impurity scatterings (t^+).

A formula for the infrared conductivity within BCS theory was first derived by Mattis and Bardeen (1957). The expression for the real part of the conductivity (which is our only interest in this thesis) in the superconducting state σ_{S1} normalized by its value in the normal state σ_{N1} is

$$\frac{\sigma_{S1}(\omega)}{\sigma_{N1}(\omega)} = \frac{1}{\omega}\int_{-\infty}^{\infty} d\Omega[f(\Omega) - f(\Omega+\omega)] \times \left[Re\left(\frac{\Omega}{\sqrt{\Omega^2-\Delta^2}}\right) \cdot Re\left(\frac{\Omega+\omega}{\sqrt{(\Omega+\omega)^2-\Delta^2}}\right) + Re\left(\frac{\Delta}{\sqrt{\Omega^2-\Delta^2}}\right) Re\left(\frac{\Delta}{\sqrt{(\Omega+\omega)^2-\Delta^2}}\right)\right]. \tag{5.3.1}$$

Here, f is the usual Fermi function and Δ is the energy gap. The characteristic feature of this ratio σ_{S1}/σ_{N1} is that besides a delta function at the origin it is zero until $\omega = 2\Delta$ and approaches 1 at high frequencies. This is understood as due to the fact that an incident photon with energy smaller than 2Δ can not break a Cooper pair to create particle-hole excitations. Thus, there is no absorption until the photon energy is greater than 2Δ. For photons with energy much greater than 2Δ, the energy gap Δ will have little effect,

therefore, the absorption in the superconducting state will be equal to that in the normal state. A delta function at origin is present due to the perfect *dc* conductance in the superconducting state. The amplitude of this delta function is determined by the sum rule [Ashcroft and Mermin (1976)]

$$\int_0^\infty d\omega\sigma_1(\omega) = \frac{\omega_p^2}{8} \tag{5.3.2}$$

where ω_p is the plasma frequency. This sum rule should always be satisfied.

We should point out that formula (5.3.1) applies only for the dirty limit by which we mean the mean free path l is much smaller than the superconducting coherent length ξ. In the clean limit there would be no absorption even above 2Δ due to the momentum conservation law. The momentum of a photon is generally quite small compared with that of the excited particle-hole pair for which energy has been conserved. Therefore additional elastic scattering events are required for the momentum to be conserved. In BCS theory such scattering events are from impurities since the interaction between electrons and other excitations, such as phonons, is not taken into account. As we discussed before, however, in the dirty limit anisotropy will be totally washed out through very strong scattering. To study the effect of anisotropy on the infrared conductivity we should go to the strong coupling Eliashberg theory. In the strong coupling theory where boson-mediated interaction between quasiparticles has been fully considered, there will be absorption in the clean limit since phonons, for example, can carry the extra momentum for the momentum conservation through Umklapp processes. At

$T = 0K$ the absorption in Eliashberg theory will begin at 2Δ plus the minimum energy of phonons available provided there exists no other scattering mechanism. Another characteristic feature of strong coupling effects in the infrared conductivity is the Holstein processes, *i.e.*, the processes with absorption through the combined excitation of a particle-hole pair and a phonon mode or other low lying modes. The Holstein processes contain the information about the coupling between electrons and other low lying excitations and appear in the conductivity as fine structures which are absent in the results of BCS theory.

Based on Eliashberg theory, two formulas for the infrared conductivity with arbitrary impurity concentration have been derived. One starts on the imaginary axis [Bickers, *et al.* (1990)] and then analytically continues to the real frequency axis, and the other starts directly on the real frequency axis [Nam (1967a,b); Lee, Rainer and Zimmermann (1989)]. Here we will write down both formulas modified to including anisotropy only. References [Bickers, *et al.* (1990); Nam (1967a,b); Lee, Rainer and Zimmermann (1989)] should be consulted for details of the derivation of these formulas for an isotropic case.

Following Bickers *et al.* (1990), the infrared conductivity is related to the real frequency axis analytic continuation of the current-current correlation function $\Pi(i\nu_n)$, in general a three by three tensor, as

$$\sigma_{jk}(\omega) = \frac{i}{\omega}\Pi_{jk}(i\nu_n \rightarrow \omega + i0^+). \tag{5.3.3}$$

The function $\Pi_{jk}(i\nu_n)$ is given in terms of Green's functions as

$$\Pi_{jk}(i\nu_n) = \frac{2T}{N}\sum_{m,\vec{p}} Tr\{ev_j(\vec{p})\mathbf{G}(\mathbf{p}, i\nu_n + i\omega_m)\mathbf{G}(\mathbf{p}, i\omega_m)ev_k(\vec{p})\} \tag{5.3.4}$$

where Tr is the trace, e is the electron charge, v_j is the Fermi velocity in the j-direction of the momentum space and T is temperature. The vertex correction is taken to the lowest order. Since the Green's function of quasiparticles in the superconducting state $\mathbf{G}(\mathbf{p}, i\omega_m)$ is given by [Schrieffer (1964)] (here τ_i is the Pauli matrix given by formula (3.3.4))

$$\mathbf{G}_s(\mathbf{p}, i\omega_m) = \frac{\tilde{\omega}_{\vec{p}}(i\omega_m)\tau_0 + \epsilon_{\vec{p}}\tau_3 + \tilde{\Delta}_{\vec{p}}(i\omega_m)\tau_1}{\tilde{\omega}^2_{\vec{p}}(i\omega_m) - \epsilon^2_{\vec{p}} - \tilde{\Delta}^2_{\vec{p}}(i\omega_m)}, \tag{5.3.5}$$

one can work out, after some algebra, $\Pi_{jk}(i\nu_n)$ in terms of the pairing potential $\tilde{\Delta}_{\vec{p}}(i\omega_n)$ and renormalized frequency $\tilde{\omega}_{\vec{p}}(i\omega_n)$,

$$\Pi_{jk}(i\nu_n) = \langle 2e^2N(0)v_j(\vec{p})v_k(\vec{p})\pi T\sum_m S_{\vec{p}}(m,n)\rangle \tag{5.3.6}$$

with $\langle\rangle$ the Fermi surface average (see (4.2.7)), $N(0)$ the quasiparticle density of states at Fermi level, and

$$S_{\vec{p}}(m,n) = \frac{\tilde{\omega}_{\vec{p}}(i\omega_m)(\tilde{\omega}_{\vec{p}}(i\omega_m) + \tilde{\omega}_{\vec{p}}(i\omega_{m+n})) + \tilde{\Delta}_{\vec{p}}(i\omega_m)(\tilde{\Delta}_{\vec{p}}(i\omega_m) - \tilde{\Delta}_{\vec{p}}(i\omega_{m+n}))}{R_{\vec{p}}(m)P_{\vec{p}}(m,n)}$$
$$- \frac{\tilde{\omega}_{\vec{p}}(i\omega_{m+n})(\tilde{\omega}_{\vec{p}}(i\omega_{m+n}) + \tilde{\omega}_{\vec{p}}(i\omega_m)) + \tilde{\Delta}_{\vec{p}}(i\omega_{m+n})(\tilde{\Delta}_{\vec{p}}(i\omega_{m+n}) - \tilde{\Delta}_{\vec{p}}(i\omega_m))}{R_{\vec{p}}(m+n)P_{\vec{p}}(m,n)},$$
$$\text{for } (n \neq 0, -2n-1),$$

$$= \tilde{\Delta}_{\vec{p}}(i\omega_m)^2/R_{\vec{p}}(m)^3, \qquad \text{for } (n=0),$$
$$= 1/R_{\vec{p}}(m). \qquad \text{for } (m=-2n-1). \tag{5.3.7}$$

Here, $R_{\vec{p}}(m) = \sqrt{\tilde{\omega}^2_{\vec{p}}(i\omega_m) + \tilde{\Delta}^2_{\vec{p}}(i\omega_m)}$ and $P_{\vec{p}}(m,n) = \tilde{\omega}^2_{\vec{p}}(i\omega_m) - \tilde{\omega}^2_{\vec{p}}(i\omega_{m+n}) + \tilde{\Delta}^2_{\vec{p}}(i\omega_m) - \tilde{\Delta}^2_{\vec{p}}(i\omega_{m+n})$. The effect of impurities on $\Pi_{jk}(i\nu_n)$ comes from $\tilde{\omega}_{\vec{p}}(i\omega_m)$ and $\tilde{\Delta}_{\vec{p}}(i\omega_m)$ which are calculated from the Eliashberg equations given in Eqs. (2.3.8)-(2.3.9).

Formula (5.3.7) can be further deduced for the Fermi surface average as we did in section 4.2 ((4.2.7)-(4.2.10)). The off-diagonal term with $j \neq k$ vanishes and the diagonal term is

$$\Pi_{jj}(i\nu_n) = 2e^2N(0)\pi T \int_{-\frac{\pi}{c}}^{\frac{\pi}{c}} \frac{cdp_z}{2\pi} v_j^2 \sum_m S_{\vec{p}}(m,n) \tag{5.3.6a}$$

with

$$v_x^2 = v_y^2 = \frac{\epsilon_F}{m^*}[1 - \frac{\mu}{\epsilon_F}(1 + cos(p_z c))] \quad \text{and} \quad v_z^2 = \mu^2 c^2 sin^2(p_z). \tag{5.3.8}$$

A formula for the conductivity written directly on the real frequency axis has been derived in a similar way [Lee, Rainer and Zimmermann (1989)]. It starts with the real frequency formalism of the current-current correlation function $\Pi(\omega + i\delta)$ which is given in terms of Green's function:

$$\Pi_{jk}(\omega+i\delta) = \Big\langle 2e^2N(0)v_j(\vec{p})v_k(\vec{p})Tr\Big\{\int d\epsilon \int d\Omega f(\Omega)\frac{-1}{\pi}Im\mathbf{G}_s(\mathbf{p},\Omega+i\delta)\times \Big[\mathbf{G}_s(\mathbf{p},\Omega+\omega+i\delta)+\mathbf{G}_s(\mathbf{p},\Omega-\omega-i\delta)\Big]\Big\}\Big\rangle \tag{5.3.9}$$

with f the usual Fermi function and the Green's function (see formula (3.3.3))

$$\mathbf{G}_s(\mathbf{p},\omega+i\delta) = \frac{\tilde{\omega}_{\vec{p}}(\omega+i\delta)\tau_0+\epsilon_{\vec{p}}\tau_3+\tilde{\Delta}_{\vec{p}}(\omega+i\delta)\tau_1}{\tilde{\omega}^2_{\vec{p}}(\omega+i\delta)-\epsilon^2_{\vec{p}}-\tilde{\Delta}^2_{\vec{p}}(\omega+i\delta)}. \tag{5.3.10}$$

All other quantities in formula (5.3.9) are defined the same as in formula (5.3.4). The final form of the conductivity can be written as

$$\begin{aligned}\sigma_{jj}(\omega) &= \frac{i}{\omega}\Pi_{jj}(\omega+i\delta) = \\ &\Big\langle \frac{e^2N(0)v_j^2}{\omega}\Big\{\int_0^\infty d\Omega tanh(\frac{\Omega}{2T})\frac{i}{E(\Omega)+E(\Omega+\omega)}\Big[1-N(\Omega)N(\Omega+\omega)-P(\Omega)P(\Omega+\omega)\Big] \\ &+\int_0^\infty d\Omega tanh(\frac{\Omega+\omega}{2T})\frac{i}{E^\dagger(\Omega)+E^\dagger(\Omega+\omega)}\Big[1-N^\dagger(\Omega)N^\dagger(\Omega+\omega)-P^\dagger(\Omega)P^\dagger(\Omega+\omega)\Big] \\ &+\int_0^\infty d\Omega\Big[tanh(\frac{\Omega+\omega}{2T})-tanh(\frac{\Omega}{2T})\Big]\frac{i}{E(\Omega+\omega)-E^\dagger(\Omega)}\Big[1+N^\dagger(\Omega)N(\Omega+\omega)+P^\dagger(\Omega)P(\Omega+\omega)\Big] \\ &+\int_{-\omega}^0 d\Omega tanh(\frac{\Omega+\omega}{2T})\Big(\frac{i}{E^\dagger(\Omega)+E^\dagger(\Omega+\omega)}\Big[1-N^\dagger(\Omega)N^\dagger(\Omega+\omega)-P^\dagger(\Omega)P^\dagger(\Omega+\omega)\Big] \\ &\qquad +\frac{i}{E(\Omega+\omega)-E^\dagger(\Omega)}\Big[1+N^\dagger(\Omega)N(\Omega+\omega)+P^\dagger(\Omega)P(\Omega+\omega)\Big]\Big)\Big\}\Big\rangle\end{aligned} \tag{5.3.11}$$

with

$$E(\omega)=\sqrt{\tilde{\omega}^2_{\vec{p}}(\omega)-\tilde{\Delta}^2_{\vec{p}}(\omega)},\quad N(\omega)=\frac{\tilde{\omega}_{\vec{p}}(\omega)}{\sqrt{\tilde{\omega}^2_{\vec{p}}(\omega)-\tilde{\Delta}^2_{\vec{p}}(\omega)}},\quad \text{and}\quad P(\omega)=\frac{\tilde{\Delta}_{\vec{p}}(\omega)}{\sqrt{\tilde{\omega}^2_{\vec{p}}(\omega)-\tilde{\Delta}^2_{\vec{p}}(\omega)}}. \tag{5.3.12}$$

Here, $\tilde{\omega}_{\vec{p}}(\omega)$ and $\tilde{\Delta}_{\vec{p}}(\omega)$ are the solutions of Eliashberg equations on the real frequency axis, Eqs. (2.3.10)-(2.3.11). The term $\sigma_{jk}(\omega)$ with $j \neq k$ is zero and v_j is given in (5.3.8). The symbol † in formula (5.3.11) represents the complex conjugate of that quantity. A very useful relation is $E(-\omega) = -E^{\dagger}(\omega)$.

It is worth noting that formula (5.3.11) can be reduced to formula (5.3.1) under the BCS and dirty limit. In BCS theory the frequency renormalization is neglected ($\tilde{\omega} = \omega$). While in the dirty limit there will be no anisotropy as we discussed before (see section 2.2) and $E(\omega) \simeq i/2\tau$ with $\tau \to 0$. The last equality comes from the relation in an isotropic case:

$$E(\omega) = \sqrt{\tilde{\omega}_d^2(\omega) - \tilde{\Delta}_d^2(\omega)} = \sqrt{\tilde{\omega}_c^2(\omega) - \tilde{\Delta}_c^2(\omega)} + \frac{i}{2\tau} \tag{5.3.13}$$

where subscripts d and c stand for with and without impurities, respectively. One can also get the well known Drude conductivity for electrons in the normal state from formula (5.3.11) by setting the pairing potential $\tilde{\Delta} = 0$ and the renormalized frequency $\tilde{\omega} = \omega$ which is

$$\sigma(\omega) = \frac{\omega_p^2}{4\pi} \frac{\tau}{1 - i\omega\tau}. \tag{5.3.14}$$

Here, we have used the relation (5.1.13) and the plasma frequency ω_p has been defined as $\omega_p^2/4\pi = ne^2/m \simeq 2e^2N(0)v^2$.

The imaginary axis formulation of the conductivity, Eqs. (5.3.5)-(5.3.8), is numerically much faster to evaluate on a computer than the real axis formulation, Eqs. (5.3.11)-(5.3.12), although the Padé approximates is

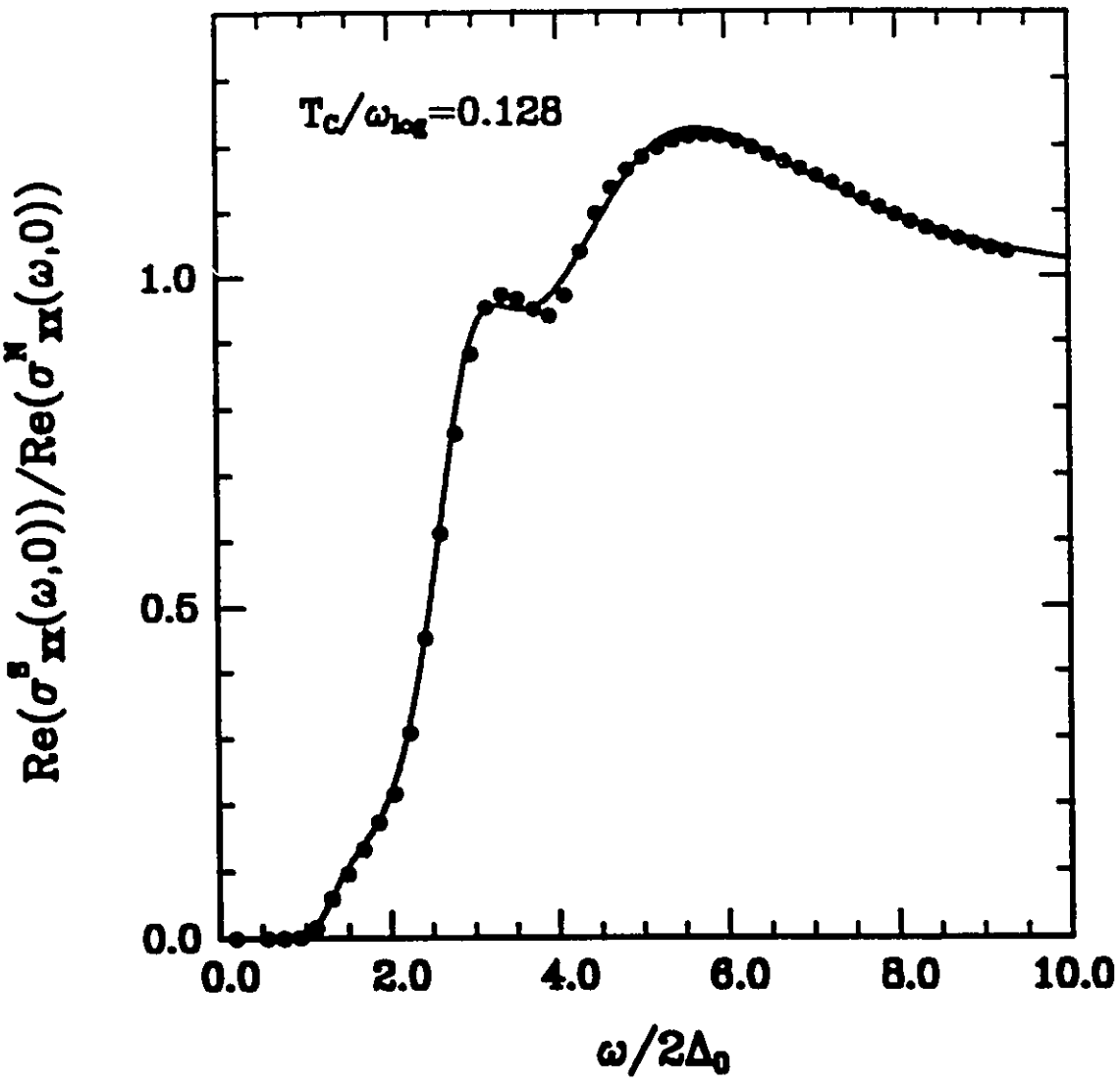

Fig. 5.3.1) The normalized ratio $Re(\sigma^S_{xx}(\omega,0))/Re(\sigma^N_{xx}(\omega,0))$ as a function of normalized frequency $\omega/2\Delta_0$ at zero temperature for the clean limit and intermediate coupling ($T_c/\omega_{log} = 0.128$). The anisotropic parameter g_{10} equals 0.5 and Δ_0 is the energy gap at $0K$ for the isotropic case with same coupling strength. The solid curve was obtained using the imaginary frequency axis formulation, Eqs. (5.3.5)-(5.3.8), with analytic continuation. The solid dots shown for comparison are the results of the real frequency axis formulation, Eqs. (5.3.11)-(5.3.12).

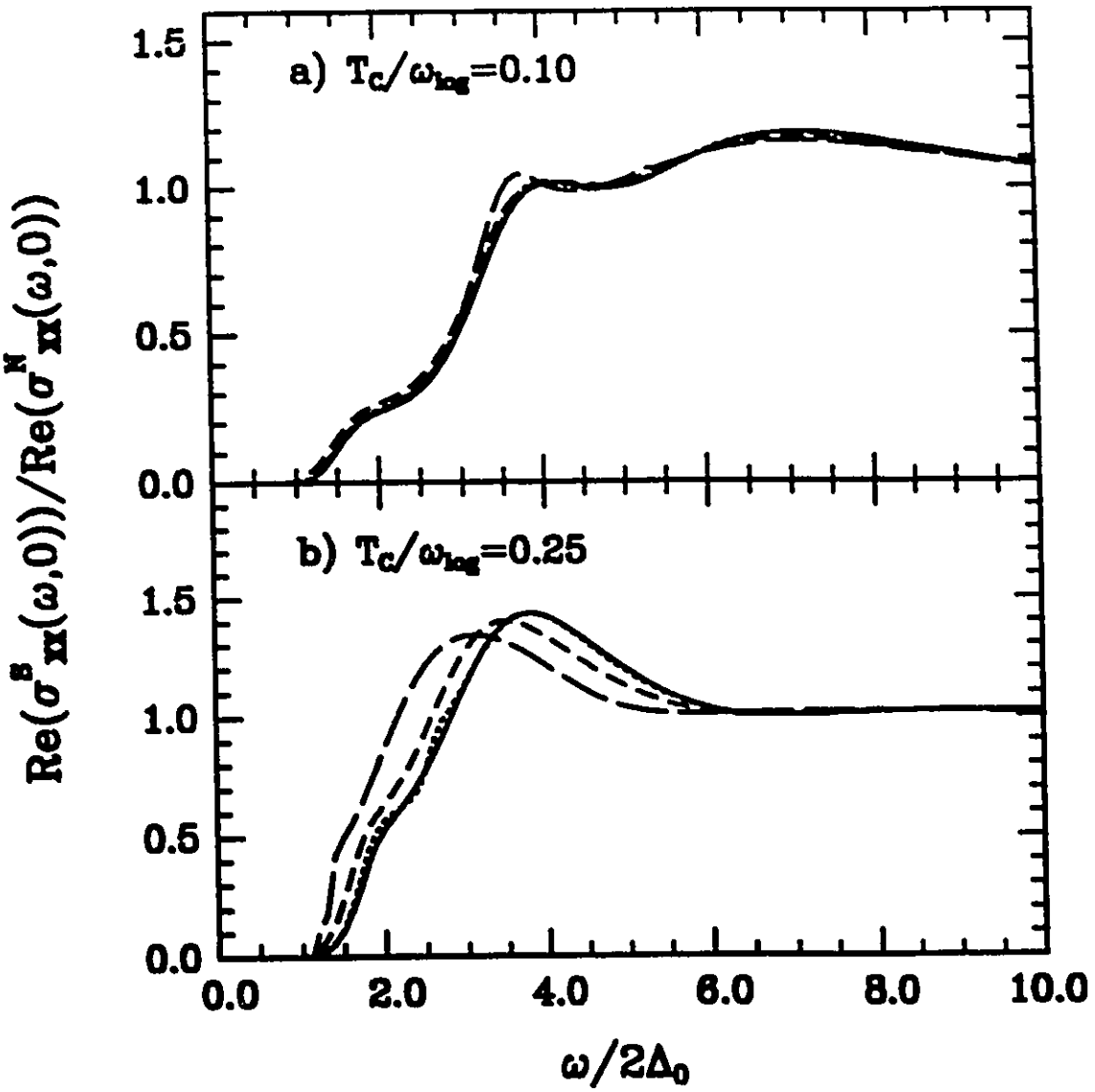

Fig. 5.3.2) The normalized ratio $Re(\sigma^S_{xx}(\omega,0))/Re(\sigma^N_{xx}(\omega,0))$ at $T = 0K$ in the clean limit as a function of normalized frequency $\omega/2\Delta_0$ with Δ_0 the isotropic energy gap value for various anisotropy values, namely, $g_{10} = 0.0$ (solid curve) isotropic case, 0.2 (dotted curve), 0.5 (short-dashed curve), and finally 0.8 (long-dashed curve). The top frame is for intermediate coupling ($T_c/\omega_{log} = 0.1$), compared with strong coupling in the bottom frame ($T_c/\omega_{log} = 0.25$).

not reliable at high temperature $T \sim T_c$ (see the discussion in section 2.2). At low temperature $T \sim 0K$, however, the imaginary axis formulation and the real frequency axis formulation will yield almost identical results. In Fig. 5.3.1 we plot the normalized ratio of the real part of the conductivity $Re(\sigma^S_{xx}(\omega,0))/Re(\sigma^N_{xx}(\omega,0))$ at $T = 0K$ as a function of normalized frequency $\omega/2\Delta_0$ with Δ_0 the corresponding energy gap in the isotropic case. Here, we used $T_c/\omega_{log} = 0.128$ (intermediate coupling), $g_{10} = 0.5$ and $g_{20} = 0.0$ (moderate anisotropy), $\mu/E_F = 0.1$ for v_x (same as before), and $\tau \rightarrow \infty$ (the clean limit). The solid curve is the results from formula (5.1.5) and the solid dots are the results from formula (5.3.11). Two sets of data are identical except for some small deviations around $\omega/2\Delta_0 = 4.0$. As to the effect of anisotropy on the infrared conductivity, it will be sufficient to show the results at zero temperature only. At high temperature $T \sim T_c$ the thermal excitations will reduce the effectiveness of anisotropy. From the discussion above (Fig. 5.3.1) we will use the imaginary axis formulation of the conductivity for our studies hereafter.

In Fig 5.3.2 the normalized ratio $Re(\sigma^S_{xx}(\omega,0))/Re(\sigma^N_{xx}(\omega,0))$ at $T = 0K$ in the clean limit is plotted as a function of normalized frequency $\omega/2\Delta_0$ with Δ_0 the energy gap in the isotropic case for various anisotropies, namely $g_{10} = 0.0$ (solid curve) isotropic case for comparison, $g_{10} = 0.2$ (dotted curve), $g_{10} = 0.5$ (short-dashed curve), $g_{10} = 0.8$ (long-dashed curve). The top frame is for intermediate coupling ($T_c/\omega_{log} = 0.1$), which is to be compared with strong coupling in the bottom frame ($T_c/\omega_{log} = 0.25$). We see that the conductivity curves in both frames shift towards lower frequency as the anisotropy is increased. This is expected since the gap minimum is decreasing when the anisotropic parameter g_{10} is increased (see Fig. 3.3.2 where the quasiparticle

density of states is plotted). The effect of the anisotropy even for a quite large anisotropic value ($g_{10} = 0.8$) is, however, not very significant at least for the cases we showed here. If one looks at the BCS formula for the conductivity (5.3.1) and disregards the dirty limit restriction [Clem (1966)], which will be in contrast to any anisotropy (see section 2.2), one would expect the absorption to begin right at the minimum gap. This is hardly seen in Fig. 5.3.2. The main reason for this, we believe, is that we are in the clean limit. As we pointed out above, in the clean limit, the infrared absorption depends not only on the quasiparticle density of states but also the low energy excitations available because of the momentum conservation. For the $\alpha^2F(\omega)$ of Pb which we used the number of phonons with energy close to zero is very small. This makes the absorption increase very slowly at beginning in Fig. 5.3.2 compared with a sharp increase which the BCS dirty limit formula (5.3.1) would predict. The absorption in Fig. 5.3.2 is too small to see an onset precision. To avoid this difficulty and retain the anisotropic effect we introduce a small amount of normal impurities ($t^+ = 0.1meV$) into the system. We would like to see a relatively sharp onset of the absorption with sufficient anisotropy. The results are shown in Fig. 5.3.3 where the curves have a one to one correspondence to the curves in Fig. 5.3.2 except now $t^+ = 0.1meV$ is used here instead of $t^+ = 0.0meV$. Now we see a relatively sharp onset of absorption which starts at a lower energy with increasing anisotropy. This is just what we expect since now the extra momentum from particle-hole excitations will be balanced through elastic scattering with normal impurities instead of phonons in the clean limit.

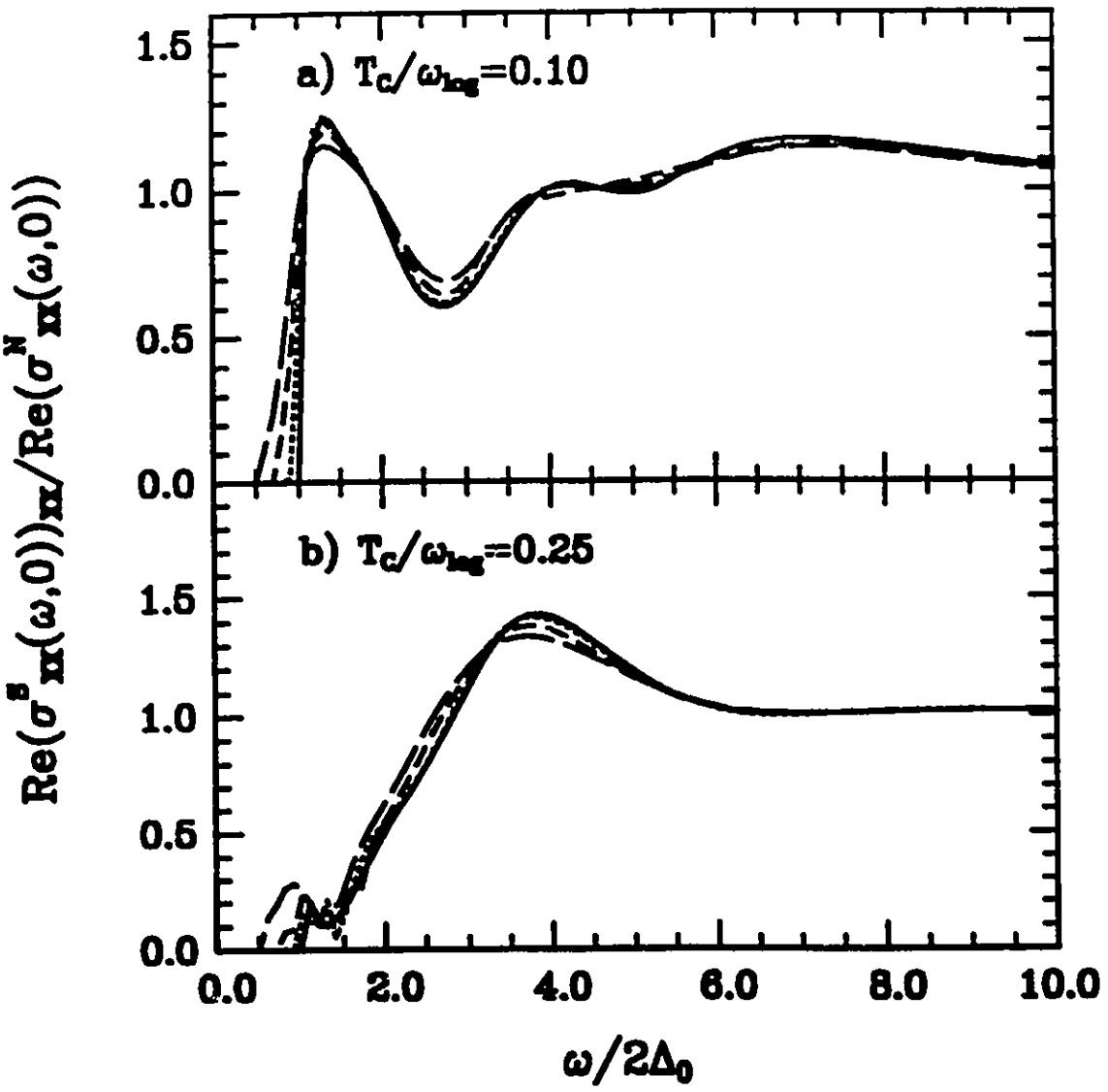

Fig. 5.3.3) The normalized ratio $Re(\sigma^S_{xx}(\omega,0))/Re(\sigma^N_{xx}(\omega,0))$ at $T = 0K$ as a function of normalized frequency $\omega/2\Delta_0$ with Δ_0 the isotropic energy gap value for various anisotropy values, namely, $g_{10} = 0.0$ (solid curve) isotropic case, 0.2 (dotted curve), 0.5 (short-dashed curve), and finally 0.8 (long-dashed curve). The normal impurity concentration $t^+ = 0.1meV$ The top frame is for intermediate coupling ($T_c/\omega_{log} = 0.1$), compared with strong coupling in the bottom frame ($T_c/\omega_{log} = 0.25$).

Last, we would like to show how the anisotropy effect decreases with increasing normal impurity concentration. In Fig. 5.3.4 we plot the normalized ratio $Re(\sigma_{xx}^S(\omega,0))/Re(\sigma_{xx}^N(\omega,0))$ as a function of normalized frequency $\omega/2\Delta_0$ for various normal impurity concentrations with $T_c/\omega_{log} = 0.1$ (intermediate coupling) and $g_{10} = 0.5$ (substantial anisotropy). The solid curve is for the clean limit ($t^+ = 0.0meV$), the dotted curve is for $t^+ = 0.1meV$, the short-dashed is for $t^+ = 0.5meV$ and the long-dashed curve is for $t^+ = 1.0meV$. It is evident that the effect of anisotropy on the infrared conductivity is diminished as the normal impurity concentration t^+ increases. It is totally washed out when the normal impurity concentration is $t^+ = 1.0meV$. The onset of absorption in the long-dashed curve, corresponding to $t^+ = 1.0meV$, starts right at $2\Delta_0$ twice the value of the energy gap for the isotropic case. We should point out that the amount of normal impurity required to wash out completely the effect of anisotropy depends on the coupling strength. Higher impurity concentration are needed for stronger coupling. In the dirty limit ($t^+ \to \infty$), however, no anisotropy effect will be left.

It is clear from the results shown in Figs. (5.3.2)-(5.3.4) that the absorption edge in the infrared conductivity will move towards lower energy with introducing anisotropy, as the gap minimum is lowered. It is hardly visible, however, in the clean limit and becomes more evident with the additional of a small amount of normal impurities. On the other hand, anisotropy effects will be washed out quickly as the normal impurity concentration is increased. All the results showed here are for the xx component of the infrared conductivity. The effect of planar anisotropy on the zz component of the conductivity are quite similar in our model which implies coherent motion of the quasiparticles in the z-direction. We should point out that for

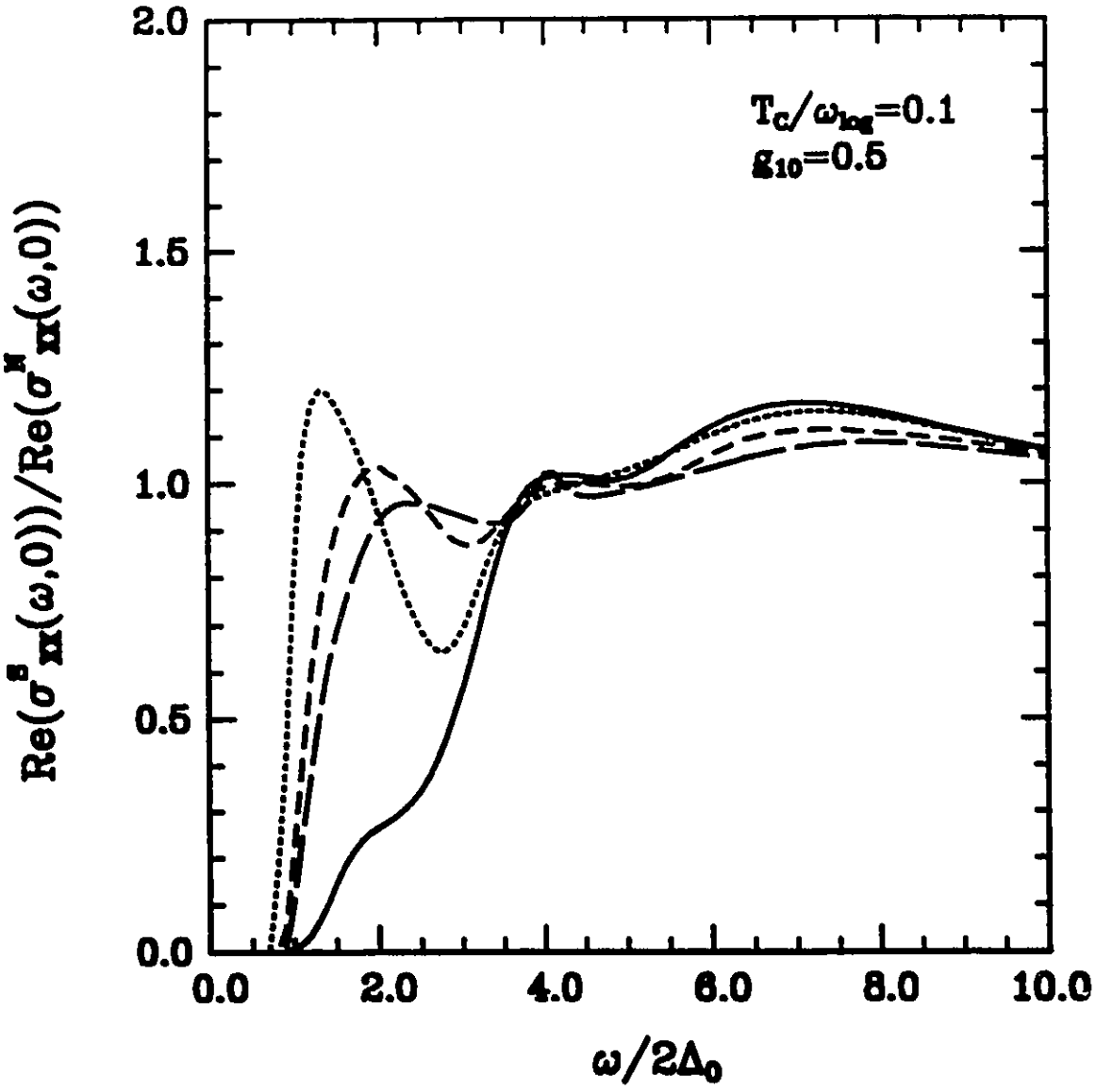

Fig. 5.3.4) The normalized ratio $Re(\sigma^S_{xx}(\omega,0))/Re(\sigma^N_{xx}(\omega,0))$ at $T = 0K$ as a function of normalized frequency $\omega/2\Delta_0$ for different values of normal impurity concentration, namely $t^+ = 0.0$ (solid curve) the clean limit, $t^+ = 0.1meV$ (dotted curve), $t^+ = 0.5meV$ (short-dashed curve) and $t^+ = 1.0meV$ (long-dashed curve). The coupling index $T_c/\omega_{log} = 0.1$, the anisotropy index $g_{10} = 0.5$ and Δ_0 is the energy gap for the isotropic case with same coupling index.

the high-T_c oxide superconductors the conductivity along the z-direction is semiconductor-like and is believed to be incoherent. Also, the Holstein structure appearing in all the above figures has not been observed in the high-T_c oxide superconductors. The Holstein structure and some other features of the infrared conductivity, *e.g.*, the temperature dependence in the normal state, depends strongly on the electron-boson spectrum density $\alpha^2F(\omega)$ used. In the case of high-T_c oxide superconductors the Pb spectrum density $\alpha^2F(\omega)$ which we used is very unlikely to be appropriate. Phenomenological spectrum densities based on some electronic mechanisms has been proposed [Varma (1989); Varma *et al.* (1990)] to describe the unusual normal state conductivity (linear dependence on temperature $\sigma \sim T$) as well as the absence of the Holstein structure of the high-T_c oxide superconductors. It is beyond the scope of this thesis to discuss these problems in details.

5.4 CONCLUSIONS

Using the anisotropic Eliashberg equations we have studied the effect of planar anisotropy on several electromagnetic properties in a self-consistent way. For London penetration depth $[\Lambda^L(0)/\Lambda^L(t)]^2$ introducing anisotropy usually lowers the results below its isotropic curve. The effect is stronger for a weaker coupling and in the z-direction perpendicular to the planes. For intermediate coupling ($T_c/\omega_{log} = 0.1$) the results we obtained are well below the results from two fluid model [Gorter and Casimir (1934a,b); Ginsburg and Landau (1950)]. In order to get results close to the two fluid model, which is favored in high-T_c oxide superconductors, a large coupling strength is needed $T_c/\omega_{log} = 0.3$. For a such strong coupling anisotropy is not very effective in both directions (parallel and perpendicular to the planes) at least within the

range of anisotropic parameters we have explored. More complicated models for the anisotropy may change quantitatively the results obtained but not qualitatively.

The effect of planar anisotropy on the Yosida function $Y(T)$ and the nuclear spin-lattice relaxation rate is quite significant too. Compared with an isotropic superconductor with the same coupling index, the layered anisotropy induces a larger $Y(T)$ at lower temperature and a strong depression of the Hebel-Slichter peak in the normalized ratio of nuclear spin-lattice relaxation rate R_s/R_n. Some effort was made to compare our theoretical results with experimental data in the high-T_c oxide superconductors by taking Fermi liquid corrections [Monien and Pines (1990)] into account. Good agreements were achieved for reasonable values of coupling, anisotropic and Fermi liquid correction parameters. It is found that a much larger value of the Fermi liquid correction parameter, which corresponds to a stronger antiferromagnetic instability, is needed for coppers in the planes than for those in the chains in $YBa_2Cu_3O_{7-x}$. This is in agreement with the picture of strong antiferromagnetic spin fluctuation in the planes for these compounds [Walstedt (1990); Pines (1990); Monien and Pines (1990)].

The layered anisotropy will also move the absorption edge in the infrared conductivity towards lower energy since the minimum energy gap in the electronic excitation spectrum is lowered as anisotropy is increased. For the spectrum density $\alpha^2F(\omega)$ of Pb which we used it is necessary, however, to add a small amount of normal impurities ($t^+ = 0.1meV$) to make this effect evident. In the clean limit ($t^+ = 0.0meV$) the absorption increases too smoothly to see clearly where it starts, but the effect of anisotropy will be washed out entirely if the normal impurity concentration is too high.

Chapter 6

The Phonon Self-Energy

Since the discovery of high-T_c oxide superconductors, the mechanism of superconductivity in these materials has remained an open question. Although it is generally acknowledged that the conventional phonon mediated pairing mechanism cannot be, at least alone, responsible for the superconductivity in these materials due to the very high transition temperature and the novel normal state properties, there is growing interest in knowing what part the phonons contribute to superconductivity in these materials. The changes of the phonon self-energy upon entering the superconducting state in the high-T_c oxide superconductors has been measured by many groups [Macfarlane, Rosen and Seki (1987); Cooper *et al.* (1988); Thomsen *et al.* (1988, 1990, 1991); Genzel *et al.* (1990); Friedl, Thomsen and Cardona (1990); Altendorf, Chrzanowski and Irwin (1991); McCarty *et al.* (1991)]. For several phonon modes quite large shifts in the frequency and changes in the width have been observed. Using the strong coupling theory of the phonon self-energy for an

isotropic superconductor [Zeyher and Zwicknagl (1988, 1990)], people have attempted to estimate the coupling strength between phonons and charge carriers and to extract an energy gap from the experimental data. In this chapter we will extend the theory by Zeyher and Zwicknagl (1988, 1990) to anisotropic superconductors. We would like to study the effects of strong coupling as well as planar anisotropy on the phonon self-energy. Our interest here is to see the changes that anisotropy may bring into the interpretation of the experimental data. The questions we would like to answer are: is it possible to tell the symmetry of the superconducting pairing from the phonon self-energy measurement? and how is the energy gap to be identified, if there is one, when anisotropy is present? In the next section we will discuss some background material associated with the phonon self-energy. A strong coupling formulation for the phonon self-energy with anisotropy will be given of section 6.2. In section 6.3 we will present the numerical results obtained using the formulas in section 6.2 and discuss the effects of strong coupling, anisotropy, *etc.* A qualitative comparison with some experimental data will also be made. We will conclude this chapter with a short conclusion in section 6.4.

6.1 INTRODUCTION

As we discussed at the beginning of this thesis (chapter 1 and 2), for most conventional superconductors, the phonon mediated attractive interaction between charge carries is the key to superconductivity [Carbotte (1990)]. Theoretically, stronger coupling between phonons and charge carriers is related to higher superconducting transition temperature T_c and larger energy gap Δ [Allen and Dynes (1975)]. On the other hand, the coupling between

phonons and charge carriers will affect the phonon spectrum as well. The shift in phonon frequencies and the change in phonon widths are expected to result upon entering the superconducting state since the charge carriers are condensed into a new ground state, the Cooper pair state.

The phonon spectrum can be measured experimentally by inelastic neutron scattering, Raman scattering, *etc.* The general principles underlying these measurements are much the same. One measures the energy lost (or gain) and/or the change in angles of the incident particles (either neutrons or photons) while interacting with a crystal and view that as being due to the emission (or absorption) of phonons. The information one extracts from these measurements, however, is different. The difference is primarily a result of the very different energy-momentum relations of neutrons and photons [Ashcroft and Mermin (1976)]:

$$\text{Neutrons}: \quad E_n = \frac{p^2}{2M_n}$$
$$M_n = 1838.65 m_e = 1.67 \times 10^{-24}\text{gm}, \tag{6.1.1}$$

$$\text{Photons}: \quad E_\gamma = pc$$
$$c = 2.99792 \times 10^{10}\text{cm/sec}. \tag{6.1.2}$$

With inelastic neutron scattering one can measure the phonon spectrum over the whole Brillouin zone while Raman scattering gives information only about optical phonons in the immediate neighborhood of the origin of the

zone ($\vec{k} = 0$). For the investigation of low-frequency phonons, however, Raman scattering is more powerful since it has much higher resolution than inelastic neutron scattering [Thomsen and Cardona (1989)]. Low-frequency phonons are extremely important for most conventional superconductors.

In conventional superconductors the actual changes in the frequency and width of phonons due to superconductivity are usually very small. This is due to the fact that the phonon spectrum is determined by virtual electron-hole excitations over an energy range of many eV's whereas BCS theory tells us that superconductivity only affects electronic states in a region ($\sim \hbar\omega_D$) around the Fermi level with $\hbar\omega_D$ of the order of meV's. Thus, the changes of the phonon spectrum due to superconductivity for conventional superconductors will be only a few percent or less. Despite this, the changes of the phonon spectrum upon entering the superconducting state have been successfully measured in several conventional materials. Using inelastic neutron scattering Axe and Shirane (1973a,b) studied transverse-acoustic-phonon frequencies and linewidths in Nb_3Sn ($T_c = 18.3K$). They found a sharp decrease in linewidths for several phonon modes with frequencies less than 2Δ, where Δ is the energy gap, upon entering the superconducting state. For phonons with frequencies larger than 2Δ the linewidths increased as zero temperature was approached. These behaviors come from the fact that phonons with energy less than 2Δ are energetically incapable of decaying by excitation of electron-hole pairs whereas phonons with energy larger than 2Δ will decay more rapidly through breaking electron-hole pairs. Thus, the changes in phonon linewidths can be used to determine the energy gap. From the measurements by Axe and Shirane (1973a,b) the energy gap in Nb_3Sn at zero

temperature was estimated at $2\Delta(0) = (4.4 \pm 0.6)k_B T_c$. This is fairly consistent with the values of the gap obtained from other means [Shen (1972); Bosomworth and Cullen (1967)]. Similar measurements were done on Nb ($T_c = 9.2K$) by Shirane *et al.* (1973) and Shapiro *et al.* (1975). The energy gap at zero temperature was estimated at $2\Delta = 3.9 \pm 0.1 k_B T_c$ which is also consistent with the measurements of the gap from other methods. We should point out that inelastic neutron scattering measurements are done along certain crystal directions. It will give different gap values for different directions if there is anisotropy. Measurements from other methods sometimes give only the averaged gap values. The observed changes in phonon linewidths for both Nb_3Sn and Nb were of the order of 10 percent. As for the shifts of phonon frequencies, a lowering of frequency (softening) for several phonons was detected. The softening was typically of the order of 1 percent. Interestingly, the softenings were observed for phonons with energies both above and below 2Δ.

The situation is quite different in the case of high-T_c oxide superconductors. Due to the low concentration of charge carriers and high transition temperature (T_c) quite large shifts in phonon frequencies and changes in phonon linewidths have been observed through Raman scattering measurements [Thomsen and Cardona (1989)]. The Raman active phonon modes $\sim$ 340 and $440cm^{-1}$ in $YBa_2Cu_3O_{7-x}$, for example, shift $\sim -8.0 \pm 0.5cm^{-1}$ (softening) and $\sim 4.0 \pm 0.5cm^{-1}$ (hardening) from $90K$ to $10K$, respectively [Thomsen *et al.* (1990)]. The linewidths of the two phonon modes also increases by $\sim$ 3.7 and $2.7cm^{-1}$ (broadening), respectively, at the same time [Friedl, Thomsen and Cardona (1990)]. As was the case for conventional superconductors Nb_3Sn and Nb, these experimental results have been used to

try to determine a value for the energy gap Δ as well as the electron-phonon coupling strength in $YBa_2Cu_3O_{7-x}$. The strong coupling theory of the phonon self-energy by Zeyher and Zwicknagl (1988, 1990) has been mostly used to fit the data. The resulting energy gap is quite large as the twice of the gap $2\Delta \sim 5k_BT_c$ or even bigger, where $T_c \sim 90K$. We should point out, however, that the problem of an energy gap in high-T_c oxide superconductors is still controversial, and even more so the size of the electron-phonon coupling.

In the next section, we will show the strong coupling formalism of the phonon self-energy on the imaginary axis first, following Zeyher and Zwicknagl (1988,1990). Then we will extend it to the real frequency axis. The real axis formalism is necessary for finite temperature calculations. BCS formulas for the phonon self-energy at zero temperature will also be given for instructiveness. All formulas include planar anisotropy. To study the effects of planar anisotropy on the phonon self-energy is the main purpose here.

6.2 FORMALISM

Following Zeyher and Zwicknagl (1988,1990) the phonon self-energy in Matsubara representation (imaginary axis), assuming a polarization bubble diagram with no vertex corrections, is given by

$$\Sigma_\lambda(\vec{q}, i\nu_n) = \frac{T}{N}\sum_{\vec{p}}\sum_{m} \mid g_\lambda(\vec{p}, \vec{p}+\vec{q}) \mid^2 Tr\{\tau_3 \mathbf{G}(\vec{p}+\vec{q}, i(\omega_m+\nu_n))\tau_3 \mathbf{G}(\vec{p}, i\omega_m)\} \tag{6.2.1}$$

where τ_3 is a Pauli matrix (see formula (3.3.4)), $\mathbf{G}(\vec{p}, i\omega_m)$ is the fully interacting Green's function, ω_m (ν_n) is the fermion (boson) Matsubara frequency and $g_\lambda(\vec{p}, \vec{p}+\vec{q})$ is the electron-phonon matrix element for scattering of an

electron from momentum $\vec{p}$ to $\vec{p}+\vec{q}$ with absorbing or emitting a phonon of momentum $\vec{q}$ and branch index λ. In Eliashberg theory the superconducting Green's function in Nambu formalism is given by [Schrieffer (1964)]

$$\mathbf{G}_s(\mathbf{p}, i\omega_m) = \frac{\tilde{\omega}_{\vec{p}}(i\omega_m)\tau_0 + \epsilon_{\vec{p}}\tau_3 + \bar{\Delta}_{\vec{p}}(i\omega_m)\tau_1}{\tilde{\omega}^2_{\vec{p}}(i\omega_m) - \epsilon^2_{\vec{p}} - \bar{\Delta}^2_{\vec{p}}(i\omega_m)}, \tag{6.2.2}$$

with τ_i the Pauli matrix (see 3.3.4). Quantities $\bar{\Delta}_{\vec{p}}(i\omega_m)$ and $\tilde{\omega}_{\vec{p}}(i\omega_m)$ are calculated from the Eliashberg equations, Eqs. (2.3.8) and (2.3.9). Substitution of Eq. (6.2.2) into Eq. (6.2.1) and taking the limit $\vec{q} \to 0$ gives

$$\Sigma^S_\lambda(i\nu_n) = 2\pi TN(0) \mid g_\lambda \mid^2 \Bigg\langle \sum_m \frac{\left[\sum_j \sum_k g_{jk} cos(jp_z c) cos(kp_z c)\right]^2}{\sqrt{\tilde{\omega}^2_{\vec{p}}(i\omega_m) + \bar{\Delta}^2_{\vec{p}}(i\omega_m)} + \sqrt{\tilde{\omega}^2_{\vec{p}}(i\omega_{m+n}) + \bar{\Delta}^2_{\vec{p}}(i\omega_{m+n})}} \times$$
$$\left\{1 - \frac{\tilde{\omega}_{\vec{p}}(i\omega_m)\tilde{\omega}_{\vec{p}}(i\omega_{m+n}) + \bar{\Delta}_{\vec{p}}(i\omega_m)\bar{\Delta}_{\vec{p}}(i\omega_{m+n})}{\sqrt{\tilde{\omega}^2_{\vec{p}}(i\omega_m) + \bar{\Delta}^2_{\vec{p}}(i\omega_m)}\sqrt{\tilde{\omega}^2_{\vec{p}}(i\omega_{m+n}) + \bar{\Delta}^2_{\vec{p}}(i\omega_{m+n})}}\right\}\Bigg\rangle. \tag{6.2.3}$$

Here we have converted the sum over $\vec{p}$ into an integral over energy and a Fermi surface average $\langle\rangle$ as we did before:

$$\sum_{\vec{p}} = \int d\epsilon N(\epsilon)\langle\rangle = \int d\epsilon N(\epsilon) \int_{-\frac{\pi}{c}}^{\frac{\pi}{c}} \frac{c\,dp_z}{2\pi} \int_0^{2\pi} \frac{d\varphi}{2\pi}. \tag{6.2.4}$$

The integral over energy ϵ has been carried out as usual. In Eq. (6.2.3) the angular dependent electron-phonon matrix $g_\lambda(\vec{p}, \vec{p}')$ has been expanded as

$$g_\lambda(\vec{p},\vec{p}\,') = g_\lambda \sum_j \sum_k g_{jk} cos(jp_z c) cos(kp_z{}'c), \tag{6.2.5}$$

the same as we did for the spectral density $(\alpha^2F(\omega))_{\vec{p}\vec{p}'}$. In the numerical calculations we will truncate the expansion series in (6.2.5) as we did in solving the Eliashberg equations for $\tilde{\Delta}_{\vec{p}}$ and $\tilde{\omega}_{\vec{p}}$ (see section 2.3).

The phonon self-energy in the normal state $\Sigma_\lambda^N(i\nu_n)$ can be obtained by setting the pairing potential $\tilde{\Delta}_{\vec{p}} = 0$ in Eq. (6.2.3). It is conventional to present the normalized phonon self-energy between the superconducting and normal state

$$\frac{\Delta\Pi(i\nu_n)}{N(0)} = \frac{\Delta\Sigma_\lambda(i\nu_n)}{|\,g_\lambda\,|^2\,N(0)} = \frac{\Sigma_\lambda^S(i\nu_n) - \Sigma_\lambda^N(i\nu_n)}{|\,g_\lambda\,|^2\,N(0)}. \tag{6.2.6}$$

Here, g_λ the averaged electron-phonon matrix element $\langle\langle g_\lambda(\vec{p}\vec{p}\,')\rangle\rangle'$, $N(0)$ is the electronic density of states at Fermi level and $\Pi(i\nu_n) = \Sigma_\lambda(i\nu_n)/|g_\lambda\,|^2$ is called the polarization. The quantity $\Delta\Pi(i\nu_n)/N(0)$ has very little dependence on the actual shape of the spectral density $\alpha^2F(\omega)$ [Akis (1991)], although the phonon self-energy strongly depends on the electron-phonon coupling of particular materials through the matrix element g_λ. For a general discussion it is convenient to calculate $\Delta\Pi(i\nu_n)/N(0)$ without having any particular material dependent parameters involved.

The imaginary axis quantity $\Delta\Pi(i\nu_n)/N(0)$ needs to be analytically continued to the real frequency axis ($i\nu_n \rightarrow \nu + i\delta$ with δ a positive infinitesimal). The real part of $\Delta\Pi(\nu + i\delta)/N(0)$ is proportional to the shift in phonon

frequencies and the imaginary part is proportional to the change in phonon widths due to the superconducting phase transition. The analytically continuation method (Padé approximates) is again only reliable at very low temperature ($T \sim 0K$). To calculate the phonon self-energy at finite temperature it is desirable to have a formula written directly on the real frequency axis with no Padé approximates involved. The way to achieve this is to use the spectral representation of the Green's function

$$\mathbf{G}(\vec{p}, i\omega_m) = \int_{-\infty}^{\infty} \frac{d\omega}{\pi} \frac{Im\{\mathbf{G}(\vec{p}, \omega + i\delta)\}}{i\omega_m - (\omega + i\delta)}. \tag{6.2.7}$$

The superconducting Green's function on the real frequency axis $\mathbf{G}_s(\vec{p}, \omega + i\delta)$ is given by

$$\mathbf{G}_s(\vec{p}, \omega + i\delta) = \frac{\tilde{\omega}_{\vec{p}}(\omega + i\delta)\tau_0 + \epsilon_{\vec{p}}\tau_3 + \tilde{\Delta}_{\vec{p}}(\omega + i\delta)\tau_1}{\tilde{\omega}^2_{\vec{p}}(\omega + i\delta) - \epsilon^2_{\vec{p}} - \tilde{\Delta}^2_{\vec{p}}(\omega + i\delta)}. \tag{6.2.8}$$

Substitution of Eq. (6.2.7), instead of Eq. (6.2.2), into Eq. (6.2.1) and taking the limit $\vec{q} \to 0$ yields [Akis (1991); Marsiglio, Akis and Carbotte (1992)]

$$\Sigma^S_\lambda(\nu + i\delta) = \frac{-1}{2\pi i} \sum_{\vec{p}} \mid g_\lambda(\vec{p}, \vec{p}) \mid^2 \int_{-\infty}^{\infty} d\omega f(\omega) Tr\Big\{\tau_3\Big[\mathbf{G}_s(\vec{p}, \omega + \nu + i\delta) + \mathbf{G}_s(\vec{p}, \omega - \nu - i\delta)\Big] \times \tau_3\Big[\mathbf{G}_s(\vec{p}, \omega + i\delta) - \mathbf{G}_s(\vec{p}, \omega - i\delta)\Big]\Big\}. \tag{6.2.9}$$

Here, we have done the sum over m and set $i\nu \rightarrow \nu + i\delta$, $f(\omega)$ is the usual Fermi function.

Eq. (6.2.9) can be further deduced by substituting Eqs. (6.2.5) and (6.2.8) into it and replacing the sum over $\vec{p}$ with an energy integral and a Fermi surface average as we did above (see Eq. (6.2.4)), and then carrying out the integral over energy. The final form of the phonon self-energy on the real frequency axis can be written as

$$
\begin{aligned}
\Sigma_\lambda^S(\nu+i\delta) &= \mid g_\lambda \mid^2 \Pi(\nu+i\delta) \\
&= \mid g_\lambda \mid^2 N(0)\left\langle\left[\sum_j\sum_k g_{jk}cos(jp_zc)cos(kp_zc)\right]^2\right. \\
&\times\left\{\int_0^\infty d\omega tanh(\frac{\omega}{2T})\frac{i}{E(\omega)+E(\omega+\nu)}\left[1-N(\omega)N(\omega+\nu)+P(\omega)P(\omega+\nu)\right]\right. \\
&+\int_0^\infty d\omega tanh(\frac{\omega+\nu}{2T})\frac{i}{E^\dagger(\omega)+E^\dagger(\omega+\nu)}\left[1-N^\dagger(\omega)N^\dagger(\omega+\nu)+P^\dagger(\omega)P^\dagger(\omega+\nu)\right] \\
&+\int_0^\infty d\omega\left[tanh(\frac{\omega+\nu}{2T})-tanh(\frac{\omega}{2T})\right]\frac{i}{E(\omega+\nu)-E^\dagger(\omega)}\left[1+N^\dagger(\omega)N(\omega+\nu)-P^\dagger(\omega)P(\omega+\nu)\right] \\
&+\int_{-\nu}^0 d\omega tanh(\frac{\omega+\nu}{2T})\left(\frac{i}{E^\dagger(\omega)+E^\dagger(\omega+\nu)}\left[1-N^\dagger(\omega)N^\dagger(\omega+\nu)+P^\dagger(\omega)P^\dagger(\omega+\nu)\right]\right. \\
&\left.\left.\left.+\frac{i}{E(\omega+\nu)-E^\dagger(\omega)}\left[1+N^\dagger(\omega)N(\omega+\nu)-P^\dagger(\omega)P(\omega+\nu)\right]\right)\right\}\right\rangle
\end{aligned}
\tag{6.2.10}
$$

with

$$
\begin{aligned}
E(\omega) &= \sqrt{\tilde{\omega}_{\vec{p}}^2(\omega)-\tilde{\Delta}_{\vec{p}}^2(\omega)}, \\
N(\omega) &= \frac{\tilde{\omega}_{\vec{p}}(\omega)}{\sqrt{\tilde{\omega}_{\vec{p}}^2(\omega)-\tilde{\Delta}_{\vec{p}}^2(\omega)}},
\end{aligned}
$$

and

$$P(\omega) = \frac{\tilde{\Delta}_{\vec{p}}(\omega)}{\sqrt{\tilde{\omega}^2_{\vec{p}}(\omega) - \tilde{\Delta}^2_{\vec{p}}(\omega)}}. \tag{6.2.11}$$

Here, quantities $\tilde{\omega}_{\vec{p}}(\omega)$ and $\tilde{\Delta}_{\vec{p}}(\omega)$ are the solutions of the real axis Eliashberg equations, Eqs. (2.3.10)-(2.3.11). The symbol † in formula (6.2.10) represents the complex conjugate. Some symmetric relations should also be mentioned:

$$\tilde{\omega}(-z) = -\tilde{\omega}(z), \qquad \tilde{\omega}^*(z) = \tilde{\omega}(z^*);$$

$$\tilde{\Delta}(-z) = \tilde{\Delta}(z), \qquad \tilde{\Delta}^*(z) = \tilde{\Delta}(z^*);$$

and

$$E(-\omega) = -E^{\dagger}(\omega). \tag{6.2.12}$$

Setting the pairing potential $\tilde{\Delta}_{\vec{p}}(\omega) = 0$ in Eq. (6.2.10) we will have the normal state phonon self-energy on the real frequency axis $\Sigma^N_\lambda(\nu + i\delta)$. Once again only the normalized difference between the superconducting and normal state

$$\frac{\Delta\Pi(\nu + i\delta)}{N(0)} = \frac{\Delta\Sigma_\lambda(\nu + i\delta)}{\mid g_\lambda \mid^2 N(0)} \tag{6.2.13}$$

will be of interest. The shift in phonon frequencies $\Delta\nu$ and the change in phonon widths $\Delta\gamma$ due to the superconducting phase transition are related to the polarization $\Pi(\nu + i\delta)$ as

$$\Delta\Sigma_\lambda(\nu+i\delta)=\Delta\nu-i\Delta\gamma=\mid g_\lambda(\nu)\mid^2\Delta\Pi(\nu+i\delta). \tag{6.2.14}$$

The electron-phonon matrix element $g_\lambda(\nu)$ is generally frequency dependent.

Both the imaginary and real axis formalism of the phonon self-energy, Eqs. (6.2.3) and (6.2.10), are quite complicated and need to be evaluated numerically. To have a look at some qualitative features, it will be interesting to take the BCS limit. In the BCS limit we neglect the frequency dependence of the energy gap $\tilde{\Delta}_{\vec{p}}(\omega)=\Delta_{\vec{p}}$ and the renormalization of frequencies $\tilde{\omega}_{\vec{p}}(\omega)=\omega$. At $T=0K$ Eq. (6.2.11) can be reduced to a much simpler form:

$$\frac{\Delta\Pi(\nu+i\delta)}{N(0)}=\begin{cases}\left\langle -\frac{2}{\sqrt{(1-\bar{v}_{\vec{p}}^2)\bar{v}_{\vec{p}}^2}}\tan^{-1}\sqrt{\frac{\bar{v}_{\vec{p}}^2}{(1-\bar{v}_{\vec{p}}^2)}}\right\rangle, & \text{if } \bar{v}_{\vec{p}}<1;\\ \left\langle \frac{1}{\sqrt{(\bar{v}_{\vec{p}}^2-1)\bar{v}_{\vec{p}}^2}}\left\{\ln\left(2\bar{v}_{\vec{p}}^2-1+\sqrt{\bar{v}_{\vec{p}}^2(\bar{v}_{\vec{p}}^2-1)}\right)-i\pi\right\}\right\rangle, & \text{if } \bar{v}_{\vec{p}}>1\ ;\end{cases} \tag{6.2.15}$$

where $\bar{v}_{\vec{p}}=\nu/2\Delta_{\vec{p}}$ and $\langle\rangle$ is the Fermi surface average. From Eq. (6.2.15) we can see a few things immediately. 1) For frequencies smaller than twice of the energy gap ($\nu<2\Delta_{\vec{p}}$) phonons will become soften ($\Delta\nu<0$) and there will be no changes in phonon widths (the imaginary part is zero). 2) For frequencies greater than twice of the energy gap ($\nu>2\Delta_{\vec{p}}$) phonons will become harden ($\Delta\nu>0$) and phonon widths will also become broaden ($\Delta\gamma\propto -Im(\Delta\Pi/N(0))>0$). Introducing strong coupling and finite temperature will bring in some smearing effects, but most of changes will be quantitative rather than qualitative. We will discuss these in some details in the next section. We would like to point out again that formulas (6.2.3), (6.2.10) and

(6.2.15) are derived in the limit $\vec{q} \to 0$. Things will be different for finite $\vec{q}$'s [Marsiglio (1992)]. It is beyoud the scope of this thesis to discuss any finite $\vec{q}$ effects.

6.3 NUMERICAL RESULTS AND DISCUSSIONS

In this section, we will use the formulas given in the previous section for the limit $\vec{q} \to 0$ to study the effects of strong coupling and planar anisotropy on the changes of phonon self-energy due to the superconducting phase transition. We would like to see the features that anisotropy could introduce that might be identified in experiment. All the results will be presented as the difference of the polarization function $\Pi(\omega)$ between the superconducting and normal states $\Delta\Pi(\omega)/N(0)$. As we pointed out above (see 6.2.14) the shift in phonon frequencies is proportional to $Re(\Delta\Pi(\omega)/N(0))$ (the real part) while the change in phonon widths is proportional to $Im(\Delta\Pi(\omega)/N(0))$ (the imaginary part).

We begin with the zero temperature results for isotropic superconductors with different coupling strengths. Similar results have been obtained by Zeyher and Zwicknagl (1990) using the imaginary axis formulation and by Akis (1991) and Marsiglio, Akis and Carbotte (1992) using the real axis formulation. Here, we show these results for comparison with both sets of previous results [Zeyher and Zwicknagl (1990); Akis (1991); Marsiglio, Akis and Carbotte (1992)] and with the results for anisotropic superconductors which we are going to show later. In Fig. 6.3.1 the quantity $\Delta\Pi(\omega)/N(0)$ is plotted as a function of normalized frequency $\omega/2\Delta$ for three coupling cases, namely the weak coupling BCS limit (solid curve), intermediate coupling with $T_c/\omega_{log} = 0.1$ (dotted curve) and strong coupling with $T_c/\omega_{log} = 0.25$

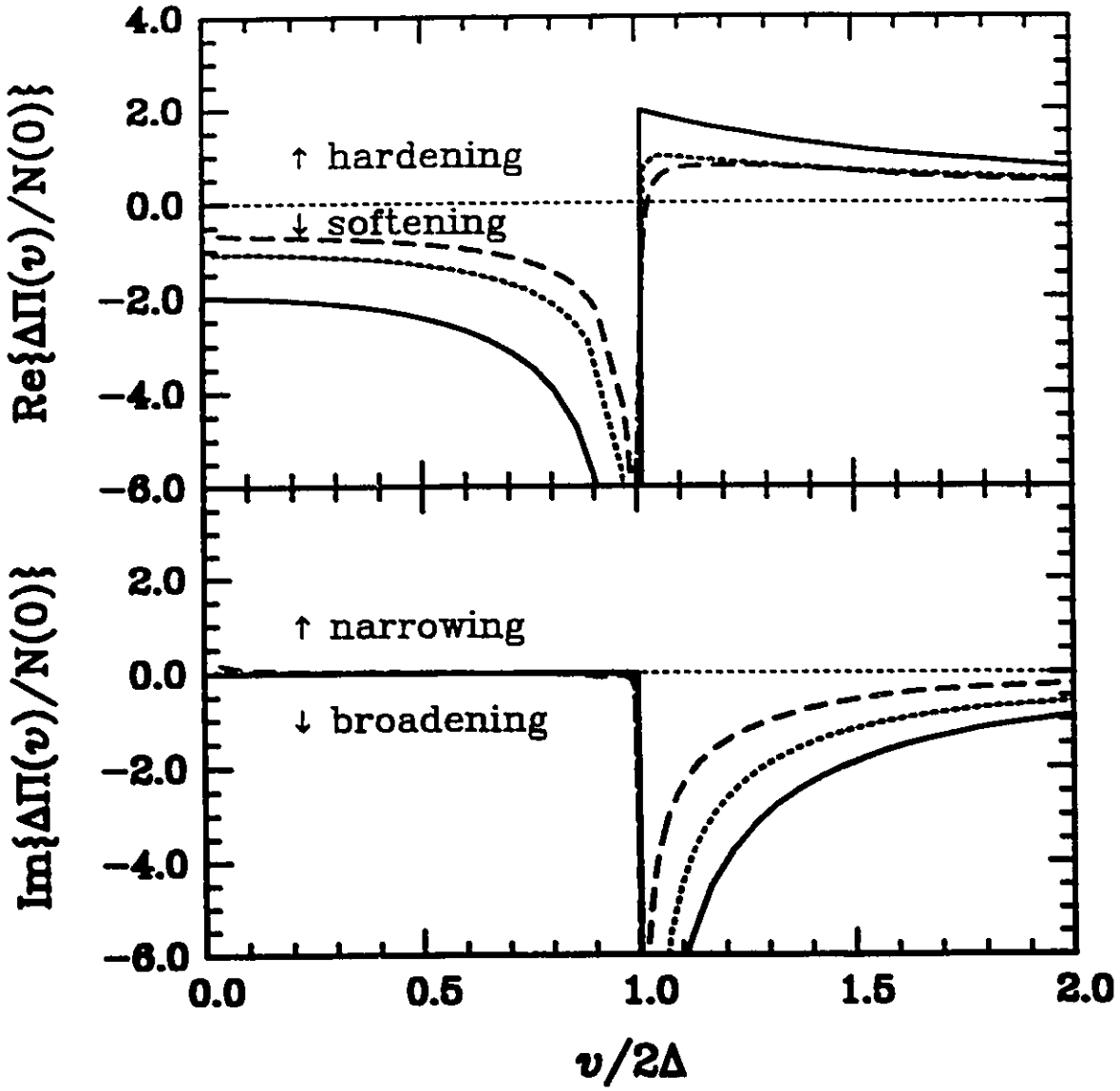

Fig. 6.3.1) The frequency dependence of $\Delta\Pi(\omega)/N(0)$ at zero temperature for isotropic superconductors with different coupling strengths: the weak coupling BCS limit (solid curve), intermediate coupling $T_c/\omega_{log} = 0.1$ (dotted curve), and strong coupling $T_c/\omega_{log} = 0.25$ (short-dashed curve). The top frame is the real part while the bottom is the imaginary part. Negative (positive) values correspond to softening (hardening) in the top frame and broadening (sharpening) in the bottom frame.

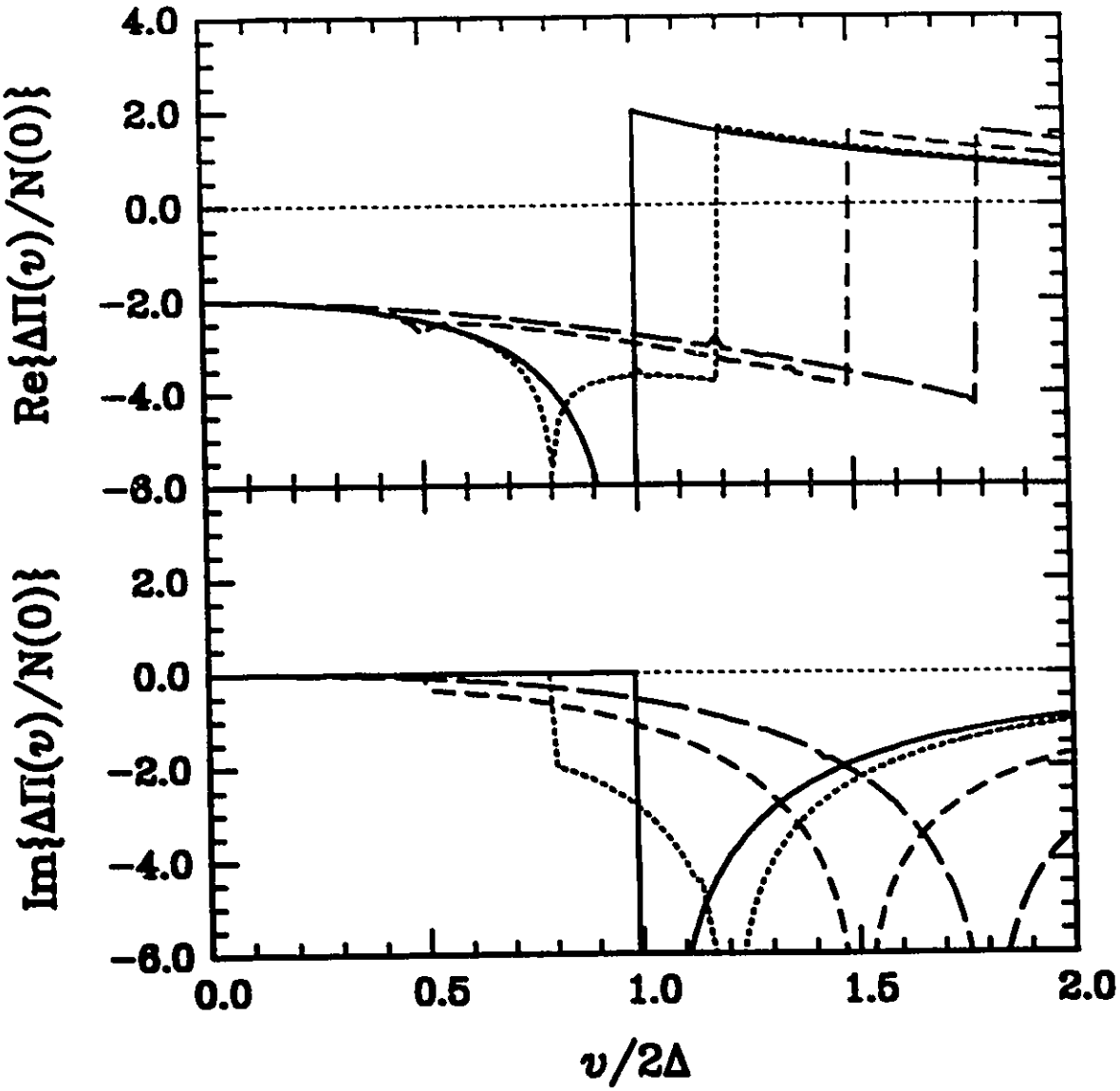

Fig. 6.3.2) The frequency dependence of $\Delta\Pi(\omega)/N(0)$ at zero temperature in the BCS limit for various anisotropic values, namely $\alpha = 0.0$ (solid curve) isotropic case for comparison, $\alpha = 0.2$ (dotted curve), $\alpha = 0.5$ (short-dashed curve), and $\alpha = 0.8$ (long-dashed curve). The anisotropy is introduced through an ansatz $\Delta_{\vec{p}} = \Delta(1+\alpha cos(p_z c))$, where Δ is the isotropic BCS energy gap, α is the anisotropic parameter and c is the lattice constant along the z-direction. The top frame is the real part and the bottom is the imaginary part.

(short-dashed curve). The top frame is the real part and the bottom frame is the imaginary part. First, we see that the BCS results (solid curve) has a singularity at $\omega/2\Delta = 1.0$ for both the real and imaginary part. This singularity is closely related to the singularity in the quasiparticle density of states under the same conditions (the BCS limit and $T = 0K$). Introducing strong coupling washes out the singularity in the phonon self-energy as well as in the quasiparticle density of states as we knew (see section 3.3). At low temperature ($T \sim 0K$), however, the smearing from strong coupling is not very significant as we see in the dotted curve for intermediate coupling ($T_c/\omega_{log} = 0.1$) and short-dashed curve for strong coupling ($T_c/\omega_{log} = 0.25$). The characteristic features for three coupling cases are essentially the same. For $\omega/2\Delta < 1.0$ we have softening, *i.e.*, phonons shift to lower frequencies ($\Delta\nu \propto Re\{\Delta\Pi/N(0)\} < 0$), and the same width ($\Delta\gamma \propto -Im\{\Delta\Pi/N(0)\} = 0$). For $\omega/2\Delta > 1.0$ we have hardening, *i.e.*, phonons shift to higher frequencies since $\Delta\nu > 0$, and broadening since $\Delta\gamma > 0$. The effect from strong coupling is to depress the sharp structures in the vicinity of $\nu = 2\Delta$. These results agree well with the results obtained by other people [Zeyher and Zwicknagl (1990); Akis (1991); Marsiglio, Akis and Carbotte (1992)].

Introducing anisotropy we will suppress the sharp peak (a singularity in the BCS limit) in the quasiparticle density of states as we have shown in section 3.3. Similar effects are seen in the phonon self-energy. In Fig 6.3.2 we plot the zero temperature results in the BCS limit for several anisotropic values. The anisotropy is introduced through the ansatz $\Delta_{\vec{p}} = \Delta(1+\alpha cos(k_z c))$ with Δ the isotropic BCS energy gap, α the anisotropic parameter and c the lattice constant in the z-direction. The solid curve here is for $\alpha = 0.0$ the isotropic case and is for comparison, the dotted curve is for $\alpha = 0.2$, the

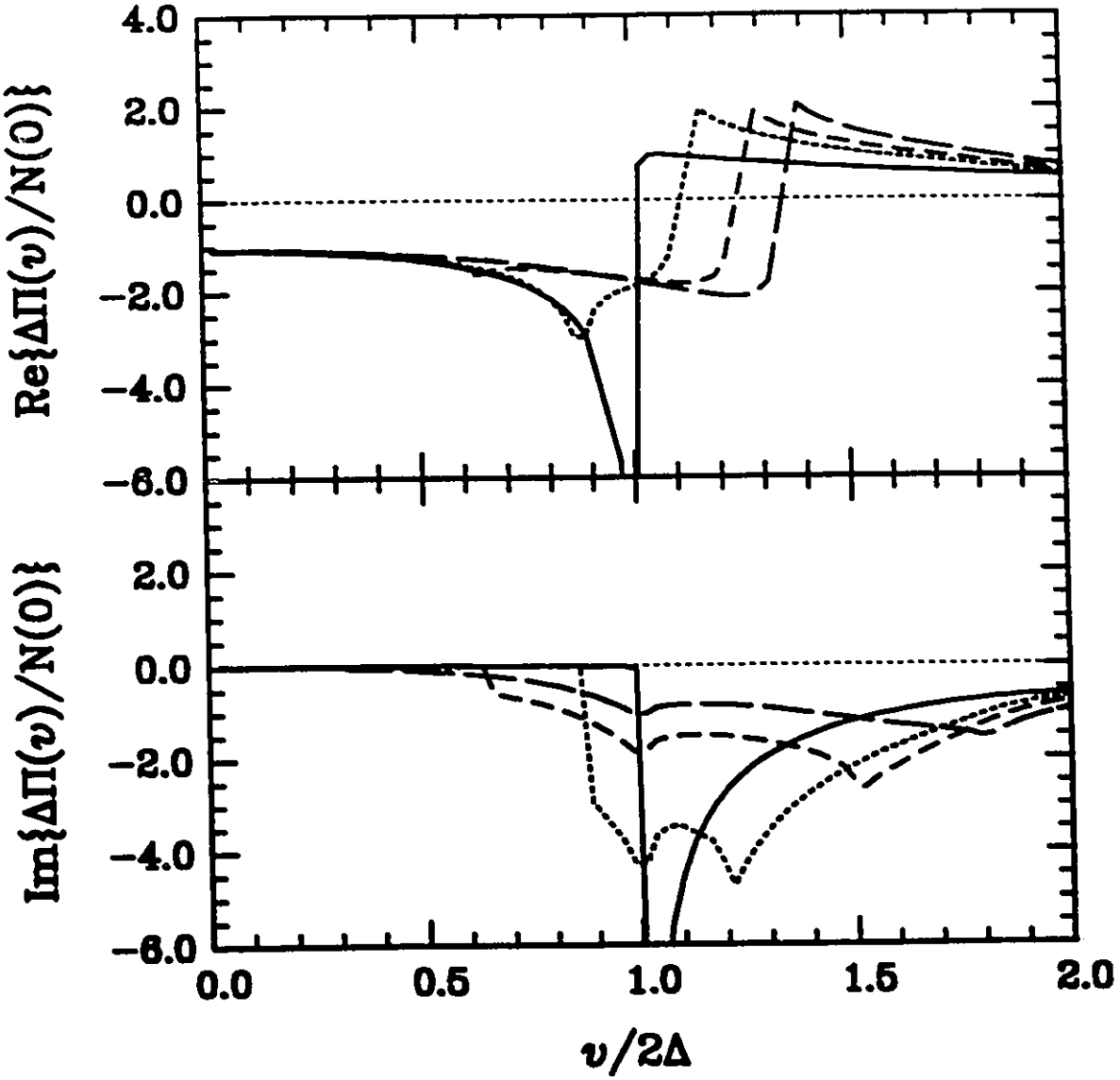

Fig. 6.3.3) The frequency dependence of $\Delta\Pi(\omega)/N(0)$ at low temperature ($t = T/T_c = 0.2$) for intermediate coupling ($T_c/\omega_{log} = 0.1$) and various anisotropic values, namely $g_{10} = 0.0$ (solid curve) isotropic case for comparison, $g_{10} = 0.2$ (dotted curve), $g_{10} = 0.5$ (short-dashed curve), and $g_{10} = 0.8$ (long-dashed curve). The anisotropic Eliashberg equations, Eqs. (2.3.10) and (2.3.11), have been solved for $\tilde{\Delta}_{\vec{p}}(\omega)$ and $\tilde{\omega}_{\vec{p}}(\omega)$. The top frame is the real part and the bottom is the imaginary part.

short-dashed curve is for $\alpha = 0.5$, and the long-dashed curve is for $\alpha = 0.8$. We see clearly, especially for the real part in the top frame, that the singularity in the isotropic case has been greatly depressed with the introduction of anisotropy. For the imaginary part (the bottom frame) we also see this depression although it is not as strong as for the real part. The most interesting feature here, perhaps, is the coexistence of the softening (top frame) and broadening (bottom frame) of phonon lines. What we see in Fig. 6.3.2 is that the real part becomes positive only after $\omega > 2\Delta(1+\alpha)$ and the imaginary part becomes negative for $\omega > 2\Delta(1-\alpha)$. For frequencies from $2\Delta(1-\alpha)$ to $2\Delta(1+\alpha)$ we have softening as well as broadening. This is qualitatively different from the results of an isotropic superconductor in Fig. 6.3.1 where broadening is accompanied by hardening only.

The results for strong coupling superconductors with anisotropy are shown in Fig. 6.3.3 ($T_c/\omega_{log} = 0.1$) and 6.3.4 ($T_c/\omega_{log} = 0.25$). All the results are calculated using the real axis formula, Eq. (6.2.10), after solving the anisotropic Eliashberg equations (2.3.10) and (2.3.11) for $\tilde{\Delta}_{\vec{p}}(\omega)$ and $\tilde{\omega}_{\vec{p}}(\omega)$ at the reduced temperature $T/T_c = 0.2$, which we believe is low enough to simulate zero temperature. For both figures the solid curve is for the anisotropic parameter $g_{10} = 0.0$ (isotropic case for comparison), the dotted curve is for $g_{10} = 0.2$, the short-dashed curve is for $g_{10} = 0.5$ and the long-dashed curve is for $g_{10} = 0.8$. The quantity Δ should be understood as the energy gap in the isotropic case with the same coupling index T_c/ω_{log}. For cases with anisotropy the value of $\nu/2\Delta = 1$ does not simply correspond to the twice of the energy gap (see section 3.3). It is obvious that the results here, Fig. 6.3.3 and 6.3.4, have the same qualitative features as those in Fig. 6.3.2. For stronger anisotropy we have smaller changes in the magnitude of both the

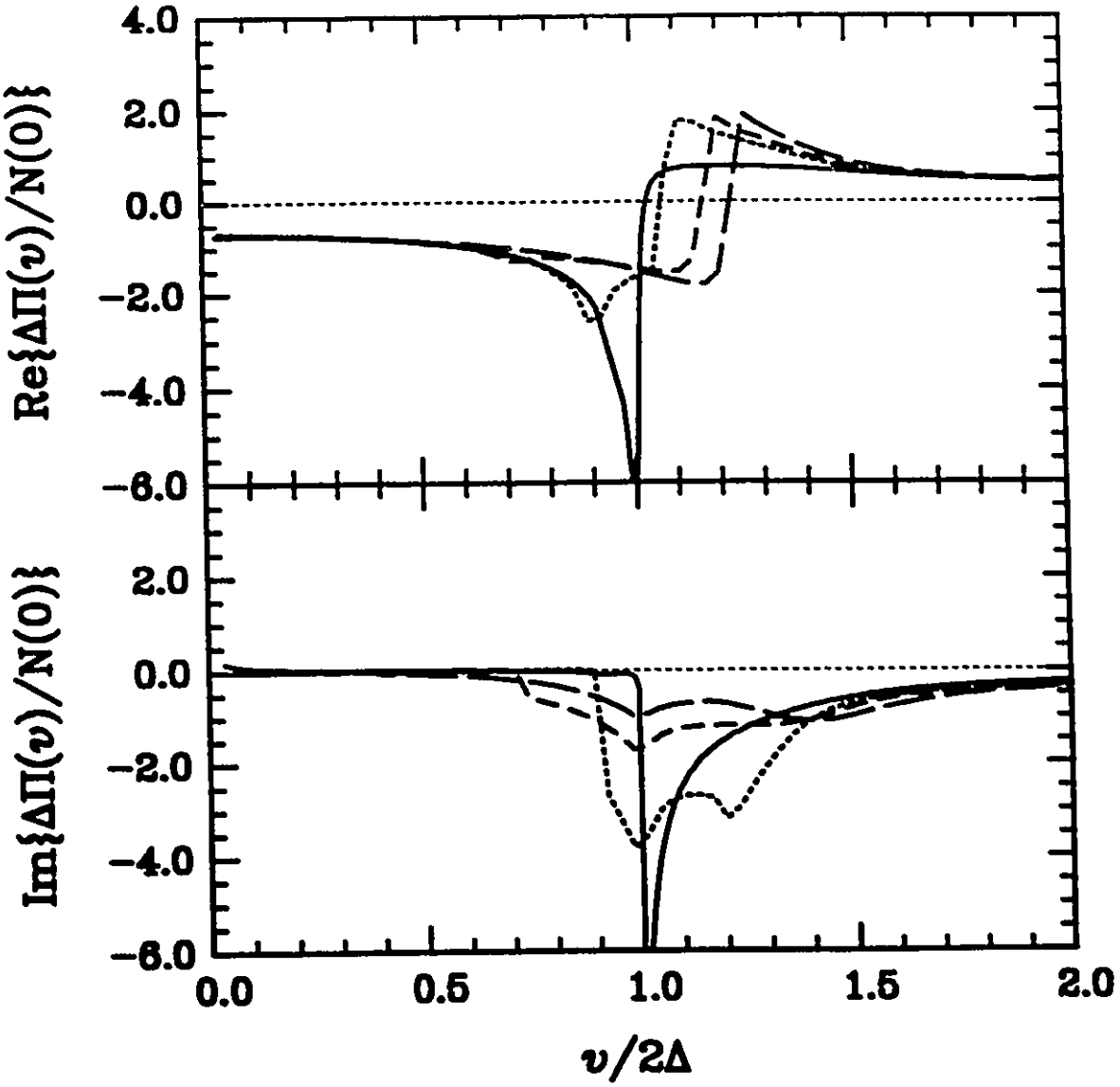

Fig. 6.3.4) The frequency dependence of $\Delta\Pi(\omega)/N(0)$ at low temperature ($t = T/T_c = 0.2$) for strong coupling ($T_c/\omega_{log} = 0.25$) and various anisotropic values, namely $g_{10} = 0.0$ (solid curve) isotropic case for comparison, $g_{10} = 0.2$ (dotted curve), $g_{10} = 0.5$ (short-dashed curve), and $g_{10} = 0.8$ (long-dashed curve). The anisotropic Eliashberg equations, Eqs. (2.3.10) and (2.3.11), have been solved for $\tilde{\Delta}_{\vec{p}}(\omega)$ and $\tilde{\omega}_{\vec{p}}(\omega)$. The top frame is the real part and the bottom is the imaginary part.

real and imaginary part of the polarization $\Pi(\omega)$ and larger coexistent range of softening (top frame) and broadening (bottom frame). As to the effects of strong coupling the magnitude of changes is smaller for stronger coupling, the same as for the peak in the quasiparticle density of states (see section 3.3). The coexistent range of softening and broadening is also smaller for stronger coupling. This is consistent with the fact that strong coupling will reduce the effectiveness of anisotropy which we knew from our studies in the previous chapters.

It is also interesting to examine the temperature dependence of the phonon self-energy for an anisotropic superconductor. In Fig. 6.3.5 we show the results for intermediate coupling ($T_c/\omega_{log} = 0.1$) with anisotropic parameter $g_{10} = 0.2$ for several reduced temperature $t = T/T_c$, namely $t = 0.2$ (solid curve), $t = 0.5$ (dotted curve), $t = 0.75$ (short-dashed curve), $t = 0.9$ (long-dashed curve) and $t = 0.95$ (short-dash-dotted curve). The long-dash-dotted curve in the figure is for the corresponding isotropic case ($T_c/\omega_{log} = 0.1$ and $g_{10} = 0.0$) at $t = 0.95$ as a comparison. The quantity Δ on the x axis is again the energy gap of an isotropic superconductor with the same T_c/ω_{log} at $T/T_c = 0.2$. We see that the structures in both the real (top frame) and imaginary (bottom frame) part of $\Delta\Pi(\omega)/N(0)$ move towards lower frequencies as temperature is increased. This is due to the decrease of the energy gap, or more precisely, the position of the peak in the quasiparticle density of states (see section 3.3). The magnitude of the structures also gets smaller as we approach T_c because of the thermal smearing. The thermal smearing has a large influence as well on the effects of anisotropy. At $t = 0.95$ the thermal smearing is so large that the effects of anisotropy is almost invisible, compared the short-dash-dotted curve with long-dash-dotted curve in

both the top and bottom frame. The temperature dependence of the phonon self-energy for other coupling strengths (the BCS limit and strong coupling $T_c/\omega_{log} = 0.25$) and other anisotropic parameters ($g_{10} = 0.5$ and $g_{10} = 0.8$) has also been studied but nothing qualitatively new has been found. The results for different coupling strengths follow the same trends as those compared in Figs. (6.3.2)-(6.3.4).

In the last figure, Fig. 6.3.6, we plot our theoretical results for different anisotropic models together with the experimental data presented by Thomsen *et al.* (1990) for the phonon shifts (top frame) and by Friedl, Thomsen and Cardona (1990) for the phonon widths (bottom frame). The theoretical results are calculated for strong coupling $T_c/\omega_{log} = 0.25$ at $T/T_c = 0.2$. The solid curve is for the isotropic case, the dotted curve is for the anisotropic parameter $g_{10} = 0.2$, and the short-dashed curve is for $g_{10} = 0.5$. The experimental data has been plotted as solid dots assuming $2\Delta = 380\text{cm}^{-1}$. We can see that none of three curves can fit the experimental data very well. At this point, no firm conclusions can be made with regard to the symmetry of the energy gap. We have not tried to find a set of parameters which would best fit the data. Nevertheless, we can conclude that the effects of anisotropy is important in the analyses of the experimental data. If there is anisotropy the value $\nu = 2\Delta$ does not correspond to the twice of the energy gap. Instead it corresponds to the average of the minimum and maximum gaps in the anisotropic models we have studied. Anisotropy will also have effects on the determination of the electron-phonon coupling parameter $|\, g_\lambda(\vec{p}, \vec{p}')\,|^2$.

We should point out that all the results above are for the clean limit ($\tau \rightarrow \infty$) only. Impurity scattering could be introduced through the anisotropic Eliashberg equations, Eqs. (2.3.10) and (2.3.11) but that is not

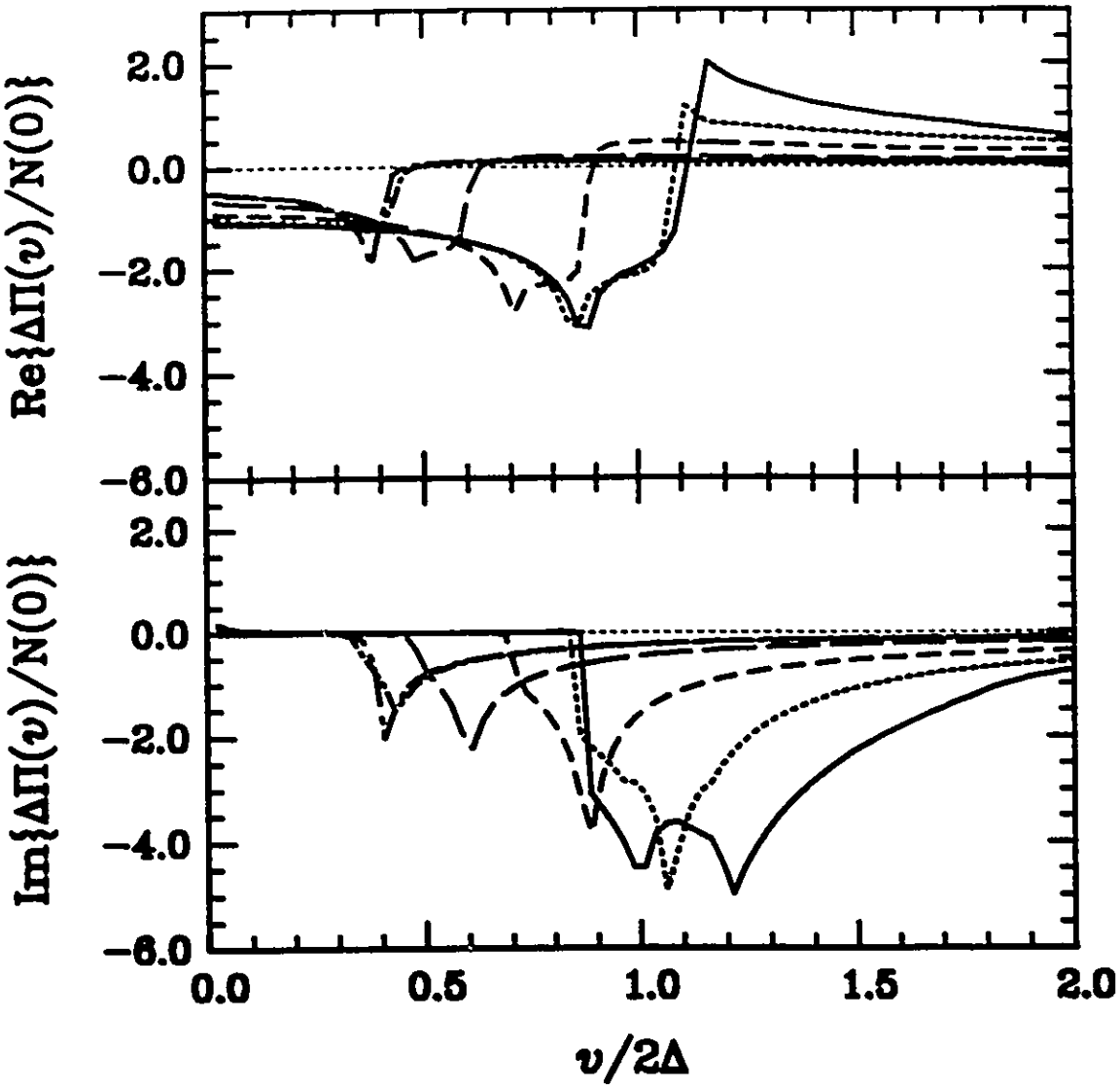

Fig. 6.3.5) The frequency dependence of $\Delta\Pi(\omega)/N(0)$ at finite temperature for intermediate coupling ($T_c/\omega_{log} = 0.1$) and anisotropic parameter $g_{10} = 0.2$. Curves are drawn for $T/T_c = 0.2$ (solid), 0.5 (dotted), 0.75 (short-dashed) 0.9 (long-dashed curve), and 0.95 (short-dash-dotted). The long-dash-dotted curve here is for the corresponding isotropic case at $T/T_c = 0.95$ as a comparison. The anisotropic Eliashberg equations, Eqs. (2.3.10) and (2.3.11), have been solved for $\tilde{\Delta}_{\vec{p}}(\omega)$ and $\tilde{\omega}_{\vec{p}}(\omega)$. The top frame is the real part and the bottom is the imaginary part.

our interest here. For an isotropic superconductor, the impurity effects have been studied by Zeyher and Zwicknagl (1990), by Akis (1991), and by Marsiglio, Akis and Carbotte (1992). The major effect coming from impurity scattering is to suppress and smear the structures in the phonon self-energy. It is the results with a large amount of normal impurities ($\tau^{-1} = 2\Delta$) for a strong coupling isotropic superconductor by Zeyher and Zwicknagl (1990) (the imaginary axis formulation) that are being used by Thomsen *et al.* (1990) and Friedl, Thomsen and Cardona (1990) to fit their experimental data. Compared with the real frequency axis formulation the imaginary axis formulation loses the sharp structures in the range around $\nu = 2\Delta$ [Akis (1991)]. For a detailed discussion of the problem of impurity scattering the above literature should be consulted.

6.4 CONCLUSIONS

In this chapter, we have studied phonon self-energy effects that arise upon entering the superconducting state for different coupling strengths and anisotropic models in the limit $\vec{q} \to 0$ and $\tau \to \infty$. Both the BCS formulation (the weak coupling limit) at $T = 0K$ and the real frequency axis formulation for strong coupling with anisotropy at finite temperature have been used. The following conclusions can be reached after a close study of the results: 1) Most qualitative features of the phonon self-energy at low temperature ($T \sim 0K$) can be well described by the simple BCS formula (6.2.15). 2) The most important feature due to anisotropy is the coexistence of the softening and broadening. This can be used as one of the signatures by which anisotropy may be detected in experiment provided that temperature is low ($T \sim 0K$) and the coupling is not very strong. 3) Increasing coupling strength will

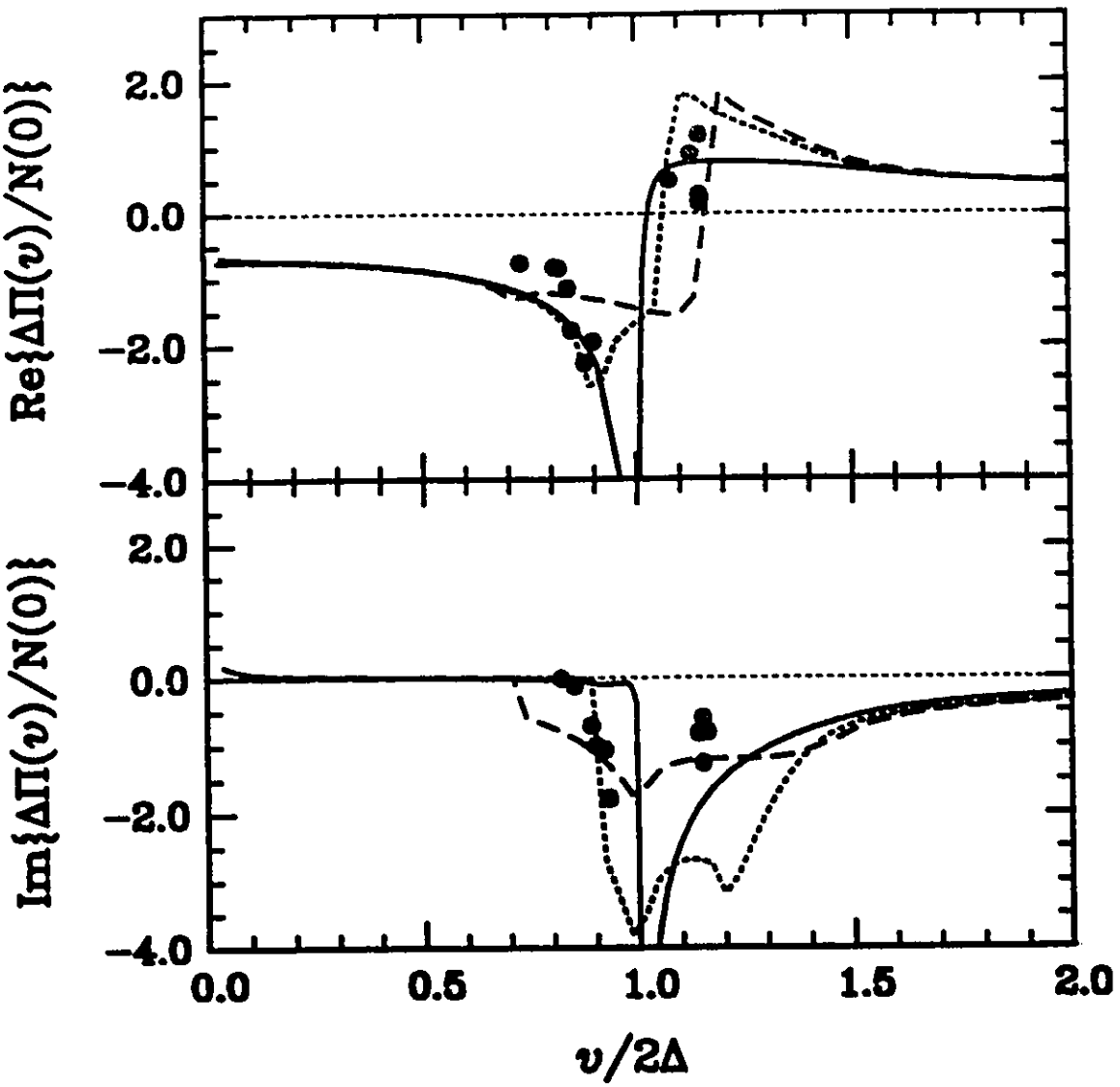

Fig. 6.3.6) A comparison between the date of Thomsen *et al.* (1990) (real part) and Friedl *et al.* (1990) (imaginary part) and the theoretical results for different anisotropic models. The experimental data has been plotted as solid dots by assuming $2\Delta = 380\text{cm}^{-1}$. The solid curve is for the isotropic case, the dotted curve is for the model with anisotropic parameter $g_{10} = 0.2$, and the short-dashed curve is for the model with $g_{10} = 0.5$. All three curves are calculated for strong coupling $T_c/\omega_{log} = 0.25$ at $T/T_c = 0.2$. Again, the top frame is the real part and the bottom is the imaginary part.

round off some sharp structures and reduce the effectiveness of anisotropy. Increasing temperature will have similar effects on these sturctures and push them towards lower frequencies because of a smaller energy gap. 4) For the cases with anisotropy we cannot determine the energy gap value directly from the structures in the phonon self-energy. The value $\nu = 2\Delta$ usually corresponds to the average of the minimum and maximum gaps in these cases. Finally, the effects of anisotropy on the phonon self-energy are significant only for weak coupling, low temperature, and the clean limit. This is also the case for many other properties studied in the previous chapters.

Chapter 7

Summary

In this thesis, we have investigated the effects of planar anisotropy on many superconducting properties within the context of strong coupling Eliashberg theory. Planar anisotropy is of interest for superconductors having layered crystal structure, such as the metallic transition metal dichalcogenide superconductors and, especially, the high-T_c oxide superconductors. To describe planar anisotropy, we used a model dispersion relation in which the single particle electronic states are free-particle-like for motion parallel to the layers and of the tight-binding form for motion perpendicular to the layers. One important consequence of this dispersion relation is that the quasiparticle density of states is constant around Fermi level ($\sim \hbar\omega_D$) provided that Fermi energy is high enough. We, then, modified the general anisotropic Eliashberg equations for the model. After solving the modified anisotropic

Eliashberg equations for the pairing potential $\tilde{\Delta}_{\vec{p}}(\omega)$ and renormalized frequency $\tilde{\omega}_{\vec{p}}(\omega)$, we studied various superconducting properties. Here, we give a summary of the work and results which have been reported.

We began with the study of the critical temperature T_c, the thermodynamic critical field $H_c(T)$ which is closely related to the free energy difference between the normal and superconducting state, and the quasiparticle density of states for different coupling strengths and anisotropic parameters (Chapter 3). Within the parameter space that we have explored, T_c can be enhanced by as much as 40%. The thermodynamic critical field, however, always decreases with the introduction of anisotropy. The change of the quasiparticle density of states due to anisotropy is the most interesting. Instead of a square root type singularity at the energy gap, which we would normally see in an isotropic superconductor at zero temperature, a sharp edge at the minimum energy gap with no attendant square root type singularity has been observed for an anisotropic superconductor. The sharp edge will get smeared and, in principle, the density of states is finite all the way down to zero frequency at finite temperature. This makes it difficult to define an unambiguous finite temperature gap value. If the coupling is not strong, however, the smearing will not be severe and we often can find a well defined peak structure in the density of states. The position of the peak follows a temperature dependence that is only slightly modified from the temperature variation of a BCS energy gap. Another interesting structure in the density of states is the so-called phonon structure. For an isotropic superconductor, the attendant phonon structure usually appears at an energy equal to the sum of the energy gap plus the peak value in the $\alpha^2F(\omega)$ used. If the coupling is not strong the phonon structure in the quasiparticle density

of states for an anisotropic superconductor can also be used to track the underlying temperature dependence of the gap or the peak position provided that we know the anisotropy. For strong coupling there are no well defined structures in the density of states at finite temperature at all, even for an isotropic superconductor. In such cases where a clear cut structure does not exist in the density of states, we may view the concept of an energy gap as a measure of the degree of the redistribution of the density of states due to the superconducting phase transition.

Next, in chapter 4, the effects of planar anisotropy on the specific heat, the ultrasound attenuation and the thermal conductivity were studied for different anisotropic models and coupling strengths. We saw that the specific heat jump and the slope of the specific heat jump at T_c were depressed below their isotropic value when anisotropy was introduced. On the other hand, the introduction of anisotropy increases the electronic specific heat at low temperature. This increase reflects an effectively smaller gap for a larger anisotropy. The effectively smaller gap at low temperature due to the anisotropy also affects the ultrasound attenuation and thermal conductivity. Both the ultrasound attenuation and thermal conductivity increase at low temperature with added anisotropy. For temperatures near T_c, however, the ultrasound attenuation is weaker for stronger anisotropy. This indicates an effectively larger gap at T near T_c for stronger anisotropy. For the thermal conductivity, adding anisotropy always makes it increase although the difference between the anisotropic and isotropic cases is relatively bigger at lower temperature. Whether the effective gap of an anisotropic superconductor is larger or smaller depends on temperature, the portion of the Fermi surface

considered, and the properties under study, *etc.* The contribution from the minimum and maximum gaps is usually different.

The studies in chapter 5 were devoted to some electromagnetic properties. For the London penetration depth, the introduction of anisotropy usually lowers the results below its isotropic values. The effect is stronger in the z-direction perpendicular to the planes. Only in very strong coupling cases are the results close to the two fluid model, which is favored for the high-T_c oxide superconductors. In such strong coupling cases anisotropy is not very effective in both directions (parallel and perpendicular to the planes), at least within the range of anisotropic parameters we have explored. For the Yosida function $Y(T)$ and the nuclear spin-lattice relaxation rate, the layered anisotropy induces a larger $Y(T)$ at lower temperature and a strong depression of the Hebel-Slichter peak, compared with the isotropic case with the same coupling index. Compared with experimental data in the high-T_c oxide superconductors, fair agreements could be achieved for reasonable values of coupling, anisotropic and Fermi liquid correction parameters. It was found that a much larger value of the Fermi liquid correction parameter, which corresponds to a stronger antiferromagnetic instability, is needed for coppers in the planes than for those in the chains in $YBa_2Cu_3O_{7-x}$. For the infrared conductivity, the absorption edge moves towards lower energy as anisotropy is increased. To see this clearly a small amount of normal impurity should be added. The effect is hardly visible in the clean limit with the spectrum density $\alpha^2F(\omega)$ we used. However, if the normal impurity concentration is too high the effect of anisotropy will be washed out.

Finally, in chapter 6, we studied the phonon self-energy of superconductors with various coupling strengths and anisotropic parameters. In the

limit $\vec{q} \to 0$ and $\tau \to \infty$, the changes of the phonon self-energy upon entering the superconducting state for different coupling strengths and anisotropic models have been calculated. The most important effect due to anisotropy is the existence of a frequency range where phonon lines soften and broaden. This is contrary to the phenomenon which we see in an isotropic superconductor where softening is accompanied by narrowing only at least at low temperature. This feature, softening and broadening, might be used as one of the signatures of the role anisotropy may display in experiment. Increasing coupling strength will round off some sharp structures and reduce the effectiveness of anisotropy. Increasing temperature has similar effects and pushs the structures towards lower frequencies because of a smaller energy gap. Anisotropy also affects the determination of an energy gap value from the structures in the phonon self-energy.

For all the properties which we have studied, it is generally true that the effects of anisotropy are significant only for weak coupling, low temperature, and the clean limit.

Appendix A

Asymptotic Limit for T_C of An Anisotropic Superconductor

In chapter 3 we claimed that the effects of anisotropy would be washed out if the coupling between electrons and phonons went to infinity (the asymptotic limit). In this appendix we will show this to be so for the superconducting transition temperature T_c within a simple model. This is sufficient, we believe, to give us a general idea of the effects of anisotropy in the asymptotic limit for other superconducting properties.

We start with the general anisotropic Eliashberg equations for T_c

$$\tilde{\Delta}_{\vec{p}}(i\omega_n) = \pi T \sum_{m=0}^{\infty} \left([\lambda_{\vec{p}\vec{p}'}(n-m) + \lambda_{\vec{p}\vec{p}'}(n+m-1)] \frac{\tilde{\Delta}_{\vec{p}'}(i\omega_m)}{\tilde{\omega}_{\vec{p}'}(i\omega_m)} \right)' \tag{A.1}$$

and

$$\tilde{\omega}_{\vec{p}}(i\omega_n) = \omega_n + \pi T \Big\langle \Big[\lambda_{\vec{p}\vec{p}'}(0) + 2\sum_{l=1}^{n}\lambda_{\vec{p}\vec{p}'}(l)\Big] \Big\rangle_{\vec{p}'}, \tag{A.2}$$

with

$$\lambda_{\vec{p}\vec{p}'}(n-m) = \int_0^\infty \frac{2\omega(\alpha^2F(\omega))_{\vec{p}\vec{p}'}d\omega}{\omega^2 + (\omega_n - \omega_m)^2}. \tag{A.3}$$

These equations are deduced from Eqs. (2.2.1)-(2.2.3) by simply setting the pairing potential $\tilde{\Delta}_{\vec{p}}(i\omega_n)$ equal to zero in the denominators. We have also ignored the Coulomb pseudopotential μ^* and impurity scatterings t^+ and t^- here for simplicity.

Now we assume that the directional electron-phonon spectral density $(\alpha^2F(\omega))_{\vec{p}\vec{p}'}$ can be written as

$$(\alpha^2F(\omega))_{\vec{p}\vec{p}'} = \alpha^2F(\omega)f(\vec{p}\,\vec{p}') = \alpha^2F(\omega)g(\vec{p})g(\vec{p}') \tag{A.4}$$

with the Fermi surface average of the function $g(\vec{p})$ to be $\langle g(\vec{p})\rangle = 1$ and $\langle 1/g(\vec{p})\rangle = \beta \geq 1$. By this, we separated the frequency dependent part from the angular dependent part for $(\alpha^2F(\omega))_{\vec{p}\vec{p}'}$ and used a separable model for the angular dependent part. The conditions for the Fermi surface average of function $g(\vec{p})$ are similar to what we did in the text (see Chapter 2).

Substitution of Eqs. (A.2)-(A.4) into Eq. (A.1) yields

$$\tilde{\Delta}_{\vec{p}}(i\omega_n) = \pi T g(\vec{p}) \sum_{m=0}^{\infty} [\lambda(n-m) + \lambda(n+m-1)] \left\langle \frac{g(\vec{p}\,')\tilde{\Delta}_{\vec{p}'}(i\omega_m)}{\omega_m + \pi T g(\vec{p}\,')[\lambda(0) + 2\sum_{l=1}^{m}\lambda(l)]} \right\rangle'. \tag{A.5}$$

Here, we have used the condition $\langle g(\vec{p}) \rangle = 1$. It is obvious now, from Eq. (A.5), that the pairing potential $\tilde{\Delta}_{\vec{p}}(i\omega_n)$ should have the form of $\tilde{\Delta}_{\vec{p}}(i\omega_n) = \tilde{\Delta}(i\omega_n)g(\vec{p})$, i.e., the angular dependent part of it is the function $g(\vec{p})$. From this relation, Eq. (A.5) becomes

$$\tilde{\Delta}(i\omega_n) = \pi T \sum_{m=0}^{\infty} [\lambda(n-m) + \lambda(n+m-1)] \left\langle \frac{g^2(\vec{p}\,')\tilde{\Delta}(i\omega_m)}{\omega_m + \pi T g(\vec{p}\,')[\lambda(0) + 2\sum_{l=1}^{m}\lambda(l)]} \right\rangle'. \tag{A.6}$$

To solve for T_c from Eq. (A.6) we use a single Matsubara gap approximation or the one-gap model, $\tilde{\Delta}(i\omega_n) = \Delta_0\delta_{0,n}$ [Allen and Dynes (1975); Carbotte (1990)]. With this model the algebra for solving for T_c is greatly simplified and the results are sufficient to make our points clear. It is easy to see that, under the one-gap model, Eq. (A.6) reduces to

$$\tilde{\Delta}_0 = \pi T[\lambda(0) + \lambda(1)]\tilde{\Delta}_0 \left\langle \frac{g^2(\vec{p}\,')}{\omega_0 + \pi T g(\vec{p}\,')\lambda(0)} \right\rangle'. \tag{A.7}$$

According to the definition of the Matsubara frequency $\omega_n = \pi T(2n+1)$ and of the function $\lambda(n-m)$ (see Eq. (A.3)), we have

$$\omega_0 = \pi T,$$

$$\lambda(0) = 2\int_0^\infty d\omega\, \alpha^2 F(\omega)/\omega = \lambda,$$

and

$$\lambda(1) = 2\int_0^\infty d\omega\, \omega\alpha^2 F(\omega)/[\omega^2 + (2\pi T)^2].$$

(A.8)

The quantity λ in the second equality here is a measure of the coupling strength between electrons and phonons and often called the mass enhancement factor. If temperature T is large we can approximately write the third equality in Eq. (A.8) as

$$\lambda(1) = \frac{\lambda < \omega^2 >}{(2\pi T)^2} \quad \text{with} \quad < \omega^2 >= \frac{2}{\lambda}\int_0^\infty d\omega\, \omega\alpha^2 F(\omega)$$

(A.9)

provided $2\pi T >> \langle\omega^2\rangle^{1/2}$ [Allen and Dynes (1975)].

Substituting Eqs. (A.8) and (A.9) into Eq. (A.7), we solve for T_c. The result is

$$T_c^2 = \frac{\lambda < \omega^2 >}{4\pi^2} \Big/ \left\{ \frac{\lambda}{\left(\frac{g(\vec{p})}{1+1/(\lambda g(\vec{p}))}\right)} - \lambda \right\}.$$

(A.10)

Under the asymptotic limit, $\lambda >> 1$, $\lambda g(\vec{p}) >> 1$ provided that $g(\vec{p})$ is finite for any $\vec{p}$ value as we had in the text. We, then, have the expansion

$$[1 + \frac{1}{\lambda g(\vec{p})}]^{-1} \simeq 1 - \frac{1}{\lambda g(\vec{p})} + \frac{1}{(\lambda g(\vec{p}))^2}$$

(A.11)

and Eq. (A.10) becomes

$$T_c^2 = \frac{\lambda < \omega^2 >}{4\pi^2} \Big/ \left\{ \frac{\lambda}{\langle g(\vec{p})[1 - 1/(\lambda g(\vec{p})) + 1/(\lambda g(\vec{p}))^2] \rangle} - \lambda \right\}.$$
$$= \frac{\lambda < \omega^2 >}{4\pi^2} \Big/ \left\{ \frac{\lambda}{1 - 1/\lambda + \beta/\lambda^2} - \lambda \right\} \tag{A.12}$$

Here, we used the conditions $\langle g(\vec{p}) \rangle = 1$ and $\langle 1/g(\vec{p}) \rangle = \beta \geq 1$ (a finite number). After some algebra we have the final form of T_c for an anisotropic superconductor which is

$$T_c^2 = \frac{\lambda < \omega^2 >}{4\pi^2} \Big/ \left\{ 1 - \frac{(\beta - 1)\lambda + \beta}{\lambda^2 - \lambda + \beta} \right\}. \tag{A.13}$$

Now we see that, at $T = T_c$, the large T requirement in Eq.(A.9) is satisfied in the asymptotic limit ($\lambda \to \infty$) since T_c is proportional to $\sqrt{\lambda}$.

Following the above procedures we can easily work out the T_c formula for an isotropic superconductor under the same conditions, which is

$$T_c^2 = \frac{\lambda < \omega^2 >}{4\pi^2}. \tag{A.14}$$

Compared Eq. (A.13) with Eq. (A.14) we see that adding anisotropy increases T_c, since $1 - [(\beta - 1)\lambda + \beta]/(\lambda^2 - \lambda + \beta) < 1$. This is consistent with the results in chapter 3. In the asymptotic limit $\lambda \to \infty$, $1 - [(\beta - 1)\lambda + \beta]/(\lambda^2 - \lambda + \beta) \to 1$ and Eq. (A.13) will be identical to Eq. (A.14). This is just what we expected. In the asymptotic limit the effect of anisotropy on T_c will be washed out.

Although the asymptotic limit is an idealized model, it is very useful in getting some simply analytical formulas of superconducting properties. These simple analytical formulas are instructive for problems with large but finite electron-phonon coupling strengths. Many superconducting properties of an isotropic superconductor have been studied under the asymptotic limit [Carbotte (1990)].

Appendix B

Effects of Non-Constant Density of States for Eliashberg Superconductors

In this appendix we will describe the Eliashberg equations with an energy dependent electronic density of states, $N(\epsilon)$, on both the imaginary and real axes. We will also discuss the effects of a Lorentzian form for $N(\epsilon)$ on the quasiparticle density of states in the superconducting state. From the discussions in the text we have seen that the redistribution of the quasiparticle density of states due to the superconducting phase transition is an essential property to understand many other superconducting properties.

B.1 THE ELIASHBERG EQUATIONS WITH $N(\epsilon)$

To derive the Eliashberg equations with an energy dependent electronic density of states $N(\epsilon)$, we follow the standard procedures described in many books and review articles [Schrieffer (1964); Scalapino (1969); Allen and Mitrović (1982)]. Using the Nambu formalism for the electron self-energy of an electron-phonon interaction system, we have the Eliashberg equations

with $N(\epsilon)$ on the imaginary axis for an isotropic superconductor as [Horsch and Rietschel (1977); Nettle and Thomas (1977); Lie and Carbotte (1978); Mitrović and Carbotte (1983b,c)]

$$\tilde{\omega}(i\omega_n) = \omega_n + \pi T \sum_{m=-\infty}^{\infty} \lambda(i\omega_n - i\omega_m)\left[\frac{1}{\pi}\int_{-\infty}^{\infty} d\epsilon \frac{N(\epsilon)}{N(0)} \frac{\tilde{\omega}(i\omega_m)}{(-det\hat{G}^{-1}(\epsilon, i\omega_m))}\right] + \pi(t^+ + t^-)\left[\frac{1}{\pi}\int_{-\infty}^{\infty} d\epsilon \frac{N(\epsilon)}{N(0)} \frac{\tilde{\omega}(i\omega_n)}{(-det\hat{G}^{-1}(\epsilon, i\omega_n))}\right], \tag{B.1.1}$$

$$\chi(i\omega_n) = -\pi T \sum_{m=-\infty}^{\infty} \lambda(i\omega_n - i\omega_m)\left[\frac{1}{\pi}\int_{-\infty}^{\infty} d\epsilon \frac{N(\epsilon)}{N(0)} \frac{\epsilon + \chi(i\omega_m)}{(-det\hat{G}^{-1}(\epsilon, i\omega_m))}\right] - \pi(t^+ + t^-)\left[\frac{1}{\pi}\int_{-\infty}^{\infty} d\epsilon \frac{N(\epsilon)}{N(0)} \frac{\epsilon + \chi(i\omega_n)}{(-det\hat{G}^{-1}(\epsilon, i\omega_n))}\right], \tag{B.1.2}$$

and

$$\tilde{\Delta}(i\omega_n) = \pi T \sum_{m=-\infty}^{\infty} [\lambda(i\omega_n - i\omega_m) - \mu^*\theta(\omega_c - |\omega_m|)]\left[\frac{1}{\pi}\int_{-\infty}^{\infty} d\epsilon \frac{N(\epsilon)}{N(0)} \frac{\tilde{\Delta}(i\omega_m)}{(-det\hat{G}^{-1}(\epsilon, i\omega_m))}\right] + \pi(t^+ - t^-)\left[\frac{1}{\pi}\int_{-\infty}^{\infty} d\epsilon \frac{N(\epsilon)}{N(0)} \frac{\tilde{\Delta}(i\omega_n)}{(-det\hat{G}^{-1}(\epsilon, i\omega_n))}\right]. \tag{B.1.3}$$

Here, the determinant of the inverse of the superconducting Green's function in the Nambu formalism is given as

$$det\,\hat{G}^{-1}(\epsilon, i\omega_n) = -[\tilde{\omega}^2(i\omega_n) + (\epsilon + \chi(i\omega_n))^2 + \tilde{\Delta}^2(i\omega_n)], \tag{B.1.4}$$

and the kernel is given as

$$\lambda(i\omega_n - i\omega_m) = \int_0^\infty \frac{2\omega(\alpha^2F(\omega))d\omega}{\omega^2 + (\omega_n - \omega_m)^2}. \tag{B.1.5}$$

Other quantities in Eqs. (B.1.1)-(B.1.3) are the temperature T, the electronic density of states at the Fermi level $N(0)$, the electron-phonon spectral density $\alpha^2F(\omega)$, the Coulomb pseudopotential μ^*, and the nonmagnetic (magnetic) impurity scattering rate t^+ (t^-).

Compared with the Eliashberg equations with constant density of states [Scalapino (1969)], we have an extra equation, Eq. (B.1.2) for the function $\chi(i\omega_n)$, here. For superconductors with constant density of states, this function $\chi(i\omega_n)$ is neglected because of the particle-hole symmetry. However, if $N(\epsilon)$ is not symmetric around the Fermi level, the function $\chi(i\omega_n)$ may not be negligible [Mitrović and Carbotte (1983b,c)]. In Eqs. (B.1.1)-(B.1.3), the integral over ϵ is yet to be done since the form of $N(\epsilon)$ has not yet been specified.

The Eliashberg equations on the real frequency axis can be derived in a similar way [Mitrović and Carbotte (1983b,c)]. The corresponding equations to Eqs. (B.1.1)-(B.1.5) on the real frequency axis are given as

$$\begin{aligned}\tilde{\omega}(\omega) =& \omega + \pi T \sum_{m=-\infty}^{\infty} \lambda(\omega - i\omega_m)\left[\frac{1}{\pi}\int_{-\infty}^{\infty} d\epsilon \frac{N(\epsilon)}{N(0)} \frac{\tilde{\omega}(i\omega_m)}{(-det\hat{G}^{-1}(\epsilon, i\omega_m))}\right] \\ &+ \pi \int_0^\infty d\Omega \alpha^2F(\Omega)\Big\{[n(\Omega) + f(\Omega - \omega)]\left[\frac{1}{\pi}\int_{-\infty}^{\infty} d\epsilon \frac{N(\epsilon)}{N(0)} \frac{\tilde{\omega}(\Omega - \omega)}{(-det\hat{G}^{-1}(\epsilon, \Omega - \omega))}\right] \\ &+ [n(\Omega) + f(\Omega + \omega)]\left[\frac{1}{\pi}\int_{-\infty}^{\infty} d\epsilon \frac{N(\epsilon)}{N(0)} \frac{\tilde{\omega}(\Omega + \omega)}{(-det\hat{G}^{-1}(\epsilon, \Omega + \omega))}\right]\Big\}\end{aligned}$$

$$+\pi(t^+ + t^-)\left[\frac{1}{\pi}\int_{-\infty}^{\infty} d\epsilon \frac{N(\epsilon)}{N(0)} \frac{\tilde{\omega}(\omega)}{(-det\hat{G}^{-1}(\epsilon,\omega))}\right], \tag{B.1.6}$$

$$\begin{aligned}\chi(\omega) = &-\pi T \sum_{m=-\infty}^{\infty} \lambda(\omega - i\omega_m)\left[\frac{1}{\pi}\int_{-\infty}^{\infty} d\epsilon \frac{N(\epsilon)}{N(0)} \frac{\epsilon + \chi(i\omega_m)}{(-det\hat{G}^{-1}(\epsilon, i\omega_m))}\right] \\ &-\pi \int_0^{\infty} d\Omega \alpha^2 F(\Omega)\Big\{[n(\Omega) + f(\Omega - \omega)]\left[\frac{1}{\pi}\int_{-\infty}^{\infty} d\epsilon \frac{N(\epsilon)}{N(0)} \frac{\epsilon + \chi(\Omega - \omega)}{(-det\hat{G}^{-1}(\epsilon, \Omega - \omega))}\right] \\ &+[n(\Omega) + f(\Omega + \omega)]\left[\frac{1}{\pi}\int_{-\infty}^{\infty} d\epsilon \frac{N(\epsilon)}{N(0)} \frac{\epsilon + \chi(\Omega + \omega)}{(-det\hat{G}^{-1}(\epsilon, \Omega + \omega))}\right]\Big\} \\ &-\pi(t^+ + t^-)\left[\frac{1}{\pi}\int_{-\infty}^{\infty} d\epsilon \frac{N(\epsilon)}{N(0)} \frac{\epsilon + \chi(\omega)}{(-det\hat{G}^{-1}(\epsilon, \omega))}\right],\end{aligned} \tag{B.1.7}$$

$$\begin{aligned}\tilde{\Delta}(\omega) = &\pi T \sum_{m=-\infty}^{\infty} \lambda(\omega - i\omega_m)\left[\frac{1}{\pi}\int_{-\infty}^{\infty} d\epsilon \frac{N(\epsilon)}{N(0)} \frac{\tilde{\Delta}(i\omega_m)}{(-det\hat{G}^{-1}(\epsilon, i\omega_m))}\right] \\ &+\pi \int_0^{\infty} d\Omega \alpha^2 F(\Omega)\Big\{[n(\Omega) + f(\Omega - \omega)]\left[\frac{1}{\pi}\int_{-\infty}^{\infty} d\epsilon \frac{N(\epsilon)}{N(0)} \frac{\tilde{\Delta}(\Omega - \omega)}{(-det\hat{G}^{-1}(\epsilon, \Omega - \omega))}\right] \\ &+[n(\Omega) + f(\Omega + \omega)]\left[\frac{1}{\pi}\int_{-\infty}^{\infty} d\epsilon \frac{N(\epsilon)}{N(0)} \frac{\tilde{\Delta}(\Omega + \omega)}{(-det\hat{G}^{-1}(\epsilon, \Omega + \omega))}\right]\Big\} \\ &-\mu^*(\omega_c)\int_0^{\omega_c} d\Omega \tanh(\frac{\Omega}{2T})\left[\frac{1}{\pi} Im \int_{-\infty}^{\infty} d\epsilon \frac{N(\epsilon)}{N(0)} \frac{\tilde{\Delta}(\omega)}{(-det\hat{G}^{-1}(\epsilon, \omega))}\right] \\ &+\pi(t^+ - t^-)\left[\frac{1}{\pi}\int_{-\infty}^{\infty} d\epsilon \frac{N(\epsilon)}{N(0)} \frac{\tilde{\Delta}(\omega)}{(-det\hat{G}^{-1}(\epsilon, \omega))}\right],\end{aligned} \tag{B.1.8}$$

$$det\,\hat{G}^{-1}(\epsilon,\omega) = \tilde{\omega}^2(\omega) - (\epsilon + \chi(\omega))^2 - \tilde{\Delta}^2(\omega), \tag{B.1.9}$$

and

$$\lambda(\omega - i\omega_m) = \int_0^\infty \frac{2\Omega(\alpha^2 F(\Omega))d\Omega}{\Omega^2 - (\omega - i\omega_m)^2}. \tag{B.1.10}$$

In Eqs. (B.1.6)-(B.1.8), one of the integrals in the original Eliashberg equations on the real frequency axis has been carried out analytically, the same as what we did in chapter 2 (from Eqs. (2.2.5)-(2.2.6) to Eqs. (2.2.8)-(2.2.9)) [Marsiglio, Schossmann and Carbotte (1988)]. At finite temperature, Eqs. (B.1.6)-(B.1.10) are the most fundamental equations for the study of various superconducting properties.

Eqs. (B.1.1)-(B.1.10) can be used for any form of the electronic density of states $N(\epsilon)$. Here, we will use a Lorentzian form for $N(\epsilon)$ which is given as

$$N(\epsilon) = N_b\left(1 + s\frac{1}{\pi}\frac{a}{(\epsilon + b)^2 + a^2}\right). \tag{B.1.11}$$

Here, N_b is the background, a is the width, b is the position of the Lorentzian peak related to the origin ($\epsilon = 0$), and s is the strength of the area under the Lorentzian peak (above the background). If we set the Fermi level at $\epsilon = 0$ we can move the peak in $N(\epsilon)$ relative to the Fermi level by changing the value of b. We can also change the shape of $N(\epsilon)$ by changing the width a for a fixed strength s.

Knowing $N(\epsilon)$, Eq. (B.1.11), we can carry out the integral over ϵ in Eqs. (B.1.1)-(B.1.3) and Eqs. (B.1.6)-(B.1.8) analytically. The resulting equations are, on the imaginary axis

$$\tilde{\omega}(i\omega_n) = \omega_n + \pi T \sum_{m=-\infty}^{\infty} \lambda(i\omega_n - i\omega_m) \frac{\tilde{\omega}_m}{[\tilde{\omega}_m^2 + \tilde{\Delta}_m^2]^{1/2}} \hat{N}(i\omega_m) + \pi(t^+ + t^-) \frac{\tilde{\omega}_m}{[\tilde{\omega}_n^2 + \tilde{\Delta}_n^2]^{1/2}} \hat{N}(i\omega_n), \tag{B.1.12}$$

$$\chi(i\omega_n) = -\pi T \sum_{m=-\infty}^{\infty} \lambda(i\omega_n - i\omega_m) \frac{N_b}{N(0)} \frac{s}{\pi} \frac{\chi(i\omega_m) - b}{(a + \sqrt{\tilde{\omega}^2(i\omega_m) + \tilde{\Delta}^2(i\omega_m)})^2 + (\chi(i\omega_m) - b)^2} - \pi(t^+ + t^-) \frac{N_b}{N(0)} \frac{s}{\pi} \frac{\chi(i\omega_n) - b}{(a + \sqrt{\tilde{\omega}^2(i\omega_n) + \tilde{\Delta}^2(i\omega_n)})^2 + (\chi(i\omega_m) - b)^2}, \tag{B.1.13}$$

$$\tilde{\Delta}(i\omega_n) = \pi T \sum_{m=-\infty}^{\infty} [\lambda(i\omega_n - i\omega_m) - \mu^* \theta(\omega_c - |\omega_m|)] \frac{\tilde{\Delta}_m}{[\tilde{\omega}_m^2 + \tilde{\Delta}_m^2]^{1/2}} \hat{N}(i\omega_m) + \pi(t^+ - t^-) \frac{\tilde{\Delta}_n}{[\tilde{\omega}_n^2 + \tilde{\Delta}_n^2]^{1/2}} \hat{N}(i\omega_n), \tag{B.1.14}$$

with

$$\hat{N}(i\omega_n) = \frac{N_b}{N(0)} \left\{ 1 + \frac{s}{\pi} \frac{a + \sqrt{\tilde{\omega}^2(i\omega_m) + \tilde{\Delta}^2(i\omega_m)}}{(a + \sqrt{\tilde{\omega}^2(i\omega_m) + \tilde{\Delta}^2(i\omega_m)})^2 + (\chi(i\omega_n) - b)^2} \right\}, \tag{B.1.15}$$

and on the real frequency axis

$$\tilde{\omega}(\omega) = \omega + i\pi T \sum_{m=-\infty}^{\infty} \lambda(\omega - i\omega_m) \frac{\tilde{\omega}(i\omega_m)}{\sqrt{\tilde{\omega}^2(i\omega_m) + \tilde{\Delta}^2(i\omega_m)}} \hat{N}(i\omega_m)$$
$$+ i\pi \int_0^\infty d\Omega \alpha^2 F(\Omega) \Big\{ [n(\Omega) + f(\Omega - \omega)] \frac{\tilde{\omega}(\omega - \Omega)}{\sqrt{\tilde{\omega}^2(\omega - \Omega) - \tilde{\Delta}^2(\omega - \Omega)}} \hat{N}(\omega - \Omega)$$
$$+ [n(\Omega) + f(\Omega + \omega)] \frac{\tilde{\omega}(\omega + \Omega)}{\sqrt{\tilde{\omega}^2(\omega + \Omega) - \tilde{\Delta}^2(\omega + \Omega)}} \hat{N}(\omega + \Omega) \Big\}$$
$$+ i\pi(t^+ + t^-) \frac{\tilde{\omega}(\omega)}{\sqrt{\tilde{\omega}^2(\omega) - \tilde{\Delta}^2(\omega)}} \hat{N}(\omega), \tag{B.1.16}$$

$$\chi(\omega) = -\frac{N_b}{N(0)} \frac{s}{\pi} \Big\{ \pi T \sum_{m=-\infty}^{\infty} \lambda(\omega - i\omega_m) \frac{\chi(i\omega_m) - b}{(a + \sqrt{\tilde{\omega}^2(i\omega_m) + \tilde{\Delta}^2(i\omega_m)})^2 + (\chi(i\omega_m) - b)^2}$$
$$+ \pi \int_0^\infty d\Omega \alpha^2 F(\Omega) \Big([n(\Omega) + f(\Omega - \omega)] \frac{\chi(\omega - \Omega) - b}{(a - i\sqrt{\tilde{\omega}^2(\omega - \Omega) - \tilde{\Delta}^2(\omega - \Omega)})^2 + (\chi(\omega - \Omega) - b)^2}$$
$$+ [n(\Omega) + f(\Omega + \omega)] \frac{\chi(\omega + \Omega) - b}{(a - i\sqrt{\tilde{\omega}^2(\omega + \Omega) - \tilde{\Delta}^2(\omega + \Omega)})^2 + (\chi(\omega + \Omega) - b)^2} \Big)$$
$$+ \pi(t^+ + t^-) \frac{\chi(\omega) - b}{(a - i\sqrt{\tilde{\omega}^2(\omega) - \tilde{\Delta}^2(\omega)})^2 + (\chi(\omega) - b)^2} \Big\}, \tag{B.1.17}$$

$$\tilde{\Delta}(\omega) = i\pi T \sum_{m=-\infty}^{\infty} \lambda(\omega - i\omega_m) \frac{\tilde{\Delta}(i\omega_m)}{\sqrt{\tilde{\omega}^2(i\omega_m) + \tilde{\Delta}^2(i\omega_m)}} \hat{N}(i\omega_m)$$
$$+ i\pi \int_0^\infty d\Omega \alpha^2 F(\Omega) \Big\{ [n(\Omega) + f(\Omega - \omega)] \frac{\tilde{\Delta}(\omega - \Omega)}{\sqrt{\tilde{\omega}^2(\omega - \Omega) - \tilde{\Delta}^2(\omega - \Omega)}} \hat{N}(\omega - \Omega)$$
$$+ [n(\Omega) + f(\Omega + \omega)] \frac{\tilde{\Delta}(\omega + \Omega)}{\sqrt{\tilde{\omega}^2(\omega + \Omega) - \tilde{\Delta}^2(\omega + \Omega)}} \hat{N}(\omega + \Omega) \Big\}$$
$$- \mu^*(\omega_c) \int_0^{\omega_c} d\Omega \tanh(\frac{\Omega}{2T}) Re \Big(\frac{\tilde{\Delta}(\omega)}{\sqrt{\tilde{\omega}^2(\omega) - \tilde{\Delta}^2(\omega)}} \hat{N}(\omega) \Big)$$

$$+ i\pi(t^+ - t^-)\frac{\tilde{\Delta}(\omega)}{\sqrt{\tilde{\omega}^2(\omega) - \tilde{\Delta}^2(\omega)}}\hat{N}(\omega), \tag{B.1.18}$$

with

$$\hat{N}(\omega) = \frac{N_b}{N(0)}\left\{1 + \frac{s}{\pi}\frac{a - i\sqrt{\tilde{\omega}^2(\omega) - \tilde{\Delta}^2(\omega)}}{(a - i\sqrt{\tilde{\omega}^2(\omega) - \tilde{\Delta}^2(\omega)})^2 + (\chi(\omega) - b)^2}\right\}. \tag{B.1.19}$$

Next we will study the effects of $N(\epsilon)$ on the quasiparticle density of states in the superconducting state.

B.2 THE QUASIPARTICLE DENSITY OF STATES WITH $N(\epsilon)$

In terms of Green's functions, the quasiparticle density of states is given as (see chapter 3)

$$N(\omega) = -\frac{1}{\pi}\int_{-\infty}^{\infty} d\epsilon N(\epsilon) Im\Big(G(\epsilon,\omega)\Big) \tag{B.2.1}$$

Here, the electron Green's function $G(\epsilon,\omega)$ in the superconducting state is given as

$$G_s(\epsilon,\omega) = \frac{\tilde{\omega}(\omega + i\delta) + \epsilon + \chi(\omega + i\delta)}{\tilde{\omega}^2(\omega + i\delta) - (\epsilon + \chi(\omega + i\delta))^2 - \tilde{\Delta}^2(\omega + i\delta)}. \tag{B.2.2}$$

For $N(\epsilon)$ with a Lorentzian form, Eq. (B.1.11), we can work out the integral over ϵ in Eq. (B.2.1) and get

$$N(\omega) = Re\left\{ \frac{\tilde{\omega}(\omega)}{\sqrt{\tilde{\omega}^2(\omega) - \tilde{\Delta}^2(\omega)}} \left(1 + \frac{s}{\pi} \frac{a - i\sqrt{\tilde{\omega}^2(\omega) - \tilde{\Delta}^2(\omega)}}{(a - i\sqrt{\tilde{\omega}^2(\omega) - \tilde{\Delta}^2(\omega)})^2 + (\chi(\omega) - b)^2} \right) - \frac{s}{\pi} \frac{i(\chi(\omega) - b)}{(a - i\sqrt{\tilde{\omega}^2(\omega) - \tilde{\Delta}^2(\omega)})^2 + (\chi(\omega) - b)^2} \right\} \tag{B.2.3}$$

After solving for the pairing potential $\tilde{\Delta}(\omega)$, the renormalized frequency $\tilde{\omega}(\omega)$ and the function $\chi(\omega)$ from Eqs. (B.1.15)-(B.1.17), we can use this formula, (B.2.3), to calculate the quasiparticle density of states in the superconducting state as a function of temperature for various values of parameters (s, a, b, T_c/ω_{log}, *etc.*).

Now we show some numerical results of the effects of $N(\epsilon)$ with a Lorentzian form on the quasiparticle density of states in the superconducting state $N(\omega)$. The parameters we used for $N(\epsilon)$ are $s = 10meV$ a fixed strength of the Lorentzian peak, and $b = 0$ a symmetric form of $N(\epsilon)$ about the Fermi level and, therefore, the function $\chi(\omega) = 0$ for simplicity. The width a is adjusted for the fixed strength s to give various shapes of the Lorentzian peak. The background N_b does not need to be specified since we always present the results for a normalized ratio $N(\omega)/N_b$. In solving the Eliashberg equations, Eqs. (B.1.15)-(B.1.17), for $\tilde{\omega}(\omega)$ and $\tilde{\Delta}(\omega)$, we use the spectral density $\alpha^2F(\omega)$ of Pb. The height of this function is adjusted for various shapes of $N(\epsilon)$ to give a fixed ratio 0.1 of T_c/ω_{log} as we did before.

In Fig. B.2.1, we plot $N(\omega)/N_b$ as a function of the reduced frequency ω/T_c for several temperatures. The solid curve is for $t = T/T_c = 0.1$, the dotted curve is for $t = 0.6$, the short-dashed curve is for $t = 0.8$, the long-dashed curve is for $t = 0.95$, and the short-dash-dotted curve is for $t = 0.985$.

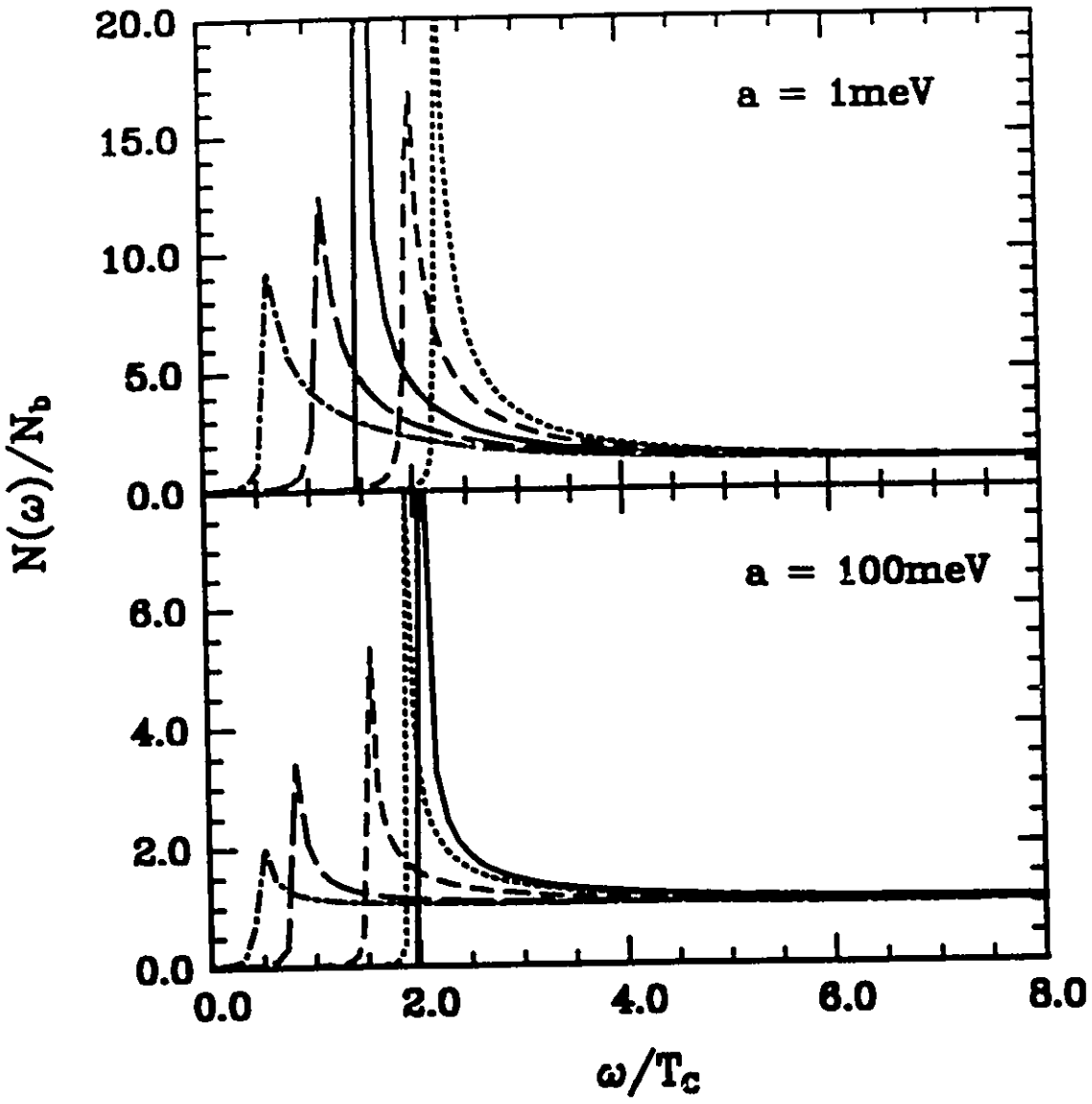

Fig. B.2.1) The quasiparticle density of states $N(\omega)/N_b$ as a function of the reduced frequency ω/T_c for various temperatures, namely, $t = T/T_c = 0.1$ the solid curve, $t = 0.6$ the dotted curve, $t = 0.8$ the short-dashed curve, $t = 0.95$ the long-dashed curve, and $t = 0.985$ the short-dash-dotted curve. The Lorentzian form for $N(\epsilon)$ is centered at the Fermi level with a strength $s = 10meV$. The top frame is for the width $a = 1meV$ and the bottom frame is for $a = 100meV$. The ratio T_c/ω_{log} is fixed at 0.1.

In the top frame we have the width $a = 1meV$ which corresponds to a fairly strong peak in $N(\epsilon)$ at the Fermi level, while in the bottom frame we have the width $a = 100meV$ which gives a very flat distribution of $N(\epsilon)$ around the Fermi level (very close to a constant electronic density of states situation). Comparing the top frame with the bottom frame we see that at $t = 0.1$ (solid curve) the peak position in the quasiparticle density of states $N(\omega)$ is lower in frequency in the top frame than in the bottom frame. This is because that the strong peak in $N(\epsilon)$ at the Fermi level (top frame) reduces the electron-phonon coupling needed for a given T_c compared with the case where the strength of $N(\epsilon)$ is the same but the peak at the Fermi level is very small (bottom frame). From Fig. B.2.1, we also see that in the top frame the peak in $N(\omega)/N_b$ moves first towards higher frequencies before it goes to zero as temperature is increased from zero to T_c, although there are some thermal smearings of $N(\omega)$ into the low frequency region at finite temperature. This is very interesting since it is qualitatively different from the results for superconductors with constant electronic density of states. A constant electronic density of states is similar to the situation shown in the bottom frame where the peak in $N(\omega)/N_t$ decreases monotonically as T is increased. To see this effect more clearly we plot the temperature dependence of the peak in $N(\omega)$ in Fig. B.2.2. The top and bottom frames in Fig. B.2.2 correspond to the top and bottom frames in Fig. B.2.1, respectively. It is clear from Fig. B.2.2 that a strong peak in $N(\epsilon)$ at the Fermi level will change the temperature dependence of the peak in the quasiparticle density of states $N(\omega)$ in the superconducting state qualitatively. This change also shows up

in the temperature dependence of many other superconducting properties [Jiang and Carbotte (1992f)].

We have also studied various transport superconducting properties, *e.g.*, the thermal conductivity, the infrared conductivity, and the nuclear spin relaxation rate, with a Lorentzian form for $N(\epsilon)$. Due to the length of this thesis, we will not discuss these results in detail here.

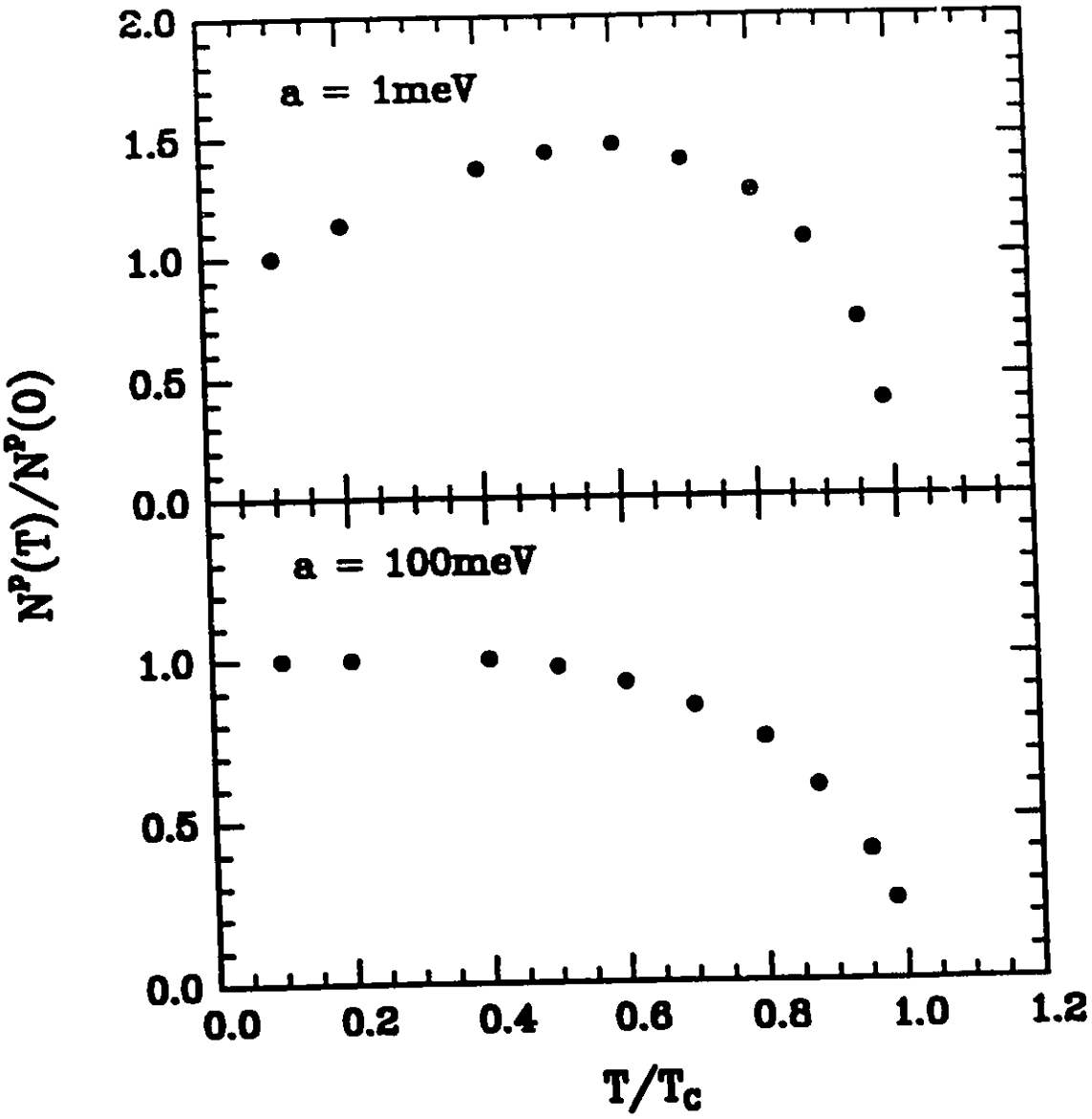

Fig. B.2.2) The temperature dependence of the peak in the quasiparticle density of states normalized by its zero temperature value $N^p(T)/N^p(0)$ for $N(\epsilon)$ with a Lorentzian form. The Lorentzian peak is centered at the Fermi level with a strength $s = 10meV$. The top frame is for the width $a = 1meV$ and the bottom frame is for $a = 100meV$. The ratio T_c/ω_{log} is fixed at 0.1.

Bibliography

Abragam, A., The Principles of Nuclear Magnetism, (Clarendon Oress, Oxford, 1961).

Abrikosov, A.A., *Soviet Phys. JETP* **5**, 1174 (1957).

Akis, R., Ph.D Thesis, McMaster University, 1991 (unpublished).

Akis, R. and J.P. Carbotte, *J. Low Temp. Phys.* **76**, 65 (1989a).

Akis, R. and J.P. Carbotte, *Physica C* **159**, 395 (1989b).

Akis, R. and J.P. Carbotte, *Pyhsica C* **162-163**, 1491 (1989c).

Akis, R., C. Jiang, and J.P. Carbotte, *Physica C* **176**, 485 (1991).

Aleksashin, B.A., *et al.* , *Physica C* **153-155**, 339 (1988).

Aleksashin, B.A., *et al.* , *Soviet Physics (JETP)* **95**, 678 (1989).

Allen, P.B. and R.C. Dynes, *Phys. Rev. B* **12**, 905 (1975).

Allen, P.B. and B. Mitrović, *Solid State Phys.* **37**, 1 (1982).

Allen, P.B. and D. Rainer, *Nature* **349**, 396 (1991).

Altendorf, E., J. Chrzanowski, and J.C. Irwin, *Physica C* **175**, 47 (1991).

Ambegaokar,V. and L. Tewordt, *Phys. Rev.* , 134, A805 (1964).

Anderson, P.W., *J. Phys. Chem. Solids* **11**, 26 (1959).

Ashcroft, N.W. and N.D. Mermin, Solid State Physics (Holt, Rinehart and Winston, Philadelphia, 1976).

Axe, J.D. and G. Shirane, *Phys. Rev. Lett.* **30**, 214 (1973a).

Axe, J.D. and G. Shirane, *Phys. Rev. B* **8**, 1965 (1973b).

Bardeen, J., L.N. Cooper, and J.R. Schrieffer, *Phys. Rev.* **108**, 1175 (1957).

Bardeen, J. and J.R. Schrieffer, in Progress in Low Temperature Physics, Vol. III, edited by C.J. Gorter (North-Holland, Amsterdam, 1961).

Bardeen, J. and M. Stephen, *Phys. Rev.* **136**, A1485 (1964).

Bedell, K.S., D. Coffey, D.E. Meltzer, D. Pines, and J.R. Schrieffer, Ed. High Temperature Superconductivity (Addison-Wesley, New York, 1990).

Bednorz, J.G. and K.A. Müller, *Z. Phys. B* **64**, 189 (1986).

Bickers, N.E., D.J. Scalapino, R.T. Collins, and Z. Schlesinger, *Phys. Rev. B* **42**, 67 (1990).

Blaschke, R., and R. Blocksdorf, *Z. Phys. B* **49**, 99 (1982).

Blezius, J.W., Ph.D Thesis, McMaster University, 1987 (unpublished).

Bosomworth, D.R. and G.W. Culler, *Phys. Rev.* **160**, 346 (1967).

Bulaevskii, L.N. and O.V. Dolgov, *Physica C*, **153-155**, 242 (1988a).

Bulaevskii, L.N. and O.V. Dolgov, *Solid State Comm.* **67**, 63 (1988b).

Butler, W.H. and P.B. Allen, in Superconductivity in d- and f- band Metals, edited by D.H. Douglass (Plenum Press, New York, 1976), p. 73.

Carbotte, J.P., *Sci. Prog. Oxf.* **71**, 327 (1987).

Carbotte, J.P., *Rev. Mod. Phys.* **62**, 1027 (1990).

Chu, C.W., J. Bechtold, L. Gao, P.H. Hor, Z.J. Huang, R.L. Meng, Y.Y. Sun, Y.Q. Wang, and Y.Y. Xue, *Phys. Rev. Lett.* **60**, 941 (1988).

Clem, J.R., *Annals of Physics*, **40**, 268 (1966).

Cohn, J.L., S.D. Peacor, and C. Uher, *Phys. Rev. B* **38**, 2892 (1988).

Cooke, D.W., R.L. Huston, R.S. Kwok, M. Maez, H. Rempp, M.E. Schillaci, J.L. Smith, J.O. Willis, R.L. Lichti, K.C.B. Chan, C. Boekema, S.P. Weathersby, J.A. Flint, and J. Oostens, *Phys. Rev. B* **37**, 9401 (1988a).

Cooke, D.W., R.L. Huston, R.S. Kwok, M. Maez, H. Rempp, M.E. Schillaci, J.L. Smith, J.O. Willis, R.L. Lichti, K.C.B. Chan, C. Boekema, S.P. Weathersby, J.A. Flint, and J. Oostens, *Phys. Rev. B* **39**, 2748 (1988b).

Cooper, L.N., *Phys. Rev.* **104**, 1189 (1956).

Cooper. S.L., M.V. Klein, B.G. Pazol, J.P. Rice, and D.M. Ginsberg, *Phys. Rev. B* **37**, 5920 (1988).

Craven, R.A., G.A. Thomas, and R.D. Park, *Phys. Rev. B* **7**, 157 (1973).

Crawford, M.K., M.N. Kunchur, W.E. Farneth, E.M. McCarron III and S.J. Poon, *Phys. Rev. B* **41**, 283 (1990).

Daams, J.M., Ph.D Thesis, McMaster University, 1979 (unpublished).

Daams, J.M. and J.P. Carbotte, *J. Low Temp. Phys.* **43**, 263 (1981).

Dobbs, E.R. and J.M. Perz, *Rev. Mod. Phys.* **36**, 257 (1964).

Eliashberg, G.M., *Sov. Phys.-JETP* **11**, 696 (1960).

Emery, V.J. and G. Reiter, *Phys. Rev. B* **38**, 4547 (1988).

Fetter, A.L. and P.C. Hohenberg, in Superconductivity R.D. Parks, editor, (Dekker, New York, 1969), p. 817.

Fine, H.L., M. Lipsieas, and M. Strongin, *Phys. Lett.* **29A**, 366 (1969).

Fiory, A.T., A.F. Hebard, P.M. Mankiewich, and R.E. Howard, *Phys. Rev. Lett.* **61**, 1419 (1988).

Fisher, R.A., J.E. Gordon and N.E. Phillips, *J. of Superconductivity* **1**, 231 (1988).

Franck, J.P., J. Jung, G.J. Salomons, W.A. Miner, M.A.K. Mohamed, J. Chrzanowski, S. Gygax, J.C. Irwin, D.F. Mitchell, I. Sproule, *Physica C* **162-164**, 753 (1990a).

Franck, J.P., J. Jung, M.A.K. Mohamed, S. Gygax, and G.I. Sproule, *Physica B* **165-166**, 697 (1990b).

Frick, M. and T. Schneider, *Z. Phys. B* **78**, 159 (1990).

Friedl, B., C. Thomsen and M. Cardona, *Phys. Rev. Lett.* **65**, 915 (1990).

Fröhlich, H., *Phys. Rev.* **79**, 845 (1950).

Gavaler, J.R., *Appl. Phys. Lett.* **23**, 480 (1973).

Gavaler, J.R., M.A. Janocko, and C.K. Jones, *J. Appl. Phys.* **45**, 3009 (1974).

Genzel, L., A. Wittlin, M. Bauer, M. Cardona, E. Schönherr, and A. Simon, *Phys. Rev. B* **40**, 2170 (1990).

Ginzburg, V.L. and L.D.J. Landau, *Sov. Phys. JETP* **20**, 1064 (1950).

Ghosh, A.K. and M. Strongin, in Superconductivity in d- and f-Band Metals, edited by H. Suhl and M.B. Maple (Academic Press, New York, 1980), p. 305.

Goodman, B.B., *Rept. Progr. Phys.* **29**, 445 (1966).

Gorter, C.J. and H.B.G. Casimir, *Phys. Z.* **35**, 963 (1934a).

Gorter, C.J. and H.B.G. Casimir, *Z. Techn. Phys.* **15**, 539 (1934b).

Halley, J.W., Ed. Theories of High Temperature Superconductivity (Addison-Wesley, New York, 1988).

Harshman, D.R., G. Aeppli, E.J. Ansaldo, B. Batlogg, J.H. Brewer, J.F. Carolan, R.J. Cava, M. Celio, A.C.D. Chaklader, W.N. Hardy, S.R. Kreitzman, G.M. Luke, D.R.Noakes, and M. Senba, *Phys. Rev. B* **36**, 2386 (1987).

Harshman, D.R., L.F. Scheemeyer, J.V. Waszczak, G. Aeppli, R.J. Cava, B. Batlogg, L.W. Rupp, E.J. Ansaldo, and D.Ll.Williams, *Phys. Rev. B* **39**, 851 (1989).

Hebel, L.C. and C.P. Slichter, *Phys. Rev.* **107**, 901 (1957).

Hebel, L.C. and C.P. Slichter, *Phys. Rev.* **113**, 1504 (1959).

Hong, K.M. and J.P. Carbotte, *Can. J. Phys.* **56**, 1395 (1978).

Horsch, P. and H. Rietschel, *Z. Phys. B* **27**, 153 (1977).

Hulm, J.K. and B.T. Matthias, *NATO Adv. Study Inst. Sev.*, **B68**, 1 (1981).

Imai, T., T Shimizu, H. Yasuoka, Y. Ueda, and K. Kosuge, *J. Phys. Soc. Jap.* **57**, 2280 (1988).

Ishiguro, T. and K. Yamaji, Organic Superconductors (Springer-Verlag, Berlin, 1990).

Jinag, C. and J.P. Carbotte, 1992a (unpublished).

Jiang, C. and J.P. Carbotte, *Phys. Rev. B* **45**, 7368 (1992b).

Jiang, C. and J.P. Carbotte, to be published in the Proceedings of Darmstadt International Conference on the Physics of Transition Metals (Germany, July 1992c).

Jiang, C. and J.P. Carbotte, *Phys. Rev. B* **45**, 10670 (1992d).

Jiang, C. and J.P. Carbotte, *J. Low Temp. Phys.* **87**, 95 (1992e).

Jiang, C. and J.P. Carbotte, to be published in the Proceedings of Beijing International Conference on High T_c Superconductivity (China, May 1992f).

Junod, A., A. Bezinge, D. Eckhart, T. Graf and J. Muller, *Physica C* **152**, 495 (1988).

Junod, A., in Physical Properties of High Temperature Superconductors II, edited by D.M. Ginsberg (World Scientific, Singapore, 1990), p. 13.

Kaplan, S.B., C.C. Chi, D.N. Langenberg, J.J. Chang, S. Jafarey, and D.J. Scalapino, *Phys. Rev. B* **14**, 4854 (1976).

Karakozov, A.E., E.G. Maksimov, and A.A. Mikhailovsky, *Solid State Comm.* **79**, 329 (1991).

Kasowski, R.V., *Phys. Rev. Lett.* **30**, 1175 (1973).

Kats, E.I., *Sov. Phys. JETP* **29**, 897 (1969).

Kats, E.I., *Sov. Phys. JETP* **31**, 787 (1970).

Kirtley, J.R., *Int. J. Mod. Phys. B* **4**, 201 (1990).

Kittel, C., Introduction to Solid State Physics (John Wiley and Sons, New York, 1986).

Klemm, R.A., PhD. Thesis, Harvard University, 1974 (unpublished).

Klein, B.M., D.A. Papaconstantopoulos, and L.L. Boyer, in Superconductivity in d- and f-Band Metals, edited by H. Suhl and M.B. Maple (Academic Press, New York, 1980), p. 455.

Lawrence, W. and S. Doniach, in Proceedings of the Twelfth International Conference on Low Temp. Phys., edited by E. Kanda (Academic of Japan, Kyoto, 1971), p. 361.

Leavens, C.R. and J.P. Carbotte, *Annals of Physics*, **70**, 268 (1972).

Leavens, C.R. and D.S. Ritchie, *Solid State Comm.* **53**, 137 (1985).

Lee, M., A. Kapitulnik, and M.R. Beasley, in Machanisms of High-Temperature Superconductivity, edited by H. Kamimura and A. Oshiyama (Springer-Verlag, Heidelberg, 1989), p. 220.

Lee, W., D. Rainer, and W. Zimmermann, *Physica C* **159**, 535 (1989).

Lie, S. G. and J.P. Carbotte, *Solid State Comm.* **26**, 511 (1978).

Lie, S. G. and J.P. Carbotte, *Solid State Comm.* **35**, 127 (1980).

Loram, J. and K.A. Mirza, *Physica C* **153-155**, 1020 (1988).

Love, R.E. and R.W. Shaw, *Rev. Mod. Phys.* **36**, 260 (1964).

MacFarlane, R.M., H. Rosen and H. Seki *Solid State Comm.* **63**, 831 (1987).

MacLaughlin, D.E., in Solid State Physics, edited by H. Ehrenreich, F. Seitz and D. Turnbull (Academic Press, New York, 1976), Vol. **31**, p. 1.

Maeda, H., Y. Tanaka, M. Fakutomi, T. Asano, *Jpn. J. Appl. Phys.* **27**, L209 (1988).

Markowitz, D. and L.P. Kadanoff, *Phys. Rev.* **131**, 563 (1963).

Marsiglio, F., R. Akis, and J.P. Carbotte, *Phys. Rev. B* **45**, 9865 (1992).

Marsiglio, F. and J.P. Carbotte, *Phys. Rev. B* **33**, 6141 (1986).

Marsiglio, F., M. Schossmann, and J.P. Carbotte, *Phys. Rev. B* **37**, 4965 (1988).

Marsiglio, F., Ph.D. thesis, McMaster University, 1988 (unpublished).

Marsiglio, F. and J.P. Carbotte, *Phys. Rev. B* **41**, 8765 (1990).

Marsiglio, F., J.P. Carbotte, and J. Blezius, *Phys. Rev. B* **41**, 6457 (1990).

Marsiglio, F. (unpublished, 1992).

Masuda, Y. and A.G. Redfield, *Phys. Rev.* **125**, 159 (1962).

Mattheiss, L.F., *Phys. Rev. Lett.* **30**, 784 (1973a).

Mattheiss, L.F., *Phys. Rev. B* **8**, 3719 (1973b).

Mattis, D.C. and J. Bardeen, *Phys. Rev.* **111**, 412 (1958).

Maxwell, E., *Phys. Rev.* **78**, 477 (1950).

McCarty, K.F., H.B. Radousky, J.Z. Liu, and R.N. Shelton, *Phys. Rev. B* **43**, 13751 (1991).

McMillan, W.L. and J.M. Rowell, *Phys. Rev. Lett.* **14**, 108 (1965).

McMillan, W.L. and J.M. Rowell, in Superconductivity R.D. Parks, editor, (Dekker, New York, 1969), p. 561.

Meissner, W. and R. Ochsenfeld, *Naturwiss.* **21**, 787 (1933).

Migdal, A.B., *Sov. Phys.-JETP* **34**, 996 (1958).

Mitra, S., J.H. Cho, W.C. Lee, D.C. Johnston, and V.C. Kogan, *Phys. Rev. B* **40**, 2674 (1989).

Mitrović, B and J.P. Carbotte, *Can. J. Phys.* **61**, 758 (1983a).

Mitrović, B and J.P. Carbotte, *Can. J. Phys.* **61**, 784 (1983b).

Mitrović, B and J.P. Carbotte, *Can. J. Phys.* **61**, 872 (1983c).

Mitrović, B., H.G. Zarate, and J.P. Carbotte, *Phys. Rev. B* **29**, 184 (1984).

Monceau, P. and G. Waysand, *Solid State Comm.* **14**, 221 (1974).

Monien, H. and D. Pines, *Phys. Rev. B* **41**, 6297 (1990).

Morse, R.W. and H.V. Bohm, *Phys. Rev.* **108**, 1094 (1957).

Morse, R.W., T. Olsen, and J.D. Gavenda, *Phys. Rev. Lett.* **3**, 15 (1959).

Nam, S.B., *Phys. Rev.* **156**, 470 (1967a).

Nam, S.B., *Phys. Rev.* **156**, 487 (1967b).

Nettle, S.J. and H. Thomas,*Solid State Comm.* **21**, 683 (1977).

Newns, D.M., P.C. Pattnaik, and C.C. Tsuei, *Phys. Rev. B* **43**, 3075 (1991).

Onnes, H.K., *Leiden Comm.*, 1206 (1911).

Parks, R.D., Ed. Superconductivity (Dekker, New York, 1969).

Peacor, S.D, R.A. Richardson, J. Burn, C. Uher, and A.B. Kaiser, *Phys. Rev. B* **42**, 2684 (1990).

Pickett, W.E., in Superconductivity in d- and f-Band Metals, edited by H. Suhl and M.B. Maple (Academic Press, New York, 1980), p. 77.

Pines, D., in High Temperature Superconductivity, edited by K.S. Bedell, D. Coffey, D.E. Meltzer, D. Pines, and J.R. Schrieffer (Addison-Wesley, New York, 1990), p. 240 and 392.

Pint, W., E. Langmann, and E. Schachinger, *Physica C* **157**, 415, (1989).

Reynolds, C.A., B. Serin, W.H. Wright, and L.B. Nesbitt, *Phys. Rev.* **78**, 487 (1950).

Rickayzen, G., Theory of Superconductivity (Wiley, New York, 1965).

Saint-James, D., G. Sarma and E.J. Thomas, Type II Superconductor (Pergamon Press, 1968).

Salamon, M.B., in Physical Properties of High Temperature Superconductors I, edited by D.M. Ginsberg (World Scientific, Singapore, 1989), p. 39.

Saunders, G.A. and A.W. Lawson, *Phys. Rev.* **135**, A1161 (1964).

Scalapino, D.J., in Superconductivity R.D. Parks, editor, (Dekker, New York, 1969), p. 449.

Schilling, A., H.R. Ott and F. Hulliger, *Physica C* **161**, 626 (1989).

Schneider, T. and D. Baeriswyl, *Z. Phys. B* **73**, 5 (1988).

Schneider, T., H. De Raedt, and M. Frick, *Z. Phys. B* **76**, 3 (1989).

Schneider, T. and M.P. Sörensen, *Z. Phys. B* **80**, 331 (1990a).

Schneider, T. and M.P. Sörensen, *Z. Phys. B* **81**, 3 (1990b).

Schrieffer, J.R., Theory of Superconductivity (Addison-Wesley, New York, 1964)

Serin, B., in Superconductivity R.D. Parks, editor, (Dekker, New York, 1969), p. 925.

Shapiro, S.M., G. Shirane and J.D. Axe, *Phys. Rev. B* **12**, 4899 (1975).

Shen, L.Y., *Phys. Rev. Lett.* **29**, 1082 (1972).

Sheng, Z.Z. and A.M. Herman, *Nature* **332**, 55 (1988a).

Sheng, Z.Z. and A.M. Herman, *Nature* **332**, 138 (1988b).

Shirane, G., J.D. Axe, and S.M. Shapiro, *Solid State Comm.* **13**, 1893 (1973).

Slichter, C.P., Principles of Magnetic Resonance (Springer-Verlag, Berlin, 1978).

Statt, B.W., *Phys. Rev. B* **42**, 605 (1990a).

Statt, B.W., *Physica B* **165-166**, 1059 (1990b).

Stewart, G.R., *Rev. Mod. Phys.* **56**, 755 (1984).

Tewordt, L. and Th. Wölkhausen *Solid State Comm.* **70**, 839 (1989).

Tewordt, L. and Th. Wölkhausen *Solid State Comm.* **75**, 515 (1990).

Thompson, A.H., *Solid State Comm.* **13**, 1911 (1973).

Thomsen, C. and M. Cardona in Physical Properties of High Temperature Superconductors I , edited by D.M. Ginsberg (World Scientific, Singapore, 1989), p. 409.

Thomsen, C., M. Cardona, B. Friedl, C.O. Rodriguez, I.I. Mazin, and O.K. Anderson, *Solid State Comm.* **75**, 219 (1990).

Thomsen, C., B. Freidl, M. Cieplak and M. Cardona, *Solid State Comm.* **78**, 727 (1991).

Timusk, T. and D.B. Tanner, in Physical Properties of High Temperature Superconductors I, D.M. Ginsberg, editor (World Scientific, Singapore, 1989), p. 339.

Tinkham, M., Superconductivity, (McGraw-Hill Inc., New York, 1975).

Tsuei, C.C, D.M. Newns, C.C. Chi, and P.C. Pattnaik, *Phys. Rev. Lett.* **65**, 2724 (1990).

Valles Jr., J.M., R.C. Dynes, A.M. Cucolo, M. Gurvitch, L.F. Schneemeyer, J.P. Garno, and J.V. Waszczak, *Phys. Rev. B* **44**, 11986 (1991).

Varma, C.M., *Int. J. Mod. Phys. B* **3**, 2083 (1989).

Varma, C.M., P.B. Littlewood, S. Schmitt-Rink, E. Abrahams, and A. Ruckenstein, *Phys. Rev. Lett.* **63**, 1996, (1989).

Varma, C.M., P.B. Littlewood, S. Schmitt-Rink, E. Abrahams, and A. Ruckenstein, *Phys. Rev. Lett.* **64**, 497, (1990).

Vidberg, H.J. and J.W. Serene, *J. Low Temp. Phys.* **29**, 179 (1977).

Walstedt, R., in High Temperature Superconductivity, edited by K.S. Bedell, D. Coffey, D.E. Meltzer, D. Pines, and J.R. Schrieffer (Addison-Wesley, New York, 1990), p. 229.

Werthamer, N.R. and W.L. McMillan, *Phys. Rev.* , 158, 415 (1967).

Wilson, J.A. and A.D. Yoffe, *Advan. Phys.* **18**, 193 (1969).

Winter, J., Magnetic Resonance in Metals, (Clarendon Press, Oxford, 1971).

Wu, M.K., J.R. Ashburn, C.J. Torng, P.H. Hor, R.L. Meng, L. Gao, Z.J. Huang, Y.Q. Wang, and C.W. Chu, *Phys. Rev. Lett.* **58**, 908 (1987).

Yosida, K., *Phys. Rev.* **107**, 901 (1957).

Yosida, K., *Phys. Rev.* **110**, 769 (1958).

Yvon, K. and M. Francois, *Z. Phys. B* **76**, 413 (1989).

Zeyher, R. and G. Zwicknagl, *Solid State Comm.* **66**, 617 (1988).

Zeyher, R. and G. Zwicknagl, *Z. Phys. B* **78**, 175 (1990).

Zhou, C. and H.J. Schulz, *Phys. Rev. B* **45**, 7397 (1992).